ISSN 0711-6659

canadian acoustics
acoustique canadienne

Journal of the Canadian Acoustical Association - Journal de l'Association Canadienne d'Acoustique

JUNE 2007
Volume 35 -- Number 2

JUIN 2007
Volume 35 -- Numéro 2

canadian acoustics

acoustique canadienne

THE CANADIAN ACOUSTICAL ASSOCIATION
P.O. BOX 1351, STATION "F"
TORONTO, ONTARIO M4Y 2V9

L'ASSOCIATION CANADIENNE D'ACOUSTIQUE
C.P. 1351, SUCCURSALE "F"
TORONTO, ONTARIO M4Y 2V9

CANADIAN ACOUSTICS publishes refereed articles and news items on all aspects of acoustics and vibration. Articles reporting new research or applications, as well as review or tutorial papers and shorter technical notes are welcomed, in English or in French. Submissions should be sent directly to the Editor-in-Chief. Complete instructions to authors concerning the required camera-ready copy are presented at the end of this issue.

CANADIAN ACOUSTICS is published four times a year - in March, June, September and December. The deadline for submission of material is the first day of the month preceeding the issue month. Copyright on articles is held by the author(s), who should be contacted regarding reproduction. Annual subscription: $20 (student); $60 (individual, institution); $300 (sustaining - see back cover). Back issues (when available) may be obtained from the CAA Secretary - price $10 including postage. Advertisement prices: $600 (centre spread); $300 (full page); $175 (half page); $125 (quarter page). Contact the Associate Editor (advertising) to place advertisements. Canadian Publication Mail Product Sales Agreement No. 0557188.

ACOUSTIQUE CANADIENNE publie des articles arbitrés et des informations sur tous les domaines de l'acoustique et des vibrations. On invite les auteurs à soumettre des manuscrits, rédigés en français ou en anglais, concernant des travaux inédits, des états de question ou des notes techniques. Les soumissions doivent être envoyées au rédacteur en chef. Les instructions pour la présentation des textes sont exposées à la fin de cette publication.

ACOUSTIQUE CANADIENNE est publiée quatre fois par année - en mars, juin, septembre et décembre. La date de tombée pour la soumission de matériel est fixée au premier jour du mois précédant la publication d'un numéro donné. Les droits d'auteur d'un article appartiennent à (aux) auteur(s). Toute demande de reproduction doit leur être acheminée. Abonnement annuel: $20 (étudiant); $60 (individuel, société); $300 (soutien - voir la couverture arrière). D'anciens numéros (non-épuisés) peuvent être obtenus du Secrétaire de l'ACA - prix: $10 (affranchissement inclus). Prix d'annonces publicitaires: $600 (page double); $300 (page pleine); $175 (demi page); $125 (quart de page). Contacter le rédacteur associé (publicité) afin de placer des annonces. Société canadienne des postes - Envois de publications canadiennes - Numéro de convention 0557188.

GUEST EDITORIAL / ÉDITORIAL INVITÉ

In this special issue of Canadian Acoustics, we are focusing on the higher end of the acoustic spectrum; ultrasound in the megahertz range. More specifically, contributions to this issue centre on the biomedical applications of ultrasound. Just like the frequencies in question are varied, so is the range of applications. In this issue you will find original research articles and review articles spanning such disparate topics as acoustic elastography to Doppler flow imaging. Even so, this issue presents only a coarse sampling of the full "bandwidth" of biomedical ultrasound research and development in Canada. For instance, nationally, we have two manufacturers of biomedical ultrasound devices; each pushing the envelope in their respective niches. Canada has also been the home of several key advances in ultrasound; the development of very high-frequency (above 30 MHz) transducers and devices for use in ultrasound biomicroscopy, the invention of 3D ultrasound imaging, and the first measurements of acoustic scattering from single biological cells – to name just three.

We begin the issue with a reprint of a recent review article that gives a thorough background on many aspects of biomedical ultrasound. You can then read more about the use of ultrasound for measuring blood flow in two different papers. Next are two articles about signal processing techniques; the first, a piece of work focused on raising the signal-to-noise ratio through coded excitation, the other, a work concerning the development of filters to attempt to classify between living and dying tissues. In the following research article, the authors present results of their use of ultrasound to characterise the mechanical properties of arteries and kidneys. The penultimate paper shows that ultrasound imaging can be used to measure the precise movement of muscles. Finally, we learn in the last article that ultrasound is being used therapeutically in dentistry. It's clear from the contents of this special issue that ultrasound has come a long way from the fuzzy obstetric scans that we are all familiar with!

Dans cette édition spéciale de l'Acoustique Canadienne, nous nous concentrons sur les fréquences les plus élevées du spectre acoustique; les ultrasons dans la gamme mégahertz. Plus spécifiquement, les contributions à cette publication sont dédiées principalement aux applications biomédicales des ultrasons. Justement, comme les fréquences en question seront variées, l'envergure des applications le sera aussi. Dans ce numéro vous trouverez des articles originaux de recherches et des comptes-rendus parcourant l'ampleur des matières différentes telles que l'elastographie acoustique et l'imagerie d'écoulement Doppler. Néanmoins, ce numéro présente seulement un « sous-échantillonage » de la recherche et du développement des ultrasons biomédicaux au Canada. Par exemple, nous avons au Canada deux fabricants de dispositifs d'ultrasons biomédicaux; chacun poussant la croissance du développement de dans leurs domaines de spécialisation. Le Canada a également été à l'avant garde de plusieurs progrès majeurs dans le domaine des ultrasons; le développement de transducteurs et d'instruments à très hautes fréquences (au-delà de 30 MHz) pour l'usage dans la biomicroscopie ultrasonore, l'invention de la formation d'images ultrasonores 3D et les premières mesures de la diffusion acoustique de cellules biologiques individuelles – pour seulement en nommer trois.

Nous débutons ce numéro avec une réimpression d'un article de revue qui offre les éléments de base de plusieurs aspects des ultrasons biomédicaux. Vous pourrez ensuite lire deux articles au sujet de l'utilisation des ultrasons dans les mesures d'écoulement du sang. Les deux articles qui suivent présentent des techniques de traitement de signaux; dans le premier, une étude dédiée à l'augmentation du rapport signal/bruit par l'excitation codée et, dans le second, un travail au sujet du développement de filtres pour tenter de différencier entre les tissus vivants et morts. Dans l'article de recherche suivant, les auteurs présentent des résultats de leur usage des ultrasons pour caractériser les propriétés méca-

---

WHAT'S NEW ??

Promotions
Deaths
New jobs
Moves
Retirements
Degrees awarded
Distinctions
Other news

Do you have any news that you would like to share with Canadian Acoustics readers? If so, send it to:

QUOI DE NEUF ?

Promotions
Décès
Offre d'emploi
Déménagements
Retraites
Obtention de diplômes
Distinctions
Autres nouvelles

Avez-vous des nouvelles que vous aimeriez partager avec les lecteurs de l'Acoustique Canadienne? Si oui, écrivez-les et envoyer à:

Steven Bilawchuk, aci Acoustical Consultants Inc., Edmonton, Alberta, Email: **stevenb@aciacoustical.com**

As our journal is increasingly being indexed by the major reference compendiums (e.g., Elsevier B.V.'s Scopus), articles published in Canadian Acoustics are being more easily found by scientists and engineers around the world. I hope that this motivates more of you to submit your work for publication here. To facilitate the process, with the help of Dr. Simant Upreti (Department of Chemcial Engineering, Ryerson University), a LaTeX template for article submission is now available on the CAA web site.

I also encourage you to consider joining us in downtown Montreal for the 2007 CAA Annual Conference will be held at Concordia University, October 9 to 12.

Ralph E. Baddour
Assistant Editor
Department of Medical Biophysics
University of Toronto

niques des artères et des reins. Le papier pénultième montre que l'imagerie ultrasonore peut être employée pour mesurer le mouvement précis des muscles. Finalement, nous apprenons dans le dernier article que les ultrasons sont employés thérapeutiquement dans la médecine dentaire. C'est clair du contenu de cette édition spéciale que les applications des ultrasons ont bien évolué et ne sont plus que les balayages obstétriques brouillés auxquels on est tous accoutumés!

Comme notre journal est de plus en plus indexé par les annuaires principaux de référence (par ex., Scopus de Elsevier B.V.), les articles publiés dans l'Acoustique Canadienne sont davantage retrouvés par les scientifiques et les ingénieurs autour du monde. J'espère que ceci vous encouragera à publier vos travaux dans ce journal. Avec l'aide du Dr Simant Upreti (département du Génie Chimique de l'université Ryerson), un modèle de format LaTeX est maintenant disponible sur le site web de l'ACA pour faciliter la soumission d'articles.

Je vous encourage également de vous joindre à nous au centre-ville de Montréal du 9 au 12 octobre pour le Congrès Annuel 2007 de l'ACA qui se tiendra à l'université Concordia.

Ralph E. Baddour
Rédacteur adjoint
Département de biophysique médicale
Université de Toronto

Medical Diagnostic Ultrasound

E. Carr Everbach
Swarthmore College, Swarthmore, PA, USA

ABSTRACT

Although the roots of medical ultrasound lie in military technology, many of the past decade's advances have come from exploiting new understandings in the physics of mammalian tissues.

As early as 250 BCE, captains of ancient Greek ships would drop lead weights overboard to provide an estimate of water depth. They would count until those "sounders" produced an audible thud and in that way measure the propagation time of the falling weight. Even though the practice has given way to other technologies for sounding, one still hears the phrase "to sound something out." In the 17th century, Isaac Newton became fascinated with sound propagation and was one of the first to describe relationships between the speed of sound and measurable properties of the propagation medium, such as density and pressure. Section 8 of Book 2 of the Principia, for example, is devoted to "the motion propagated through fluids" and includes the proposition that the sound speed is given by the square root of the ratios of the "elastic force" to the density of the medium.

Newton's calculations, however, contained a systematic error for which he could not account, so his estimates of sound speed were always lower than measured values. It took until the advent of thermodynamics in the 19th century for Pierre Simon Laplace and other scientists to discover that acoustic propagation is usually adiabatic rather than isothermal. That is because free propagation does not allow sufficient time for heat exchange between compressive and rarefactive portions of the sound wave. Only in the boundary layer adjacent to a solid surface is the process approximately isothermal, a fact exploited in creating refrigerators whose only moving part is a loudspeaker (see PHYSICS TODAY, June 1999, page 18).

THE DAWN OF ULTRASOUND

Soon after the sinking of the Titanic, piezoelectric materials such as quartz or Rochelle salt were fashioned into acoustic sources whose thickness could be altered slightly by an imposed voltage. Thus underwater "sound navigation and ranging," or sonar, became possible. During World War II, both sonar and its cousin radar (radio detecting and ranging) grew in military importance; after the war they became important to civilian commerce. Sonar's familiar ping enabled vessels to use time-of-flight measurements of echoes to estimate target range and size. Modern biomedical ultrasound began during and immediately after World War II as an extension of sonar to higher frequencies and to the human body.

In the 1950s a single piezoelectric crystal was first employed in contact with skin to launch an acoustic wave into human tissue. The wave consisted of several cycles at a frequency of 20 kHz, beyond the capacity of human hearing. A series of reflections returned to the crystal at different times because of mismatches of acoustic impedance (density x sound speed) between organs or between organs and bone.

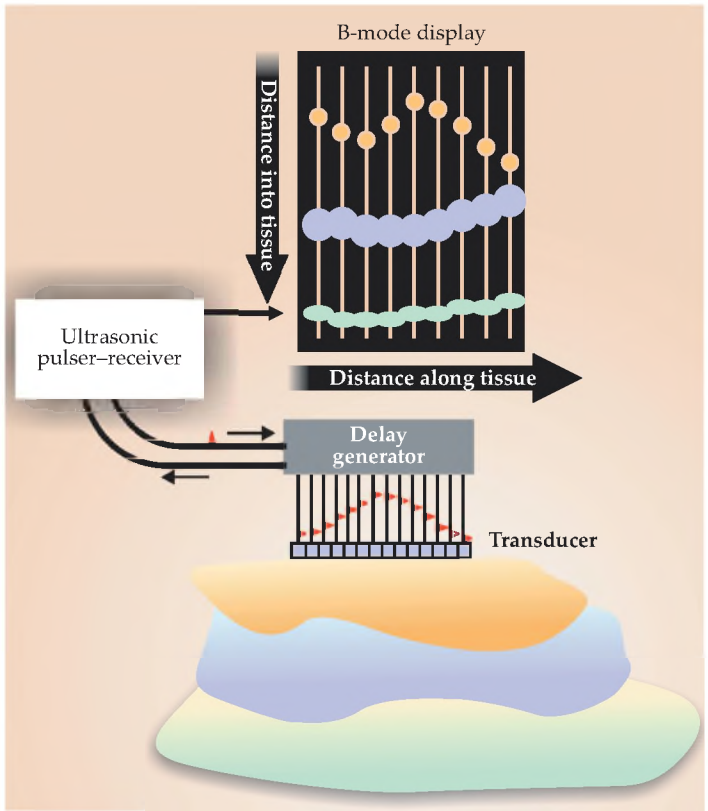

Figure 1. In a B-mode ultrasound image, a transducer scans along a tissue surface and the amplitudes of the reflected ultrasound pulses are encoded as brightness. The display plane is defined by the ultrasound beam and the scanning direction. (Courtesy of Pierre D. Mourad and Shahram Vaezy, University of Washington, Seattle.)

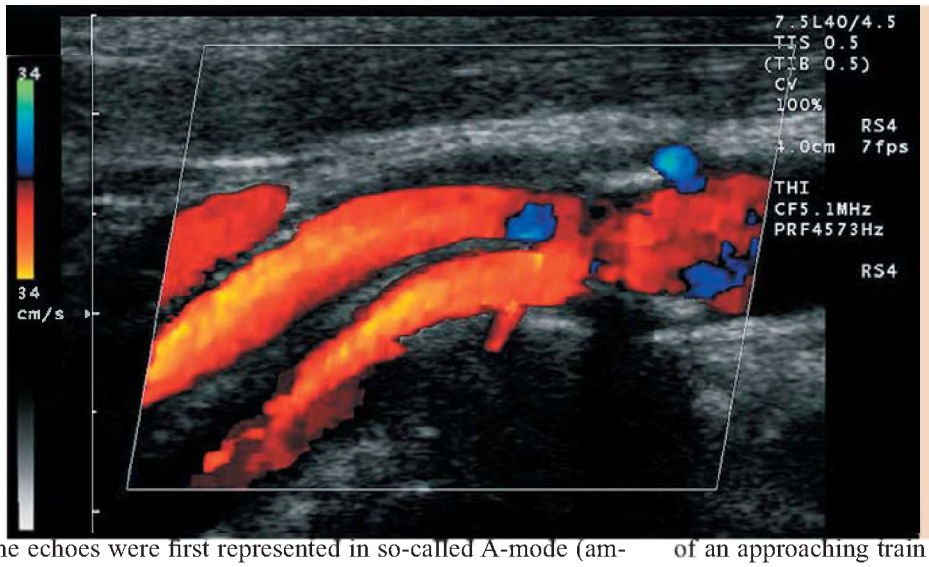

Figure 2. Color flow Doppler image showing blood flow in an artery. The blue regions show regurgitation—blood flow reversed from the principal flow indicated in orange. (Image from Siemens/Acuson, 2003.)

The echoes were first represented in so-called A-mode (amplitude) displays as vertical deflections on the screen of an oscilloscope whose beam scanned horizontally at a constant speed; the result was a series of blips.

Because tissue absorbs acoustic energy as heat, the later the blips occur, the smaller their amplitude. Assuming the speed of sound in human soft tissue has the constant value of 1540 m/s, one can interpret the time between reflections as the distance between tissue layers, and the relative amplitude changes can convey information about the impedance mismatch between one layer and the next. Some pathologies previously diagnosable only with surgery were identified using that early, noninvasive ultrasound technology.

The 1960s saw the development of commercial ultrasound systems that exploited the mass production of cathode-ray tubes. If A-mode amplitudes are represented by the brightness of dots on a phosphor screen and the transducer that generates the ultrasound pulses scans across the tissue, a B-mode (brightness) image results. Assuming, among other things, that the speed of sound is constant allows quantitative imaging of deep tissues, as seen in figure 1. The Quick Study on page 84 of March 2007 issue of *Physics Today* [Ref. 1] discusses the various assumptions that go into ultrasound imaging and the artifacts that arise if those assumptions are violated.

Modern ultrasound scanners use the linear superposition of spherical or cylindrical wavefronts of tiny piezoelectric crystals, usually lead zirconate titanate. Those crystals are arrayed to produce waveforms that can be steered or focused based upon the timing of the crystals' excitations. Both the emitted and received waves may be formed by suitably manipulating timing delays and adjustable gains in the individual elements' amplifiers. Thus a great deal of engineering goes into obtaining the image of a beating heart in an echocardiogram or of a fetus in a sonogram that may be parents' first glimpse of their new child.

DOPPLER ULTRASOUND

The Doppler effect is familiar to all who have heard the horn of an approaching train or considered the redshift of the expanding universe. In 1957 Shigeo Satomura demonstrated that the idea could be applied to ultrasound. If a sinusoidal acoustic frequency f is emitted by a fixed transducer located at an angle θ with respect to a blood vessel inside of which blood cells move with average velocity V, the signals reflected to the transducer will be shifted in frequency by $\Delta f = (2Vf/c)\cos\theta$, where c is the speed of sound in tissue. Thus for blood cells, the Doppler shift, measured by a continuous-wave ultrasound probe transducer, can provide clinical information about blood flow.

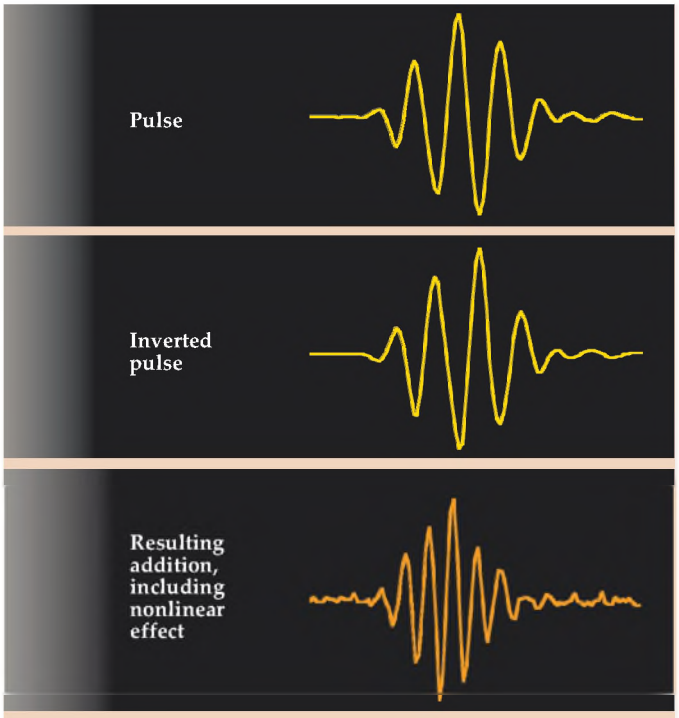

Figure 3. Tissue harmonic imaging relies on the nonlinear properties of tissue. A pulse and its inverse meet in tissue but because of nonlinearities the two pulses do not cancel. Instead, second-harmonic and other components arise. (Courtesy of Kirk D. Wallace, Washington University, St. Louis, Missouri.)

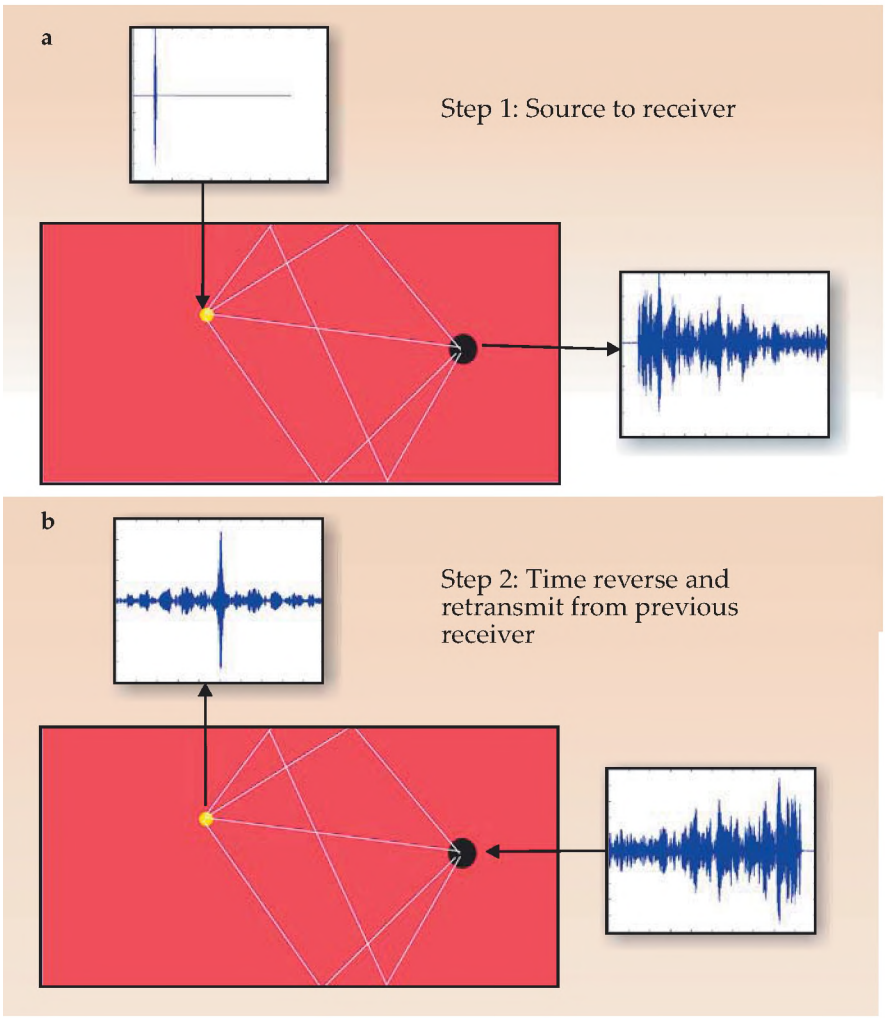

Figure 4. Time-reversal acoustics allows for impressive focusing of ultrasound pulses. **(a)** The yellow dot represents the region in which, ultimately, ultrasound is to be focused. But in the first step of TRA, that region acts as the source of a short burst. The signal received at the black dot is quite complicated. **(b)** Now the source is at the black dot and the initial waveform is the time reversal of the complicated signal received in panel a. The result is high temporal and spatial focusing at the yellow dot, the original source location. (Courtesy of Armen Sarvazyan, Artann Laboratories, West Trenton, New Jersey.)

One complication, however, is that blood is effectively a non-Newtonian fluid whose viscosity is a strong function of shear flow rate. Its sound speed varies with red blood cell concentration, which differs between capillaries and larger vessels. Because red blood cells have a diameter of only about 7 microns – much smaller than the typical acoustic wavelengths of 750 to 150 μm for 2- to 10-MHz ultrasound – they cannot be resolved individually. Instead, the 250 000 to 450 000 red blood cells in each microliter act as an ensemble and scatter back to the transducer a fluctuating pattern of constructive and destructive interference called ultrasonic speckle. Nevertheless, for a continuous-wave Doppler system, the bulk motion of the flowing red blood cells typically provides a frequency shift that falls conveniently in the audio range. The characteristic squee-choo-squee-choo sound of the Doppler audio signal from the pulsatile flow of heartbeats is common in many hospitals and obstetricians' offices.

The biggest limitation of continuous-wave Doppler, however, is its spatial ambiguity. The difficulty arises because the Doppler signal is sensitive to all the vessels that intersect the beam. Pulsed-wave Doppler was developed in the 1970s to provide high spatial resolution; dolphins, bats, and other animals use an analogous technique to locate and identify prey. Finite-length tone bursts are emitted whose durations correspond to the size of the volume to be interrogated. Unlike the continuous-wave case, for which the Doppler-shifted received frequency is compared with the transmitted one, in pulsed-wave Doppler each received echo is compared with a similar echo from the previous transmission. Because the pulse-repetition frequency is high, only small changes in tissue geometry and absorption occur from pulse to pulse. The result is relatively high sensitivity to overall arrangement of overlaying tissues.

In the 1980s a signal-processing breakthrough allowed for the development of color flow Doppler, also called color flow imaging (CFI). At the time, clinicians knew that variations in blood flow velocities in an interrogated volume give rise not to a single Doppler shift, but rather to a whole spectrum of shifted frequencies. Fast-Fourier-transform methods for examining the spectra were too slow and the results too variable to be clinically useful. The new CFI technique estimated the average Doppler-shifted frequency by means of the small relative phase shifts from on reflected pulse to the next. Admittedly, those phase shifts result from slightly different sets of blood cells being present in the interrogated volume from one pulse to the next an so are not, strictly speaking, Doppler shifts of individual scatterers. Nevertheless, as long as the change in scatterer distribution varies only slightly, from pulse to pulse, CFI determines not only the average blood velocity but also a spectrum of velocities that can be color coded to represent forward and reverse blood flow. Such flow data are typically overlaid on the B-mode image in modern ultrasound scanners, as shown in figure 2.

One CFI variation that has found significant use in the past 10 years is so-called power Doppler, in which the integral over all frequencies of the square of the flow speed is shown as a color overlay on the B-mode image. Although information about the direction of flow is lost, the signal-to-

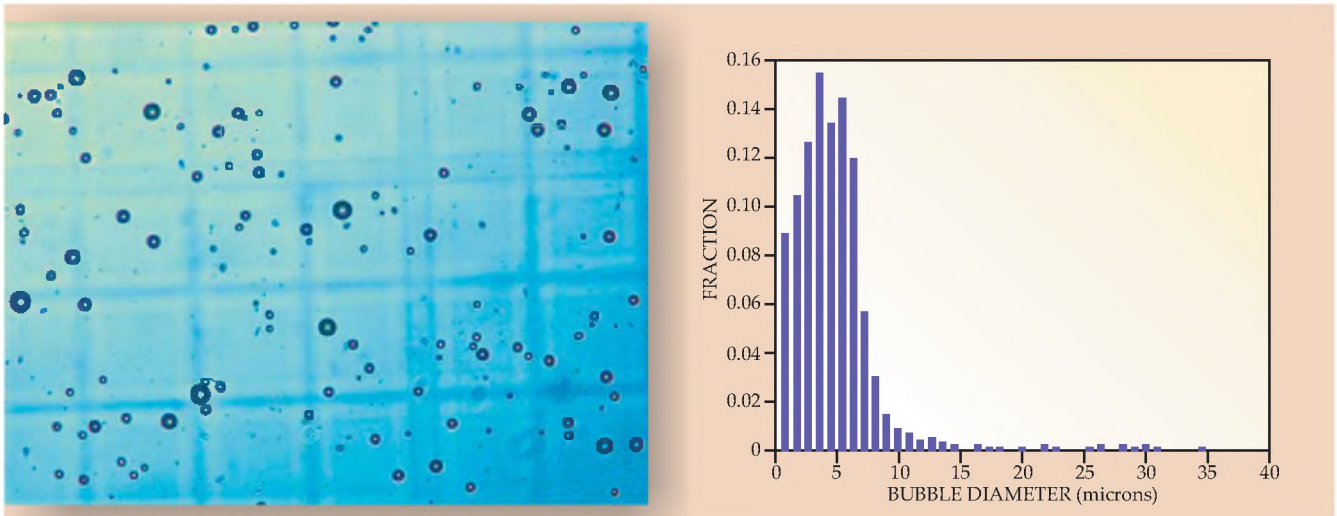

Figure 5. Microscopic bubbles are echo-contrast agents, strong reflectors of ultrasound. They may be used for diagnosis or may incorporate drugs that are delivered to specific sites. The microscope image to the left has a field of view roughly 300 microns across. The histogram to the right shows the size distribution of the bubbles seen in the micrograph. (Courtesy of Pierre D. Mourad and Shahram Vaezy, University of Washington, Seattle.)

noise ratio is increased so that power Doppler can detect tiny speed, or speed of tiny amounts of fluid. It can even image flow in capillaries.

Color flow imaging methods have contributed greatly to the success of ultrasound as a medically important modality. By providing a dynamic picture of blood flow, CFI Doppler has allowed physicians to diagnose leaking heart valves, vessel-blocking plaques and clots, and other abnormalities that would otherwise be difficult to detect.

NONLINEAR ACOUSTICS

The stiffness of biological tissue does not obey Hooke's law. As a consequence, the speed of sound varies locally with pressure and temperature and produces waveform distortion that compounds with propagation distance. If two wave-forms with different frequencies overlap in space and time, the tissue's essential nonlinearity produces sum and difference frequencies in the overlap region.

The acoustic nonlinearity parameter, defined as the ratio of the quadratic to the linear term in a Taylor-series expansion of pressure as a function of density, measures the deviation of the stiffness from Hooke's Law. Because the ratio is sensitive to subtle changes in material composition not reflected in acoustic impedance mismatches, a method of imaging the nonlinearity parameter could add complementary clinical information. To accomplish so-called nonlinear imaging of tissue, one can measure the strength of the sum or difference frequency by scanning a point where two ultrasound pulses intersect. For example, the sum or difference signal can be filtered and detected by a hydrophone or skin mounted sensor. Then the location of the coincident spot can be moved. The amplitude of the signal is proportional to the tissue nonlinearity at each point.

One relatively simple application of nonlinearity is tissue harmonic imaging. Developed in the late 1990s, the technique involves the combination of waveforms with the same frequency but opposite phase. Figure 3 shows a typical imaging pulse emitted from one piezoelectric element of an ultrasound transducer, with time on the horizontal axis and voltage, or pressure, on the vertical. If another array element is excited simultaneously with the inverse signal, the two pulses will mostly cancel each other's fundamental frequency where they overlap. Tissues nonlinearities, however, tend to move energy from the fundamental up to the second harmonic, which has twice the fundamental frequency. The effect of such distortion is slightly different for the pulse and its inverse, and the result is a reinforcement of the second harmonic. The focal area of the transducer, in sum, sees a pulse with a frequency and hence spatial resolution twice that of its B-mode equivalent and reflects that pulse back to the receiving elements of the transducer. Indeed, most ultrasound scanners in use today transmit signals at one frequency and listen to the returning echoes at twice that frequency, thus achieving better spatial resolution and improved signal-to-noise ratio.

To use nonlinear superposition, large-amplitude pulses must be made to intersect within the tissue volume. Since the late 1990s, a techniques known as time-reversal acoustics (TRA) has provided a new tool to help accomplish that task. The basic idea is shown schematically in Figure 4. In the first step, an acoustic source produces a pulse that propagates along many different rays to a receiver; the result is a complicated impulse response. In the second step, the pattern of pulse arrivals at the receiver is reversed, and the receiver now acts as a transmitter. Because the wave equation is time-reversal invariant, the pulses follow the step-1 rays in reverse and end up coinciding at the original source as a highly spatially and temporally focused pulse. In effect, the tine-reversed signal at the receiver acts as an optimum

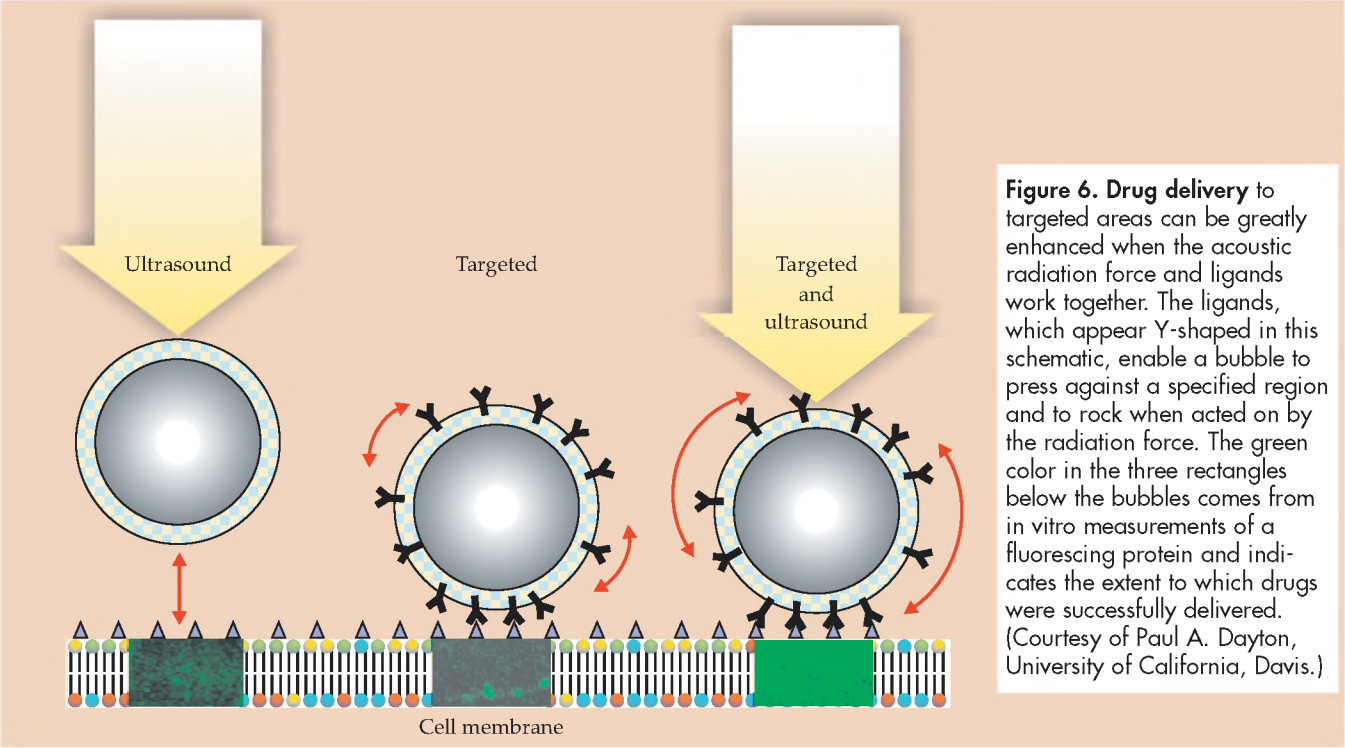

Figure 6. Drug delivery to targeted areas can be greatly enhanced when the acoustic radiation force and ligands work together. The ligands, which appear Y-shaped in this schematic, enable a bubble to press against a specified region and to rock when acted on by the radiation force. The green color in the three rectangles below the bubbles comes from in vitro measurements of a fluorescing protein and indicates the extent to which drugs were successfully delivered. (Courtesy of Paul A. Dayton, University of California, Davis.)

filter to deliver subwavelength focusing at the original source location.

In practice, TRA required that a source be placed in the body, although that source could be the tip of a biopsy need used to reflect incident ultrasound. If the receiver is not a single transducer but many transducers mounted on a surface, a highly focused spot can be generated at the site of the original source. TRA may be combined with other modalities to further improve focusing. One therapeutic application is to brain tumors at which ultrasound is applied. In that case, computed technology (CT) x-ray data can be used to compensate for the attenuation of the skull and the aberrations it causes to the acoustic field. Such dual-modality techniques are becoming more popular because techniques such as CT or magnetic resonance imaging provide information complementary to the mechanical parameters determined by ultrasound and thereby aid detection of pathology.

TINY BUBBLES

An increasingly important technique in diagnostic ultrasound involves blood-cell-sized microbubbles of perfluorocarbon gas, coated with proteins, lipids, or polymers (see figure 5). Such echo-contrast agents act as reflectors of ultrasound and are especially useful for quantifying blood flow in capillary beds or, when the bubbles' coatings contain biochemical markers called ligands, for helping doctors identify pathologies. Indeed, clot-sticking coatings may help not only to identify stroke-causing blood clots but also to treat them, since high-amplitude ultrasound pulses may destroy bubbles and release clot-dissolving drugs.

Due to the acoustic impedance mismatch between bubbles and blood, bubbled reflect ultrasound strongly. The resulting reaction force, called the acoustic radiation force, pushes bubbles away from a transducer producing an ultrasound beam, or toward the pressure antinodes in an acoustic standing wave.

Each bubble has an acoustic resonance frequency related to the mass of the liquid around the bubble and the stiffness of the gas inside it. For an ultrasonic beam with a dominant frequency component near a bubble's resonance frequency, the acoustic radiation force can be strong enough to push the bubble to a vessel wall where drugs in the bubble coating can be released. As shown in figure 6, the combination of ligands to help the bubbles stick to the surface with an acoustic radiation force to press and wiggle the bubbles on the vessel wall enables a dramatic improvement in drug delivery compared with cases in which either the ultrasound or ligands are absent. A specific example of targeted drug delivery using ultrasound and bubbles is the delivery of chemotherapeutic agents to a tumor only, rather than systemically.

When a bubble is driven near resonance at a sufficiently large acoustic amplitude, its diameter can change appreciably during an acoustic cycle. If the maximum diameter is less than twice the undisturbed diameter, the bubble is said to undergo stable acoustic cavitation; its motion is mainly governed by the stiffness of the gas inside it. If the diameter more than doubles, the motion is controlled by the mass of the liquid surrounding the bubble; it undergoes inertial cavitation. Inertial cavitation bubbles commonly implode with such force that pressures thousands of atmospheres and temperatures of tens of thousands of Kelvin occur at their centers (see the article by Detlef Lohse in *PHYSICS TODAY*,

Continued on Page 9

SOUNDBOOK

Multichannel SLM IEC61672-1, IEC60804 & IEC60651 Type 1
SAMURAI Basic Software includes Sound Recorder, Frequency Analyzer, Reverberation time measurement
2/4/8/channels with 40kHz bandwidth, 2x tacho, 5 AUX and 2/4 analog outputs
Various software options for Acoustics and Vibration
Remote Control, Netwotk Integration & wireless synchronization of several devices possible
Alternative packages for ME'scope(direct device), si++workbench, SINUS MATLAB Toolbox
PTB Type Approval

SINUS
G.R.A.S. SOUND & VIBRATION
LDS DACTRON
01dB-Stell
Dytran Instruments, Inc.
MetroLaser, Inc.
Vibrant Technology, Inc.

Integrated Solutions from World Leaders

Precision Measurement Microphones
Intensity Probes
Outdoor Microphones
Hydrophones
Ear Simulation Devices
Speech Simulation Devices
Calibrators
Array Microphones
Sound Quality
Sound Intensity
Sound Power
Room Acoustics
Noise Monitoring
Dynamic Signal Analyzers
Multi Channel Dynamic Analyzer/Recorders
Electro Dynamic Shaker Systems
Advanced Sound & Vibration Level Meters
Doppler Laser Optical Transducers (Laser Vibrometers)

New KEMAR Manikin

Ottawa
613-598-0026
info@noveldynamics.com

NOVEL DYNAMICS INC.
Dynamic Test and Analysis Systems

Toronto
519-853-4495
Ametelka@cogeco.ca

Continued from Page 7

February 2003, page 36). Nearby tissues can be destroyed – a result to be avoided in diagnostic applications but one that can be useful for therapy. Nowadays, microbubble-ultrasound interactions also see applications that range from breaking kidney stones with acoustic shock waves (lithotripsy) to noninvasive removal of cholesterol plaque from arteries. If the echo-contrast bubbles span an appropriate size range, both kinds of cavitation may be present simultaneously. Because stable cavitation generates acoustic emissions below the beam frequency and inertial cavitation produces broadbandwidth acoustic noise at the moment of implosion, bubble activity can be detected and quantified. Such monitoring may make it possible to harness the potentially destructive effects of ultrasound for new therapies while avoiding adverse bioeffects in diagnostic applications, a greater understanding of the nonlinear mechanical properties of tissues, of bubbles, and of their interactions hold the promise of more advances in the medical use of ultrasound.

[**Note:** This article expands on a tutorial lecture first presented on 17 October 2005 at the Acoustical Society of America meeting in Minneapolis, Minnesota]

REFERENCES

1. Kremkau, F. W. "Seeing is believing? Sonographic artifacts," Physics Today, 60(3), pp 84-85, 2007.

ADDITIONAL READING

F.V. Hunt, Origins in Acoustics: The Science of Sound from Antiquity to the Age of Newton, Yale U. Press, New Haven, CT (1978).

R.T. Beyer, Sounds of Our Times: Two Hundred Years of Acoustics, AIP Press/Springer, New York (1999).

T.L. Szabo, Diagnostic Ultrasound Imaging: Inside Out, Elsevier Academic Press, Burlington, MA (2004).

Noise Pollution

The SLARM™ Solution

The **SLARM**™ developed in response to increased emphasis on hearing conservation and comfort in the community and workplace incorporates **ACOustAlert**™ and **ACOustAlarm**™ technology. Making the **SLARM**™ a powerful and versatile sound monitoring/alarm system.

Typical Applications Include:

Community

- ♦Amphitheaters
- ♦Outdoor Events
- ♦Nightclubs/Discos
- ♦Churches
- ♦Classrooms

Industrial

- ♦Machine/Plant Noise
- ♦Fault Detection
- ♦Marshalling Yards
- ♦Construction Sites
- ♦Product Testing

FEATURES

- √ **Wired and Wireless (opt)**
- √ **USB, Serial, and LAN(opt) Connectivity**
- √ **Remote Display s and Programming**
- √ **SPL, Leq, Thresholds, Alert and Alarm**
- √ **Filters (A,C,Z), Thresholds, Calibration**
- √ **Multiple Profiles (opt)**
- √ **100 dB Display Range:**
- √ **20-120 dBSPL and 40-140 dBSPL**
- √ **Real-time Clock/Calendar**
- √ **Internal Storage: 10+days @1/sec**
- √ **Remote Storage of 1/8 second events**
- √ **7052S Type 1.5™ Titanium Measurement Mic**

ACO Pacific

2604 Read Ave., Belmont, CA 94002 Tel: 650-595-8588 FAX: 650-591-2891

www.acopacific.com acopac@acopacific.com

ACOustics Begins With ACO™

FREQUENCY-BASED SIGNAL PROCESSING FOR ULTRASOUND COLOR FLOW IMAGING

Alfred C.H. Yu, K. Wayne Johnston, and Richard S.C. Cobbold
Institute of Biomaterials and Biomedical Engineering, University of Toronto
164 College Street, Toronto, ON, Canada. M5S 3G9
cobbold@ecf.utoronto.ca

ABSTRACT

In ultrasound color flow imaging, the computation of flow estimates is well-recognized as a challenging problem from a signal processing perspective. The flow visualization performance of this imaging tool is often affected by error sources such as the lack of abundant signal samples available for processing, the presence of wideband clutter in the acquired signals, and the flow signal distortions that may arise during clutter suppression. In this article, we review existing frequency-based signal processing approaches reported in the ultrasound literature and evaluate their theoretical advantages as well as limitations. In particular, four major classes of clutter filter designs are considered: FIR/IIR filtering, polynomial regression, clutter-downmixing, and eigen-regression. Also, three types of frequency estimators are discussed: lag-one autocorrelation, autoregressive modeling, and MUSIC. In examining these approaches, it was concluded that eigen-based methods like the eigen-regression filter and the MUSIC estimator can better adapt to the Doppler signal characteristics, and thus they seem to have more potential for obtaining flow estimates that are less affected by the signal processing error sources.

SOMMAIRE

En imagerie couleur en flux d'ultrasons, le calcul des estimations d'écoulement est un problème bien connu d'un point de vue traitement de signaux. La performance de cet outil d'imagerie au niveau de la visualisation, est souvent affectée par différentes sources d'erreur telles que le manque de signaux disponibles par échantillon pour le traitement, la présence de clutter à bande large durant l'acquisition, et les déformations de signal d'écoulement qui peuvent surgir pendant la suppression des clutter à bandes larges. Dans cet article, nous passons en revue les approches actuelles décrites dans la littérature de traitements de signaux basées sur la fréquence, et nous évaluons leurs avantages théoriques ainsi que leur limitations. En particulier, les principales classes de conceptions de filtre de clutter considérées incluent: la filtration FIR/IIR, la régression polynomiale, le bas-mélange de clutter, et l'eigen-régression. Trois types d'estimateurs de fréquence sont discutés, à savoir, l'autocorrélation lag-one, la modelisation auto-régressif, et MUSIC. En examinant ces approches, nous avons pu conclure que les méthodes basées sur eigen- tel que le filtre de régression eigen et l'estimateur de MUSIC peuvent mieux s'adapter aux caractéristiques de signal de Doppler. Par conséquent, les stratégies de traitement de signaux basées sur eigen semblent être pus aptes à obtenir des estimations d'écoulement qui sont moins affectées par les sources d'erreur de traitement de signaux.

1. INTRODUCTION

Ultrasound color flow imaging is a diagnostic tool that is useful to the study of cardiovascular flow dynamics. As reviewed by Ferrara and DeAngelis [1], it has been used to identify the presence of vascular stenoses, assess complicated flow patterns, diagnose for the development of aneurysms and tumors, study the patency of implanted shunts, and visualize blood regurgitations between heart chambers during a cardiac cycle. More recently, this diagnostic tool has found new applications such as micro-circulation assessment in the eyes [2], treatment response monitoring during cancer therapies [3], contractility examination of heart muscles [4], and guidance of interventional devices [5]. Comparing with other non-invasive vascular imaging modalities such as magnetic resonance angiography, ultrasound color flow imaging has the advantage of being able to provide flow information in real-time [6]. Further-more, it is an imaging tool that is more affordable by most clinics.

Given the widespread use of ultrasound color flow imaging in medical diagnostics, it is important for these images to provide accurate visualization of the vascular flow dynamics. As pointed out in some evaluation studies (e.g. see [7][8]), failure to provide accurate flow information in color flow images may lead to an increased risk of mis-

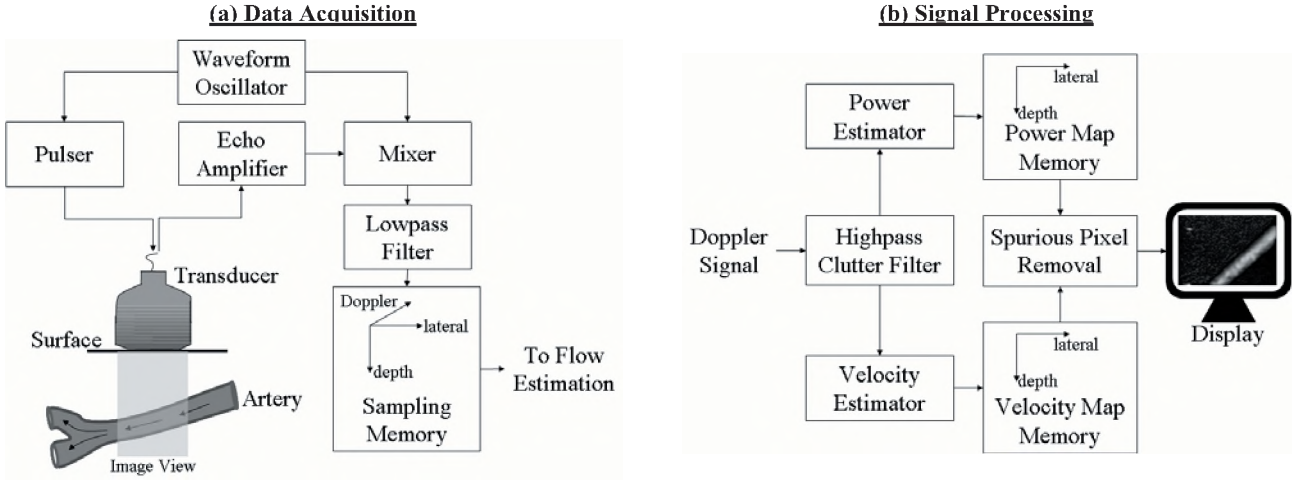

Figure 1. Overview of a generic ultrasound color flow imaging system. Shown in (a) and (b) are the block diagrams for the data acquisition and signal processing stages.

diagnosis and may cause assessment difficulties during long-term patient monitoring. However, from a signal processing perspective, there are several factors that tend to reduce the accuracy of blood flow estimates displayed in color flow images. These sources of errors can generally be divided into two categories: 1) those that arise during suppression of clutter in the color flow data, and 2) those that arise during estimation of blood flow velocities. The main signal processing sources of errors encountered during clutter suppression are mainly associated with the small Doppler ensemble size (less than 20 samples) available for data processing and the possible presence of wideband clutter when using longer data acquisition periods. On the other hand, the primary signal processing error source in velocity estimation is related to the blood signal distortions resulting from the clutter filtering process. In terms of their impact, these error sources may lead to the appearance of spurious or erroneous flow map pixels (commonly referred to as flash artifacts) in the color flow images. In turn, they may obscure visualization of the underlying flow dynamics.

The intent of this paper is to point out the origin of signal processing problems encountered in ultrasound color flow imaging and survey the approaches that have been reported previously to resolve these problems. In particular, it is our intent to theoretically compare various clutter filter designs and frequency-based flow estimation methods reported in the ultrasound literature. To help formulate our discussion, we begin with a general overview on the principles of color flow imaging. The signal processing error sources and existing solutions will then be described later on. Note that many of the signal processing strategies covered in this article are also used in advanced color flow imaging schemes like three-dimensional (3D) flow mapping [9], dual-beam vector flow studies [10], high-frequency flow imaging [11], and contrast-enhanced flow studies [12]. However, this article will not directly discuss the issues specific to these advanced imaging techniques.

2. OVERVIEW OF ULTRAOUND COLOR FLOW IMAGING

2.1. Fundamental Principles

As recently pointed out in a historical account by Cobbold [13] (Sec. 10.7), ultrasound color flow imaging was first commercially introduced in the 1980s. This technique is based on the periodic transmission of finite-duration ultrasound pulses into the imaging view and the subsequent processing of pulse echoes returned from tissue as well as blood scatterers. For this technique, flow information is derived by measuring the relative time shifts between pulse echoes (i.e. pulse-to-pulse changes in the echo return time), whereby the shift magnitude is dependent on the scatterer velocity. As derived in various ultrasound textbooks (e.g. see Sec. 10.2 in [13]), the inter-pulse time shift t_D can be described by the following expression:

$$t_D = \frac{2vT_{PRI}}{c_o}\cos\theta, \tag{1a}$$

where v is the scatterer velocity, T_{PRI} is the pulse repetition interval, c_o is the speed of sound, θ is the beam-flow angle, and the factor of two indicates round-trip propagation. Note that the time shifts described in (1a) can actually be interpreted as a frequency-shift mechanism. In particular, given that frequency is equal to the phase change over time (by definition), the time shift between pulse echoes carries the following frequency interpretation:

$$f_D = \frac{\Delta\phi}{\Delta t} \approx \frac{f_o t_D}{T_{PRI}} = \frac{2vf_o}{c_o}\cos\theta, \tag{1b}$$

where $\Delta\phi = f_o t_D$ indicates the phase change between pulse echoes. It is worth pointing out that (1b) essentially has the same form as the Doppler equation that is well-known in physics. Hence, color flow imaging is often perceived as a Doppler-based flow visualization technique.

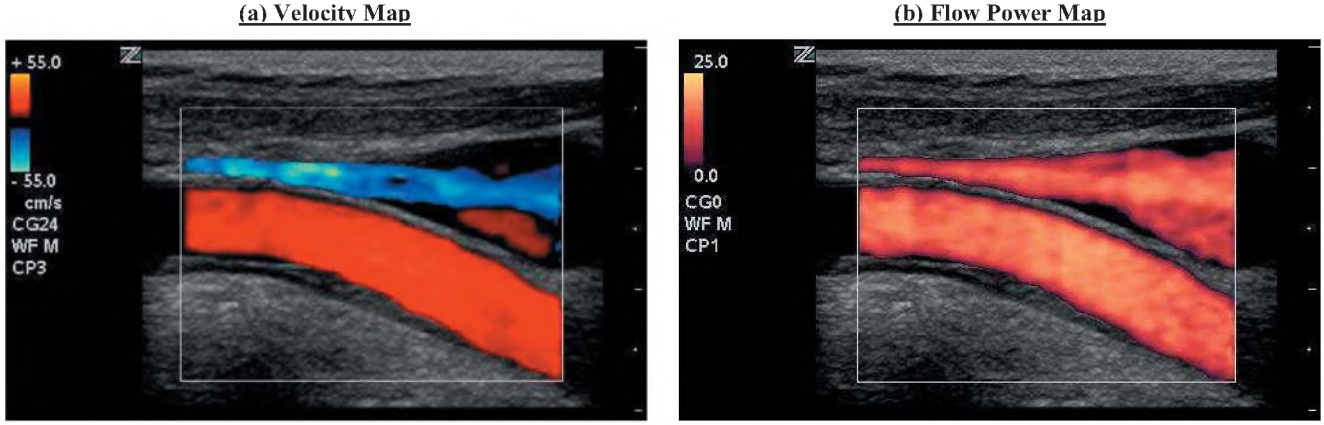

Figure 2. Color flow images for an in-plane slice of a human common carotid artery and jugular vein. (a) Velocity map showing directional flow in red and blue hues; (b) Flow power map showing blood signal strength in pale-red hues. Reproduced with permission from ZONARE Medical Systems (Mountain View, CA, USA).

2.2. System-Level Description

Data Acquisition

From a system-level perspective, the formation of each color flow image can be divided into two main stages: data acquisition and signal processing. As illustrated in Figure 1a, the data acquisition stage first involves the use of an ultrasound transducer (often an array transducer) to transmit the pulse firings and collect the returned echoes. In order to produce an image, the pulse firing sequence is repeated for different beam lines within the field of view. Subsequently, the received echoes from the different pulse firings are individually downmixed to baseband by mixing the echoes with the carrier frequency of the transmitted pulse and applying a lowpass filter to retain only the baseband spectral components in the mixed echoes. For this downmixing process, the in-phase/quadrature (I/Q) demodulation scheme is often implemented so that the analytic form of the pulse echoes can be obtained for subsequent analysis. After the pulse echoes are downmixed, they are sampled at time points that correspond to various depths in order to study the inter-pulse phase changes or time shifts at various axial and lateral positions (i.e. sample volumes) within the field of view. The resulting data samples can then be arranged into a 3D data array: one dimension for pulse number, one for depth/axial position, and the other for line/lateral position. Since the pulse-number dimension of the 3D data array essentially contains information on the inter-pulse phase changes, this dimension is also referred to as the Doppler axis[1]. As well, the ensemble of pulse echo samples for a particular sample volume is referred to as the Doppler signal. Note that, in general, this entire data acquisition procedure can be considered as a sampling mechanism in which one Doppler data sample is collected for each sample volume along a beam line during each pulse firing.

[1] The pulse-number dimension is also referred to as the "slow-time" axis, while the depth dimension is sometimes called the "fast-time" axis.

Signal Processing

In the signal processing stage of ultrasound color flow imaging, a flow power map and a velocity map are computed from the array of Doppler signals acquired through the pulse firings. Most commercial systems compute these two forms of flow information through a frequency-based estimation approach (i.e. by studying the inter-pulse phase changes) because of its relatively simpler computation complexity as compared to time-shift-based estimation approaches (see Sec. 4.5.3 in [14]). As shown in Figure 1b, the frequency-domain flow estimation process first involves the use of a digital highpass filter to suppress low-frequency echoes that may be present in each Doppler signal. This filtering operation is carried out in attempt to distinguish the Doppler echoes of blood scatterers from signal clutter originating from acoustic reverberations of nearby tissues (whose strength can reach 60-80 dB greater than blood depending on the scanner's dynamic range). After the filtered data samples are obtained, the average power of each post-filter Doppler signal is estimated by simply finding the mean-squared signal value. The velocity estimate for each sample volume is also determined by first finding the mean Doppler frequency of the filtered signal and then converting this estimate into a velocity value via the Doppler equation (and assuming that the other parameters are constants). Once the power and velocity estimates are computed for all the sample volumes, they are turned into image pixels by respectively mapping the flow estimates onto a power map color scale and a velocity map color scale. Since blood flow may not be present in all places within the field of view, spurious map pixels are removed from the power and velocity maps if their corresponding filtered Doppler power is below a threshold. Finally, the resulting flow map is superimposed onto a B-mode image to form a duplex display, thereby enabling the flow information to be related to the underlying structure.

Figure 2 shows an example of flow power map and velocity map for a human common carotid artery and the adjacent jugular vein. Note that, at large beam-flow angles, the flow power map has diagnostic advantage over the

velocity map because the echo power returned from blood scatterers is essentially independent of the beam-flow angle (while the time shift magnitude is angle-dependent). On the other hand, the velocity map has the advantage of being able to provide directional flow information that is clinically important for the identification of arteries and veins.

3. SIGNAL PROCESSING CHALLENGES IN COLOR FLOW IMAGING

3.1. Challenges in Clutter Suppression

Doppler Ensemble Size Limitations

In color flow imaging, the range of pulse repetition intervals that can be used for data acquisition is bounded by two factors: real-time imaging requirements and imaging depth limits. In particular, the maximum pulse repetition interval mainly depends on real-time constraints because all the pulse echoes from every beam line need to be acquired within a frame period that corresponds to a real-time frame rate (i.e. at least 5-10 Hz). On the contrary, the minimum pulse repetition interval depends primarily on the maximum imaging depth because sufficient time between firings is needed to collect pulse echoes from the field of view. Based on the two constraints, the pulse repetition interval T_{PRI} must be defined within the following range for a given maximum depth d_{max}, acoustic speed c_o, frame period T_F, number of beam lines N_L, and Doppler ensemble size N_D:

$$\frac{2d_{max}}{c_o} \le T_{PRI} \le \frac{T_F}{N_L N_D}. \quad (2)$$

Amongst the three dependent factors seen in the upper limit of (2), the Doppler ensemble size N_D is the only factor that can be modified for a given image dimension and frame rate. Typically, for an imaging view with 30-60 beam lines, the ensemble size available for each Doppler sample volume is limited to fewer than 20 samples so that the pulse repetition interval can be set to a value that satisfies both real-time constraints and imaging depth limits. However, with such a small ensemble size, it becomes more difficult to suppress low-frequency clutter in the Doppler signal because the transient response of digital filters tends to dominate the filter output for small input ensembles [15]. In order to address this problem, it is necessary to develop strategies that can mitigate the transient filtering effects.

Wideband Clutter Problems

Since the Doppler ensembles are sampled data after all, they are inherently limited to a finite Doppler spectral resolution. From sampling theory, it is well-known that the spectral resolution inversely depends on the ensemble period (i.e. $f_{D(res)} = 1/N_D T_{PRI}$). By substituting this relation into the Doppler equation as given by (1b), the velocity resolution of a Doppler ensemble is given by:

$$v_{res} = \frac{c_o}{2 f_o N_D T_{PRI} \cos\theta}. \quad (3)$$

As seen in (3), an increase in ensemble period $N_D T_{PRI}$ or ultrasound frequency f_o can result in an improved velocity resolution, which is often important for studying slow flow dynamics. However, amongst these two factors, it is only feasible to increase the ensemble period when imaging low-velocity flow at greater depths because high-frequency ultrasound cannot penetrate well into tissue. Such a lengthening of the ensemble period though may be a problem because tissues may undergo substantial motion over this extended period. As pointed out by Heimdal and Torp [16], the clutter component of the Doppler signal may become more wideband as a result and may actually be shifted away from zero frequency. To account for this wideband Doppler clutter, it may be possible to simply use a highpass filter that has a widened stopband (plus suitable transient-reduction methods). Nonetheless, this approach may concomitantly suppress a substantial portion of the blood echoes.

3.2. Challenges in Velocity Estimation

Carrier Frequency Variations

Given the filtered Doppler signal, one simple way of estimating the mean flow velocity is to compute the mean Doppler frequency from the Doppler spectral moments and then use (1b) to convert the mean frequency estimate into velocity. However, the resulting velocity estimates may be biased when there are variations in the carrier frequency of returned echoes simply because the pulse carrier frequency is one of the governing factors in the Doppler equation [17]. As described in a few studies [18][19], attenuation and scattering are the two primary distortion mechanisms that affect the pulse carrier frequency. They tend to bring about a gradual shift in the pulse carrier frequency as the imaging depth increases, and the shift magnitude per unit depth is mainly dependent on the bandwidth of the transmit pulse. Fortunately, this problem is usually of less concern in color flow imaging because narrowband transmit pulses (in the form of multi-cycle sinusoidal bursts) typically need to be used in order to improve the blood echo sensitivity and maintain adequate blood-signal-to-noise ratios. Nonetheless, variations in the carrier frequency can become a significant velocity biasing problem when wideband transmit pulses are used for data acquisition.

Clutter Filter Distortions

The primary side effect of using a filter to suppress low-frequency clutter is that the blood component of the Doppler signal may be distorted due to non-idealities in the filter's frequency response [20][21]. The distortions can be particularly severe if the blood signal's Doppler spectral components are located near the cutoff frequency and its transition region. As a result of these potential distortions, there may be a bias in the mean velocity estimates computed from the filtered Doppler signal. Note that, at low blood-signal-to-noise ratios, the biasing problem becomes worse because the clutter filter also distorts the background white noise and thereby adds further bias to the flow estimates. Hence, the clutter filter is often considered as a principal source of bias in the velocity estimation process.

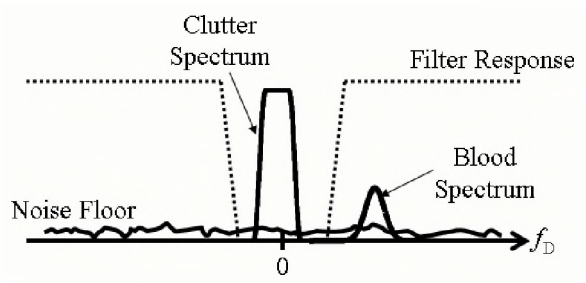

Figure 3. Illustration of the typical spectral contents in a Doppler signal (before digital sampling). Prior to flow estimation, it is often necessary to suppress the high-energy, low-frequency clutter in the Doppler signal.

To avoid this biasing source, it is beneficial to develop velocity estimation methods that can be directly applied to the raw (i.e. unfiltered) Doppler data.

4. EXISTING CLUTTER FILTER DESIGNS

4.1. Non-Adaptive Filters

Background Considerations

To facilitate description of clutter filter designs, we first consider a simple Doppler signal model for an individual sample volume (or map pixel location). As shown in Figure 3, the Doppler signal is consisted of low-frequency clutter echoes, blood echoes, and random white noise. For a given Doppler ensemble size N_D, this signal model can be written in the following vector form:

$$\mathbf{x} = [x(0), x(1), \ldots, x(N_D - 1)]^T = \mathbf{b} + \mathbf{c} + \mathbf{w}, \quad (4)$$

where $x(n)$ is the n^{th} Doppler data sample, while $\mathbf{x}$, $\mathbf{b}$, $\mathbf{c}$, and $\mathbf{w}$ are vectors of length N_D for the Doppler signal, the blood echoes, the clutter echoes, and white noise respectively. To study the Doppler frequency (or time shifts) of blood echoes in the Doppler signal, it is often necessary to first use a highpass filter to suppress the high-energy, low-frequency clutter. From a vector space perspective, this filtering task can be considered as the application of a linear matrix operator on the Doppler signal vector. As such, the filtered Doppler signal vector $\mathbf{y}$ can be expressed as follows:

$$\mathbf{y} = [y(0), y(1), \ldots, y(N_D - 1)]^T = \mathbf{F}\mathbf{x}, \quad (5)$$

where $y(n)$ is the n^{th} filtered sample and $\mathbf{F}$ is an $N_D \times N_D$ filter matrix. Note that, depending on how the filter matrix is formed, the clutter filter may have a time-variant frequency response. Thus, as pointed out by Torp [15], the filter's frequency response may not be equal to the Fourier transform of its impulse response. Nevertheless, it is still possible to numerically compute the frequency response of these time-variant clutter filters by finding the filter's output power for different complex sinusoid inputs. Based on this notion, the filter response $H(f_D)$ at a particular Doppler frequency can be expressed as follows:

$$H(f_D) = \left\| \mathbf{F}\mathbf{v}_{CS} \right\|^2 = \mathbf{v}_{CS}^H \mathbf{F}^H \mathbf{F} \mathbf{v}_{CS}, \quad (6a)$$

where $\mathbf{v}_{CS}$ is a complex sinusoid vector of length N_D, and is given by:

$$\mathbf{v}_{CS} = \left[1, e^{j2\pi f_D}, \ldots, e^{j2\pi f_D (N_D - 2)}, e^{j2\pi f_D (N_D - 1)}\right]^T. \quad (6b)$$

FIR and IIR Filters

It is well-known that the finite impulse response (FIR) filter and the infinite impulse response (IIR) filter are the two common types of linear filters used in signal processing. As described in various signal processing textbooks (e.g. see Ch. 6 and 7 in [22]), the FIR filter is a non-recursive filter whose output samples only depend on the input data samples, and hence its impulse response has a finite duration. On the other hand, the IIR filter is a recursive filter whose output samples depend on both input data samples and past output, and correspondingly its impulse response carries on for an infinite time. For both types of filters, the filter order is essentially equivalent to the number of input samples that each filter output depends on. A higher filter order can yield a sharper transition band and a more uniform passband in the filter's steady-state frequency response, but it also brings about a lengthening of the filter's transient response. Note that, for a K^{th}-order IIR filter, its n^{th} output sample can be expressed as follows:

$$y(n) = -\sum_{k=1}^{K} c_k y(n-k) + \sum_{k=0}^{K} b_k x(n-k), \quad (7a)$$

where c_k and b_k are the respective weights of past output samples and input samples used in the filter, and they can be found using approaches like Butterworth and Chebyshev design methods. The output for FIR filters essentially has the same form as shown in (7a) except that all the weights of past output samples are set to zero (i.e. c_k=0). The input weights for FIR filters can be found using approaches such as the windowing method and the Parks-McClellan algorithm.

From a state-space perspective, the output of both FIR and IIR filters can be considered as a joint contribution from the filter's initial state and the input samples. In particular, as described by Bjaerum *et al.* [23], the filter output can be expressed in the following vector form:

$$\mathbf{y} = \mathbf{T}\mathbf{v}_{init} + \mathbf{S}\mathbf{x}, \quad (7b)$$

where $\mathbf{v}_{init}$ is the initial filter state vector of length K (i.e. the filter order), while $\mathbf{T}$ and $\mathbf{S}$ are respectively the transient filter matrix (of size $N_D \times K$) and the steady-state filter matrix (of size $N_D \times N_D$) whose entries depend on the filter weights c_k and b_k shown in (7a). For FIR filters, the initial filter state vector only affects the filter output for a finite duration; however, for IIR filters, this vector has an effect on the filter output all the time since the filter's impulse response never vanishes. As such, the initial state vector should be defined in a way so that the filter's transient effects can be mitigated. Based on this notion, a few studies have considered the use of time-variant initialization approaches like step initialization and projection initialization [24][25]. Recently, Bjaerum *et al.* [23] have shown that projection initialization is more effective because it gives a stopband frequency response that looks the most similar to the steady-state response. This initialization approach, as

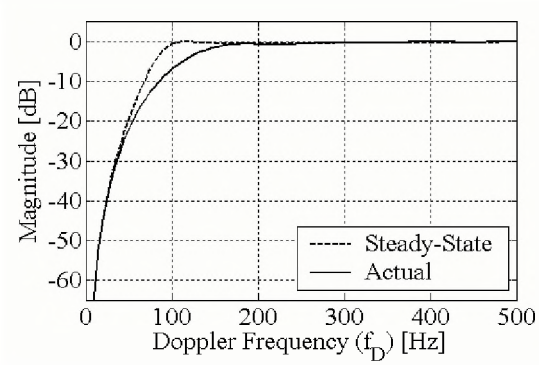

Figure 4. Actual and steady-state filter response of a projection-initialized IIR filter. Shown are the responses for a 3rd-order Chebychev IIR filter (100 Hz nominal cutoff) when N_D=10. The Doppler sampling rate was 1 kHz.

originally proposed by Chornoboy [26], works by setting the initial state vector as the complement of the least-squares fitting coefficients between the transient filter matrix and the steady-state filter output. In particular, the initial state vector for projection initialization can be expressed as follows:

$$\mathbf{v}_{\text{init}} = -(\mathbf{T}^{\text{H}}\mathbf{T})^{-1}\mathbf{T}^{\text{H}}\mathbf{S}\mathbf{x} = -\mathbf{T}^{+}\mathbf{S}\mathbf{x}, \tag{8a}$$

where the '+' superscript denotes a pseudoinverse operation (i.e the singular matrix equivalent of a square matrix's inverse). Correspondingly, by combining (5), (7b), and (8a), the overall filter matrix with projection initialization can be written as:

$$\mathbf{F} = [\mathbf{I} - \mathbf{T}\mathbf{T}^{+}]\mathbf{S}, \tag{8b}$$

where $\mathbf{I}$ is an $N_D \times N_D$ identity matrix. Figure 4 shows an example of the frequency response for projection-initialized IIR filters. This figure was computed by substituting (8b) into (6a), and it shows that the actual response of the projection-initialized IIR filter is suboptimal, but close, to the steady-state filter response. Note that, besides the use of filter initialization schemes, minimum-phase filters can also be used to reduce transient filtering effects. For instance, Bjaerum *et al.* [23] have studied the use of minimum-phase FIR filters and have shown that they can improve the filtering performance.

Polynomial Regression Filters

Another method of suppressing clutter is to use a regression filter in place of FIR and IIR filters. This type of filter works by first modeling the clutter as a series of curve shapes and then computing the least-squares fitting residual between the Doppler signal and the given clutter model. From a subspace perspective, such regressive fitting is equivalent to a least-squares projection of the Doppler signal vector onto the orthogonal complement of the clutter model subspace. As described in various algebra textbooks (e.g. see Sec. 3.4.1 in [27]), the least-squares projection of a vector $\mathbf{x}$ onto the orthogonal complement of a subspace matrix $\mathbf{C}$ is given by:

$$\mathbf{y} = [\mathbf{I} - \mathbf{C}(\mathbf{C}^{\text{H}}\mathbf{C})^{-1}\mathbf{C}^{\text{H}}]\mathbf{x} = [\mathbf{I} - \mathbf{C}\mathbf{C}^{+}]\mathbf{x}. \tag{9a}$$

Correspondingly, the filter matrix for a regression filter can be expressed as follows:

$$\mathbf{F} = \mathbf{I} - \mathbf{C}\mathbf{C}^{+}. \tag{9b}$$

In terms of the curve shapes used for the clutter model, low-order polynomials are often suitable because clutter echoes are generally consisted of low frequency components. Thus, polynomial basis vectors are typically used for the columns of the clutter subspace matrix. For a K^{th}-order polynomial clutter model $\hat{\mathbf{c}}$, the subspace matrix $\mathbf{C}$ is an $N_D \times (K+1)$ matrix that has the following form:

$$\hat{\mathbf{c}} = \sum_{k=0}^{K} \chi_k \mathbf{p}_k \Leftrightarrow \mathbf{C} = \begin{bmatrix} | & | & & | \\ \mathbf{p}_0 & \mathbf{p}_1 & \cdots & \mathbf{p}_K \\ | & | & & | \end{bmatrix}, \tag{10}$$

where χ_k and $\mathbf{p}_k$ are the respective least-squares fitting coefficient and the length-N_D basis vector for the k^{th}-order polynomial (usually ranged between –1 and +1). Based on this notion, Hoeks *et al.* [28] have considered using first and second order polynomial clutter models, while Kadi and Loupas [25] have evaluated the use of polynomial models up to the fourth order. Torp [15] has subsequently generalized this filtering approach by using orthogonal polynomials such as Legendre or Chebyshev polynomials[2] for the clutter model. In terms of its performance, Bjaerum *et al.* [23] have shown that, for the same filter order, the polynomial regression filter have a similar frequency response as the one for the projection-initialized IIR filter at low nominal cutoff frequencies. However, the polynomial regression filter has lesser flexibility in adjusting the width of the filter stopband since the filter response can only be changed by varying the filter order (whereas IIR filters can also vary the nominal cutoff frequency). Note that, besides the use of polynomials, other basis sets such as wavelets can also be used for the regression filter. For instance, Cloutier *et al.* [29] have modeled clutter as a sum of Gabor wavelets (orthogonal bases with different frequencies and Gaussian envelopes) that match the principal Doppler signal contents.

4.2. Adaptive Filters

Background Considerations

When using non-adaptive filters for clutter suppression, it is inherently assumed that the clutter spectral contents of all the mapped pixels would fall within a certain low Doppler frequency band. As such, the same clutter filter is often applied to the Doppler signal of all map pixels. Nonetheless, clutter suppression would likely be more effective if the filter stopband can be selected adaptively according to the local clutter characteristics of individual map pixels. For instance, in performing clutter filtering on Doppler data acquired under substantial tissue motion, the filter stopband may need to be dynamically adjusted because the Doppler clutter of some map pixels may not be centered around zero frequency. Based on this principle, Yoo *et al.* [30] have proposed the use of a filter bank approach whereby the width of the filter stopband can be changed depending on the magnitude of the mean clutter

[2] Legendre and Chebyshev polynomials can be obtained by orthogonalizing the polynomial set $\{1, n, n^2, \ldots\}$.

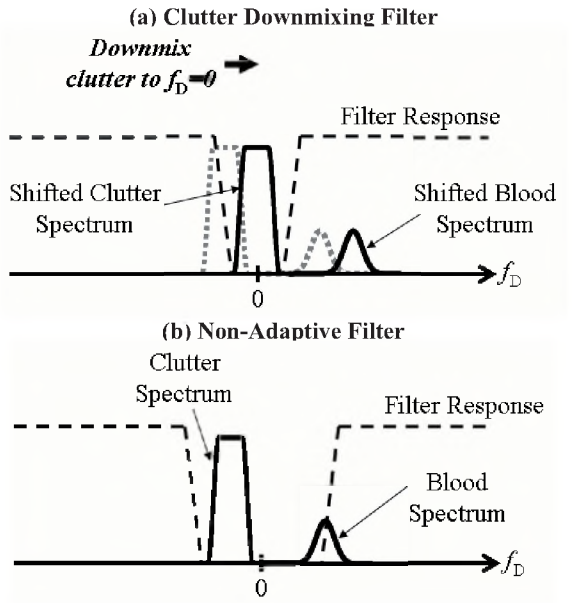

Figure 5. Illustration of the difference between (a) an adaptive filter based on clutter downmixing and (b) a non-adaptive clutter filter. For the non-adaptive filter, a wider stopband is needed to suppress clutter, but its use causes parts of the blood spectrum to be attenuated.

frequency. However, when a wider filter stopband is used, this clutter suppression approach may concomitantly suppress a substantial portion of the blood echoes in the Doppler spectrum, and as a result the sensitivity of flow detection may be decreased. In order to effectively suppress clutter originating from tissue motion, it is beneficial to design filters that can adapt its stopband to the clutter spectral characteristics. This rationale is the fundamental basis of adaptive clutter filters.

Clutter-Downmixing Filters

In the presence of tissue motion, one intuitive way of adaptively suppressing Doppler clutter is to design and use a bandpass filter whose stopband is centered at the mean clutter frequency. To implement this approach, however, high computation power would be required because of the need to design a different bandpass filter for each map pixel. As an equivalent way of realizing the same bandpass filter operation, it is possible to first downmix the Doppler signal with the mean clutter frequency before carrying out a highpass filtering operation. An illustration of this clutter downmixing strategy, which was originally introduced by Thomas and Hall [31] and Brands *et al.* [32], is shown in Figure 5. Mathematically, the n^{th} sample of the downmixed Doppler signal $x_{\text{DM}}(n)$ can be expressed as:

$$x_{\text{DM}}(n) = x(n)e^{-j\phi(n)} \quad \text{for } \phi(n) = 2\pi f_{\text{D(c)}} n T_{\text{PRI}}, \qquad (11a)$$

where $\phi(n)$ is the instantaneous phase of the downmixing carrier, while $f_{\text{D(c)}}$ denotes the mean clutter frequency that can be estimated using closed-form estimators like the lag-one autocorrelator (to be described in Section 5). From a vector space perspective, the downmixing operation is equivalent to applying a diagonal matrix operator **D** (of size $N_{\text{D}}\times N_{\text{D}}$) to the Doppler signal vector **x**. As such, the downmixed Doppler signal vector $\mathbf{x}_{\text{DM}}$ can be written as:

$$\mathbf{x}_{\text{DM}} = \mathbf{D}\mathbf{x} \quad \text{for } \mathbf{D} = \text{diag}[e^{-j\phi(0)}, e^{-j\phi(1)}, \ldots, e^{-j\phi(N_{\text{D}}-1)}]. \qquad (11b)$$

After the downmixing, any type of non-adaptive filter can generally be used to suppress the zero-frequency centered Doppler clutter. Correspondingly, the overall filter matrix of a filter with clutter downmixing is simply equal to the multiplication between the original filter matrix **F** and the downmixing operator **D**. As seen in Figure 5, this filtering strategy is particularly useful when clutter and blood scatterers give Doppler frequency components of different signs (i.e. when they move in opposite directions), because in this case the blood spectrum can more likely be preserved after the downmixing step. Note that, as described by Bjaerum *et al.* [33], the performance of the downmixing filter can be further improved if instantaneous clutter frequencies are used for the phase terms in the downmixing operator. Nevertheless, to accurately estimate the instant-aneous frequencies, one would require the use of multiple Doppler signal vectors that are statistically stationary.

Eigen-Regression Filters

Another way of adaptively suppressing Doppler clutter is to directly analyze the composition of the Doppler signal and remove a composition subset that corresponds to clutter. This filtering strategy is essentially the same as using a regression filter whose clutter model consists of a subset of components seen in the Doppler signal composition. In terms of its implementation, the signal analysis can be effectively carried out by decomposing the Doppler data into a series of adaptable, orthogonal basis functions (as opposed to fixed ones like the Fourier expansion). As discussed in algebra textbooks (e.g. see Sec. 6.8 in [27]), such decomposition is often referred to as the Karhunen-Loeve (KL) expansion or principal component analysis, and it can be computed through eigen-decomposition of the Doppler signal's correlation matrix. For a Doppler ensemble size N_{D}, the KL expansion is given by:

$$\mathbf{x} = \sum_{k=1}^{N_{\text{D}}} \gamma_k \mathbf{e}_k \quad \text{for } \text{E}\{\gamma_k \gamma_l\} = \begin{cases} \lambda_k & , k = l \\ 0 & , k \neq l \end{cases}, \qquad (12a)$$

where γ_k is the k^{th} expansion coefficient, while λ_k and $\mathbf{e}_k$ are the respective eigenvalue and eigenvector corresponding to the k^{th} orthogonal basis function. Note that the eigenvalues and eigenvectors are related to the signal vector by:

$$\sum_{k=1}^{N_{\text{D}}} \lambda_k \mathbf{e}_k \mathbf{e}_k^{\text{H}} = \text{E}\{\mathbf{x}\mathbf{x}^{\text{H}}\} = \mathbf{R}_{\text{x}}, \qquad (12b)$$

where $\mathbf{R}_{\text{x}}=\text{E}\{\mathbf{x}\mathbf{x}^{\text{H}}\}$ refers to the statistical correlation matrix of the Doppler signal. In practice, this matrix can be estimated via ensemble averaging as follows:

$$\mathbf{R}_{\text{x}} \approx \frac{1}{M}\sum_{m=1}^{M} \mathbf{x}_m \mathbf{x}_m^{\text{H}}, \qquad (12c)$$

where M is the number of Doppler signal vectors (or snapshots) that are statistically stationary and $\mathbf{x}_m$ indicates the Doppler signal vector for the m^{th} snapshot.

Since clutter often has a much higher strength than blood echoes and white noise, the signal decomposition

Table 1. Comparison of Existing Clutter Filter Designs

Type	*Filter Equation*	*Stopband Adjustment*	*Advantage*	*Limitation*
IIR + proj. initialization	$\mathbf{y} = [\mathbf{I}-\mathbf{T}\mathbf{T}^*]\mathbf{S}\mathbf{x}$ (both **T**, **S** are fixed state-space matrices)	Through changes in filter order and nominal cutoff freq.	Simple to carry out once filter coefficients are found	Does not adapt to Doppler signal; efficacy depends on choice of filter parameters
Polynomial regression	$\mathbf{y} = [\mathbf{I}-\mathbf{C}\mathbf{C}^*]\mathbf{x}$ (**C** is a fixed polynomial matrix)	By choice of clutter polynomial order	Same as above	Same as above
Clutter downmixing	$\mathbf{y} = \mathbf{F}\mathbf{D}\mathbf{x}$ (**F** is a fixed filter matrix; **D** is an adaptive downmixing matrix)	From changes to stopband of the non-adaptive filter	Improves highpass filtering by first downmixing clutter to zero frequency	Efficacy depends on choice of non-adaptive filter and accuracy of downmixing matrix
Eigen-regression	$\mathbf{y} = [\mathbf{I}-\mathbf{C}\mathbf{C}^*]\mathbf{x}$ (**C** is an adaptive clutter subspace matrix)	Via selection of clutter eigen-space dimension	Adapts filter matrix to Doppler signal contents via KL expansion	Needs multiple snapshots to find correlation matrix; efficacy depends on choice of clutter dimension

given in (12a) would have high-energy basis functions (or principal components) that correspond to clutter. Hence, as pointed out by Bjaerum *et al.* [33], Doppler clutter can be suppressed by using the basis vectors of these high-energy components as the clutter model for a regression filter. In particular, when K of the N_D basis functions correspond to clutter (i.e. with a clutter eigen-space dimension equal to K), the resulting clutter model and the clutter subspace matrix for an eigen-based regression filter can be expressed as:

$$\hat{\mathbf{c}} = \sum_{k=1}^{K} \chi_k \mathbf{e}_k \Leftrightarrow \mathbf{C} = \begin{bmatrix} | & | & & | \\ \mathbf{e}_1 & \mathbf{e}_2 & \cdots & \mathbf{e}_K \\ | & | & & | \end{bmatrix}, \qquad (13)$$

and the filter matrix would carry the same form shown in (10). Similar forms of this eigen-based filter have been reported in studies on swept-scan-based flow imaging [34] as well as strain-flow imaging [35]. Note that, as described by Ledoux *et al.* [36], the same filtering strategy can also be performed by applying singular value decomposition (SVD) to a multi-snapshot data matrix constructed from stacking together a number of stationary Doppler signal vectors. As well, as reported by Gallippi and Trahey [37], the Doppler spectral analysis can be carried out using another approach called independent component analysis that decomposes a signal into a series of statistically independent basis functions (as opposed to orthogonal ones). This latter approach has been applied to suppress clutter in acoustic radiation force imaging [38].

4.3. Comparison of Clutter Filters

Table 1 summarizes and compares the main features of the four types of clutter filters described in this section. From this table, it can be seen that the two non-adaptive filters (projection-initialized IIR and polynomial regression) are simpler to implement than adaptive filters because their filter matrix remains the same for a given set of filter parameters. However, the primary shortcoming of these non-adaptive filters is that they do not adapt to the Doppler signal contents. Because of this limitation, they inherently need a wider stopband to suppress Doppler clutter that has wideband characteristics and ones that are shifted away from zero frequency. On another note, it is worth pointing out that amongst the two non-adaptive filters, the projection-initialized IIR filter seems to have more flexibility in defining the stopband since it can modify the filter response via changes in both the filter order and the nominal cutoff.

In contrast to the two non-adaptive filters, the clutter downmixing filter can be perceived as a partially adaptive filter. Specifically, its filter matrix is a joint product between a fixed matrix operator that makes use of non-adaptive filtering principles as well as an adaptive matrix operator that is intended to downmix the Doppler clutter to zero frequency. The advantage of this filtering approach is that the highpass filtering operation can likely be improved since the downmixed Doppler clutter is supposedly centered at zero frequency. Nevertheless, because of the hybrid nature of its filter matrix, the clutter downmixing filter's efficacy is inherently dependent on two factors: 1) the choice of the non-adaptive filter used for the fixed matrix operator, and 2) the accuracy of the downmixing matrix operator found by estimating the mean or instantaneous clutter frequencies of the Doppler data.

Amongst the four classes of filters considered, the eigen-regression filter seems to have the best adaptability to the Doppler signal contents. In particular, the filter matrix of this filter is defined adaptively according to the most principal basis vectors in the Doppler signal's KL expansion. In turn, the eigen-regression filter can more likely preserve non-clutter components of the Doppler signal unless they share the same principal basis vectors with clutter components. However, the formulation for this filter inherently requires the availability of Doppler data from multiple sample volumes with similar signal characteristics (i.e. statistically stationary). As such, this filter may be challenging to implement in some vascular imaging studies where it is difficult to segment out regions with similar Doppler data statistics. Another limitation of the eigen-regression filter is that its efficacy is rather sensitive to the choice of the clutter eigen-space dimension owing to the filter's adaptive nature. Hence, it is necessary to develop an effective algorithm for this filter to select the clutter eigen-space dimension.

5. EXISTING VELOCITY ESTIMATION METHODS

5.1. Non-Parametric Estimators

Background Considerations

As already pointed out, a two-stage process is often used to compute velocity estimates in color flow imaging. First, a clutter filter is applied to the Doppler signal of each sample volume to remove low-frequency echoes originating from tissues and vessel walls. The filtered signal is then passed into a non-parametric flow estimator to compute the mean flow velocity. For this two-stage estimation approach, it is presumed that the clutter filter can adequately suppress clutter so that the filtered Doppler data consists of just the blood echoes and filtered white noise. Based on this notion, the filtered Doppler data vector $\mathbf{y}$ (of length N_D) can be described by the following signal model:

$$\mathbf{y} = [y(0), y(1), \ldots, y(N_D - 1)]^T = \mathbf{b} + \mathbf{w}_f, \quad (14)$$

where $y(n)$ is the n^{th} filtered sample, while $\mathbf{b}$ and $\mathbf{w}_f$ respectively denote the signal vectors for blood echoes and filtered white noise. This signal model often serves as the starting point in the derivation of various non-parametric mean velocity estimators.

Frequency-Based Methods

One approach for finding the mean flow velocity is to first estimate the mean frequency of the filtered Doppler signal and then use the Doppler equation to convert the frequency estimate into a velocity value. In this estimation approach, the mean Doppler frequency can theoretically be computed by dividing between the first-order and zeroth-order Doppler spectral moments. Alternatively, by making use of the Wiener-Khinchin relation, the same computations can be carried out in a more efficient manner through an analysis of the Doppler autocorrelation function (i.e. without directly analyzing the Doppler spectrum). As first described by Kasai *et al.* [39] in the context of color flow imaging, the autocorrelation-based approach would lead to the following expression for the mean Doppler frequency:

$$f_{D(est)} = \frac{\arg[R_y(1)]}{2\pi T_{PRI}} \quad \text{for } R_y(1) = \sum_{n=1}^{N_D-1} y(n)y^*(n-1), \quad (15)$$

where $R_y(1)$ is the Doppler autocorrelation function at a lag of one sample. Based on this equation, it can be seen that the lag-one autocorrelation phase is the primary factor in the mean Doppler frequency estimate. The phase quantity, however, is affected by signal aliasing due to the sampled nature of the Doppler data, and such a problem is often considered as a theoretical limitation of the autocorrelation estimator. Nevertheless, the aliasing limit is actually appreciated in practice because the unaliased velocity range is often used to define the mapping scale when designing the color map. Also, as pointed out by Tamura *et al.* [40], aliasing is sometimes introduced intentionally in color flow images to improve visualization of streamlines and laminar flow within the field of view.

The estimation variance of the lag-one autocorrelator given by (15) can be reduced by expanding the Doppler autocorrelation into a two-dimensional (2D) function based on multiple Doppler signal snapshots within a given depth range [41]. However, its use in color flow data processing is often not vital because the estimation variance can also be reduced via spatial averaging of the velocity estimates from adjacent map pixels within the imaging view. As pointed out by Loupas *et al.* [42][43], another possible advantage of the 2D autocorrelation approach is that it can be used to jointly estimate both the mean Doppler frequency and the instantaneous carrier frequency. Such feature is useful for correcting the Doppler frequency biases originating from carrier frequency variations that arise when wideband pulses are used to acquire color flow data (even though this is not common in color flow imaging as noted in Section 3.2).

Time-Shift-Based Methods

Another approach for estimating the mean flow velocity is to find the average inter-pulse time shift between post-filter echo envelopes of the same beam line and then apply (1a) to convert the time shift estimate into a velocity value. As reviewed by Alam and Parker [44], this time-shift-based estimation approach is essentially derived from target track-ing principles that are used in radar and sonar. In terms of its implementation, time shift estimation can be performed in two different ways. The first way, as initially applied to color flow imaging by Bonnefous and Pesque [45], involves finding the average time lag that yields the maximum cross-correlation between successive echo envelopes of the beam line. The second way, as proposed by Ferrara and Algazi [46][47] as well as Alam and Parker [48], involves computing a time-shift likelihood function from geometric projection principles and then searching for its location of maximum. For both implementation approaches, their per-formance is not affected by carrier frequency variations because inter-pulse time shifts are not physically dependent on the carrier frequency (as seen in (1a)). They also do not suffer from aliasing problems since they are not based on the analysis of Doppler frequencies. However, the theo-retical advantages offered by these estimators appear to be non-essential to color flow data processing (e.g. aliasing is indeed preferred in some flow studies as noted earlier). As such, time-shift estimators are often not used in color flow imaging, even though they have been a significant part of early research efforts in color flow signal processing.

5.2. Parametric Estimators

Background Considerations

In using non-parametric estimators to find flow velocities, estimation biases can be expected whenever the clutter filter distorts parts of the blood signal or fails to adequately suppress clutter. An illustration of this problem for a frequency-based non-parametric estimator is given in Figure 6a. Note that, at low blood-signal-to-noise ratios, further estimation biases can be anticipated because the filtered noise (i.e. colored noise) becomes a significant part of the filtered Doppler signal and in turn adds bias to the flow estimates. One of the ways to account for these clutter

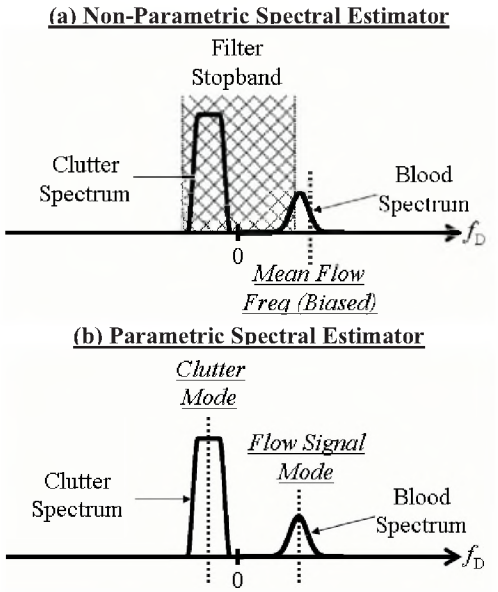

Figure 6. Difference between the spectral estimates of (a) non-parametric and (b) rank-two parametric flow estimators. Note that the mean estimate in (a) is biased away from the blood spectral peak because of filter distortions, while the two spectral modes in (b) are relatively unbiased.

filter biases is to apply a *post facto* correction factor to the flow estimates. For instance, Rajaonah *et al.* [49] have reported a frequency-based bias correction scheme that applies a correction factor based on the mean Doppler frequency of colored noise samples. Their approach, however, is intended to work with time-invariant clutter filters such as FIR filters, and thus it is not suitable for time-variant filters like projection-initialized IIR filters.

To effectively account for clutter filter biases, it is theoretically advantageous to use estimation strategies that can be directly applied to the raw Doppler signal. This rationale has motivated the development of parametric estimators that work by analyzing the principal Doppler spectral contents (i.e. they are frequency-based estimators). For these estimators, their principles are generally related to the following principal-component signal model:

$$\mathbf{x} = \mathbf{b} + \mathbf{c} + \mathbf{w} \approx \sum_{k=1}^{K} \chi_k \mathbf{v}_{\mathrm{CS}(k)} + \mathbf{w} \cdot \qquad (16a)$$

In the above expression, **x**, **b**, **c**, and **w** respectively denote the length-N_D vectors for raw Doppler signal, blood echoes, clutter, and white noise; also, K is the number of principal components in the signal model, while χ_k and $\mathbf{v}_{\mathrm{CS}(k)}$ are the weight and complex sinusoid vector of the k^{th} component. Note that $\mathbf{v}_{\mathrm{CS}(k)}$ essentially has the following vector form:

$$\mathbf{v}_{\mathrm{CS}(k)} = \left[1, z_k, z_k^2, \ldots, z_k^{(N_D-1)}\right]^T \quad \text{for } z_k = e^{j2\pi f_{D,k} T_{PRI}} . \qquad (16b)$$

where $f_{D,k}$ is the k^{th} principal Doppler frequency. It should be pointed out that, from a subspace perspective, this principal-component signal model is equivalent to the eigen-structure of a raw Doppler signal whose rank is equal to K. An illustration of the principal frequencies found using a rank-two parametric estimator is shown in Figure 6b.

Autoregressive Modeling

Autoregressive (AR) modeling (also known as linear prediction) is a type of parametric estimation approach that computes the principal Doppler frequencies through an all-pole signal analysis. As reviewed by Vaitkus and Cobbold [50] in the context of Doppler ultrasound, this approach begins by expressing each Doppler data sample as a linear combination of white noise and past data samples. In particular, for a K^{th}-order AR model, the n^{th} sample of the Doppler signal $x(n)$ is mathematically described by the following difference equation:

$$x(n) = w(n) - \sum_{k=1}^{K} c_k x(n-k) , \qquad (17a)$$

where $w(n)$ and c_k are respectively the white noise sample and the k^{th} model fitting coefficient. Correspondingly, this difference equation has the following all-pole form in the discrete frequency domain:

$$X_{\mathrm{AR}}(f_D) = \left. \frac{1}{1 + c_1 z^{-1} + \ldots + c_K z^{-K}} \right|_{z = e^{j2\pi f_D T_{PRI}}} , \qquad (17b)$$

where z_k is the k^{th} characteristic mode (i.e. the k^{th} root of the denominator polynomial). From discrete-time signal theory, it is well-established that the difference equation's natural response takes on the same form as the principal-component signal model given in (16a) when no repeated modes are present. As such, the characteristic modes of the difference equation can be used to estimate the principal frequencies of the Doppler signal. Specifically, since z is defined as $\exp\{j2\pi f_D T_{PRI}\}$, the k^{th} principal Doppler frequency can be found from the k^{th} characteristic mode as follows:

$$f_{D,k} = \frac{\arg[z_k]}{2\pi T_{PRI}} . \qquad (18)$$

In turn, the modal flow frequency can be identified from the principal spectral estimate that has the largest magnitude:

$$f_{D(\mathrm{est})} = f_{D,k_b} \quad \text{for } k_b = \arg\max_k \left\{ \left| f_{D,k} \right| \; \forall \; k \in [1, K] \right\} . \qquad (19)$$

In the AR model, the coefficients c_k in (17) are actually the main parameters that the characteristic modes depend on. These coefficients can be found by fitting the Doppler samples onto the data model. As discussed in spectral analysis textbooks (e.g. see Ch. 3 in [51]), an effective way of optimizing these coefficients is to minimize the mean-squared fitting error from both forward and backward regression perspectives. Such a least-squares fit can be computed using the Prony forward-backward fitting method (also known as modified covariance method). The forward-backward fitting procedure may be carried out recursively via an approach known as the Burg method.

In the context of color flow data processing, Loupas and McDicken [52] first considered the use of AR modeling in flow estimation. They showed that a first-order AR estimator, which only finds one Doppler spectral mode, is essentially equivalent to the lag-one autocorrelator shown in (15). Subsequently, Ahn and Park [53] attempted to use AR modeling in flow estimation studies that work with raw Doppler data. In particular, they developed a second-order AR estimator to simultaneously find the principal Doppler frequency of clutter and blood echoes. However, in this estimator, clutter is inherently assumed to be a single low-

frequency complex sinusoid. Such an assumption may not always be valid, especially in cases with wideband clutter.

Multiple Signal Classification

Another way of finding principal Doppler frequencies is to perform eigen-analysis on the correlation statistics of the Doppler signal. In particular, a form of eigen-analysis called multiple signal classification (MUSIC) has shown potential in obtaining flow estimates from the raw Doppler data. As applied to Doppler ultrasound by Allam and Greenleaf [54], the MUSIC method begins by decomposing the Doppler signal into a set of orthogonal bases though an eigen-decomposition of the Doppler correlation matrix (just like the eigen-regression filter as seen in (12)). Since the Doppler signal contents are mainly contained in the high-energy basis functions (due to their greater strength), the eigen-functions of the decomposition can then be divided into signal and noise components, thereby forming two mutually orthogonal subspaces. From this signal separation, a frequency pseudo-spectrum can subsequently be computed by finding the reciprocal of the cross-correlation between noise components and various complex sinusoids (with spectral peaks appearing at frequencies where the cross-correlation approaches zero). Specifically, for a Doppler signal with K principal components, its frequency pseudo-spectrum $X_{\text{MUSIC}}(f_D)$ can be expressed as:

$$X_{\text{MUSIC}}(f_D) = \frac{1}{\left\|\mathbf{E}_n^H \mathbf{v}_{CS}\right\|^2} = \frac{1}{\mathbf{v}_{CS}^H \mathbf{E}_n \mathbf{E}_n^H \mathbf{v}_{CS}}, \qquad (20a)$$

where $\mathbf{v}_{CS}$ is the complex sinusoid vector as seen in (6b) and $\mathbf{E}_n$ is a noise subspace matrix consisting of the N_D–K+1 least dominant eigenvectors:

$$\mathbf{E}_n = \begin{bmatrix} | & | & & | \\ \mathbf{e}_{K+1} & \mathbf{e}_{K+2} & \cdots & \mathbf{e}_{N_D} \\ | & | & & | \end{bmatrix}. \qquad (20b)$$

As shown in spectral analysis textbooks (e.g. see Sec. 4.5 in [51]), the denominator in (20a) is a $(2N_D-1)^{\text{th}}$-order polynomial with K modes, and its polynomial coefficients are equal to the sum of elements along each diagonal of the matrix $\mathbf{E}_n\mathbf{E}_n^H$. Hence, like AR modeling, the eigen-modes in the MUSIC pseudo-spectrum can be found numerically by solving for the denominator roots, and correspondingly the modal flow frequency can be found from the principal frequency estimates using (18) and (19). Based on this root-finding principle, Vaitkus and Cobbold [55] developed a closed-form parametric estimator called Root-MUSIC to estimate principal flow velocities from raw Doppler data. Their approach, which uses a rank-two eigenstructure to model the raw Doppler signal, was analyzed using *in vivo* Doppler data whose clutter can be sufficiently modeled as a single complex sinusoid [56]. Note that another way to solve for the MUSIC eigen-modes is to use a peak searching algorithm to find the principal peaks in the pseudo-spectrum. Such an approach was used by Allam *et al.* [57] to process Doppler data acquired from a string phantom and a reflective surface that respectively simulate blood flow and stationary clutter.

Table 2. Comparison of Existing Frequency-Based Velocity Estimators

Type	*Advantage*	*Limitation*
Lag-one autocorrelator	Simple to implement with low computation demand	Only works on filtered Doppler data; prone to biases from filter distortions
AR estimator	Finds flow velocity directly from raw Doppler data without clutter filtering	Least-squares fit of c_k fails at high white noise levels; efficacy depends on choice of model order
MUSIC	Same as AR estimator, but more resilient to white noise	Needs multiple data snapshots to find correlation matrix; efficacy depends on eigen-structure rank

5.3. Comparison of Velocity Estimators

Like the comparison on clutter filter designs, Table 2 summarizes the advantages and limitations of the three frequency-based velocity estimators covered in this section. As indicated, the lag-one autocorrelator has the advantage of being computationally efficient. Indeed, the low computing burden of this estimator is well appreciated in early research and developments because of processing power limitations. However, as already pointed out, the lag-one autocorrelator can only be applied to filtered Doppler data, and thus, its velocity estimates are inherently prone to biases from clutter filter distortions.

Contrary to the lag-one autocorrelator, the AR estimator has the theoretical advantage of being able to obtain velocity estimates by directly processing the raw Doppler data. This estimator first uses a least-squares fitting procedure to compute the characteristic modes of the raw Doppler signal and then identifies the modal flow component based on the largest-frequency mode, thereby avoiding the need for clutter filtering. Nevertheless, the primary shortcoming of the AR estimator is that the least-squares fitting solution to the model coefficients assumes that the Doppler data samples are free of noise perturbations. Thus, its accuracy tends to degrade significantly as the noise level increases. Another limitation with the AR estimator is that its flow estimation performance is dependent on the choice of the model order (or eigen-structure rank). Specifically, a wrong choice of model order would give rise to spurious spectral modes and in turn give incorrect modal velocity estimates.

Unlike the AR estimator, the MUSIC estimator is more resilient to white noise because it first makes use of an eigen-decomposition procedure to separate the signal bases from noise floor components. Therefore, when applied to raw Doppler data with high noise levels, this estimator can obtain modal velocity estimates that are less biased than the ones found from AR modeling. On the other hand, it is worth pointing out that the formulation of MUSIC begins with the same eigen-decomposition step as seen for the eigen-regression filter. As such, MUSIC has a limitation

that is similar to the eigen-regression filter: it needs multiple signal snapshots that are statistically stationary in order to form an accurate estimate of the Doppler correlation matrix. Another limitation of the MUSIC approach is that, as similar to AR modeling, the performance of this estimator is contingent upon suitable choice of the eigen-structure rank. Thus, an adaptive rank selection algorithm is needed in order for this estimator to be effective in general.

6. CONCLUDING REMARKS

As seen in the previous two sections, eigen-based signal processing strategies have been the focus of the most recent research efforts in color flow data processing. In particular, both the eigen-regression filter and the MUSIC estimator have shown better potential than other signal processing methods in adapting to the Doppler signal characteristics. As such, eigen-based strategies seem to be more capable of obtaining flow estimates that are less affected by the signal processing error sources mentioned earlier in this article.

In terms of latest developments, a number of current research studies have been devoted to address the practical challenges of using eigen-based signal processing strategies. For instance, Lovstakken *et al.* [58] have recently studied the computational aspect of eigen-regression filters and have considered how the clutter eigen-space dimension can be adaptively selected based on the eigenvalue gradient in the KL expansion. They are also pursuing the development of a maximum-likelihood estimator that makes use of principal component analysis concepts [59]. Complementary to these studies, we have recently reported a new eigen-based clutter filter that works with single snapshots of Doppler data via the notion of principal Hankel component analysis [60]. As well, we have proposed a new eigen-based parametric estimator called the Matrix Pencil that treats velocity estimation as a generalized eigenvalue problem [61]. We have also developed an adaptive rank selection algorithm that is based on the spectral spread of the principal Doppler frequencies [62].

ACKNOWLEDGEMENTS

We are very grateful for Aziza Manceur's help on the French version of our abstract. We also wish to thank Larry Mo and ZONARE Medical Systems for supplying us with clinical flow images from their scanners.

This work was supported in part by grants from the Canadian Institutes of Health Research and the Natural Sciences and Engineering Research Council of Canada.

REFERENCES

[1] K Ferrara and G DeAngelis, "Color flow mapping", *Ultrasound Med. Biol.*, vol. 23, pp. 321-345, 1997.

[2] TH Williamson and A Harris, "Color Doppler ultrasound imaging of the eye and orbit", *Surv. Ophthalmol.*, vol. 40, pp. 255-267, 1996.

[3] R Lagalla, G Caruso, and M Finazzo, "Monitoring treatment response with color and power Doppler", *Euro. J. Radiology*, vol. 28, pp. S149-S156, 1998.

[4] AD Waggoner and SM Bierig, "Tissue Doppler imaging: a useful echocardiographic method for the cardiac sonographer to assess systolic and diastolic ventricular function", *J. Am. Soc. Echocardiogr.*, vol. 14, pp. 1143-1152, 2001.

[5] G Armstrong, L Cardon, D Vilkomerson, *et al.*, "Localization of needle tip with color Doppler during pericardiocentesis: in vitro validation and initial clinical application", *J. Am. Soc. Echocardiogr.*, vol. 14, pp. 29-37, 2001.

[6] KW Beach, AC Keith, JF Primozich, *et al.*, "Ultrasonic color flow mapping: the visualization of four-dimensional cardiac and vascular flow phenomena using two dimensions and real-time", *Ultrasound Med. Biol.*, vol. 23, pp. 347-363, 1997.

[7] P Arbeille, MH Bouin-Pineau, and S Herault, "Accuracy of the main Doppler methods for evaluating the degree of carotid stenosis (continuous wave, pulsed wave, and color Doppler)", *Ultrasound Med. Biol.*, vol. 25, pp. 65-73, 1999.

[8] SFC Stewart, "Effects of transducer, velocity, Doppler angle, and instrument settings on the accuracy of color Doppler ultrasound", *Ultrasound Med. Biol.*, vol. 27, pp. 551-564, 2001.

[9] A Fenster, DB Downey, and HN Cardinal, "Three-dimensional ultrasound imaging", *Physics Med. Biol.*, vol. 46, pp. R66-R99, 2001.

[10] B Dunmire, KW Beach, KH Labs, *et al.*, "Cross-beam vector Doppler ultrasound for angle-independent velocity measurements",*Ultrasound Med. Biol.*, vol. 26, pp. 1213-1235, 2000.

[11] SG Foster, CJ Pavlin, KA Harasiewicz, *et al.*, "Advances in ultrasound biomicroscopy", *Ultrasound Med. Biol.*, vol. 26, pp. 1-27, 2000.

[12] PJA Frinking, A Bouakaz, J Kirkhorn, *et al.*, "Ultrasound contrast imaging: current and new potential methods", *Ultrasound Med. Biol.*, vol. 26, pp. 965-975, 2000.

[13] RSC Cobbold, *Foundations of Biomedical Ultrasound.* New York City, USA: Oxford University Press, 2006.

[14] DH Evans and WN McDicken, *Doppler Ultrasound: Physics, Instrumentation and Signal Processing.* 2nd Ed. West Sussex, UK: John Wiley & Sons Ltd., 2000.

[15] H Torp, "Clutter rejection filters in color flow imaging: a theoretical approach", *IEEE Trans. Ultrason. Ferroelec. Freq. Contr.*, vol. 44, pp. 417-424, 1997.

[16] A Heimdal and H Torp, "Ultrasound Doppler measurements of low velocity blood flow: limitations due to clutter signals from vibrating muscles", *IEEE Trans. Ultrason. Ferroelec. Freq. Contr.*, vol. 44, pp. 873-881, 1997.

[17] KW Ferrara, VR Algazi, and J Liu, "The effect of frequency dependent scattering and attenuation on the estimation of blood velocity using ultrasound", *IEEE Trans. Ultrason. Ferroelec. Freq. Contr.*, vol. 39, pp. 754-767, 1992.

[18] WH Round and RHT Bates, "Modification of spectra of pulses from ultrasonic transducers by scatterers in non-attenuating and attenuating media", *Ultrason. Imaging*, vol. 9, pp. 18-28, 1987.

[19] PM Embree and WD O'Brien Jr, "Pulsed Doppler accuracy assessment due to frequency-dependent attenuation and Rayleigh scattering error sources", *IEEE Trans. Biomed. Eng.*, vol. 37, pp. 322-326, 1990.

[20] JC Willemetz, A Nowicki, JJ Meister, *et al.*, "Bias and variance in the estimate of the Doppler frequency induced by a wall motion filter", *Ultrason. Imaging*, vol. 11, pp. 215-225, 1989.

[21] C Tysoe and DH Evans, "Bias in mean frequency estimation of Doppler signals due to wall clutter filters", *Ultrasound Med. Biol.*, vol. 21, pp. 671-677, 1995.

[22] AV Oppenheim, RW Schafer, and JR Buck, *Discrete-time signal processing.* 2nd Ed. Upper Saddle River, USA: Prentice-Hall Inc., 1999.

[23] S Bjaerum, H Torp, and K Kristoffersen, "Clutter filter design for ultrasound color flow imaging", *IEEE Trans. Ultrason. Ferroelec. Freq. Contr.*, vol. 49, pp. 204-216, 2002.

[24] RB Peterson, LE Atlas, and KW Beach, "A comparison of IIR initialization techniques for improved color Doppler wall filter performance", *Proc. IEEE Ultrason. Symp.*, pp. 1705-1708, 1994.

[25] AP Kadi and T Loupas, "On the performance of regression and step-initialized IIR clutter filters for color Doppler systems in diagnostic medical ultrasound", *IEEE Trans. Ultrason. Ferroelec. Freq. Contr.*, vol. 42, pp. 927-937, 1995.

[26] ES Chornoboy, "Initialization for improved IIR filter performance", *IEEE Trans. Signal Processing*, vol. 40, pp. 543-550, 1992.

[27] TK Moon and WC Stirling, *Mathematical methods and algorithms for signal processing*. Upper Saddle River, USA: Prentice-Hall Inc., 2000.

[28] APG Hoeks, JJW van de Vorst, A Dabekaussen, *et al.*, "An efficient algorithm to remove low frequency Doppler signals in digital Doppler systems", *Ultrason. Imaging*, vol. 13, pp. 135-144, 1991.

[29] G Cloutier, D Chen, and LG Durand, "A new clutter rejection algorithm for Doppler ultrasound", *IEEE Trans. Med. Imag.*, vol. 22, pp. 530-538, 2003.

[30] YM Yoo, R Managuli, and Y Kim, "Adaptive clutter filtering for ultrasound color flow imaging", *Ultrasound Med. Biol.*, vol. 29, pp. 1311-1320, 2003.

[31] L Thomas and A Hall, "An improved wall filter for flow imaging of low velocity flow", *Proc. IEEE Ultrason. Symp.*, pp. 1701-1704, 1994.

[32] PJ Brands, APG Hoeks, and RS Reneman, "The effect of echo suppression on the mean velocity estimation range of the RF cross-correlation model estimator", *Ultrasound Med. Biol.*, vol. 21, pp. 945-959, 1995.

[33] S Bjaerum, H Torp, and K Kristoffersen, "Clutter filters adapted to tissue motion in ultrasound color flow imaging", *IEEE Trans. Ultrason. Ferroelec. Freq. Contr.*, vol. 49, pp. 693-704, 2002.

[34] DE Kruse and KW Ferrara, "A new high resolution color flow system using an eigendecomposition-based adaptive filter for clutter rejection", *IEEE Trans. Ultrason. Ferroelec. Freq. Contr.*, vol. 49, pp. 1384-1399, 2002.

[35] C Kargel, G Hobenreich, B Trummer, and MF Insana, "Adaptive clutter rejection filtering in ultrasonic strain-flow imaging", *IEEE Trans. Ultrason. Ferroelec. Freq. Contr.*, vol. 50, pp. 824-835, 2003.

[36] LAF Ledoux, PJ Brands, and APG Hoeks, "Reduction of the clutter component in Doppler ultrasound signals based on singular value decomposition: a simulation study", *Ultrason. Imaging*, vol. 19, pp. 1-18, 1997.

[37] CM Gallippi and GE Trahey, "Adaptive clutter filtering via blind source separation for two-dimensional ultrasonic blood velocity measurement", *Ultrason. Imaging*, vol. 24, pp. 193-214, 2002.

[38] CM Gallippi, KR Nightingale, and GE Trahey, "BSS-based filtering of physiological and ARFI-induced tissue and blood motion", *Ultrasound Med. Biol.*, vol. 29, pp. 1583-1592, 2003.

[39] C Kasai, K Namekawa, A Koyano, and R Omoto, "Real-time two-dimensional blood flow imaging using an autocorrelation technique", *IEEE Trans. Sonics Ultrason.*, vol. 32, pp. 458-464, 1985.

[40] T Tamura, RSC Cobbold, and KW Johnston, "Quantitative study of steady flow using color Doppler ultrasound", *Ultrasound Med. Biol.*, vol. 17, pp. 595-605, 1991.

[41] H Torp, K Kristoffersen, and BAJ Angelson, "Autocorrelation techniques in color flow imaging: signal model and statistical properties of the autocorrelation estimates", *IEEE Trans. Ultrason. Ferroelec. Freq. Contr.*,vol. 41, pp. 604-612, 1994.

[42] T Loupas, JT Powers, and RW Gill, "An axial velocity estimator for ultrasound blood flow imaging, based on a full evaluation of the Doppler equation by means of a two-dimensional autocorrelation approach", *IEEE Trans. Ultrason. Ferroelec. Freq. Contr.*, vol. 42, pp. 672-688, 1995.

[43] T Loupas, RB Peterson, and RW Gill, "Experimental evaluation of velocity and power estimation for ultrasound blood flow imaging, by means of a two-dimensional autocorrelation approach", *IEEE Trans. Ultrason. Feeroelec. Freq. Contr.*, vol. 42, pp. 689-699, 1995.

[44] SK Alam and KJ Parker, "Implementation issues in ultrasonic flow imaging", *Ultrasound Med. Biol.*, vol. 29, pp. 517-528, 2003.

[45] O Bonnefous and P Pesque, "Time domain formulation of pulsed-Doppler ultrasound and blood velocity estimation by cross correlation", *Ultrason. Imaging*, vol. 8, pp. 73-85, 1986.

[46] KW Ferrara and VR Algazi, "A new wideband spread target maximum likelihood estimator for blood velocity estimation—part I: theory", *IEEE Trans. Ultrason. Ferroelec. Freq. Contr.*, vol. 38, pp. 1-16, 1991.

[47] KW Ferrara and VR Algazi, "A new wideband spread target maximum likelihood estimator for blood velocity estimation—part II: evaluation of estimators with experimental data", *IEEE Trans. Ultrason. Ferroelec. Freq. Contr.*, vol. 38, pp. 17-26, 1991.

[48] SK Alam and KJ Parker, "The butterfly search technique for estimation of blood velocity", *Ultrasound Med. Biol.*, vol. 21, pp. 657-670, 1995.

[49] JC Rajaonah, B Dousse, and JJ Meister, "Compensation of the bias caused by the wall filter on the mean Doppler frequency", *IEEE Trans. Ultrason. Ferroelec. Freq. Contr.*, vol. 41, pp. 812-819, 1994.

[50] PJ Vaitkus and RSC Cobbold, "A comparative study and assessment of Doppler ultrasound spectral estimation techniques. Part I: estimation methods", *Ultrasound Med. Biol.*, vol. 14, pp. 661-672, 1988.

[51] P Stoica and RL Moses, *Introduction to spectral analysis*. Upper Saddle River, USA: Prentice Hall Inc., 1997.

[52] T Loupas and WN McDicken, "Low-order complex AR models for mean and maximum frequency estimation in the context of Doppler color flow mapping", *IEEE Trans. Ultrason. Ferroelec. Freq. Contr.*, vol. 37, pp. 590-601, 1990.

[53] YB Ahn and SB Park, "Estimation of mean frequency and variance of ultrasonic Doppler signal by using second-order autoregressive model", *IEEE Trans. Ultrason. Ferroelec. Freq. Contr.*, vol. 38, pp. 172-182, 1991.

[54] ME Allam and JF Greenleaf, "Isomorphism between pulsed-wave Doppler ultrasound and direction-of-arrival estimation—Part I: basic principles", *IEEE Trans. Ultrason. Ferroelec. Freq. Contr.*, vol. 43, pp. 911-922, 1996.

[55] PJ Vaitkus and RSC Cobbold, "A new time-domain narrowband velocity estimation technique for Doppler ultrasound flow imaging. Part I: theory", *IEEE Trans. Ultrason. Ferroelec. Freq. Contr.*, vol. 45, pp. 939-954, 1998.

[56] PJ Vaitkus, RSC Cobbold, and KW Johnston, "A new time-domain narrowband velocity estimation technique for Doppler ultrasound flow imaging Part II: comparative performance assessment", *IEEE Trans. Ultrason. Ferroelec. Freq. Contr.*, vol. 45, pp. 955-971, 1998.

[57] ME Allam, RR Kinnick, and JF Greenleaf, "Isomorphism between pulsed-wave Doppler ultrasound and direction-of-arrival estimation—Part II: experimental results", *IEEE Trans. Ultrason. Ferroelec. Freq. Contr.*, vol. 43, pp. 923-935, 1996.

[58] L Lovstakken, S Bjaerum, K Kristoffersen, *et al.*, "Real-time adaptive clutter rejection filtering in color flow imaging using power method iterations", *IEEE Trans. Ultrason. Ferroelec. Freq. Contr.*, vol. 53, pp. 1597-1608, 2006.

[59] L Lovstakken, TA Tangen, S Bjaerum, and H Torp, "Optimum velocity estimation in ultrasound color flow imaging in presence of clutter noise", *Proc. IEEE Ultrason. Symp.*, pp. 2417-2420, 2006.

[60] ACH Yu and RSC Cobbold, "A new eigen-based clutter filter using the Hankel-SVD approach", *Proc. IEEE Ultrason. Symp.*, pp. 1079-1082, 2006.

[61] ACH Yu, LYL Mo, RK Warriner, and RSC Cobbold, "A new eigen-based flow estimator using the Matrix Pencil approach", *Proc. IEEE Ultrason. Symp.*, pp. 1335-1338, 2005.

[62] ACH Yu and RSC Cobbold, "A Matrix Pencil estimator with adaptive rank selection: application to *in vivo* flow studies", *Proc. IEEE Ultrason. Symp.*, pp. 2015-2018, 2006.

Dalimar Instruments Inc.

A votre service depuis 1986 / *At your service since 1986*

831 sound level meter/real time analyzer

- Consulting engineers
- Environmental noise monitoring
- Highway & plant perimeter noise
- Aircraft noise
- General Surveys
- Community noise

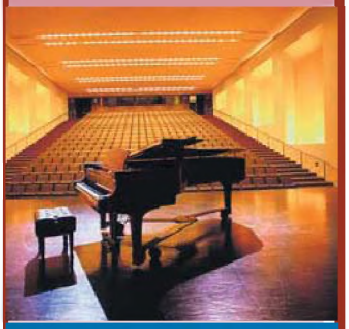

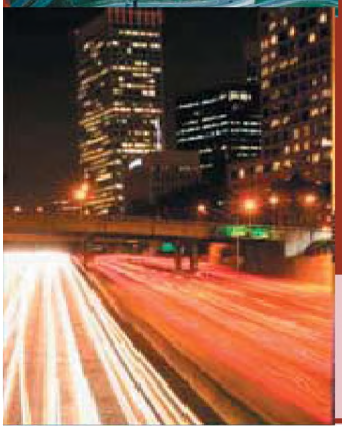

FEATURES

- Class 1/Type 1 sound level meter
- Small size with large display. Ergonomic
- User friendly operator interface
- 120MB standard memory expandable up to 2GB
- Single measurement range from 20 to 140 dB SPL
- Up to 16 hours of battery life
- Provided with utility software for instrument set-up and data download
- Field upgradeable
- AUX port for connection to USB mass storage & cellular modems

MEASUREMENT CAPABILITIES

- Real time 1/1 & 1/3 octave frequency analysis
- Simultaneous display of several noise measurements—*ANY DATA* (Leq, Lmax, Spectra, etc
- Automatic logging of user selectable noise measurements (Leq, Lmax, Spectra, etc…)
- Exceedance logging with user selectable trigger levels
- Audio and voice recording with replay

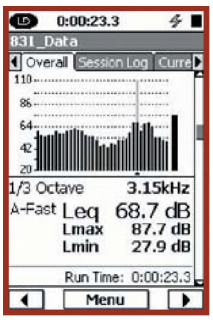

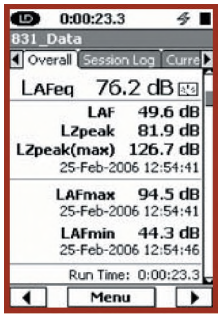

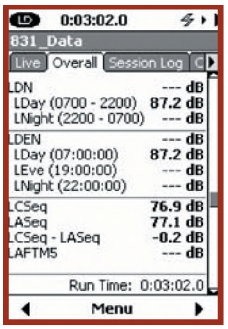

Larson Davis
A PCB Group Co.

WWW.DALIMAR.CA INFO@DALIMAR.CA

QUEBEC 450-424-0033 ONTARIO 905-707-9000 ALBERTA 403-288-4416

Recent Flow Analysis Studies in Vascular Models Using Doppler Ultrasound

Tamie L. Poepping[1,2], Meghan L. Thorne[2,4], Emily Y. Wong[2,4], Richard N. Rankin[3], and David W. Holdsworth[3,4]
Depts of Physics & Astronomy1, Medical Biophysics2, and Diagnostic Radiology & Nuclear Medicine3, at the University of Western Ontario, London, ON N6A 3K7; and The Robarts Research Institute4, 100 Perth Drive, London, ON, N6A 5K8

ABSTRACT

Vascular disease is a major source of morbidity and mortality in Western society, with stroke and heart attacks accounting for about one third of deaths in North America. The carotid artery, and in particular the carotid bifurcation, is recognized as a common source of stroke-causing emboli that travel up into the brain, thereby blocking local blood flow. This has led to an emphasis on diagnostic techniques for assessing stroke risk due to carotid artery disease. Doppler ultrasound (DUS) techniques, in particular, uniquely enable visualization of flow patterns and characterization of various flow parameters. To improve our understanding of how blood-flow velocity patterns are modified as a result of disease in the carotid artery, basic research is typically carried out in physiologically realistic vascular models. In this paper, we review the progress that has been made in the development of ultrasound-compatible vascular models, as well as demonstrate the capabilities of DUS to quantify velocity patterns, turbulence, and recirculation. Ultrasound-compatible flow systems have been developed to mimic the geometry and hemodynamics of the carotid artery, under normal conditions and at various stages of narrowing due to atherosclerosis. These in vitro systems provide a controlled environment for developing new diagnostic techniques and for investigating and characterizing blood flow using DUS. Example data are shown from vessels with both eccentric and concentric stenoses, and in stenosed vessels that have been altered by the introduction of medical devices (stents) or additional roughness (ulceration). These results demonstrate the capacity for conventional clinical Doppler ultrasound devices to provide precise measurements of blood velocity from small sample volumes within a vessel, in order to build up detailed flow maps near and downstream of vascular disease or interventional device.

SOMMAIRE

Les maladies vasculaires sont une source importante de morbidité et de mortalité dans la société occidentale. Les accidents cérébrovasculaires et les crises cardiaques sont responsables pour environ un tiers des décès en Amérique du Nord. L'artère carotide, particulièrement la bifurcation carotide, est identifiée comme une source commune d'emboles qui se propagent vers le cerveau, bloquent l'écoulement sanguin local, et provoquent ainsi des accidents cérébrovasculaires. Ceci a mené à la mise en emphase de techniques diagnostiques servant à évaluer le risque d'accidents cérébrovasculaires dû à la maladie de l'artère carotide. Les techniques d'échographie Doppler (DUS, de l'anglais), en particulier, permettent la visualisation des patterns d'écoulement et la caractérisation de leurs divers paramètres. Pour améliorer nos connaissances de la façon avec laquelle les formes d'écoulement sanguin sont modifiées par la maladie de l'artère carotide les études de recherche sont habituellement effectuées avec l'aide de modèles vasculaires physiologiquement réalistes. Dans cet article, nous passons en revue le progrès qui a été accompli dans le développement de modèles vasculaires applicables aux ultrasons, et nous démontrons les possibilités des techniques DUS pour mesurer les patterns de vélocité, de turbulence, et de vorticité. Des systèmes d'écoulement applicables aux ultrasons ont été développés pour imiter la géométrie et l'hémodynamique de l'artère carotide dans des conditions normales et à diverses étapes du rétrécissement dû à l'athérosclérose. Ces systèmes in vitro fournissent un environnement contrôlé qui facilite le développement de nouvelles techniques diagnostiques, de même que l'étude et la caractérisation de l'écoulement sanguin en utilisant les techniques DUS. Des données obtenues pour des systèmes avec sténoses excentriques et concentriques et des systèmes avec sténoses altérés par l'introduction des dispositifs médicaux (endoprothèses vasculaires) ou de rugosité additionnelle (ulcération) sont présentées. Ces résultats démontrent la capacité des techniques cliniques d'échographie Doppler conventionnelles pour mesurer précisément la vitesse sanguine dans de petits volumes d'échantillons situés à l'intérieur de systèmes d'écoulement. Ceci permet de produire des cartes détaillées d'écoulement près et en aval de régions atteintes par la maladie vasculaire, ou de dispositifs d'intervention.

1. INTRODUCTION

Ultrasound (US) has become an invaluable diagnostic and therapeutic tool that is most appealing for its rapid accessibility and low cost compared to other modalities, such as x-ray computed tomography or magnetic resonance imaging. Ultrasound imaging uses high-frequency sound waves, typically 2-10 MHz, to form images of the internal body as a function of time and space. Similarly, Doppler ultrasound (DUS) techniques use high-frequency ultrasound in order to detect the presence of blood flow or to determine the velocity of the blood. The versatility of ultrasound for both anatomical imaging, flow visualization, and velocity measurement applications makes it a prime candidate for investigating vascular disease, particularly to elucidate the connections between local hemodynamics (blood flow) and vascular tissue changes, such as due to atherosclerosis.

Atherosclerosis, which is a thickening or hardening of the arteries forming plaques, promotes the development of blood clots or thrombosis by partial obstruction of the blood flow, elevated shear stresses, or plaque disruption. These clots, or displaced bits of plaque, form emboli that can travel downstream and block blood flow in smaller arteries of the brain, resulting in an ischemic stroke. Overall, stroke is the 4th leading cause of death in Canada, accounting for 7% of all deaths with an annual cost to the Canadian economy of about $2.7 billion (Heart and Stroke Foundation of Canada, 1999; Heart and Stroke Foundation of Canada, 2002). The carotid artery bifurcation in the human neck is a common site of atherosclerotic disease and is therefore highly relevant to stroke research. To determine the risk that a particular vessel poses, doctors will often examine a patient using x-ray imaging and measure the restriction of the vessel due to disease. However, the risk of producing a clot is not only due to the narrowing of the vessel lumen, but also the way that blood flows near the obstruction. It is believed that clot formation is accelerated in regions of slow or recirculating flow, high shear rate, and increased turbulence (Stein and Sabbah, 1974; Reininger *et al.*, 1995; Holme *et al.*, 1997). Doppler ultrasound has excellent potential as a tool to assess and visualize these flow features.

Doppler ultrasound can be used to study *in vitro* effects of various modeling parameters in order to gain a better understanding of the hemodynamics. This also helps to develop DUS further as a tool towards improved *in vivo* assessment of the hemodynamics. Ultimately it is desirable to determine if advanced flow parameters derived from DUS velocity measurements can be a better indicator of disease progression and more accurately reflect the absolute stroke risk due to plaque development, thrombus formation, or plaque rupture.

In this paper, we demonstrate the ability of DUS to visualize complex 2-D flow patterns and quantitatively assess mean velocity, turbulence intensity, and spectral broadening. Through the use of vascular models and simulated pulsatile blood-flow waveforms, it is then possible to use DUS to investigate flow features, such as turbulence and recirculation, that are relevant to stroke risk.

2. BACKGROUND

2.1: Carotid arterial disease diagnosis and treatment

Standard diagnosis of carotid arterial disease consists of assessment of the stenosis severity, or maximum vessel diameter reduction, where increasing stenosis severity indicates increased relative stroke risk. Standard treatment can vary from non-invasive drug therapy, such as anti-clotting agents, to invasive interventional procedures, such as carotid endarterectomy – a surgical procedure to remove the atherosclerotic plaque, or insertion of a stent – a mesh tube expanded to re-open the lumen and stabilize the carotid plaque.

While x-ray angiography is historically the gold standard for assessing stenosis severity, Doppler ultrasound has become increasingly popular as a non-invasive method to screen possible candidates for carotid endarterectomy. Several large multi-centre clinical trials have demonstrated the benefit of carotid endarterectomy, for symptomatic patients with severe stenosis (North American Symptomatic Carotid Endarterectomy Trial (NASCET), 1991; European Carotid Surgery Trialists' Collaborative, 1998), but also have acknowledged the role of other key factors, such as the presence of ulcerations (Eliasziw *et al.*, 1994).

2.2: Role of B-mode Ultrasound Imaging in Assessing Vascular Disease

The use of B-mode ultrasound imaging has become increasingly popular for the diagnosis of carotid disease due to improved resolution and the development of 3-D ultrasound imaging techniques (Fenster *et al.*, 1997). Ultrasound imaging, in general, can be used to see arterial geometry and patency, plaque severity and shape, plaque composition, and vessel stiffness, while 3-D B-mode ultrasound has been used to measure stenosis diameter, lumen morphology, and plaque volume in the carotid arteries (Griewing *et al.*, 1996; Yao *et al.*, 1998). Ultrasound has also proved to be more accurate than angiography in determining the presence or absence of ulceration (Van Damme and Vivario, 1993), where ulcerations are associated with increased stroke risk (Eliasziw *et al.*, 1994; Rothwell *et al.*, 2000).

2.3: Role of DUS for Flow Assessment

Doppler ultrasound is typically used to identify patients with high-velocity jets within the internal carotid artery, which is an indication of vessel narrowing or stenosis, and thus a surrogate measure of vessel lumen reduction. The maximum systolic velocity was first suggested as an indicator of carotid stenosis in 1979, with the rationale that due to regulation of cerebral blood flow, a reduction in lumen diameter will lead to an increase in blood velocity, at least until the increased flow resistance of the stenosis leads to a reduction in blood flow (Spencer and Reid, 1979). The peak systolic velocity (PSV) is the most commonly used DUS indicator, often combined with the end diastolic

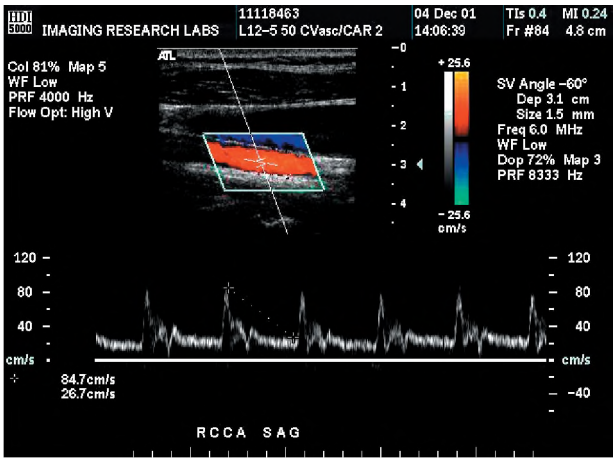

Figure 1: Example from a clinical ultrasound examination showing a B-mode (top centre) image with overlaid colour-encoded map of mean velocity (colour Doppler, shown in central box), along with a DUS spectrogram (bottom) of a sub-volume of velocities as a function of time over 5 cardiac cycles. The DUS sample volume is indicated by the crosshairs at the centre of the B-mode and colour-Doppler image.

velocity (EDV) to form a ratio (Moneta *et al.*, 1993; Schwartz *et al.*, 1997). These velocities may be assessed at the stenosis alone (Alexandrov *et al.*, 1997) or normalized by additional measurements in the common carotid artery (Arbeille *et al.*, 1999; Ranke *et al.*, 1999). Carpenter *et al.* (1996) give an excellent description of some commonly used velocity indices.

Pulsed Doppler ultrasound can be used to interrogate the blood velocities from a small finite sample volume (approx. 1-10 mm^3). A spectrogram (Fig. 1, bottom) is used to display the velocity as a function of time, where the range of velocities detected is shown along each vertical line with the energy content for each corresponding velocity encoded as the pixel intensity or brightness. Hence, a broad velocity range appears as a smeared vertical line.

The range of observed velocities is qualitatively used as an indication of the type of flow, since disturbed or turbulent flow will show a broader range of velocities for a given time point, but will also depend upon the size of the sample volume used. Pulsed DUS is limited to a relatively small sample volume (i.e. small spatial region of flow), and hence the user needs to move the sample volume around to sub-sample a larger volume.

One way to partially visualize the velocity spatial patterns over a larger volume is to use colour-Doppler techniques, which display estimates of the mean velocity as a colour-encoded map superimposed onto the B-mode image (see Fig. 1). However, current implementation is limited to reporting only the mean velocity, or similarly the integrated power for power-Doppler techniques; the mapping of peak velocity or other spectral information is not provided on standard clinical machines. Primarily, colour-Doppler ultrasound is used to assist with basic visualization of the 2-D flow field in order to ensure proper positioning of the smaller pulsed-Doppler sample volume (small cross-hair region within coloured map in Fig.1).

Arterial disease can lead to complicated flow including flow disturbances such as turbulence, vortices, and recirculation zones. Turbulence has also been shown to contribute to thrombus formation (Smith *et al.*, 1972; Stein and Sabbah, 1974). Regions of recirculation can lead to flow stagnation, with an increased risk of platelet aggregation and clot formation.

While velocity indices focus on the shape of the velocity waveform as a function of time over the cardiac cycle, they ignore the other information contained in the velocity-power spectrum that can be more difficult to assess, particularly in a quantitative manner, but are more indicative of factors such as flow disturbances. The use of additional information from Doppler ultrasound, other than peak systolic velocity in the stenosis, has been suggested to elucidate the local hemodynamics (Brown *et al.*, 1982; Rittgers *et al.*, 1983; Krause *et al.*, 1984; Kalman *et al.*, 1985; Cloutier *et al.*, 1996). Doppler ultrasound studies have demonstrated the potential for identifying various flow characteristics (such as flow separation, vortices, and turbulent regions) using various spectral parameters, such as spectral broadening (Brown *et al.*, 1982; Rittgers *et al.*, 1983), skewedness and kurtosis (Kalman *et al.*, 1985); turbulence intensity (Wu *et al.*, 1998); or turbulence-induced spectral (Bascom *et al.*, 1993) and power changes (Bascom *et al.*, 1997; Wu *et al.*, 1998).

2.4: *In vitro* studies

Experiments using flow visualization (LoGerfo *et al.*, 1981b; Ku and Giddens, 1983) and laser Doppler anemometry (LoGerfo *et al.*, 1981a; Ku and Giddens, 1987; Gijsen *et al.*, 1996) in carotid bifurcation models have clearly demonstrated some of the important flow characteristics such as flow separation, vortices, and turbulent regions. Interestingly, the carotid sinus bulb is the only part of the vascular system in which flow separation has been documented to occur (Nerem, 1992).

Most of the *in vitro* studies demonstrating turbulence or other unique flow characteristics have used simplified models of grids, 'Y'-shaped , 'T'-junction, or stenosed tubes. Stenotic vessels have typically been modeled as rigid-walled tubes with constrictions or orifices (Kim and Corcoran, 1974; Teague *et al.*, 1984). Carotid models have been either cast from averaged *in vivo* geometries representing a relatively disease-free vessel (Bharadvaj *et al.*, 1982) or cadaver specimens (Currie *et al.*, 1996) thus representing a specific case. Additionally, many flow studies use simplistic flow conditions such as steady flow or sinusoidally pulsatile flow. A comparison study by Lutz *et al.* (1983) demonstrated distinct differences in flow phenomena between steady, sinusoidal, and arterial pulsatile flow. Cavalcanti (1995) has discussed the limitations of such studies in modeling the *in vivo* flow system.

For *in vitro* flow studies to be most beneficial, it is important to replicate the range and complexity of flow regimes seen *in vivo* but in a controlled and systematic manner. Using a series of vascular models and ultrasound-

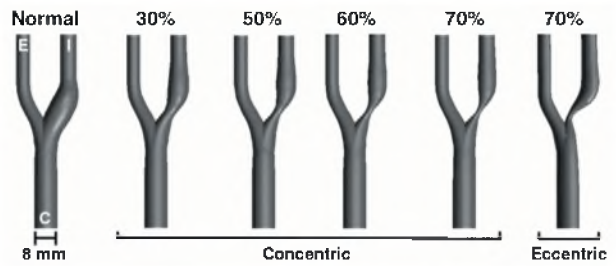

Figure 2: Idealized geometrical models of a carotid artery bifurcation (C=common carotid, I=internal carotid, E=external carotid) with a range of atherosclerotic plaque progression, leading from a normal (disease free) model to a severely stenosed model. Two configurations exist for each diseased model, representing symmetric (concentric) or asymmetric (eccentric) plaque development, as demonstrated by the two 70% stenosed models shown on the far right.

compatible phantoms, with an automated translational stage and acquisition system, it has been possible to study the flow patterns and changes corresponding to different model features. Thus it is possible to independently study the effects of various factors, such as: stenosis severity, stenosis shape, flow rate, flow resistance, the presence of ulcerations, ulceration size and geometry, or the introduction of vascular devices (e.g. stents).

3. METHODS

3.1: Models & phantoms

In vitro systems and phantoms offer a stable environment for developing and evaluating new techniques for investigating and characterizing flow. As part of an *in vitro* testing facility, a series of flow phantoms with representative geometries for various diseased states, compliance, and imaging properties has been developed. The geometrical models for the anthropomorphic carotid bifurcation phantoms are based on an *in vivo* characterization study of the carotid bifurcation by Smith *et al.* (1996) from x-ray arterial angiograms.

A family of models was derived to represent average carotid bifurcation geometries with progressing stenosis severity from a disease free (i.e. normal) geometry to mild (30%), moderate (50, 60%), and severe stenosis (70% and greater). Stenosis severity, at the point of maximum stenosis, is classified according to the NASCET criteria of percent diameter difference relative to the downstream ICA. Two sets of models exist with a different stenosis eccentricity representing different extremes in terms of plaque symmetry: a concentric model simulates a symmetrical plaque buildup within the lumen of a normal (i.e. disease free) geometry, whereas an eccentric model simulates a preferential buildup progressing inward from the lateral internal carotid artery wall. Selected geometrical models are shown in Fig. 2. As plaque builds up within a normal arterial wall, it impinges upon the arterial lumen, leaving less residual lumen for the blood flow. The geometries shown in Fig. 2 represent the residual flow lumen, such that the spatial difference between the normal model and a given stenosed model comprises the actual plaque volume.

The models can be incorporated into different types of materials. For the results shown here, we used a combination of two different methods for creating three different types of phantoms for different types of studies or for different imaging modalities. The methods include using a numerically controlled milling system and a lost-core casting technique (Smith *et al.*, 1999; Poepping *et al.*, 2004). To use these techniques to reproduce the desired geometries requires arbitrarily mouldable materials or a smoothly millable block of material. Typically this demands some compromise in properties in order to have sufficient strength to survive physiological flow pressures, reasonable modality-specific properties (e.g. tissue-mimicking acoustic properties), and ease of fabrication.

The different types of phantoms produced include: 1) a distensible, thin-walled silicone artery embedded in a gel-based tissue-mimicking material (Smith *et al.*, 1999; Poepping *et al.*, 2004), 2) an optically transparent silicone block phantom for particle-imaging techniques (Shelley Medical Imaging Technologies, London, ON), and 3) rigid ultrasound-compatible polymer phantoms.

The compliant gel-based phantoms provide a controlled, yet physiologically realistic, system for investigating how flow patterns change in a series of models that emulate typical disease progression. Here, good ultrasound compatibility is important in order to study corresponding changes in observed Doppler ultrasound spectra, and thus testing the abilities of Doppler ultrasound to identify important flow characteristics. The thin-walled silicone artery provides sufficient strength to withstand physiologically realistic pressures, and it is surrounded by an ultrasound-compatible, tissue-mimicking material (Ramnarine *et al.*, 2001).

The optically transparent silicone phantoms are comprised of a single block of silicone elastomer with a hollow flow channel with the desired carotid geometry. These phantoms are used for particle imaging techniques enable direct visualization of the complex flow patterns. Experiments using the gel-based and silicone phantoms in turn have provided for excellent comparison studies with computational fluid dynamics (CFD) (Steinman *et al.*, 2000; Khoshniat *et al.*, 2005) using identical geometrical models.

The carotid models, or other geometries, can also be milled directly into an ultrasound-compatible polymer. This technique was used in order to incorporate models of ulcerations in the geometries, test patient-specific geometries, and to test intravascular devices. With this technique, additional surface roughness and fine features, which are difficult to reproduce with a lost-core casting technique, can be precisely fabricated. Also the technique is far less time consuming than the numerous steps involved in the lost-core casting techniques required for gel-based or silicone phantoms. These plastic phantoms are useful when the goal is a direct comparison between a control model and a test model, i.e. to investigate relative flow differences due to an additional geometrical feature (e.g. ulceration) or

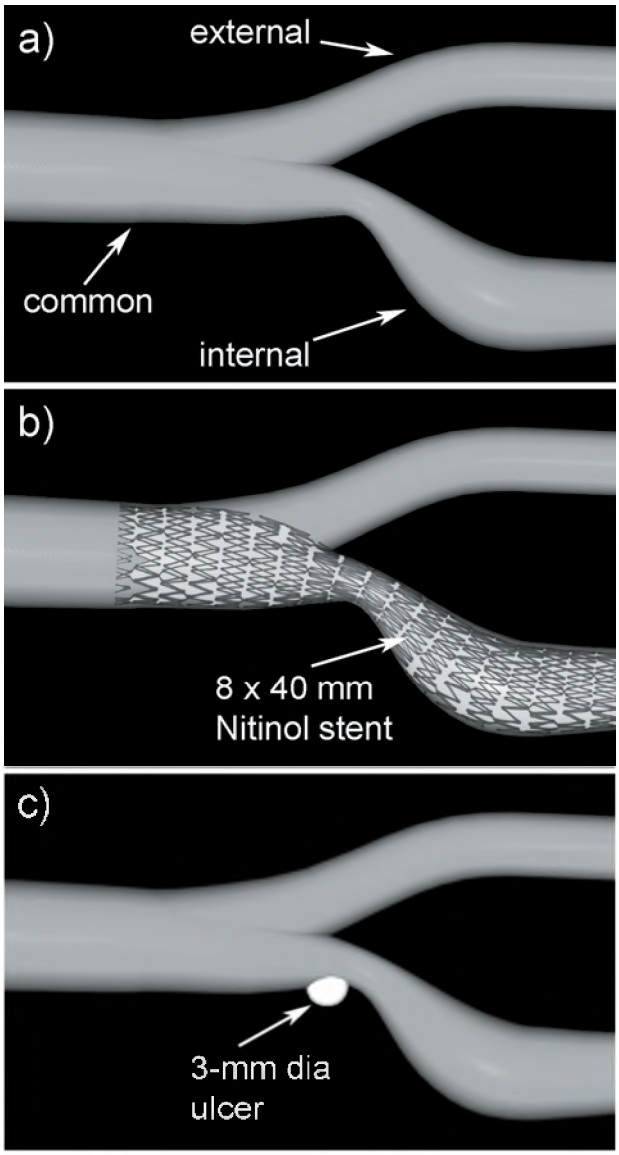

Figure 3: Schematic demonstrating a 50% eccentric carotid model before (a) and after (b) stent implantation, and (c) an identical model with a 3-mm diameter hemispherical ulceration in ICA branch extending into the impinging plaque volume.

intravascular device (e.g. stent). Hence, possible problems with refraction errors due to the differences in the material's acoustic properties are not a significant issue because of the comparative nature of the study. Additionally, the design of the rigid phantoms makes it possible to deploy a stent, for example, and later extract it for re-use, without sacrificing the integrity of the phantom.

In the study described here, a plastic phantom with 50% eccentric carotid model geometry was used to investigate the possible flow disturbances due to a stent implantation. A self-expanding Nitinol carotid stent (Cordis PRECISE, 8x40mm) was used, which extended from the common carotid artery (CCA) into the internal carotid artery (ICA), covering the external carotid artery (ECA) orifice or branch, as shown in Fig. 3b. DUS measurements were performed before and after stent implantation.

Additionally, an identical 50%-eccentric model phantom was produced with a 3-mm diameter hemispherical ulcer located on the non-flow-divider wall of the ICA at the level of the bifurcation apex, as shown in Fig. 3c.

Finally, for testing the detection of different levels of turbulence, an orifice phantom was used consisting of a 1.2-m long acrylic inlet tube with a 1.27-cm inner diameter, which was connected to a mountable interface that accepted different inserts. A 1.53-mm thick disk with a 1.6-mm diameter orifice in the center was inserted to generate constrained-jet turbulence. The long inlet length ensured fully developed laminar flow prior to the orifice. An ultrasound-compatible high-density polyethylene portion, with a 1.27-cm inner diameter and 1.9-cm outer diameter, was connected to the interface, which enabled DUS measurements up to 8 cm downstream of the orifice.

3.2: *In vitro* facility

A programmable system was used for semi-automated data acquisition over 3-D space and multiple cardiac cycles with temporal (i.e. ECG-like) gating (Poepping *et al.*, 2002). A 3-axis translational stage allowed the lumen to be interrogated with a small Doppler sample volume at the desired spatial intervals in a 3-D raster to collect 10 cardiac cycles of gated Doppler signal at each site. Thus, it is possible to collect high-resolution DUS data over a full carotid artery volume for an extended length of time. To interrogate a carotid bifurcation model at 1-mm increments, the central plane consisted of over 1000 sites, and a half-volume data set consisted of over 3200 sites.

For the steady flow experiments with the 1.6-mm orifice, 1 s of data was collected at each point within a 2-D central vertical plane, starting 1.7 cm distal to the orifice and extending 4 cm downstream producing a complete 2-D grid of 533 points with 1-mm sample spacing.

A programmable computer-controlled pump (Holdsworth *et al.*, 1991) (UHDC Flow System, Shelley Medical Imaging Technologies, London, ON) was used to perfuse the phantoms with an appropriate fluid, as described in each of the DPI and DUS sections below. The pump can be programmed to output constant or pulsatile flow including arbitrary flow waveforms, for example, to simulate the *in vivo* carotid artery waveform (Holdsworth *et al.*, 1999). For the steady flow experiments, flow rates of 5, 7.5, 10, 12.5, and 15 ml/s were used. For the pulsatile flow studies, a carotid waveform was used with a mean flow rate of 6 ml/s and peak flow rate at peak systole of 23.5 ml/s.

3.3: Doppler ultrasound (DUS)

For DUS studies, the phantoms were perfused with an ultrasound-compatible blood-mimicking fluid (Ramnarine *et al.*, 1998) with specified attenuation of 0.26 dB/cm at 5 MHz, speed of sound of 1547 m/s, and viscosity of 4.1±0.1

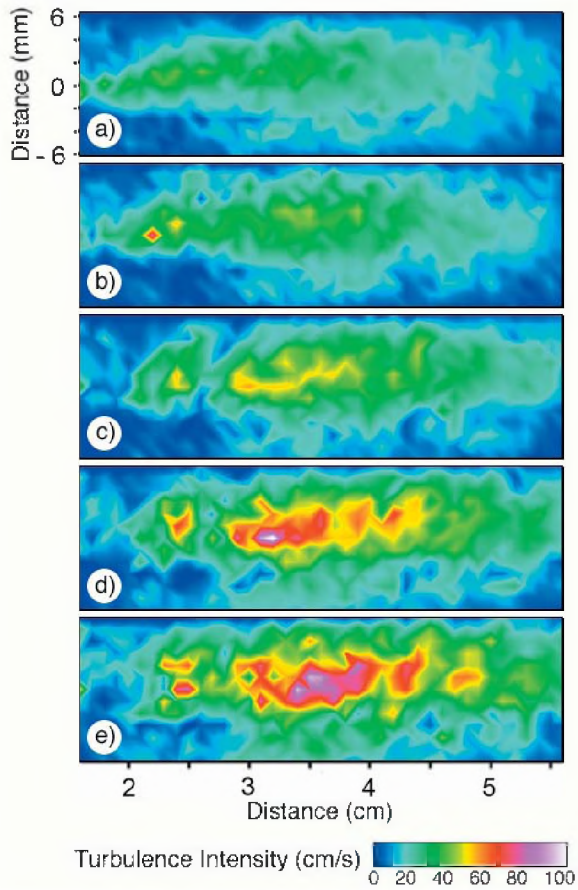

Figure 4: Colour-encoded, 2-D map of turbulence intensity for flow rates 5, 7.5, 10, 12.5, and 15 ml/s (a to e respectively) acquired 1.7 to 5.7 cm downstream of a 1.6-µm orifice.

mPa·s. The BMF has 5±2 µm nylon particles (Orgasol 2001 UD NAT 1, Elf Atochem, Paris, France) that act as Doppler scattering sites.

Data was collected using one of two conventional clinical ultrasound systems: 1) ATL Ultramark 8 (Bothell, WA), 5 MHz mechanical scanning probe (Access 10-PV), 1.5-mm sample-volume length, collecting quadrature data, 23 kHz pulse repetition frequency (PRF); or 2) ATL Ultramark 9, L7-4 (4 MHz central frequency) linear array transducer, 1.0-mm sample-volume length, collecting audio data, 18.5 kHz PRF. Acquisition parameters used were a Doppler angle of 60°, minimum sample volume length, and a minimum 50 Hz wall filter. Data was digitized at 44.1 kHz and recorded for offline analysis, including a 1024-point FFT with a 1024-point Hanning window and a 50% overlap between consecutive windows.

Spectra were analyzed with respect to mean velocity, peak velocity (velocity corresponding to 90% power), integrated power, or spectral broadening index, SBI (given by: 1 – mean velocity/peak velocity) (Brown *et al.*, 1982). Thus, a 4-D (i.e. time-varying 3-D) Doppler data set with 1.3-cm/s velocity (43 Hz frequency) resolution and 12-ms temporal resolution (approximately 79 time points per cardiac cycle) can be produced for each parameter. The data was prospectively gated, such that it was possible to derive an ensemble-averaged waveform (1 average cycle from the 10 measured cycles), for each of the spectral parameters, as well as the root-mean-square (RMS) deviation in the 10 contributing values at each time point in the ensemble-averaged waveform. Using this technique, turbulence intensity (TI) was calculated, corresponding to the RMS deviation in the mean velocity for each time point.

3.4: Digital Particle Imaging (DPI)

Digital particle imaging (DPI) is a well-established technique that is valuable as a means of visualizing the 3-D flow patterns and as a reference for comparison with the DUS data. Flow can be visualized in transparent phantoms of identical model geometry as used in DUS and CFD studies (Steinman *et al.*, 2000; Poepping *et al.*, 2001). The DPI system consisted of two 5 mW He-Ne lasers (Melles Griot, Carlsbad, CA) to produce 1-mm-thick fanbeams that illuminated the central plane of the carotid model uniformly from opposite sides. A charge-coupled-device (CCD) camera (Panasonic GP-MF552, Seacaucus, NJ) was used to record the flow of small (~400 µm diameter) reflective polystyrene particles (Amberlite IRA-904, Sigma-Aldrich, Oakville, ON) in a 2:1 mixture by volume of water-glycerol fluid. ECG-gated, 640x480, de-interlaced digital images of the central plane of the vessel model were obtained with 17 ms temporal resolution using a UNIX workstation (SGI Indy, Silicon Graphics Inc., Mountainview, CA).

4. RESULTS:

Figure 4 shows the turbulence intensity measured downstream of a 1.6-mm orifice, demonstrating the ability to quantify turbulence. The fluctuation due to standard noise, measured from a site within fully developed laminar flow (i.e. without orifice insert) was found to be 0.7 cm/s. Fig. 4 shows that for the 5 and 7.5 ml/s steady-flow rates, TI values in the jet were in the range of 30-50 cm/s, but extended up to approximately 100 cm/s at the higher flow rates of 12.5 and 15 ml/s.

It is relevant to note that the pulsatile carotid waveform used in the vascular models has a mean flow rate of 6 ml/s and maximum of 23.5 ml/s at peak systole. It is also relevant to note that for the 70% stenosed model, the diameter at the point of maximum stenosis corresponds to 1.68 mm, although with a significantly longer stenotic neck than the 1.53-mm thickness of the orifice plate used above.

Figure 5 shows results for two severely (70%) stenosed models in a comparison of DPI flow maps and 2-D central-plane maps for three different DUS spectral parameters – mean velocity, spectral broadening index, and turbulence intensity. The models differ only in the shape of the stenosis, representing a different symmetry in the buildup of plaque. The DPI data provides an important reference for identifying the flow features. Since the DPI image represents a 17-ms snapshot, each black streak traces out the path of a particle within the illuminated central plane, and the length of the particle streak is representative of the velocity. Slow or stagnant particles appear as spots. From

Fig. 5a and 5b, it can be seen that the severely stenosed models exhibit a jet stream with resultant recirculation zones on both sides of the jet and highly disturbed, or turbulent, flow downstream. However, the recirculation zones differ considerably in size. The eccentric model exhibits a larger recirculation zone ER1 and with a higher gradient of velocities (i.e. higher SBI in Fig. 5f). Recall that the SBI is determined from the velocity distribution within each approximately 1-mm^3 sample volume. The four vertical panels present different but highly complementary results. The mean velocity maps are a quantitative indication of the jet velocity, as well as the general flow behaviour. The SBI maps clearly indicate the regions of recirculation (i.e. spatial variance) and the TI maps indicate rapidly fluctuating or unstable flow (i.e. temporal variance). Note that the TI here for peak systole (i.e. peak flow of 23.5ml/s) is on the order of 50 cm/s with values extending up to 120 cm/s. Similar flow pattern comparisons have been possible using DPI and CFD (Steinman *et al.*, 2000), CFD and DUS (Khoshniat *et al.*, 2005), and DPI and DUS (Poepping *et al.*, 2001).

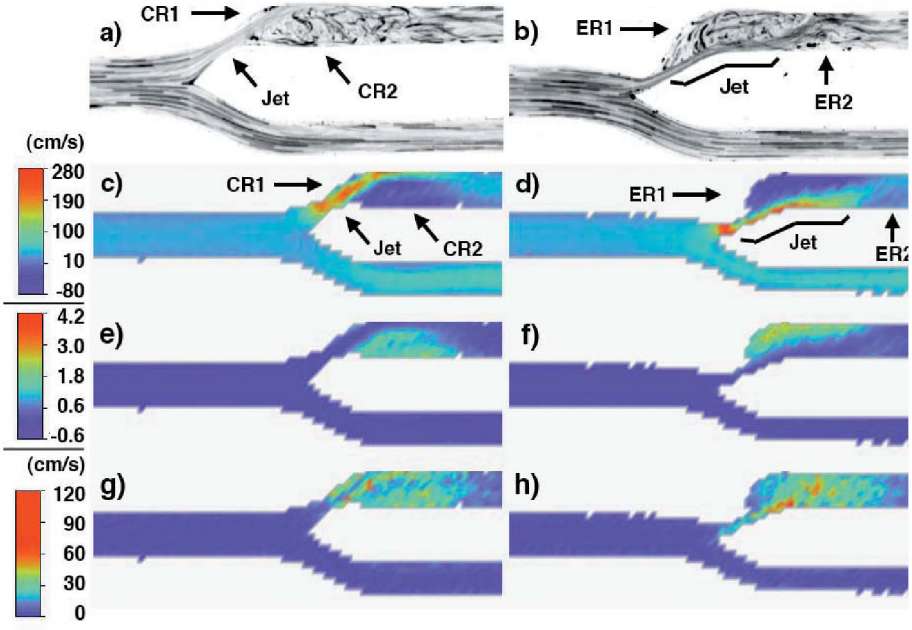

Figure 5: Comparison of DPI and DUS flow maps for carotid bifurcation models with 70% concentric stenosis (left panels) and 70% eccentric stenosis (right panels) at peak systole. Panels show DPI (a,b), DUS mean velocity (c,d), DUS spectral broadening index (e,f), and DUS turbulence intensity (g,h) with corresponding colour bar on the far left. Flow proceeds from the common carotid artery (left) and divides into the internal (top) and external (bottom) carotid arteries. The different jet paths and recirculation zones are indicated in the concentric (CR1, CR2) and eccentric (ER1, ER2) models, respectively.

Figure 6 shows the mean velocity maps and Fig. 7 the turbulence intensity maps comparing results from the three 50%-eccentric models studied here: i) before (Fig 6a, 7a) and ii) after (Fig 6b, 7b) stent implantation and iii) with a 3-mm diameter hemi-spherical plaque ulceration (Fig. 6c, 7c). The results indicate that the introduction of a self-expanding carotid stent did not have a significant effect on the measurements of mean velocity and turbulence intensity when geometry, flow rate, and Doppler parameters were maintained. Figures 6a and 6b exhibit very similar velocity patterns through the stenosis and the ICA. Slightly lower velocities can be observed in the neck of the stenosis and, in particular, in the ECA (upper branch), after flow has passed through the mesh wall of the stent, but it appears to quickly re-laminarize, as indicated by a parabolic-like colour gradient. More notably, the TI maps in Fig. 7a and 7b do not suggest notably higher levels of flow disturbance downstream in the ICA.

Finally, Fig. 6c and 7c represent mean velocity and TI flow maps for the 50%-eccentric model with an ulceration, which can also be compared with Fig. 6a and 7a of the standard (ulcer-free) 50%-eccentric model. Fig. 6c and 7c indicate that the imposed ulceration did not introduce obvious changes in downstream velocity patterns or flow disturbance.

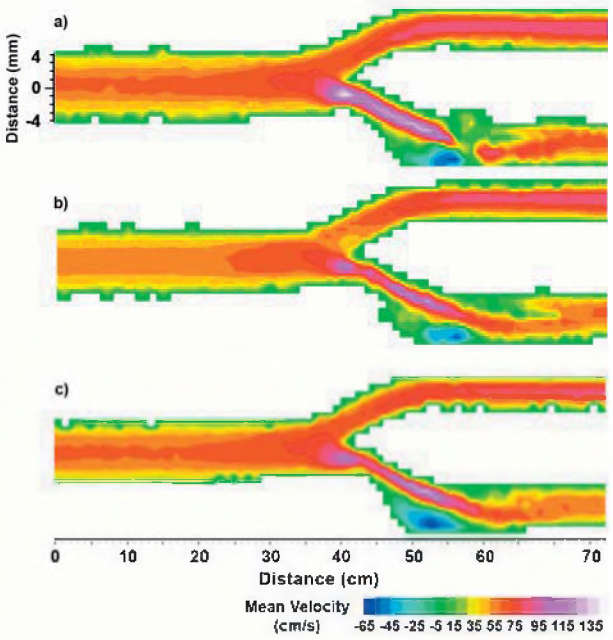

Figure 6: Colour-encoded mean velocity maps of flow in a carotid bifurcation with 50% concentric stenosis model: a) control model (no modification), b) with intravascular stent, and c) with a 3-mm diameter ulceration, as shown in Fig. 3. Flow from the common carotid artery on the left branches into the external (top) and internal (bottom) carotid arteries.

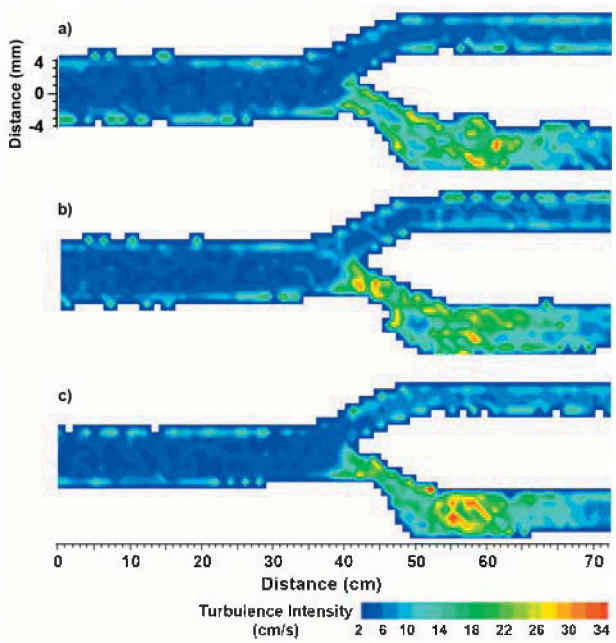

Figure 7: Colour-encoded turbulence intensity maps of flow in a carotid bifurcation with 50% concentric stenosis model: a) control model (no modification), b) with intravascular stent, and c) with a 3-mm diameter ulceration, as shown in Fig. 3. Flow from the common carotid artery on the left branches into the external (top) and internal (bottom) carotid arteries.

5. DISCUSSION & CONCLUSION

A major limitation of the current clinical implementation of DUS diagnoses of carotid disease based on peak velocities in the stenosis is that this only provides a partial description of the hemodynamic disturbances caused by the stenosis. High blood-flow velocities are only indirectly related to stroke and thrombo-embolus production. Elevated shear stress rates, the formation of turbulence, and the presence of slow or recirculating flow have all been implicated in increased clot production. Therefore other hemodynamic parameters, such as shear and turbulence, may be more directly correlated with thromboembolism production and plaque rupture in the carotid artery. Doppler ultrasound may in fact provide a more direct measurement of stroke risk based on hemodynamic factors compared to current techniques based strictly on lumen diameter reduction or some other surrogate measure.

The use of pulsatile flow is particularly important for studies in vascular models. Although the data here only shows a particular snapshot in time, the complete data set can be viewed as a cine loop or movie. By viewing the whole time sequence, the recirculation zones can be seen to form and then get flushed out, and similarly the turbulence dissipates and reforms through the cardiac cycle. Additionally, it is possible to see vortex shedding occur, particularly from the downstream recirculation zone (CR2 in Fig. 5) of the concentric model.

It is important to note that all of the ultrasound data we report was acquired with conventional clinical ultrasound equipment. This approach provides a major advantage, bringing the research one step closer to translating the work to *in vivo* studies. The DUS work shown here all has a direct application to human studies in future work, such as evaluating *in vivo* flow following carotid endarterectomy, following insertion of intravascular devices, or for improved diagnosis of vascular disease.

Future *in vitro* work can include the testing of patient-specific models using the rapid prototyping method of milling geometries directly into plastics or other materials. Also, while the ulceration model that was shown here did not introduce significant changes in downstream velocity patterns, this particular model only represents one typical category of ulceration geometry. Future work will investigate ulcerations of other geometries, including cavities with different alignment relative to the flow direction (i.e. upstream or downstream), or geometries with an obvious neck extending between the ulcer cavity and the residual lumen. Additionally, it may be desirable to further test intravascular devices in more compliant models where the stent may affect the compliance, which leads to a change in flow resistance and the velocity waveform.

The overall goal has been the development of a test facility to provide a means of evaluating and investigating various hemodynamic effects correlated with vascular disease.

ACKNOWLEDGEMENTS

The authors thank Hristo Nikolov for his technical expertise in phantom production. The authors also acknowledge financial support from the CIHR, Heart and Stroke Foundation of Canada (T-5135), NSERC (Discovery Grant and UFA salary support of T.L.P.), and the Ontario Research and Development Challenge Fund. D.W.H. is a Career Investigator supported by the Heart and Stroke Foundation of Ontario.

REFERENCES

Alexandrov AV, Vital D, Brodie DS, Hamilton P and Grotta JC. 1997 Grading carotid stenosis with ultrasound. An interlaboratory comparison. *Stroke* 28:1208-10

Arbeille P, Bouin-Pineau MH and Herault S. 1999 Accuracy of the main Doppler methods for evaluating the degree of carotid stenoses (continuous wave, pulsed wave, and color Doppler). *Ultrasound in Medicine & Biology* 25:65-73

Bascom PA, Cobbold RS, Routh HF and Johnston KW. 1993 On the Doppler signal from a steady flow asymmetrical stenosis model: effects of turbulence. *Ultrasound in Medicine & Biology* 19:197-210

Bascom PA, Johnston KW, Cobbold RS and Ojha M. 1997 Relation of the flow field distal to a moderate stenosis to the Doppler power. *Ultrasound in Medicine & Biology* 23:25-39

Bharadvaj BK, Mabon RF and Giddens DP. 1982 Steady flow in a model of the human carotid bifurcation. Part I--flow visualization. *Journal of Biomechanics* 15:349-62

Brown PM, Johnston KW, Kassam M and Cobbold RS. 1982 A critical study of ultrasound Doppler spectral analysis for

detecting carotid disease. *Ultrasound in Medicine & Biology* 8:515-23

Carpenter JP, Lexa FJ and Davis JT. 1996 Determination of duplex Doppler ultrasound criteria appropriate to the North American Symptomatic Carotid Endarterectomy Trial. *Stroke* 27:695-9

Cavalcanti S. 1995 Hemodynamics of an artery with mild stenosis. *Journal of Biomechanics* 28:387-99

Cloutier G, Allard L and Durand LG. 1996 Characterization of blood flow turbulence with pulsed-wave and power Doppler ultrasound imaging. *Journal of Biomechanical Engineering* 118:318-25

Currie IC, Wilson YG, Baird RN and Lamont PM. 1996 Detection of sub-critical arterial stenoses by hyperaemic Doppler. *European Journal of Vascular & Endovascular Surgery* 11:29-35

Eliasziw M, Streifler JY, Fox AJ, *et al.* 1994 Significance of plaque ulceration in symptomatic patients with high-grade carotid stenosis. North American Symptomatic Carotid Endarterectomy Trial. *Stroke* 25:304-8

European Carotid Surgery Trialists' Collaborative G. 1998 Randomised trial of endarterectomy for recently symptomatic carotid stenosis: final results of the MRC European Carotid Surgery Trial (ECST). *Lancet* 351:1379-87

Fenster A, Lee D, Sherebrin S, *et al.* 1997 *Three-dimensional ultrasound imaging of carotid occlusive disease,* (Amsterdam: Elsevier) pp 17-24

Gijsen FJ, Palmen DE, van der Beek MH, *et al.* 1996 Analysis of the axial flow field in stenosed carotid artery bifurcation models--LDA experiments. *Journal of Biomechanics* 29:1483-9

Griewing B, Morgenstern C, Driesner F, *et al.* 1996 Cerebrovascular disease assessed by color-flow and power Doppler ultrasonography. Comparison with digital subtraction angiography in internal carotid artery stenosis. *Stroke* 27:95-100

Heart and Stroke Foundation of Canada H 1999 The changing face of heart disease and stroke in Canada. (Ottawa, Canada

Heart and Stroke Foundation of Canada H 2002 (HSFC Homepage).

Holdsworth DW, Norley CJ, Frayne R, Steinman DA and Rutt BK. 1999 Characterization of common carotid artery blood-flow waveforms in normal human subjects. *Physiological Measurement* 20:219-40

Holdsworth DW, Rickey DW, Drangova M, Miller DJ and Fenster A. 1991 Computer-controlled positive displacement pump for physiological flow simulation. *Medical & Biological Engineering & Computing* 29:565-70

Holme PA, Orvim U, Hamers MJ, *et al.* 1997 Shear-induced platelet activation and platelet microparticle formation at blood flow conditions as in arteries with a severe stenosis. *Arteriosclerosis, Thrombosis & Vascular Biology* 17:646-53

Kalman PG, Johnston KW, Zuech P, Kassam M and Poots K. 1985 In vitro comparison of alternative methods for quantifying the severity of Doppler spectral broadening for the diagnosis of carotid arterial occlusive disease. *Ultrasound in Medicine & Biology* 11:435-40

Khoshniat M, Thorne ML, Poepping TL, *et al.* 2005 Real-time numerical simulation of Doppler ultrasound in the presence of nonaxial flow. *Ultrasound in Medicine and Biology* 31:519-28

Kim BM and Corcoran WH. 1974 Experimental measurements of turbulence spectra distal to stenoses. *Journal of Biomechanics* 7:335-42

Krause H, Segard M, Carey P, Bernstein EF and Fronek A. 1984 Doppler power frequency spectrum analysis in the diagnosis of carotid artery disease. *Stroke* 15:351-8

Ku DN and Giddens DP. 1983 Pulsatile flow in a model carotid bifurcation. *Arteriosclerosis* 3:31-9

Ku DN and Giddens DP. 1987 Laser Doppler anemometer measurements of pulsatile flow in a model carotid bifurcation. *Journal of Biomechanics* 20:407-21

LoGerfo FW, Crawshaw HM, Nowak M, *et al.* 1981a Effect of flow split on separation and stagnation in a model vascular bifurcation. *Stroke* 12:660-5

LoGerfo FW, Nowak MD, Quist WC, Crawshaw HM and Bharadvaj BK. 1981b Flow studies in a model carotid bifurcation. *Arteriosclerosis* 1:235-41

Lutz RJ, Hsu L, Menawat A, Zrubek J and Edwards K. 1983 Comparison of steady and pulsatile flow in a double branching arterial model. *Journal of Biomechanics* 16:753-66

Moneta GL, Edwards JM, Chitwood RW, *et al.* 1993 Correlation of North American Symptomatic Carotid Endarterectomy Trial (NASCET) angiographic definition of 70% to 99% internal carotid artery stenosis with duplex scanning. *Journal of Vascular Surgery* 17:152-7; discussion 7-9

Nerem RM. 1992 Vascular fluid mechanics, the arterial wall, and atherosclerosis. *Journal of Biomechanical Engineering* 114:274-82

North American Symptomatic Carotid Endarterectomy Trial C. 1991 Beneficial effect of carotid endarterectomy in symptomatic patients with high-grade carotid stenosis. *New England Journal of Medicine* 325:445-53

Poepping TL, Nikolov HN, Rankin RN, Lee M and Holdsworth DW. 2002 An in vitro system for Doppler ultrasound flow studies in the stenosed carotid artery bifurcation. *Ultrasound in Medicine and Biology* 28:495-506

Poepping TL, Nikolov HN, Thorne ML and Holdsworth DW. 2004 A thin-walled carotid vessel phantom for Doppler ultrasound flow studies. *Ultrasound in Medicine & Biology* 30:1067-78

Poepping TL, Rankin RN and Holdsworth DW. 2001 Four-dimensional Doppler ultrasound measurements in stenosed carotid bifurcation models: Effect of concentric vs. eccentric stenosis. Proc. of SPIE Medical Imaging 2001: Ultrasonic Imaging and Signal Processing, ed. MF Insana and KK Shung. 4325:305-13

Ramnarine KV, Anderson T and Hoskins PR. 2001 Construction and geometric stability of physiological flow rate wall-less stenosis phantoms. *Ultrasound in Medicine & Biology* 27:245-50

Ramnarine KV, Nassiri DK, Hoskins PR and Lubbers J. 1998 Validation of a new blood-mimicking fluid for use in Doppler flow test objects. *Ultrasound in Medicine & Biology* 24:451-9

Ranke C, Creutzig A, Becker H and Trappe HJ. 1999 Standardization of carotid ultrasound: a hemodynamic method to normalize for interindividual and interequipment variability. *Stroke* 30:402-6

Reininger AJ, Reininger CB, Heinzmann U and Wurzinger LJ. 1995 Residence time in niches of stagnant flow determines fibrin clot formation in an arterial branching model--detailed flow analysis and experimental results. *Thrombosis & Haemostasis* 74:916-22

Rittgers SE, Thornhill BM and Barnes RW. 1983 Quantitative analysis of carotid artery Doppler spectral waveforms: diagnostic value of parameters. *Ultrasound in Medicine & Biology* 9:255-64

Rothwell PM, Gibson R and Warlow CP. 2000 Interrelation between plaque surface morphology and degree of stenosis on carotid angiograms and the risk of ischemic stroke in patients with symptomatic carotid stenosis. On behalf of the European Carotid Surgery Trialists' Collaborative Group. *Stroke* 31:615-21

Schwartz SW, Chambless LE, Baker WH, *et al.* 1997 Consistency of Doppler parameters in predicting arteriographically confirmed carotid stenosis. *Stroke* 28:343-7

Smith RF, Rutt BK, Fox AJ, Rankin RN and Holdsworth DW. 1996 Geometric characterization of stenosed human carotid arteries. *Academic Radiology* 3:898-911

Smith RF, Rutt BK and Holdsworth DW. 1999 Anthropomorphic carotid bifurcation phantom for MRI applications. *Journal of Magnetic Resonance Imaging* 10:533-44

Smith RL, Blick EF, Coalson J and Stein PD. 1972 Thrombus production by turbulence. *Journal of Applied Physiology* 32:261-4

Spencer MP and Reid JM. 1979 Quantitation of carotid stenosis with continuous-wave (C-W) Doppler ultrasound. *Stroke* 10:326-30

Stein PD and Sabbah HN. 1974 Measured turbulence and its effect on thrombus formation. *Circulation Research* 35:608-14

Steinman DA, Poepping TL, Tambasco M, Rankin RN and Holdsworth DW. 2000 Flow Patterns at the Stenosed Carotid Bifurcation: Effect of Concentric Versus Eccentric Stenosis. *Annals of Biomedical Engineering* 28:415-23

Teague SM, von Ramm OT and Kisslo JA. 1984 Pulsed Doppler spectral analysis of bounded fluid jets. *Ultrasound in Medicine & Biology* 10:435-41

Van Damme H and Vivario M. 1993 Pathologic aspects of carotid plaques: surgical and clinical significance. *International Angiology* 12:299-311

Wu SJ, Shung KK and Brasseur JG. 1998 In situ measurements of Doppler power vs. flow turbulence intensity in red cell suspensions. *Ultrasound in Medicine & Biology* 24:1009-21

Yao J, van Sambeek MR, Dall'Agata A, *et al.* 1998 Three-dimensional ultrasound study of carotid arteries before and after endarterectomy; analysis of stenotic lesions and surgical impact on the vessel. *Stroke* 29:2026-31.

CODED EXCITATION METHODS FOR ULTRASOUND HARMONIC IMAGING

Roozbeh Arshadi, Alfred C.H. Yu, and Richard S.C. Cobbold
Institute of Biomaterials and Biomedical Engineering, University of Toronto
163 College Street, Toronto, ON, Canada. M5S 3G9
cobbold@ecf.utoronto.ca

ABSTRACT

Coded excitation methods offer the potential for improving the SNR without increasing the peak transmitted power and without sacrificing resolution. Our study examines the potential application of coded waveforms, specifically FM chirps, in harmonic imaging. Such a system, in which nonlinear echoes from tissue are used to form the image, requires the extraction and compression of the second harmonic portion of the echo signal. Our objective is to obtain the second harmonic using just one transmission, thereby avoiding problems of frame rate reduction and movement artifacts associated with multiple transmission schemes. With the help of an efficient method for predicting the transient nonlinear field from a focused transducer, design issues such as waveform and bandwidth selection, as well as filters for second harmonic extraction and compression are examined. Simulations reveal the presence of axial sidelobes in the compressed echo waveform as the bandwidth of the transmitted chirp is increased. These sidelobes, resulting from the overlap of the fundamental and third harmonic bands with the second harmonic, cannot be removed using conventional Fourier filtering. Alternative filtering techniques which utilize the separation of the harmonic bands of a backscattered chirp in the joint time-frequency domain are suggested.

SOMMAIRE

Les méthodes d'excitation codée ont le potentiel d'améliorer le ratio signal-bruit sans augmenter la puissance maximale transmise et sans sacrifier la résolution. Notre étude examine l'application potentielle de formes d'onde codées, plus spécifiquement de compression d'impulsions FM pour imagerie harmonique. Dans un tel système, les échos non-linéaires provenant du tissu sont utilisés afin de former l'image, ce qui requiert l'extraction et la compression de la deuxième portion harmonique du signal d'écho. Notre objectif est d'obtenir le deuxième harmonique en utilisant seulement une transmission, évitant ainsi des problèmes de réduction du temps d'image et d'artefacts de mouvement associés avec de multiples schémas de transmission. En utilisant une méthode efficace de prédiction du champs non-linéaire transitoire provenant d'un transducteur focalisé, des problèmes de conception tels que la sélection de forme d'onde et de la largeur de bande, ainsi que de filtres pour l'extraction et la compression du deuxième harmonique sont examinés. Les simulations révèlent la présence de lobes latéraux axiaux dans la forme d'onde compressée au fur et a mesure que la largeur de bande de la compression d'impulsion transmise est augmentée. Ces lobes latéraux, dus au chevauchement de la bande harmonique fondamentale et de la troisième bande avec la deuxième bande harmonique ne peuvent pas être enlevés en utilisant le filtrage conventionnel de Fourier. En tant qu'alternative, des techniques de filtrage utilisant la séparation de bandes harmoniques de compressions d'impulsions rétrodiffusés dans le domaine commun de temps-fréquence sont suggérées.

1. INTRODUCTION

Coded excitation methods have been used in ultrasound imaging to improve the signal-to-noise ratio (SNR) and to maintain a high axial resolution at greater distances without increasing the peak transmitted power. As recently reviewed by Cobbold (see Sec. 8.4 in [1]), these methods were initially developed in the radar research field in the 1950s. Their application to medical ultrasound started in the 1970s when they were first used to improve the performance of flow estimation [2] and tissue imaging [3][4]. In terms of their performance in ultrasound systems, coded excitation methods can achieve SNR gains in the range of 15-20 dB [5]. This improvement is comparatively more modest than the ones achievable in radar systems, where SNR gains on the order of several thousands are often possible.

The development of coded excitation schemes was originally motivated by Woodward's theoretical studies on the range ambiguity problem in radar systems [6]. In particular, it was postulated that a long-duration transmit

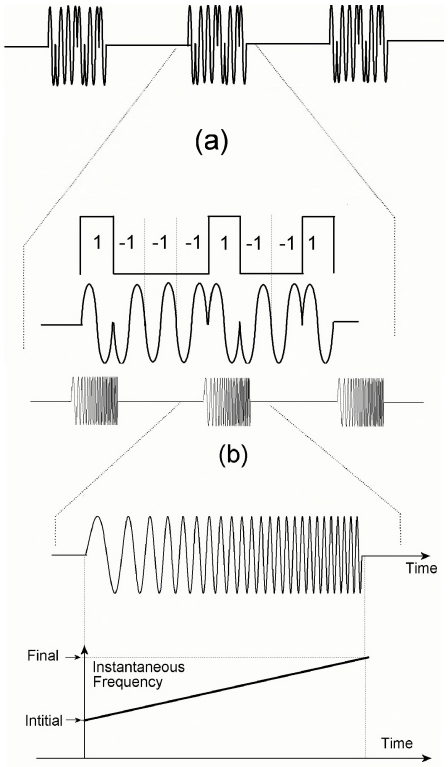

Figure 1. Types of coded excitation schemes applicable to ultrasound imaging. (a) Binary encoding (a single-cycle sinusoidal transmitted pulse has been assumed). (b) Linear frequency-modulated (FM) chirp.

waveform could be used to increase the total transmitted energy while maintaining the same peak power without any loss in spatial resolution. Even though coded signals are generally longer duration than non-coded ones, the potential loss in spatial resolution can be avoided by using a compression filter that matches the pulse echoes with the transmitted signal's time-reversed conjugate. Note that the resulting signal obtained from the cross-correlator is often known as the compressed waveform.

In the radar literature, a number of schemes have been proposed for coded excitation (see Ch. 6 & 8 in [7]). However, the applicability of many of these coding schemes in medical ultrasound is limited by the effects caused by the high attenuation of tissue and tissue motion. Nevertheless, two particular coding schemes – namely, binary codes and frequency-modulated (FM) chirps (see Figure 1) – are important for achieving significant SNR improvements in ultrasound [8]. In their comparison of these two schemes, Misaridis and Jensen [9][10] argued that binary codes appear to be suboptimal because the sharp transitions in between binary states are very high frequency contents that tend to be truncated by the limited transducer bandwidth and the effects of frequency-dependent attenuation in tissues. Based on this argument, it seems to be more appropriate to focus on the FM-chirp coding method.

Although the use of coded excitation in ultrasound imaging is well established, there have been few studies that considered the potential use of these methods in tissue harmonic imaging where the nonlinear ultrasound echoes returned from tissues are used to form images. As such, the purpose of this paper is to use simulation means to examine the primary issues related to the use of linear FM chirps for improving the SNR performance in tissue harmonic imaging. The simulations are based on the use of FM chirp coding in a single-firing harmonic imaging scheme, and these results are compared with the ones obtained from a two-pulse harmonic imaging scheme known as pulse inversion [11]. To facilitate presentation of the simulations, we shall start with brief reviews of FM chirp coding and harmonic imaging methods. Details of the simulations scheme used in our studies will subsequently be described.

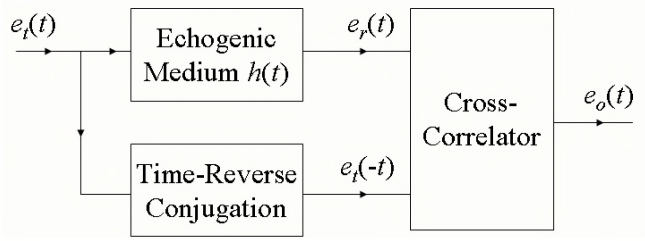

Figure 2. Generic diagram for a compression filter in which the output is the cross-correlation of the received signals and the transmitted pulse's time-reversed conjugate.

2. THEORY

2.1. Principles of FM Chirp Methods

Background Considerations

Consider the pulse compression filter shown in Figure 2, where the pulse-echo impulse response of a given echogenic medium is denoted by $h(t)$. If the transducer is excited by a waveform $e_t(t)$ and if the filtering effect of the transducer is ignored, then the received waveform $e_r(t)$ is given by the following convolution:

$$e_r(t) = e_t(t) * h(t) = \int_{-\infty}^{\infty} e_t(t-\tau)h(\tau)\,d\tau \,. \tag{1}$$

Also, the compressed waveform $e_o(t)$ (i.e. the output of the cross-correlator) can be shown to be equal to:

$$\begin{aligned} e_o(t) &= \int_{-\infty}^{\infty} e_r(t+u)e_t(-u)\,du \\ &= \int_{-\infty}^{\infty}\left[\int_{-\infty}^{\infty} e_t(t+u-\tau)e_t(-u)\,du\right]h(\tau)\,d\tau \\ &= R_{ee}(t) * h(t) \end{aligned} \tag{2}$$

where $R_{ee}(t)$ is the autocorrelation of $e_t(t)$. From (2), it can be seen that the compressed waveform is the convolution between the transmitted signal's autocorrelation function and the medium's impulse response.

General Principles

In general, a unit-amplitude FM chirp pulse whose instantaneous frequency varies linearly with time can be expressed as:

$$e_t(t) = \mathrm{rect}(t/T)\cos\left(\frac{kt^2}{2} + \omega_o t\right) \quad \text{for } |t| < \frac{T}{2}, \tag{3}$$

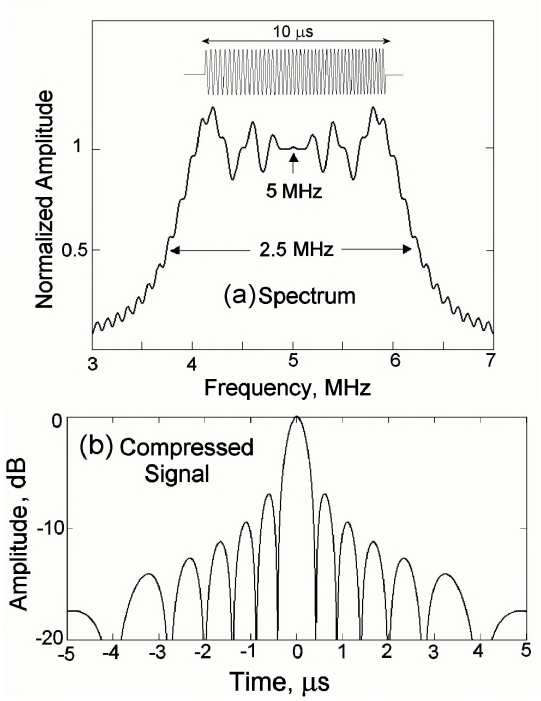

Figure 3. A non-tapered linear FM chirp of 10 μs duration, 5MHz center frequency, and 2.5MHz signal bandwidth. (a) Frequency spectrum as calculated from (4). (b) Envelope of the compressed signal as calculated from (3) without the cosine term (the total compressed signal duration is 20 μs).

where T is the pulse duration, ω_o is the center angular frequency, and k is a chirp rate parameter that controls the pulse bandwidth. Note that the instantaneous frequency of (3) is given by $\omega(t) = d\varphi/dt = \omega_o + kt$, where φ is the argument of the cosine function.

To illustrate the use of FM chirps in a coded excitation system, we consider a basic imaging scenario where the echogenic medium only contains a single point target. For such a scenario, the medium's response is simply equal to an impulse $[h(t)=\delta(t)]$, and correspondingly the compressed waveform defined in (2) is simply equal to the transmitted signal's autocorrelation function. Hence, if the FM chirp of (3) is fired into this single-target medium and if the filtering effect of the transducer is ignored, the resulting compressed waveform at the receiver output can be shown to be given by (see Sec. 6.2 in [7]):

$$e_o(t) = \sqrt{\frac{2k}{\pi}}\,\mathrm{rect}\left(t/2T\right)\frac{\sin\left[kt(T-|t|)/2\right]}{kt}\cos(\omega_o t)\cdot \qquad (4)$$

From the rect() term in the above expression, it can be seen that the compressed waveform actually extends over twice the initial chirp duration, i.e., from $-T$ to $+T$. Also, its envelope generally follows a pseudo-sinc shape as described by the $\sin[kt(T-|t|)/2]/kt$ term. Aside from the time-domain expression, it is also worth considering the compressed waveform's spectrum (which is simply the FM chirp's spectrum in this case). From Fourier analysis, this spectrum can be shown to be given by (see Sec. 6.3 in [7]):

$$E_o(\omega) = \sqrt{\frac{\pi}{4k}}e^{-j(\omega-\omega_o)^2/2k}\left[F^*(X_1)+F^*(X_2)\right], \qquad (5)$$

where $X_1 = [kT/2+(\omega-\omega_o)]/(k\pi)^{1/2}$, $X_2 = [kT/2-(\omega-\omega_o)]/(k\pi)^{1/2}$, and $F^*(X)$ is the complex conjugate of a Fresnel integral.

The above expressions can be illustrated through the example shown in Figure 3, where a 10 μs FM chirp with a center frequency of 5 MHz and a bandwidth of 2.5 MHz is assumed. Note that such a waveform has time-bandwidth product that is 25 times larger than a non-chirped pulse echo scheme. As can be seen from the figures, the compressed waveform contains *range sidelobes* (sometimes referred to as *self-noise*) with amplitudes comparable to the main lobe. As discussed by Kowatsch and Stocker [12], the sidelobes are a result of the rect() time window inherent in the transmitted chirp pulse and are directly related to the Fresnel ripples seen in the frequency spectrum. In the presence of multiple scattering targets, these sidelobes will lead to difficulties in detecting a weakly scattering target because its main lobe may be masked out by the range sidelobes of a strongly scattering target located nearby.

Pulse Shaping Considerations

To account for the sidelobe problem when using FM chirps, much effort has been devoted towards devising schemes for reducing the range sidelobe level to well below –50 dB. For instance, time-domain shaping of the transmit pulse can be used to smooth out the sharp edges associated with the chirp pulse's rectangular window. One useful way

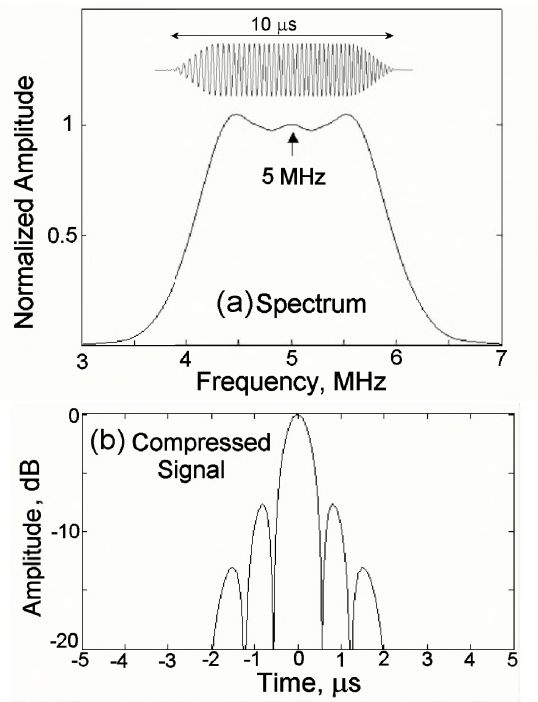

Figure 4. Effect of cosine (Tukey) amplitude tapering on the compressed envelope. Other signal parameters are the same as those in Figure 3. (a) Transmitted waveform with a cosine taper over the first and last 2.25 μs and its spectrum. (b) Envelope of the compressed signal.

of shaping a chirp pulse is to apply a cosine taper (i.e., a Tukey window) to the leading and trailing parts of the waveform. As can be seen in Figure 4, the tapered chirp

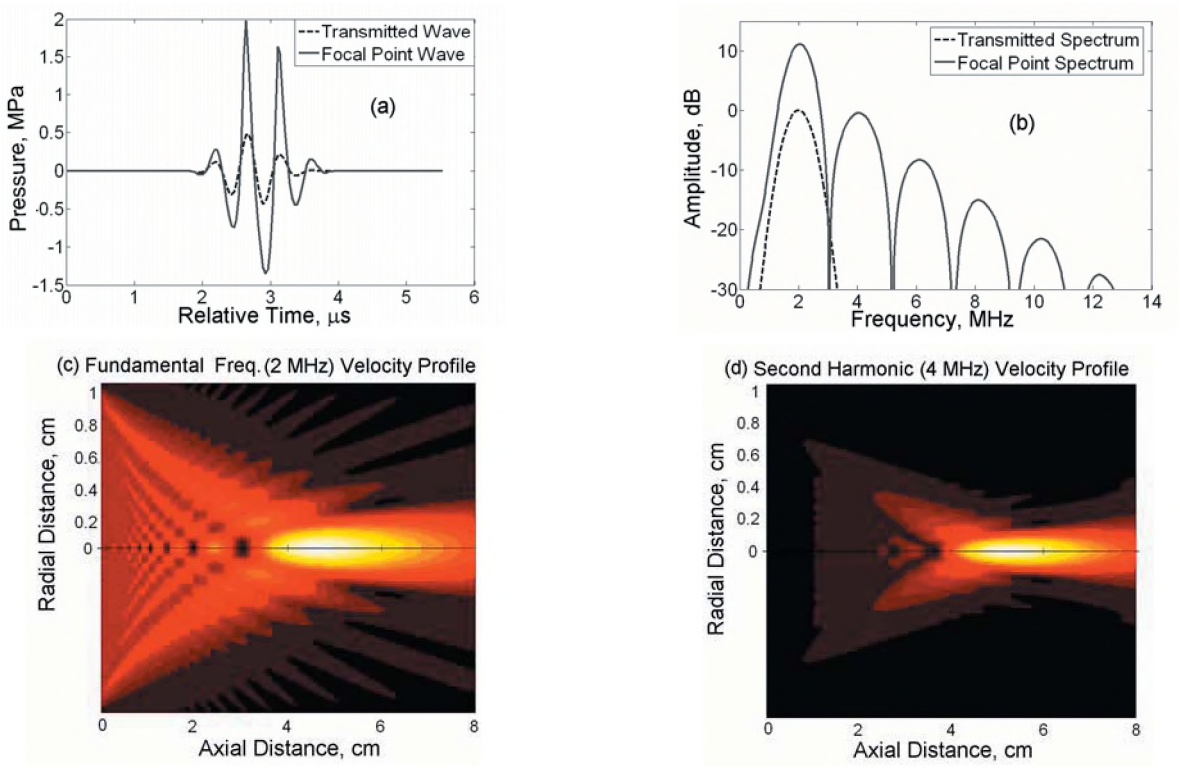

Figure 5. Simulated waveforms and profiles from transmission of a Gaussian pulse of p_o=500 kPa, f_c=2 MHz, and 60% -6 dB fractional bandwidth, from a 1 cm radius focused transducer (F= 6 cm) into a tissue-like medium (α_0 = 0.04 Np/cm/MHz, β = 4.75, c_o=1546 m/s). (a) Comparison of the transmitted waveform to the waveform at the focal point, demonstrating distortion due to nonlinearity. (b) Comparison of the spectrum of the transmitted waveform to the waveform at the focal point, demonstrating generation of new harmonic bands. (c) Normal velocity profile of the 2 MHz component of the waveform as it propagates into the medium, note the presence of lateral sidelobes. (d) Normal velocity profile of the 4 MHz component of the waveform as it propagates into the medium. Note that the lateral sidelobes do not extend very far in the lateral direction.

pulse has a much smoother spectrum, which in turn leads to significant reduction in the range sidelobes. It is worth noting that the bandpass nature of the transducer's transfer function may also be exploited to achieve similar spectral smoothing effects. In particular, if the transducer bandwidth is narrower than that of a non-tapered chirp pulse, then it is equivalent to applying a frequency-domain window to the chirp pulse's spectrum. This effect has been examined in a few studies [10][13], which showed that the transfer function of the transducer can cause a substantial reduction in the range sidelobes. Despite their advantages, however, it is important to note out that pulse shaping and spectral smoothing would concomitantly lead to a SNR reduction of a few dB and a slight loss of axial resolution due to broadening of the main lobe.

2.2. Principles of Harmonic Imaging

Background Considerations

As reviewed by Cobbold (see Sec. 8.6 in [1]), there are generally two approaches to harmonic imaging: one based on the use of a contrast agent like microbubble, and the other based on the generation of nonlinear waves in tissue. The basic rationale behind the first approach is that the nonlinear scattering properties of ultrasound contrast agents can generate signal harmonics in regions where the agents are located and in turn enhance the local signal contrast. As such, the imaging process associated with the use of contrast agents is often called *contrast media harmonic imaging*. On the other hand, the main principle behind the second approach is that tissue can too become a nonlinear scattering medium if the incident pressure fields are sufficiently high and thereby give rise to harmonic echoes. This second form of imaging, generally called *tissue harmonic imaging*, is the subject of discussion in this paper.

General Principles

To illustrate the field excitation principles behind tissue harmonic imaging, Figure 5 shows the fundamental and second-harmonic field profiles produced by transmitting a wideband Gaussian pulse from a focused disc transducer into a tissue-like medium. As seen in part (a) of this figure, there is substantial distortion (in the form of spiky wave peaks) in the incident waveform at the focal point. It turns out that these distortions are due to the signal harmonics being generated in the focal region (see (d) of the figure). On a different note, it is worth pointing out that the second-harmonic field profile is significantly more focused than its fundamental counterpart. Such focusing improvement is well-recognized as the theoretical advantage of producing images from harmonic echoes. However, a major limitation

of using harmonic echoes for imaging is that their signal strength is at least 10 dB weaker than the fundamental signals (see part (b) of figure). To address this limitation, it is beneficial to develop a technique that can boost the SNR in harmonic imaging (especially when examining for deeper structures). As suggested in some studies [10][14][15][16], the use of coded excitation may be a potential solution for such SNR improvement needs. This technique is the focus of our simulation study, and it will simply be referred to as *coded harmonic imaging* from hereon.

2.3. Design Considerations in Coded Harmonic Imaging

Pulse Selection Issues

As pointed out by Misaridis and Jensen [10], FM chirps maintain their coded phase relationship in the harmonic domain – i.e. the higher harmonics are also chirps and can be compressed using appropriately matched filters. Hence, when using FM chirps for coded harmonic imaging, compression filters like the ones for chirp-based coded excitation can be used to obtain the compressed harmonic waveform. In view of this advantage, FM chirps appear to be logical candidates for use in coded harmonic imaging. On the other hand, the use of binary codes in harmonic imaging appears to be more challenging because the phase coding relationship for fundamental signals does not carry over for harmonic echoes. This type of code is not considered in this paper. Nevertheless, it is worth noting that there are some special forms of binary codes that may be potentially useful for coded harmonic imaging [14].

Bandwidth Issues

The transmitted signal bandwidth is an important parameter in ultrasound B-mode imaging since bandwidth directly affects the axial resolution. The impact of this signal parameter in conventional harmonic imaging is also well-known: if the transmitted signal is wideband, then adjacent harmonics in the received signal may overlap in frequency. The potential occurrence of this spectral leakage creates a problem since it makes difficult for a conventional highpass filter to distinguish the spectral harmonics from the fundamental. In particular, with spectral leakage, the highpass filter can suppress the leaking fundamental signal only if some of the desired harmonic echoes are removed concomitantly, or else some of the fundamental signal will still remain. A well-known solution to such problem is to use a two-pulse transmission scheme known as "pulse inversion" (which transmits a pulse and its negated form in sequence) and then sum the two complementary pulse echoes to cancel out the fundamental signal while retaining the harmonic echoes. Nevertheless, because two firings are needed, this approach inherently leads to a reduction in frame rate. As well, as examined by Shen and Li [17], its efficacy is susceptible to spectral leakage problems when tissue motion is present.

In coded harmonic imaging, the problem of spectral leakages is even more significant. The reason is because the compression filtering procedure used to recover the axial resolution is often matched to the transmit pulse shape, and thus the harmonic compression performance will be reduced if there is a significant amount of spectral leakage present in the received signal. In turn, the compressed harmonic signal (usually done for the second harmonic) may suffer in the form of loss in axial resolution, contrast resolution, or SNR. The impact of spectral leakage on the compressed harmonic signal will be examined in detail in our simulations.

3. SIMULATION METHOD

3.1. General Overview

For all the simulations reported in this study, the pressure field was generated by a single focused circular transducer with a radius of 1 cm and a focal length of 6 cm. The medium was characterized by the following parameters of a tissue mimicking material similar to liver tissue: acoustic attenuation $\alpha = \alpha_o f$ (with $\alpha_o = 0.04$Np/cm/MHz), nonlinearity parameter $\beta = 4.7$, sound propagation speed $c_o = 1546$m/s, and density $\rho = 1000$kg/m^3. Ultrasound propagation in this medium was simulated by using a second-order operator splitting approach that uses a fractional step-marching scheme, whereby the effects of diffraction, attenuation, and nonlinearity can be computed independently over incremental steps [18]. To calculate the effects of diffraction, we took advantage of the cylindrical symmetry of the problem by making use of the Hankel transform [19] rather than the less efficient angular spectrum approach. The return echo from a single point scatterer is assumed to propagate linearly to the transducer, where the integrated received signal is processed by the receiver filter, which includes compression filtering for coded waveforms, and finally the display processing. Our simulation results assumed a homogenous medium and a sufficiently wideband transducer so as not to affect either the transmitted or received signals.

3.2. Transmitted Signal

In order to determine the effect of bandwidth on the desired second harmonic signal, linear FM chirps with -6dB fractional bandwidths ranging from 10-80% were simulated and the waveforms at the focal plane were recorded. In these simulations, a constant chirp duration of 20 μs and a center frequency of 2 MHz were used. Also, for comparison, the results from a conventional (non-coded) Gaussian pulse with the same fractional bandwidth and peak pressure were also simulated.

As pointed out earlier, the pulse shaping window has a significant influence on the sidelobe level and affects the mainlobe width. Hence, as part of the study, we investigated the effects of the following three pulse shaping windows:

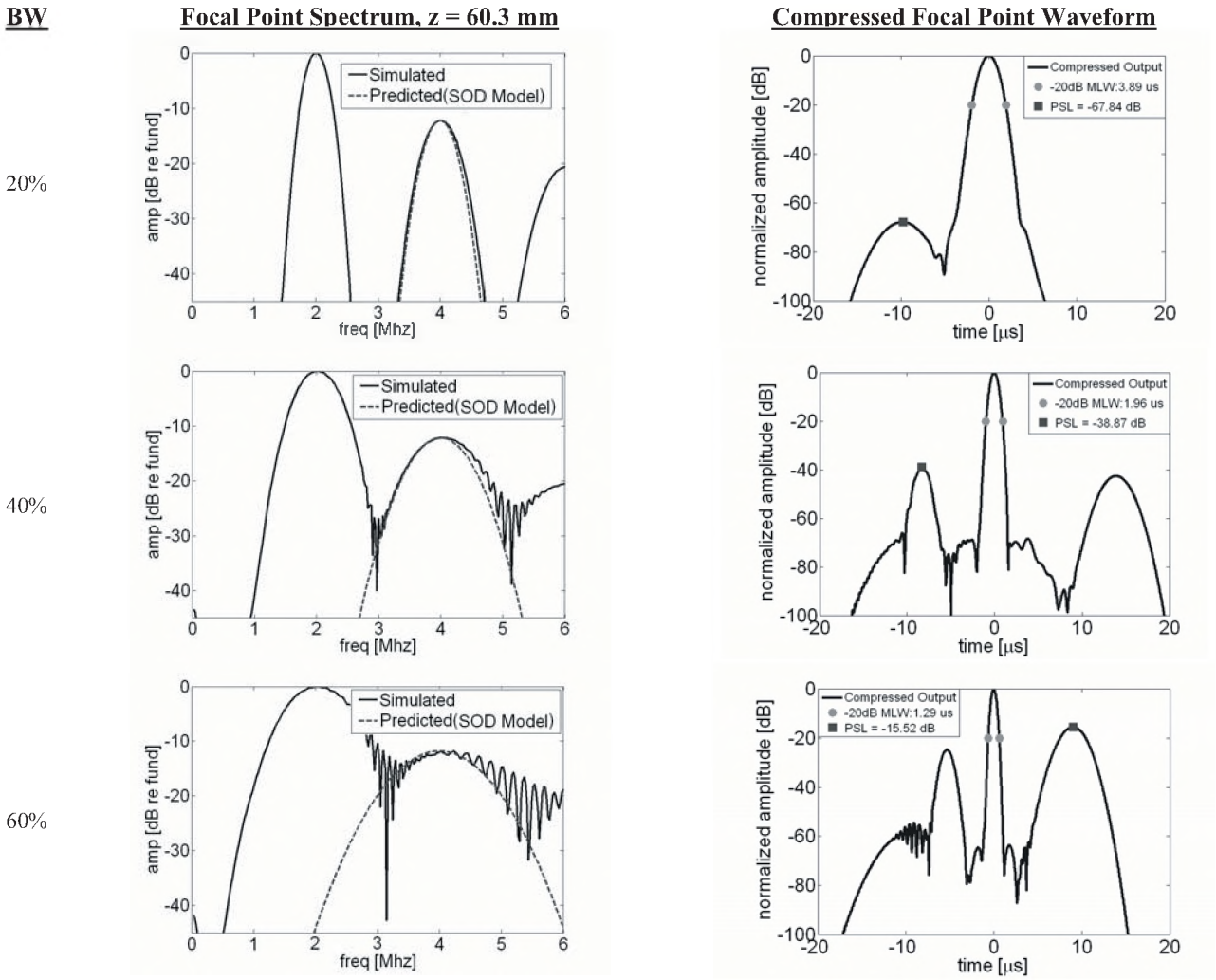

Figure 6. The left column shows the spectrum of the waveform at the focal point for transmitted chirps with fractional bandwidths of 20%, 40% and 60% and their comparison to the second harmonic as predicted by the second order distortion (SOD) model. The right column shows the corresponding compressed waveforms obtained from the SOD compression filter. The -20 dB mainlobe width and the peak side lobe levels (PSL) are marked. Note the increasing sidelobes associated with spectral leakage as the bandwidth is increased.

1. Gaussian (with $\chi = 3$, where χ is the reciprocal of the standard deviation);
2. Tapered Cosine (with R=0.65, corresponding to Matlab's *tukeywin.c*);
3. Rectangular (i.e. no tapering).

3.3. Receiver Processing

In the absence of any coding, the receiver typically includes filtering to remove components outside the second harmonic band, followed by envelope detection and display on a log scale. Another way of distinguishing the second harmonic band in non-coded imaging is to use the pulse-inversion firing scheme that involves two firings along each path (as we noted earlier). On the other hand, for FM chirps, the receiver processing must include compression filtering in order to recover the axial resolution of the received echoes. In a single firing system, the coded received signal is often passed directly to the compression filter, although bandpass filters can be used to remove some unwanted components before compression. Alternatively, if pulse inversion is used during coded harmonic data acquisition, then the field generated by both the original pulse and its negated form must first be calculated, the corresponding echoes summed together, and then passed directly to the compression filter.

3.4. Compression Filter Model

In the design of chirp-coded harmonic systems, Kim et al. [16] made use of a square law model (also known as a second order distortion model) of the propagation process to design a compression filter. Ignoring higher harmonics, this model assumes that the received signal from nonlinear propagation can be approximated as $r(t) = a_1 s(t) + a_2 s^2(t)$, where a_1 and a_2 are constants that characterize the nonlinear propagation process and $s(t)$ is the transmitted signal. This seems to be a suitable signal model since the second

harmonic is the strongest among the nonlinear harmonics; hence, it was used to predict the second harmonic portion of the received signal on which the compression filter is based. In fact, the impulse response of our compression filter for the second harmonic was defined as the time-reversed conjugate of $s^2(t)$. In the discussion given below we refer to such a compression filter as an SOD compression filter.

3.5. Performance Evaluation

For the purpose of analyzing the behavior of a coded waveform under nonlinear propagation conditions, the waveforms obtained using the aforementioned step-wise nonlinear simulator are analyzed mainly at two locations. The first is the radiation pattern at the focal plane where we can analyze the spectrum of the on-axis waveform and even apply the receiver processing directly to the waveform. The second location is at the transducer where the compressed harmonic signal can be analyzed after compression filtering.

Whether we apply the receiver processing to the focal plane signal or the received signal from a scatterer, the system performance can be quantitatively assessed by using several criteria corresponding to axial resolution, contrast resolution, and gain in SNR [9][10]. These criteria are generally used to analyze the compressed harmonic signal that is ready for display – i.e., the waveform has been processed, envelope detected and changed to a dB scale reflecting the dynamic range of the system. In our study, the -20 dB mainlobe width (MLW) of the processed time domain signal is used to assess axial resolution. The Peak Sidelobe Level (PSL) and Integrated Sidelobe Level (ISL) are also used to assess contrast resolution. In addition, the gain in SNR is assessed by finding the ratio between the peak of a compressed harmonic signal and that of a processed non-coded signal obtained from a Gaussian pulse with equal peak pressure and bandwidth.

4. RESULTS

4.1. Spectral Overlap and Effects on Compression

The left column in Figure 6 shows the spectrum of the received signal at the focal point for three transmitted Gaussian-windowed FM chirps of increasing fractional bandwidths. These focal point spectra indicate that as the bandwidth is increased, the fundamental and third harmonic bands overlap with the second harmonic band, resulting in periodic fluctuations in the spectrum as well as deviations from the assumed second order distortion model (dashed lines). Note that the nature of the overlap and its effects on spectrum shape are different than those seen with non-coded pulses. In particular, the spectral overlap is not in the form of random dephasing; instead, it is in the form of periodic fluctuations that result from the nonlinear phase of the transmitted FM chirp and its harmonics. The effects of this spectral overlap on the compressed harmonic signal can

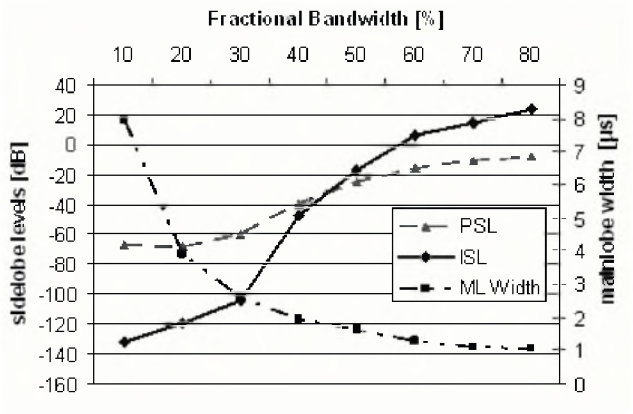

Figure 7. Effect of bandwidth on coded harmonic compression for a Gaussian transmitted signal. As fractional bandwidth of the transmitted signal is increased, the peak sidelobe level (PSL) and integrated sidelobe levels (ISL) of the compressed waveform are increased, while the mainlobe width, which is an indicator of axial resolution, is decreased.

be seen in the right column of Figure 6. As can be seen, significant sidelobe levels are produced as bandwidth is increased, even though there is improvement in the mainlobe width (and in turn the axial resolution). These sidelobes reach levels of greater than –40 dB for 40% and –20 dB for the 60% transmitted bandwidth.

For the Gaussian FM chirp, the performance criteria based on the compressed harmonic waveforms have been tabulated and are shown in Figure 7. Note that, for chirps with fractional bandwidths less than 40%, the mainlobe width appears to increase significantly and hence the axial resolution may be too low for imaging purpose. However, when the fractional bandwidth is greater than 40%, there is a substantial increase in the peak sidelobe levels (PSL) and their relative energy to the mainlobe (ISL). This pattern of increasing sidelobes at greater bandwidths also applies to the non-Gaussian chirp signals; in fact, depending on the tapering, some waveforms exhibit large sidelobes even at lower bandwidths. To suppress these high sidelobe levels, it is necessary to carry out some form of pre-processing (e.g., filtering) or use a more advanced compression filter.

4.2. Use of Pulse Inversion Prior to Compression

To confirm the role of spectral overlap in creating the high sidelobe levels, the above analysis was repeated on received signals whose fundamental and odd harmonics were suppressed with the pulse inversion method. The corresponding focal point spectra before compression are shown in Figure 8. As can be seen, the spectrum of the second harmonic in this case looks much closer to the second order distortion model since the fundamental and third harmonic bands are both suppressed via pulse inversion. Interestingly, there are still the some differences in the two spectra near 6 MHz, and these differences are likely due to the spectral overlap between the second and

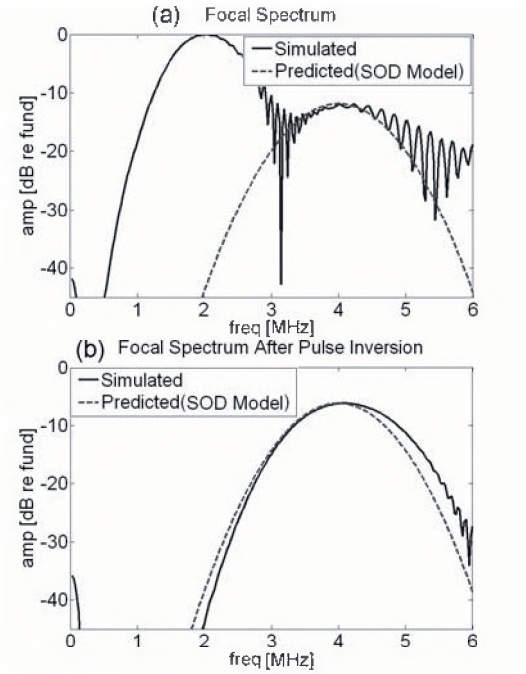

Figure 8. Effect of pulse inversion on the spectrum of the focal point waveform (bandwidth=60%). (a) Spectrum of the waveform at the focal point. (b) Spectrum obtained from addition of the focal waveform from transmission of a positive LFM and that from transmission of the inverted LFM waveform. The SOD model also plotted for reference.

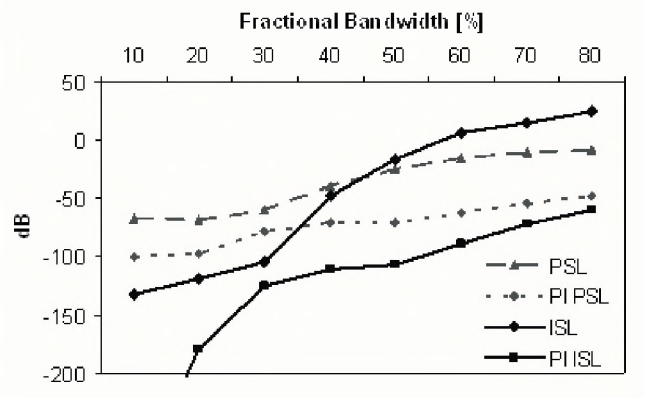

Figure 9. Effect of bandwidth on coded harmonic compression when using pulse inversion (PI). PSL–peak sidelobe level; ISL–integrated sidelobe level.

fourth harmonics. As will be shown shortly though, they do not appear to have much impact on the compression results.

As seen in Figure 9, the effect of pulse inversion (i.e., spectral overlap reduction) on the compression performance is evident by noting the reduced sidelobe levels in the compressed harmonic waveform. In particular, for fractional bandwidths greater than 40%, PSL levels have decreased by 30-40 dB while the ISL levels have reduced by as much as 80 dB. Nevertheless, it is important to bear in mind that such performance improvements come at a cost of reduced frame rate (two firings are required) and potential spectral leakage due to tissue motion [17].

4.3. Use of Conventional Filtering Prior to Compression

Perhaps a straightforward way of suppressing the sidelobes in the compressed harmonic signal is to use bandpass filtering before compression to retain only the second harmonic components. However, in doing so, we are faced with the same problem which plagues the single-firing harmonic imaging approach – that is, the desired harmonic band and the leaking bands are not completely separable in the frequency domain. In fact, this problem is more severe in the case of coded harmonic imaging due to compression filtering.

To demonstrate the pitfalls of conventional bandpass filtering, the focal-point received signal corresponding to a 60%-bandwidth chirp excitation was filtered using several ideal bandpass filters prior to compression. Figure 10a shows two examples of such bandpass filters on top of the received spectrum. The 3.25-5.25 MHz filter has reduced one of the compression sidelobes significantly – as seen in Figure 10b – yet the sidelobe levels are still within the 45 dB dynamic range. If we narrow the bandpass filter to 3.5-5.0 MHz, the secondary sidelobes are reduced further, but the mainlobe starts to widen along with its own increasing sidelobes. This inherent tradeoff between sidelobe level and mainlobe width is indeed the primary limitation of using conventional bandpass filtering to reduce the sidelobes in the compressed harmonic signal.

A potential alternative approach is to make use of second order Volterra filters. This method was examined and applied by Phukpattaranont and Ebbini [20] for separating the quadratic component generated by contrast agents for use in imaging.

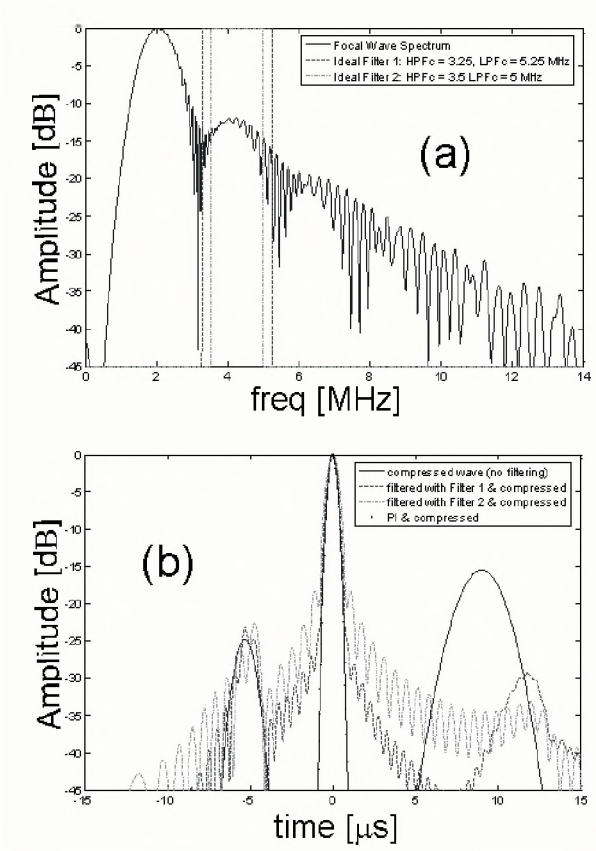

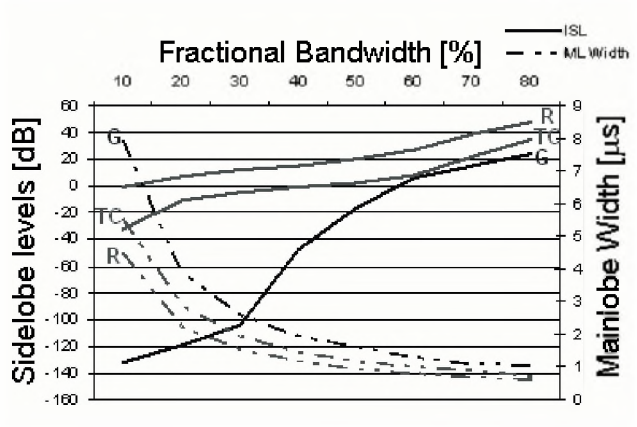

Figure 11. Effect of waveform tapering and bandwidth on coded harmonic compression. The graph compares the integrated sidelobe levels (ISL) and mainlobe width after compression for three types of pulse shaping: Rectangular (R), Tapered Cosine (TC), and Gaussian tapering (G).

4.4. Pulse Shaping and Effects on Compression Results

In the previous few sections, the presented results were obtained using Gaussian-windowed FM chirps. To generalize these findings, the analysis was repeated using other types of pulse shaping windows. The corresponding results are summarized in Figure 11, which shows a comparison on the mainlobe width and sidelobe levels of the compressed harmonic waveform obtained from transmission of three different types of tapered FM chirps. As can be seen, if a rectangular window (i.e., no tapering) is used on the transmitted signal, then high-energy sidelobes are present in the compressed harmonic signal even at small bandwidths. As transmitted signal tapering increases (from none to tapered cosine to Gaussian), these sidelobes become less prominent. On the other hand, an opposite trend is observed for the mainlobe width: no tapering actually gives narrower mainlobe widths and hence yields better axial resolution. After all, the choice of tapering is influenced by tradeoff issues between axial resolution (sidelobe levels) and temporal resolution (mainlobe width). Note that, in a practical situation, the finite operating bandwidth of the transducer would further complicate the choice.

Even though we have chosen to apply the tapering directly to the transmitted waveform, it is not the only way to reduce sidelobe levels. Alternatively, the tapering can be applied to the compression filter's impulse response so that as much energy as possible can be physically transmitted. As studied carefully by Misaridis and Jensen [9][10], such a filter can be considered as a mismatched filter.

4.5. Gain in SNR Due to Coding and Compression

As discussed previously, the purpose of coding is to increase the signal to noise ratio without changing the peak transmitted power and thereby improving the penetration range. To demonstrate this theoretical advantage, Figure 12 shows the gain in SNR by comparing the result from transmission of a non-coded pulse to that of a 20 μs coded FM chirp of equal fractional bandwidth (60%). Note that, for the non-coded pulse, pulse inversion was used to extract the second harmonic while suppressing the odd harmonics. As for the FM chirp, a compression filter based on the second order distortion model was applied to the received waveforms to obtain the compressed harmonic signal, and the procedure was repeated for received signal obtained with pulse inversion.

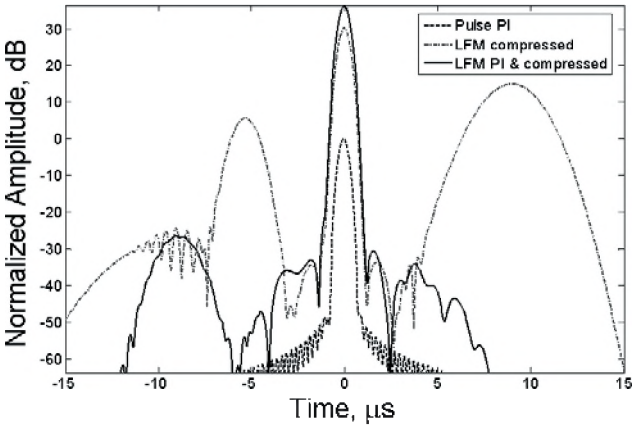

Figure 12. Gain in SNR as a result of coding. Even though axial sidelobes are present, compression has recovered the axial resolution and increased the SNR. Note the peak of the mainlobe of the compressed LFM is more than 30 dB greater than the non-coded pulse peak.

By comparing the mainlobe peaks from Figure 12, it can be seen that the FM chirp's compressed harmonic signal has an SNR gain of approximately 30 dB as compared to the non-coded pulse's received signal. Additionally, the figure confirms the benefits of suppressing the spectral overlap in the received spectra prior to compression filtering, even though the suppression was achieved using pulse inversion. Another observation evident in this figure is that the compressed harmonic signal of the FM chirp actually has a mainlobe width approximately the same as that of the non-coded pulse. This result demonstrates the ability of chirp-based coded excitation methods in obtaining compressed harmonic waveforms with high axial resolutions.

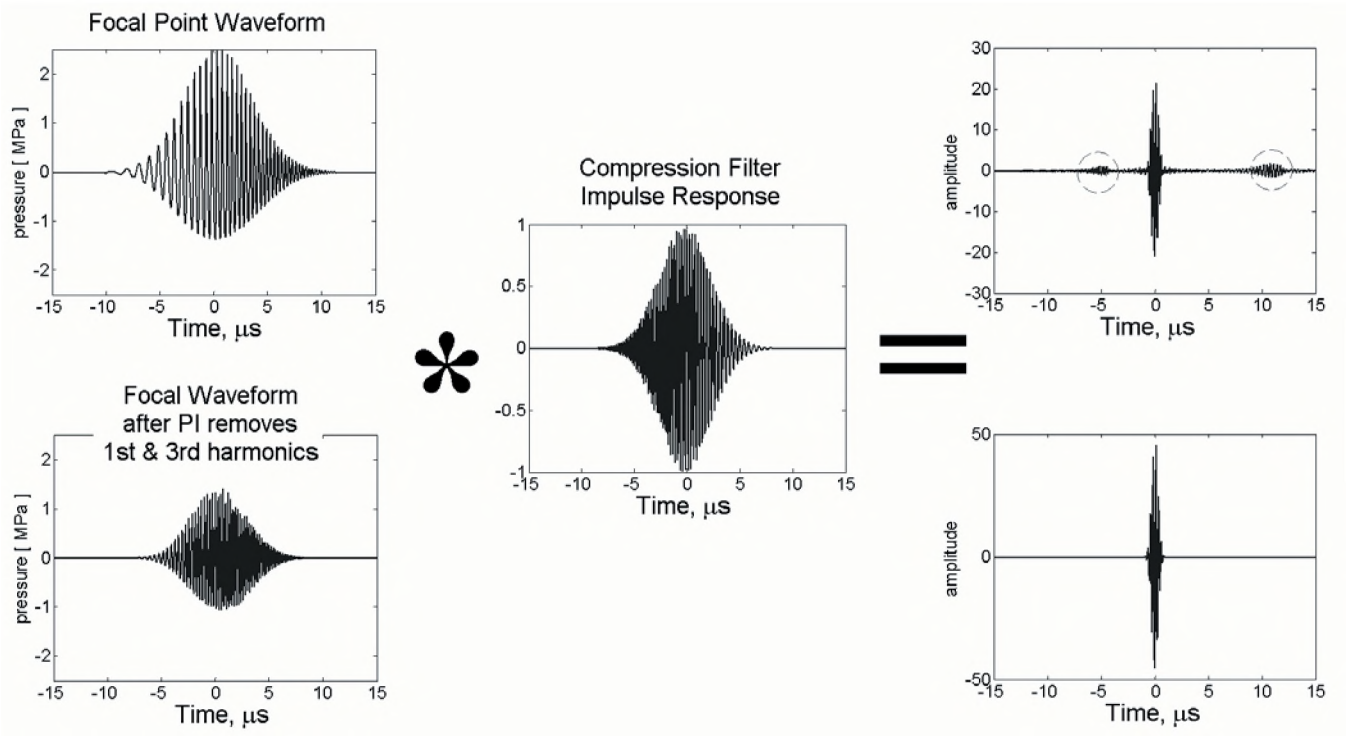

Figure 13. Example of a focal point waveform (a harmonic chirp signal) and the resulting waveform after convolution with the impulse response of the compression filter. The smaller circled waveforms to the right and left of the compressed waveform are due to the leaking fundamental and third harmonic portions of the chirp. Note that they disappear (lower part) after the fundamental and third harmonic portions of the focal waveform have been removed using the pulse inversion technique.

4.6. Compression Filtering Issues

The simulation results presented throughout this section have shown that, as the bandwidth of the transmitted FM chirp is increased to improve resolution, the spectral leakage between harmonics would give rise to high sidelobe levels in the compressed harmonic signal. In this section, we shall further discuss the origin and nature of these sidelobes and examine the potential of removing them without the need for pulse inversion by taking advantage of a chirp's time-frequency domain properties.

We begin by recalling that, as the transmitted FM chirp propagates into the medium, the waveform gradually gets distorted as the focus is approached, thereby leading to the generation of new harmonic frequencies. Nevertheless, the harmonics would still retain their coded properties (i.e., the nonlinear phase relationship which defines a chirp). Hence, the return echo at a specific point may be approximated by a higher-order signal model $r(t) = a_1 s(t) + a_2 s^2(t) + a_3 s^3(t) + \ldots$. The upper-left plot of Figure 13 shows a single-point pulse echo simulated using a third-order signal approximation and a 20 μs Gaussian FM chirp with 60% bandwidth. To process this coded received signal, it should be noted that a compression filter matched to $s^2(t)$ is the most reasonable choice because the exact parameters of the medium (i.e. nonlinearity, attenuation, etc.) are unknown in practical situations. In Figure 13, such a compression filter is used to compress the focal waveform, and the results are shown in the upper-right plot. Note that, in addition to the desired compressed second harmonic (i.e. the mainlobe), two smaller waveforms are present at its left and right (i.e. the sidelobes). On a dB scale, the magnitudes of these smaller waveforms are actually comparable to the main compressed waveform. In contrast, when pulse inversion is used to remove the fundamental and the third harmonic in the simulated waveform (bottom-left plot of Figure 13), the undesired sidelobes would disappear from the compressed harmonic signal (bottom-right plot). This result confirms that the sidelobes are caused by the leaking fundamental and third harmonic bands.

To remove the leaking bands in a single-firing system, we may be able to take advantage of properties of chirps in the time-frequency space. For instance, Figure 14 shows a typical received harmonic chirp and its corresponding waveform after compression in time, frequency, and time-frequency domains. As can be seen, the harmonics of the received chirp (left column of Figure 14) are completely overlapping in the time domain; there is also significant overlap between the harmonic bands in the frequency domain. However, in the time-frequency space of the spectrogram, the different harmonic chirps of the signal are clearly separable and have distinct time-frequency slopes. Although this example is merely based on the assumption that scatterers are well separated in space, it nevertheless illustrated the time-frequency variation characteristics of chirp echoes. In practice, it would be worthwhile to examine in more detail the time-frequency properties of

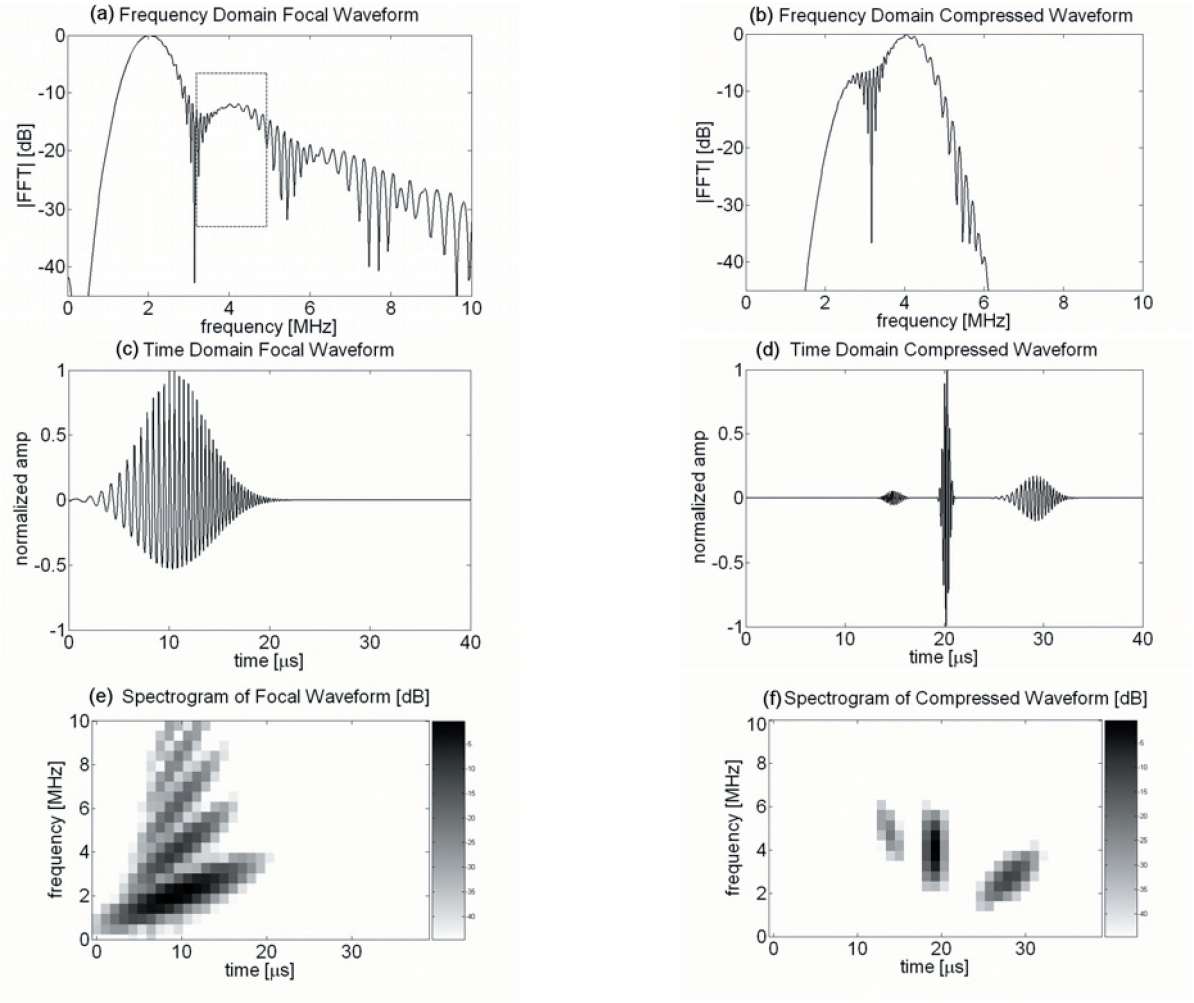

Figure 14. Typical harmonic chirp before and after compression, shown in the time, frequency, and time-frequency domains. Left column shows a typical harmonic chirp signal at the focus of the transducer; in the spectrogram, the different harmonic components of the chirp are clearly distinguishable. Right column shows the compressed waveform using a second order compression filter. While the second harmonic chirp is compressed, the leaking fundamental and third harmonic chirps result in presence of uncompressed chirps to its left and right.

chirp echoes returned from multiple scatterers that collectively give rise to signal speckling features.

More insights on the time-frequency nature of coded harmonic echoes can actually be drawn by examining the properties of the compression filter which is based on a second order distortion model. Such a filter tends to cancel out the coded phases in the second harmonic component of the received signal, thereby compressing this harmonic in the time domain as seen in the right hand column of Figure 14 (here again, the assumption of well-separated scatterers should be noted). In the time-frequency domain, the compressed second harmonic would correspond to a component with infinite time-frequency slope (i.e. parallel to the frequency axis). On the other hand, the spectral leakage components originating from the fundamental and the third harmonic would emerge in the spectrogram as chirps to the left and right of the desired second harmonic. In fact, as evident in Figure 14, leakages from the fundamental would give rise to a longer chirp to the right of the compressed second harmonic, while leakages from the third harmonic would give rise to the smaller and shorter chirp to the left. Interestingly, since these leakage chirps are separated and have different chirp rates, it may be possible to suppress them via the use of time-frequency analysis techniques.

5. SUMMARY AND CONCLUSIONS

Tissue harmonic imaging takes advantage of the nonlinear distortion of ultrasound waves in tissue and the associated generation of higher harmonics to obtain images with potentially improved clarity. However, since the generated higher harmonics are generally weaker than the fundamental signal, it may be useful to use techniques like coded excitation to increase SNR and improve signal penetration. Between the two useful types of codes in ultrasound, namely binary codes and FM chirps, FM signals are more readily applicable to tissue harmonic imaging as the harmonics still retain their coded phase relationship.

In this paper, the potential of linear FM chirps as codes in tissue harmonic imaging was examined. Specifically, we have studied the effects of bandwidth and pulse shaping on the compressed harmonic signals. The study was carried out through simulation means by using a step-wise nonlinear simulator that can compute the pressure field corresponding to the transmission of FM chirps (f_o=2 MHz, p_o=500 kPa) from a 1cm-radius focused disc transducer into a homogenous, tissue-mimicking material. The focal point signals were compressed using a filter that is matched to the square of the transmitted signal. The compressed harmonic signals were then analyzed based on several criteria, including mainlobe width, sidelobe levels, and SNR gain relative to a non-coded pulse. Our simulations indicate that even though coding potentially increases the SNR, the compression process can result in creation of high-magnitude sidelobes. Since these sidelobes increase with FM chirping bandwidth and can theoretically be eliminated using pulse inversion, it was concluded that they are attributed to spectral overlap of the adjacent harmonics. To reduce the sidelobe magnitudes, the leaking fundamental and third harmonic bands must be removed prior to computing the compressed harmonic signal. However, since these leaking frequency bands are not separable in the frequency domain, they cannot be removed effectively using conventional bandpass filtering. Alternatively, it may be possible to take advantage of the properties of FM chirps in the joint time-frequency domain where the various harmonics of a chirp are separable.

ACKNOWLEDGEMENTS

We are grateful for the help from Aziza Manceur on the French translations of our abstract. We also wish to thank Derek Wright for assisting us with some of the figures.

This work was supported in part by grants from the Canadian Institutes of Health Research and the Natural Sciences and Engineering Research Council of Canada.

REFERENCES

[1] RSC Cobbold, *Foundations of Biomedical Ultrasound*. New York City, USA: Oxford University Press, 2006.

[2] S Ohtsuki and M Okujima, "Ultrasonic Doppler velocity meter by M-sequence modultaion method" (in Japanese), *J. Acoust. Soc. Japan*, vol. 29, pp. 347-355, 1973. [See also: the conference presentation listings of 1970 in [3].]

[3] Y Takeuchi, "An investigation of a spread energy method for medical ultrasound systems. Part one: theory and investigation", *Ultrasonics*, vol. 17, pp. 175-182, 1979.

[4] Y Takeuchi, "An investigation of a spread energy method for medical ultrasound systems. Part two: proposed system and possible problems", *Ultrasonics*, vol. 17, pp. 219-224, 1979.

[5] M O'Donnell, "Coded excitation system for improving the penetration of real-time phased-array imaging systems", *IEEE Trans. Ultrason. Ferroelect. Freq. Contr.*, vol. 39, pp. 341-351, 1992.

[6] PM Woodward, *Probability and Information Theory, with Applications to Radar*. London, UK: Pergamon Press, 1953.

[7] CE Cook and M Bernfeld, *Radar Signals: An Introduction to Theory and Application*. New York City, USA: Academic Press, 1967 (republished: Artech House Inc., Boston, 1993).

[8] MA Benkhelifa, M Gindre, JY Le Huerou, and W Urbach, "Echography using correlation techniques: choice of coding signal", *IEEE Trans. Ultrason. Ferroelect. Freq. Contr.*, vol. 41, pp. 579-587, 1994.

[9] T Misaridis and JA Jensen, "Use of modulated excitation signals in medical ultrasound. Part I: Basic concepts and expected benefits", *IEEE Trans. Ultrason. Ferroelect. Freq. Contr.*, vol. 52, pp. 177-191, 2005.

[10] T Misaridis and JA Jensen, "Use of modulated excitation signals in medical ultrasound. Part II: Design and performance for medical imaging applications", *IEEE Trans. Ultrason. Ferroelect. Freq. Contr.*, vol. 52, pp. 192-207, 2005.

[11] DH Simpson, CT Chin, and PN Burns, "Pulse inversion Doppler: a new method for detecting nonlinear echoes from microbubble contrast agents", *IEEE Trans. Ultrason. Ferroelect. Freq. Contr.*, vol. 46, pp. 372-382, 1999.

[12] M Kowatsch and HR Stocker, "Effect of Fresnel ripples on sidelobe suppression in low time-bandwidth product linear FM pulse compression", *IEE Proc. Part-F*, vol. 129, pp. 41-44, 1982.

[13] M Pollakowski, H Ermert, L von Bernus, and T Schmeidl, "The optimum bandwidth of chirp signals in ultrasonic applications", *Ultrasonics*, vol. 31, pp. 417-420, 1993.

[14] RY Chiao and X Hao, "Coded excitation for diagnostic ultrasound: a system developer's perspective", *IEEE Trans. Ultrason. Ferroelect. Freq. Contr.*,vol.52, pp.160-170, 2005.

[15] PC Li, "Pulse compression for finite amplitude distortion based harmonic imaging using coded waveforms", *Ultrason. Imaging*, vol. 21, pp. 1-16, 1999.

[16] DY Kim, JC Lee, SJ Kwon, and TK Song, "Ultrasound second harmonic imaging with a weighted chirp signal", *Proc. IEEE Ultrason. Symp.*, pp. 1477-1480, 2001.

[17] CC Shen and PC Li, "Motion artifacts of pulse inversion-based tissue harmonic imaging", *IEEE Trans. Ultrason. Ferroelect. Freq. Contr.*, vol. 49, pp. 1203-1211, 2002.

[18] RJ Zemp, J Tavakkoli, and RSC Cobbold, "Modeling of nonlinear ultrasound propagation in tissue from array transducers", *J. Acoust. Soc. Am.*, vol. 113, pp. 139-152, 2003.

[19] PT Christopher and KJ Parker, "New approaches to nonlinear diffractive field propagation", *J. Acoust. Soc. Am.*, vol. 90, pp. 488-499, 1991.

[20] P Phukpattaranont and ES Ebbini, "Post-beamforming second-order Volterra filter for pulse-echo ultrasonic imaging", *IEEE Trans. Ultrason. Ferroelect. Freq. Contr.*, vol. 50, pp. 987-1001, 2003.

PARAMETRIC ANALYSIS OF ULTRASOUND BACKSCATTER SIGNALS FOR MONITORING CANCER CELL STRUCTURAL CHANGES DURING CANCER TREATMENT

Harshitha Nallapareddy[1], Sridhar Krishnan[1] and Michael Kolios[1,2]
[1]Dept. of Elec. & Comp. Engg., Ryerson University, Toronto, ON, Canada.
[2]Dept. of Physics, Ryerson University, Toronto, ON, Canada.
(hnallapa)(krishnan)@ee.ryerson.ca, mkolios@ryerson.ca

ABSTRACT

High frequency ultrasound backscattered signals (20 - 60 MHz) from normal and apoptotic cell pellets differ in their backscatter intensity, and analyzing these signals could assist in the non-invasive monitoring of cancer therapy. In this work, the reflection coefficients of the lattice prediction error filter are used as feature set for parametric analysis and signal classification. The ultrasound (US) backscattered signal databases consisted of combinations of treated (apoptotic) and untreated (normal) cells mixed in different proportions. A 40 MHz commercial ultrasound imaging system was used. A classification accuracy of 97-100% for normal and apoptotic signals were obtained with a model order 15. The positive results ascertain that the reflection coefficient is a potential tool for analyzing biomedical signals such as US backscattered signals.

SOMMAIRE

Les ultrasons à haute fréquence backscattereddes signaux (20 - 60 mégahertz) de normal et les granules apoptotic de cellules diffèrent dans leur intensité de rétrodiffusion, et l'analyse de ces signaux pourrait aider à la surveillance non envahissante de la thérapie de cancer. Dans ce travail, les coefficients de réflexion du filtre d'erreurs de prévision de trellis sont employés comme le dispositif a placé pour la classification paramétrique d'analyse et de signal. Les ultrasons (US) backscattered des combinaisons composées par bases de données de signal des cellules (normales) traitées (apoptotic) et non traitées mélangées dans différentes proportions. Un système commercial de formation image d'ultrasons de 40 mégahertz a été employé. Une exactitude de classification de 97-100% pour les signaux normaux et apoptotic ont été obtenues avec un ordre modèle 15. Les résultats positifs établissent que le coefficient de réflexion est un outil potentiel pour analyser les signaux biomédicaux tels que les ultrasons backscattered des signaux.

1 INTRODUCTION

During the cell division if the DNA is not replicated properly, the cell stops the division cycle and kills itself. This self-induced destruction or programmed cell death is called as apoptosis. However, at times cells lose ability to kill themselves and their uncontrolled cell division forms a tumor potentially. Thus any dysfunction or deregulation in apoptosis process leads to cancer. Cancer is a term for diseases in which abnormal cells divide without any control and have the ability to invade nearby tissues and can spread through the blood stream and lymphatic system to other parts of the body. Here arises a need to suppress the fast and uncontrolled cell division: one way is to forcefully induce apoptosis.

To this end, many cancer treatments are developed including radiation therapy, chemotherapy, and immunotherapy to kill the cells by apoptosis or necrosis. At this point, it is desirable to have a technique that can detect apoptotic regions in an organ or tissue which is undergoing cancer treatment (e.g., chemotherapy) in order to ascertain the success of the treatment. At present, the evaluation of the cancer therapy is usually done by physical examination, assessing tumor shrinkage, and less frequently by imaging. This is usually done only after the patient undergoes the complete treatment cycle, which takes few weeks or months. There is an increasing need for a rapid therapy detection technique.

Various techniques (both invasive and non-invasive) have been developed to determine whether the cells are undergoing apoptosis. Biological techniques developed are invasive and time consuming as well. For example, Positron Emission Tomography (PET) though non-invasive, requires the injection of radioisotopes into the body and hence scans cannot be performed repetitively. Other optical imaging methods using bioluminescence markers, though non-invasive, lack penetration depth. It has been shown that high frequency ultrasound (HFUS) imaging in the range of 20-60 MHz can be used to detect the structural changes during the cell death [1].

HFUS imaging has become a powerful clinical tool and has proved especially valuable in ophthalmology. It has several advantages: it is non-invasive, non-ionizing, provides fine-scale resolution (especially for small animal anatomy), cost effective, safe and could be used to detect and identify a wide variety of abnormal tissues.

A series of structural changes occur within a cell during cell death. During apoptosis there is cell and nucleus shrinkage, condensation of chromatin in the nucleus, and eventual nuclear fragmentation. Studies over the past decade have found that the HFUS (20-100 MHz) can be used to detect localized variations in cell morphologies in tissues and cell ensembles [1,2]. It is shown in [2] that ensembles of necrotic (heat killed), cells undergoing mitosis, and apoptosis yield an increased backscatter ultrasound signal intensity compared to cells not exposed to the drug. US backscatter signals from normal and apoptotic acute myeloid leukemia (AML) cell pellets are shown in Figure 1. Spectral analysis techniques have been used to analyze radio frequency (RF) echo signals, and have made it possible to more specifically characterize average cell structure changes in tissues and cell ensembles. However, to increase the technique sensitivity and specificity, other signal analysis techniques are explored.

Farnoud [4], using Burg-lattice based autoregressive (AR) modeling successfully classified 100 backscatter signals from normal and apoptotic cells using machine-learning algorithms with a classification accuracy ranging from 50%-97 % with different classifiers. It was shown that non-linear classifiers such as probabilistic neural networks with sigmoid activation function provided the best accuracy. Bejar [5] could monitor apoptosis by using cepstral coefficients (derived from AR coefficients) as features and local discriminant bases (LDB) algorithm. This work used 39 signals of the normal group and 36 signals of the abnormal group and achieved an overall classification accuracy rate of above 90%. Reflection coefficients, the parameters of the lattice filter, provide an alternative parameterization of signals. The reflection coefficients are computed from AR coefficients by using Levinson's recursions. There is a non-linear relation between these two coefficients. In this work we explore whether the reflection coefficients can potentially be used as signal features for the classification. With this motivation, we intend to find whether reflection coefficients may contain useful information about the US backscattered signal in such a way that the classification of the normal and apoptotic signals can be done by using simple and efficient time-domain pattern analysis approaches. To the author's best knowledge, this is the first study exploring the use of reflection coefficients for a biomedical signal classification application.

The block diagram of the proposed system is shown in Figure 2. The US backscattered signals are analyzed by using lattice prediction error filter parameters called reflection coefficients as features and classified by using simple classifier based on maximum likelihood method. The paper is structured as follows: Section 2 details the lattice prediction error filters, different algorithms to compute reflection coefficients including the Burg-lattice method. Results are discussed in Section 3, and conclusions are given in Section 4.

2 METHODOLOGY

2.1 Lattice Prediction Error Filter

The objective of a linear prediction filter is to select a linear function that minimizes the prediction error for the given data set. When the predictor is embedded in the linear filter, the predictor can be viewed as linear filtering and is called as prediction error filter (PEF).

The PEF is defined as a structure, which combines successive samples of a signal multiplied by coefficients, so that the output (prediction-error) power of the filter is minimized. There are two kinds of PEF, depending on the form of prediction error utilized. Based on a given sequence of input samples, a forward PEF is designed to minimize the mean-square value of the forward prediction error, defined as the difference between the predicted value of the input one step into the future and its actual value. On the other hand, a backward PEF is designed to minimize the mean-square value of the backward prediction error, defined as the difference between the predicted value of the input one step into the past and its actual value.

Two basic adaptive filtering implementation schemes of the prediction error filter are the tapped-delay-line (TDL) structure, which is adapted by minimizing a single, global error criterion, and lattice structure, in which the error is minimized independently for each stage of the filter. Depending on the form of calculation used, the PEF may suffer from lack of numerical stability. The lattice PEF, a form of adaptive filter, proposed by Burg [6] and independently derived by Itakura and Saito [7] provides a solution to these problems. Lattice-structure has a number of advantages [8] over the traditional TDL structure, among which are better resolution and/or stability, much better control of the filter convergence and adaptive properties (due to the orthogonalization of the data provided by the lattice, the adaptive convergence rate appears to be particularly insensitive to the conditioning or eigenvalue spread of the input signal sequence), the stage by stage approach to the estimation problem provided by the lattice filter offers the possibility of determining the optimal model order for the process. The sensitivity of the lattice filter parameters to round off noise and finite word length effects, particularly in the normalized algorithms, seems to be less than that of the equivalent TDL processor. Some important characteristics of the lattice filters are [9]:

1. It is an efficient structure for generating simultaneously the forward and backward prediction errors.

2. The lattice structure is modular: increasing the order of the filter requires adding only one extra module, leaving all other modules and its associated filter parameters the same.

3. The various stages of a lattice are decoupled from each other in the following sense: The memory of the lattice (storing $b_0(n-1), ..., b_{m-1}(n-1)$) contain orthogonal

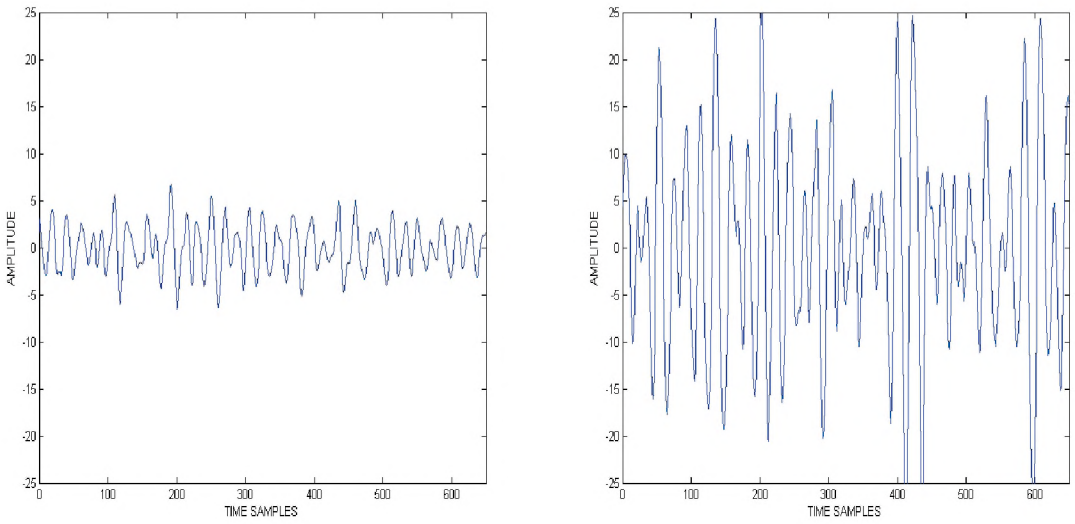

(a) (b)

Figure 1: (a) Normal signal and (b) Apoptotic signal acquired from cell pellets.

variables, thus the information contained in $u(n)$ is split in M pieces, which gradually reduces the redundancy of the signal.

The lattice structure, with superior flexibility and structural diversity find use in applications such as predictive filtering [3], adaptive filtering [10], and speech processing [15]. The lattice form filter realization first attracted great attention in the late 1960s and early 1970s, with its superiority in finite precision performance. Itakura and Saito were the first researchers who utilized this lattice form for speech coding.

2.2 Algorithms for computing reflection coefficients

Lattice filters are a well-known signal analysis and coding tool. Their parameters, the reflection coefficients, have a good robustness to noise and quantization effects [16]. In the lattice formulation, the reflection coefficients can be computed by minimizing the norm of the forward residual or the backward residual, or a combination of the two. There are several methods to calculate the reflection coefficients of a lattice filter [11]. These methods depend on different ways of correlating the forward and backward residuals. A brief description of four of these algorithms is given below:

The common basic objective of all the algorithms mentioned is to minimize the mean-squared forward and backward errors, which are the outputs of each filter stage. In other words, to obtain the lowest values of $F_i(n)$ and $B_i(n)$, defined in the following equations:

$$F_i(n) = E\left[|f_i(n)|^2\right] \tag{1}$$

$$B_i(n) = E\left[|b_i(n)|^2\right] \tag{2}$$

where $f_i(n)$ is the forward residual, $b_i(n)$ is the backward residual and $E(.)$ denotes the expected value.

Differentiating these quantities with respect to the reflection coefficient gives two values for the coefficient, by minimizing the forward and backward mean square errors separately. The equation

$$\rho_i^F(n) = \frac{C_{i-1}(n)}{B_{i-1}(n-1)} \tag{3}$$

minimizes the forward error, and

$$\rho_i^B(n) = \frac{C_{i-1}(n)}{F_{i-1}(n)} \tag{4}$$

minimizes the backward error where $C_i(n)$ is the expectation of the negative cross-power of forward and backward errors, given by

$$C_{i-1}(n) = -E\left[f_i(n) \cdot b_i^*(n-1)\right] \tag{5}$$

2.2.1 Forward-and-Backward (F+B) Algorithm

This is the most direct method suggested by Griffith [9] and is the only algorithm where the forward and backward reflection coefficients are not complex conjugates of each other. It simply uses $\rho_i^f(n)$ and $\rho_i^b(n)$ as the forward and backward reflection coefficients respectively, i.e.,

$$\rho_i^f(n) = \rho_i^F(n) \tag{6}$$

$$\rho_i^b(n) = \rho_i^B(n) \tag{7}$$

As $\rho^F \cdot (\rho^B)^* = 1$ in almost all cases either or will be greater than one, however, the reflection coefficients should

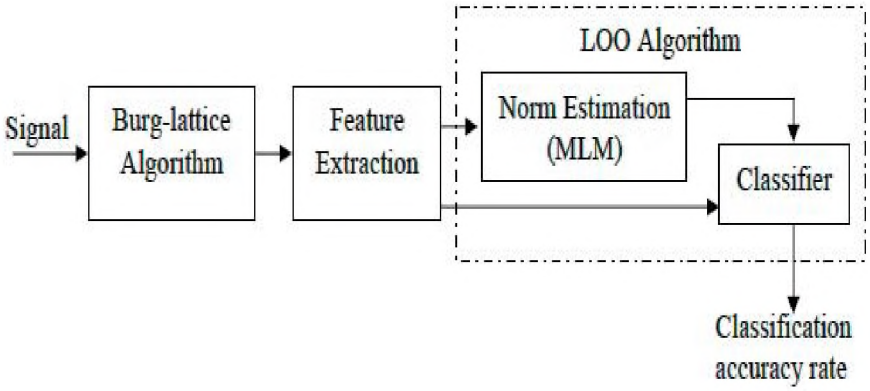

Figure 2: Block diagram of the proposed system

have a value less than one for a stable filter. Hence, the stability is not guaranteed.

2.2.2 Forward/Backward-Minimum (M) Algorithm

This algorithm provides an alternative to the F+B algorithm by following the rule that if either $\rho_i^F(n)$or $\rho_i^B(n)$ is greater than one, then the other will be less than one and hence guarantees stability. This algorithm is suggested by Makhoul [13], and is formulated as

$$\rho_i^f(n) = \rho_i^M(n) = \frac{C_{i-1}(n)}{max\left[F_{i-1}(n), B_{i-1}(n-1)\right]} \tag{8}$$

$$\rho_i^b(n) = \left[\rho_i^M(n)\right]^* \tag{9}$$

2.2.3 Geometric-Mean (G) Algorithm

This algorithm is one of the two joint estimation algorithms that try to minimize the forward and backward error expectations jointly and is derived by Itakura and Saito [7]. Here, the reflection coefficients are computed by using the geometric mean of the forward and backward error expectation.

$$\rho_i^f(n) = \rho_i^G(n) = \frac{C_{i-1}(n)}{\left[F_{i-1}(n) \cdot B_{i-1}(n-1)\right]^{1/2}} \tag{10}$$

$$\rho_i^b(n) = \left[\rho_i^G(n)\right]^* \tag{11}$$

2.2.4 Burg Algorithm

Burg method is an order- recursive algorithm and was introduced by J.P. Burg in 1967 [6]. This method uses a lattice filter and directly estimates reflection coefficients instead of autocorrelation values. The algorithm is sometimes designated as maximum entropy method because of its derivation in the context of maximum entropy methods. The key step in the algorithm involves minimizing the sum of the norm of the forward and backward residual vectors, as a function of the reflection coefficient matrices. Since the computed coefficients are the harmonic mean between the forward and backward partial autocorrelation estimates, the Burg procedure is also known as the Harmonic algorithm. This algorithm starts with a first-order model and computes the prediction parameters (reflection coefficients) for successively higher model orders. The ith reflection coefficient is a measure of the correlation between $y(n)$ and $y(n-i)$ after the correlation due to the intermediate observations $y(n-1), ..., y(n-i+1)$ has been filtered out. As the recursion constrains the filter poles to fall within the unit circle stability of the filter is gauranteed. The Burg method is particularly useful for estimating coefficients from segments of unequal length. This method is based on Levinsons recursions and estimates the AR filter parameters through the associated reflection coefficients constraining the AR coefficients to satisfy Levinson equations.

Lets assume the data measurements (US backscattered signals) be $\{y(n)\}$ for $n = 0, 1, 2, ..., N-1$ and let us consider the filter of order M.

The equations of the Burg-lattice filter are:

$$f_0(n) = b_0(n) = y(n) \tag{12}$$

$$f_i(n) = f_{i-1}(n) + k_i b_{i-1}(n-1), 1 \leq i \leq M \tag{13}$$

$$b_i(n) = k_i f_{i-1}(n) + b_{i-1}(n-1), 1 \leq i \leq M \tag{14}$$

The corresponding ith reflection coefficient k_i is obtained by minimizing the sum of the square values of the forward and backward prediction errors at the output of the ith stage.

$$k_i = \frac{-\sum_n f_{i-1}(n) b_{i-1}(n-1)}{\frac{1}{2}\sum_n \left[\left|f_{i-1}(n)\right|^2 + \left|b_{i-1}(n-1)\right|^2\right]} \tag{15}$$

As the Burg algorithm uses lattice structure, it inherits the advantages of lattice structure such as stability, modularity, computational simplicity and efficiency. Besides these,

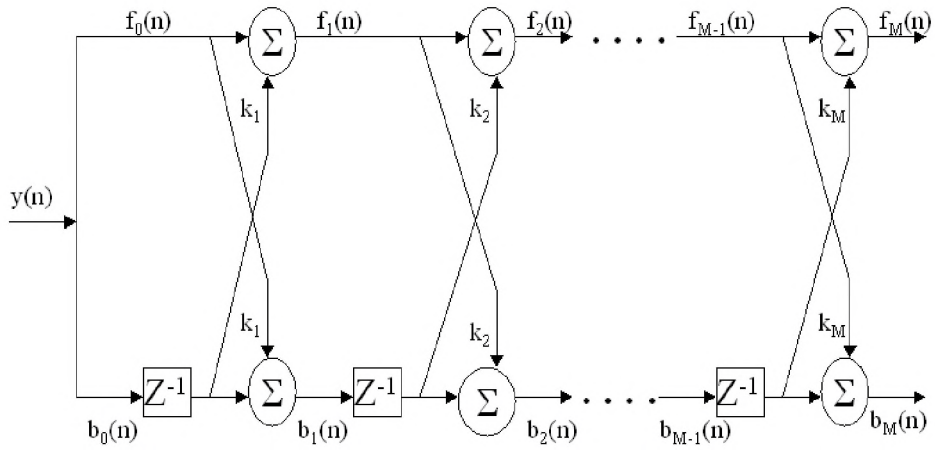

Figure 3: Burg-lattice Filter (adapted from [18])

it is proven to be an efficient linear prediction technique and is probably the most widely known method to estimate AR coefficients. Considering the advantages of Burg-lattice algorithm, in this work its reflection coefficients are used for parametric feature representation of the ultrasound backscatter signals. We also experimentally checked the time invariance property and robustness of the reflection coefficients of the Burg algorithm. In time invariance test, reflection coefficients of an apoptotic signal and its delayed version (0.2 micro seconds) are calculated. From Table 1 it can be demonstrated that the reflection coefficients are time invariant as the value of the reflection coefficients are same. In robustness test, an apoptotic signal is corrupted with random noise. The reflection coefficients for both apoptotic and noisy apoptotic signals are calculated. Then a measure of closeness of the two sets of reflection coefficients is calculated by using the correlation coefficient function. Table 2 shows the correlation coefficients obtained for different signal to noise ratio(SNR)s. The reflection coefficients are identical for a SNR of 30 dB and show strong correlations for lower SNRs (> 9dB).

2.3 Data Acquisition

AML-5 cells (at Ontario Cancer Institute) were cultured in alpha minimum essential medium (alpha MEM, Gibco 11900), supplemented with Streptomycin and Penicillin at concentrations of 100mg/L, and 5 % Fetal Bovine serum (Hyclone). The cells grew in 150ml of medium as a suspension, at concentrations of 5x105 cells/ ml, in a 370C, and 5% CO_2 incubator [19]. Pellets were made with untreated cells and treated cells. Treated cells were exposed to 10ug/ml cisplatin, a chemotherapeutic agent for 24 hours, to induce apoptosis, before processing to form a pellet. Large volumes of the treated and untreated cells were concentrated by centrifugation, at 2000rpm for 10 minutes, using a Sorval centrifuge. The cell concentrations were then determined and volumes prepared in phosphate-buffered saline, so that the final pellets would have the desired percentages of the treated and untreated cells. The final pellets for scanning were centrifuged at 3000rpm/ 10 minutes, in flat bottom cryo-tubes on a desktop swinging bucket centrifuge. The cell pellets were then immersed in phosphate-buffered saline that acted as a coupling medium for the ultrasound imaging and RF data collection. During the data acquisition process, the cells were kept at room temperature. The experimental set consists of a pellet of the normal or untreated AML cells (which are not exposed to cisplatin drug), and different mixtures of treated and untreated cells. The mixtures of cells varied from 5% treated cells mixed with 95% untreated to 100%treated cells. The cells are imaged as a function of concentration of treated cells (5, 10, 20, 80 and 100%). A 40 MHz f2 transducer with a bandwidth of approximately 100% was used to image the pellets of normal and apoptotic cells. The transducer was attached to the VS40B ultrasound imager (Visualsonics Inc., Toronto, ON, Canada) which has the ability to select regions of interest (ROI) from the B-scan images and store the raw RF backscattered data of the ROI. The RF data was digitized at 500 MHz sampling rate and stored for further analysis. Data analysis was performed in MATLAB (The Mathworks Inc., Natick, MA, USA). The experimental data were obtained in Princess Margaret Hospital, Toronto, Canada. Experimental details on the data acquisition can be found in [17].

2.4 Feature Extraction and Classification

The experimental ultrasound backscatter signals, like many other biomedical signals could be non-stationary. They are segmented into stationary segments in order to apply standard signal processing techniques such as parametric analysis. In the present work, manual fixed segmentation method is used. In the B-scan image as shown in Fig. 4, a small portion of about 1 mm at the centre of the image (0.5mm above and below the focal line of the transducer) is selected as the segment. The segment length is of 650 samples. The stationary (quasi-stationary) segments are then given to the lattice prediction error filter and the reflection coefficients are obtained by using the Burg-lattice algorithm. These reflection coefficients (partial correlation coefficients) are assumed

k_o	-0.9459	0.9215	0.1836	-0.2651	-0.0626
k_d	-0.9459	0.9215	0.1836	-0.2651	-0.0626

Table 1: Reflection coefficients of original and delayed apoptotic signal. k_o represents reflection coefficients of original apoptotic signal and k_d represents reflection coefficients of the delayed

SNR (in dB)	0	3	6	9	12	15	18	21	24	27	30
Correlation Coefficients	0.30	0.38	0.46	0.54	0.65	0.76	0.85	0.91	0.95	0.97	1.00

Table 2: Correlation coefficient values of the original apoptotic signal and corrupted apoptotic signal with random noise at different SNRs

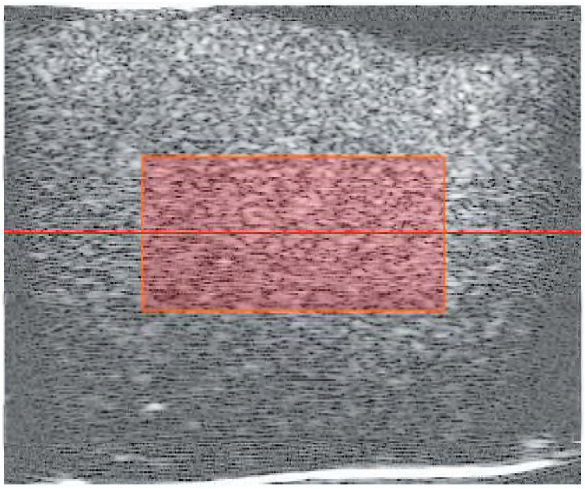

Figure 4: Segmentation The central line indicates the focal line of the transducer and the rectangle indicated the selected region of the image.

to have the discriminant statistical information of the signals and were treated as features. Model order selection is important. With appropriate number of poles, it is possible to reconstruct the signal. Typically, model order is twice the number of spectral peaks of the signal. In this work, the peaks were between 5 and 7. Hence model order of 15 is selected. A snapshot of reflection coefficients of normal and apoptotic signal after 24 hours with a model order 15 is given in the Fig. 5.

Pattern classification is the next step after feature extraction in the pattern recognition process. As indicated in [14] the four best-known approaches for pattern recognition are: 1) template matching, 2) statistical classifications, 3) syntactic or structural matching, and 4) neural networks. In statistical pattern recognition, each pattern is represented by a set of d features i.e., viewed as a d dimensional vector. When little prior knowledge about the patterns to be recognised is known, the best suitable design for the pattern recognition system is to use training or a learning procedure. The classification is operated in two modes: training (learning) and testing (classification). The classifier is first trained with the derived features and then tested. Standard statistical classification methods use descriptive parameters and distance measures using probablistic approaches. There are several distance measures that could be used [5]: Euclidean distance measure, maximum likelihood measure, Mahalanobis distance measure, and weighted distance measure. In this present work, the classification of the ultrasound signals was done by using the maximum likelihood method as it most closely approximates the Bayes classifier and obtains the best discriminative efficiency if the probability density function of the extracted features are multivariate Gaussian [5,14].

The classification accuracy is estimated by using leave-one-out (LOO) method, one of the most popular validation techniques. The LOO method is known to provide least bias estimate [14]. In this method, one sample is excluded from the dataset and the classifier is trained with the remaining samples. Then the classification accuracy is determined by testing the classifier with the excluded sample. This is repeated for all samples of the dataset. An independence between the test and the training set is maintained as each sample is excluded from the training set. The reference database consists of two template reference vectors (one for normal and the other for apoptotic signals). A test signal is extracted from the database, the distance between the test signal and the group of reference is measured. The test signal belongs to the group which has less norm.

3 RESULTS AND DISCUSSION

Each pellet data consists of 43 RF lines collected from a 40 MHz transducer. As mentioned before, the ultrasound backscattered signals from untreated cancer cells are termed as normal signals and those from the cancer cells treated with chemotherapeutic agent (which induces apoptosis) are termed as apoptotic signals. The treated cancer cells are imaged as a function of concentration of treated cells (5, 10, 20, 80 and 100%). The aim is to classify the signals at different concentrations of the treated cells. Statistical analysis of the signals helps in extracting the discriminative features.

All the signals from a database are fed as input to the Burg-lattice filter. The corresponding reflection coefficients are extracted as features. The classifier is trained with the extracted features and tested with an unknown signal. The classification results are tabulated. We compared the results obtained by using reflection coefficients as features with the results obtained by using AR coefficients and cepstral coeffi-

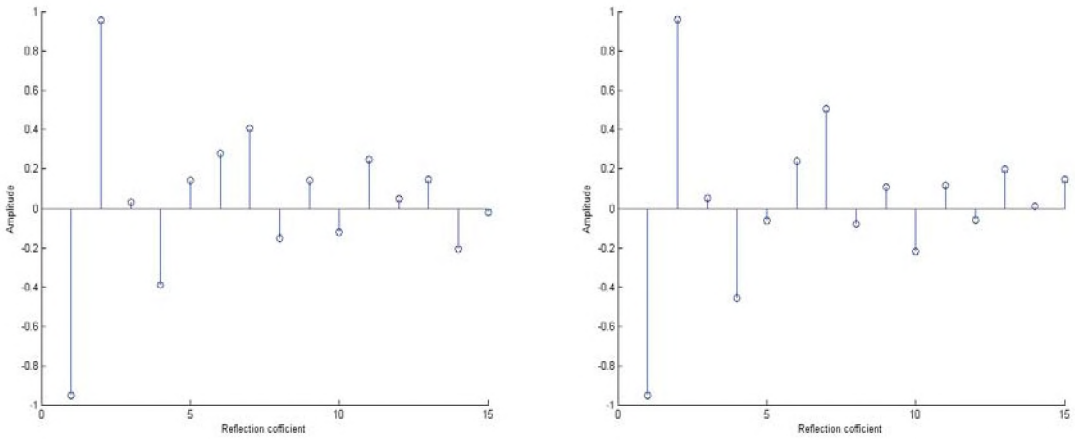

(a) (b)

Figure 5: (a). A snapshot of reflection coefficients of signal from normal cells with a model order 15 and (b). A snapshot of reflection coefficients of signal from apoptotic cells (after 24 hours of exposure to cisplatin) with a model order of 15.

% of treated cells in pellets	Accuracy rate of Normal Signals in %			Accuracy rate of Apoptotic Signals in %			Overall classification accuracy in %		
	RC	AR	Ceps	RC	AR	Ceps	RC	AR	Ceps
5	100	83.72	95.35	100	88.37	97.67	100	86.05	96.51
10	100	88.37	97.67	100	90.69	100	100	89.54	98.83
20	97.67	83.72	88.37	97.67	86.05	90.70	97.67	84.88	89.54
80	100	88.37	97.67	100	97.67	100	100	93.02	98.83
100	100	88.37	97.67	100	95.35	100	100	91.86	98.83

Table 3: Classification accuracy with model order 15. RC-reflection coefficients, AR- autoregressive coefficients and Ceps-cepstral coefficients

cients as features. The percentage represents the number of signals classified accurately. The overall classification represents the number of normal and apoptotic signals classified accurately.

Tables 3 show the classification accuracy rates obtained by comparing the normal signals with apoptotic signals at 5, 10, 20, 80, and 100 % concentrations with a model order of 15. The classification accuracy rates indicate that the relfection coefficients provide the best classification of ultrasound backscattered signals. The cepstral coefficients give better performance than the AR coefficients. The reason could be the following discussion. AR coefficients gives a relatively abstract form of feature representation. However, cepstral coefficients are well suited for signals that contain echos of a fundamental signature (ultrasound backscatter could be cosidered as a signal resulting from a convolution of the pulse sent (fundamental signature) with the scattering strength of the scatterers) and hence may be better than AR. On the other hand, reflection coefficient is also an abstract parameter and for signals with reflected components, it might do a better feature representation. The better performance may be due to higher discriminant information being present in the derived reflection coefficients from the ultrasound backscattered signals from the normal and the apoptotic cells

4 CONCLUSIONS

In this paper we evaluated the accuracy of lattice filter prediction coefficients to differentiate the ultrasound backscatter signals from normal and apoptotic cells which differ in their intensity and frequency spectrum. This is the first work in biomedical signal analysis, in which reflection coefficients are used for parametric signal analysis and classification. The positive results, demonstrate the potential discriminatory ability by using reflection coefficients as features and are worth studying. Modularity, the main advantage of lattice structure, will make hardware implementation straight forward. From a practical perspective, the lattice provides an efficient, fast, modular and robust structure suitable for hardware implementation and hence it can widen the scope of research on the use of reflection coefficients.

Although this work has been focused mainly on evaluating the reflection coefficients to contain discriminant information about normal and apoptotic signals, further work on this "hardware-friendly" DSP technique will be aimed at

evaluting the performance of reflection coefficients by testing with a larger database in real-time. Successful real-time performance will allow to reach the ultimate goal ie., hardware implementation and even extend its applications in analyzing other biomedical signals.

REFERENCES

[1] S. Brand, "Visualization of apoptotic cells using scanning acoustic microscopy and high frequency ultrasound", IEEE Symposium on Ultrasonics, vol 2, pp. 882-5, Sept. 2005.

[2] Kolios, M. C., et al., "An investigation of backscatter power spectra from cells, cell pellets and microspheres", IEEE Symposium on Ultrasonics, vol 1, pp. 752-7, Oct 2003.

[3] S.J. Ovaska, "Predictive Signal Processing in Instrumentation and Measurement: A Tutorial Review", IEEE Conference Proceedings on Instrumentation and Measurement Technology Conference, vol. 1, pp. 48 53, May 1997.

[4] Noushin R. Farnoud, Michael Kolios and Sridhar Krishnan, "Ultrasound Backscatter Signal Characterization and Classification Using Autoregressive Modeling and Machine Learning Algorithms", IEEE Conference Proceedings on Engineering in Medicine and Biology Society, vol. 3, pp. 2861 - 2864, Sep 17-21, 2003.

[5] Bejar, Jose. M. C., "Cepstral Analysis of Ultrasound Backscattered Signals for Screening Apoptotic Cancer Cells from Normal Cells", Ryerson University, Aug 2003.

[6] J. P. Burg, "Maximum Entropy Spectral Analysis", Ph.D. dissertation, Dept. of Geophysics, Stanford University, Stanford, CA, May 1975.

[7] F.Itakura and Saito, "Digital Filtering Techniques for Speech Analysis and Synthesis", Pesented at 7th Int. Cong. Acoustics, Budapest, paper 25-C-1, 1971.

[8] J. Makhoul, "Linear Prediction: A Tutorial Review", Proc. IEEE, Vol. 63, Issue 4, pp. 561-580, 1975.

[9] L. Griffiths, "A continuously-Adaptive Filter Implemented as a Lattice Structure", Proc. IEEE Int. Conf. on Acoustics, Speech, and Signal Processing, vol. 77CH1197-3, pp. 683-686, 1997.

[10] Simon Haykin, "Adaptive Filter Theory", Prentice Hall Information and System Sciences Series, New Jersey, 2002.

[11] C.J. Gibson, Simon Haykin, "A Comparision of Algorithms for the Calculation of Adaptive Lattice Filters", IEEE International Conference on Acoustics, Speech, and Signal Processing, Vol 5, pp. 978-983, 1980.

[12] Sridhar Krishnan, "Adaptive Filtering, Modeling, and Classification of Knee Joint Vibroarthrographic Signals", Masters thesis, Department of Electrical and Computer Engineering, University of Calgary, Calgary, AB, Canada, April 1996.

[13] J. Makhoul, "Stable and Efficient Lattice Methods for Linear Prediction", IEEE Trans. on Acoustics, Speech, and Signal Processing, vol. ASSP-25, pp. 423-428,1977.

[14] Anil K. Jain et al., "Statistical Pattern Recognition: A Review", IEEE Transactions on Pattern Analysis and Machine Intelligence, Vol. 22, No. 1, Jan 2000.

[15] H. K. Kwan, M. Wang, "ARMA Lattice Model for Speech Analysis and Synthesis", Proc. IEEE International Conference on Neural Networks and Signal Processing, Vol 2, pp. 912-915, Dec 2003.

[16] S. Krstulovic, F. Bimbot, "Signal modeling with non-uniform topology lattice filters", IEEE Proceedings on Acoustics, Speech, and Signal Processing, Vol. 2, pp. 845-848, May 2001.

[17] Adam S. Tunis, "Monitoring Structural Changes in Cells and Tissues with High Frequency Ultrasound Signal Statistics", M.Sc., University of Toronto (Canada), 2005.

[18] K. Roth, et al., "Frequency warped Burg's method for AR-modeling", IEEE Workshop on Applications of Signal Processing to Audio and Acoustics, pp. 5-8, Oct 2003.

[19] Czarnota G., Kolios M., Abraham J., Portnoy M., Ottensmeyer F., Hunt J. W. and Sherar M. ,"Ultrasonic Imaging of apoptosis:High-Resolution Non-invasive Imaging of Programmed Cell Death in vitro, n situ and in vivo", British Journal of Cancer 81(3), pp.520-527, 1999.

Ultrasound Micro-Elastography: A New Imaging Modality To Phenotype Hypertension In Rat Models

Roch L. Maurice[a,b], Jérémie Fromageau[a], François Yua, Ékatherina Stoyanova[a], Zhao Qin[a], Junzheng Peng[c], Pavel Hamet[d], Johanne Tremblay[c] and Guy Cloutier[a,b]

a Laboratory of Biorheology and Medical Ultrasonics, Research Center, University of Montreal Hospital, Montreal, Quebec
b Department of Radiology, Radio-Oncology and Nuclear Medicine, and Institute of Biomedical Engineering, University of Montreal, Montreal, Quebec
c Laboratory of Cellular Biology of Hypertension, Research Center, University of Montreal Hospital, Montreal, Quebec
d Laboratory of Molecular Medicine, Research Center, University of Montreal Hospital, Montreal, Quebec

ABSTRACT

New ultrasound imaging methods are proposed to non-invasively characterize the mechanical properties of superficial arteries (MicroNIVE) and kidneys (MicroNIKE) in rodents. In MicroNIVE, the vessel wall is compressed/dilated by the blood flow pulsation, whereas time-sequences of high-resolution radio-frequency (RF) ultrasound data are externally acquired. The kinematics of the vascular tissue, assessed with the Lagrangian Speckle Model Estimator (LSME), provides a strain cartography also known as elastogram. Because the LSME assumes linear elasticity conditions, strain is inversely proportional to stiffness, which is an intermediate phenotype of the hypertension (HT) trait. Results are presented for the common carotid artery of spontaneously hypertensive rats (SHR, n = 5) and control normotensive Brown Norway (BN, n = 5) rats. At 15-weeks old, the SHR rats' carotid artery (4.46 ± 1.79 % of strain) was found, on average, stiffer that of the BN's, which exhibited strains of 6.76 ± 1.48 % ($p < .059$). On the other hand, in MicroNIKE, the kidney is externally compressed with the ultrasound probe while time-sequences of high-resolution RF data are acquired. For the purpose of investigating the feasibility of MicroNIKE, a fresh excised kidney from a Recombinant Inbred (RI) rat was investigated. The elastograms, computed with the LSME, clearly exhibited the medulla with distinct mechanical properties. It is concluded that MicroNIVE and MicroNIKE are promising new imaging tools to non-invasively and longitudinally study the impact of targeted genes on vascular tissue remodeling and nephroangiosclerosis in engineered rat models of HT.

SOMMAIRE

L'hypertension est connue pour entraîner des dommages d'organes incluant les vaisseaux sanguins et les reins. Notamment, des études menées sur des modèles de rongeurs ont permis de démontrer que cette pathologie est influencée par certains facteurs structuraux et fonctionnels touchant les artères, tels l'hypertrophie et le remodelage. En d'autres termes, l'hypertension s'accompagne de modulations des propriétés mécaniques des artères. Similairement, la néphrosclérose est caractérisée par des changements de propriétés mécaniques du tissu rénal. Cet article introduit deux nouvelles modalités d'imagerie ultrasonore ayant pour objectifs la caractérisation non-intrusive des propriétés mécaniques des artères superficielles (MicroNIVE) et des reins (MicroNIKE) de rongeurs. Ceci permettrait d'étudier les artères et les reins affligés par cette pathologie dans leur milieu physiologique naturel. En ce qui concerne la MicroNIVE, la paroi vasculaire est naturellement assujettie à une cinétique induite par le flux sanguin. Un algorithme dédié, connu sous l'appellation de Lagrangian Speckle Model Estimator (LSME), est utilisé pour estimer, à partir de séquences temporelles d'images ultrasonores, le mouvement de la paroi artérielle et en déduire la déformation. Le LSME assumant des conditions d'élasticité linéaire, la déformation est inversement proportionnelle à la rigidité. L'étude, ici reportée, a été effectuée in situ sur des rats hypertendus SHR (n = 5) et normotendus BN (n = 5), âgés de 15 semaines. Il a été observé que la carotide commune des SHR, avec 4.46 ± 1.79 % de déformation, était plus rigide que celle des BN, avec 6.76 ± 1.48 % ($p < .059$). Une étude préliminaire in vitro, menée sur un rein excisé d'un rat hypertendu, est aussi reportée. Dans ce contexte, une compression externe a été appliquée pour induire une cinétique au tissu rénal lors de l'acquisition des images ultrasonores. La cartographie des déformations obtenue avec le LSME, dite élastogramme, distingue clairement les structures du rein dont la médulla avec une rigidité spécifique. Ces résultats permettent de croire dans le potentiel de la Micro-Élastographie pour des applications ultérieures dans les domaines de la pathophysiologie et de la pharmacogénétique de l'hypertension.

1. INTRODUCTION

Hypertension (HT) afflicts approximately 25% of the world population and only 13% of hypertensive patients have adequate blood pressure (BP) control [1]. HT leads to damage of organs such as the brain, the kidneys, the heart and blood vessels. The lack of controlled blood pressure and the impact on end organs are believed to be the reason that, on a global basis, HT is the leading risk factor for mortality and the third major risk factor for the burden of all diseases in terms of disability adjusted life years [2].

So far, in most studies to detect specific manifestations of HT, *i.e.* to phenotype HT, insights are provided mainly by *ex vivo* experiments using rat models' arteries or organs [3, 4, 5, 6, 7 and 8]. However, since the most important insights on a disease should come from the investigations of the afflicted tissues/organs in the presence of a physiological environment, the development of a non-invasive imaging method for *in situ* investigations of HT in rodents would be of great pathophysiological and pharmaceutical relevance.

Over the past years, researchers have selectively bred rats for high blood pressure to provide animal models of HT; the spontaneously hypertensive rat (SHR) is a very common type of such animal model. On the other hand, animals can also be selected for low blood pressure; that is the case of the Brown Norway (BN) rats, a normotensive strain that is usually considered as a reference in terms of blood pressures. It is worth mentioning that SHR and BN are progenitor strains of the recombinant inbred (RI) rats that are also developed for HT research [9]. Integration of transcriptional profiling and linkage analysis has already been achieved for the RI strain [10, 11]. In this study, carotid artery mechanical properties of SHR and BN rats were investigated to evaluate the potential of a new method, said MicroNIVE, to phenotype HT. This paper also reports preliminary data of MicroNIKE, another new method that aims to mechanically characterize the kidney.

1.1. Hypertension and blood vessel remodeling

It is known that BP is influenced by several structural and functional factors, namely hypertrophy and remodeling of arterial and arteriolar vessels. Regarding the vessel wall, this means that intrinsic alterations of its mechanical properties occur. Indeed, the arterial compliance and distensibility are modulated by HT [12]. Namely, arterial walls become less compliant with HT. Since compliance and distensibility are both dependent on the vascular tissue stiffness, we make the assumption that the vascular tissue elastic modulus, or equivalently the strain when the artery is under stress, constitutes a potential phenotype of HT.

1.2. Hypertension and nephroangiosclerosis

Nephrosclerosis, also known as nephroangiosclerosis, is literally defined as the hardening of kidneys. It is the result of scarring or replacement of the normal renal parenchyma by dense collagenous tissues. High blood pressure is a well-recognized feature in chronic renal disease, but the ability of mild to moderate hypertension to produce renal insufficiency is still poorly understood [7]. Similarly to the blood vessel remodeling context, we make the assumption that the renal tissue stiffness constitutes a potential phenotype of HT.

1.3. Ultrasound elastography

Ophir *et al.* [13] introduced elastography in the early nineties. This imaging modality was defined as biological tissue elasticity or stiffness imaging. Elastography enables the calculation of tissue deformation from sequences of radio-frequency (RF) images acquired at different load levels. Tissue mechanical properties are assessed by analyzing the kinematics of the tissue acoustical signatures within the RF data set. The primary objectives of elastography were to complement B-mode ultrasound imaging as a screening method to detect rigid areas in human breasts [14] and to investigate tissue heterogeneity in prostate cancers [15, 16].

Ultrasound elastography was also proposed for human vessel wall characterization using endovascular catheters [17,18,19,20,21]. Several groups recently proposed different approaches to non-invasively characterize superficial arteries by using standard extra-corporal array transducers [22, 23, 24]. The method was labeled as NIVE, i.e. **N**on-**I**nvasive **V**ascular **E**lastography [24]. Furthermore, in [25], our group reported *in vitro* flow phantom experiments and preliminary *in vivo* results for the carotid arteries of rat models of HT. Being the application of NIVE for the purpose of investigating small vessels in rodents, this method was labeled as MicroNIVE. In MicroNIVE, the vessel wall is naturally compressed/dilated by the blood flow pulsation and no external pulsing of the artery is required to map the strain pattern within the vessel wall. Similarly, the appellation of MicroNIKE was chosen for kidney investigations in small animals.

1.4. Objectives

This paper first reports preliminary data on MicroNIVE. The mechanical properties (namely, strain) of carotid arteries were quantitatively assessed *in situ* in SHR and BN rats. We then addressed the possibility to investigate rodents' kidneys using elastography (MicroNIKE). In this context, *ex vivo* RF data were acquired from a fresh excised RI rat's kidney. In both experimental studies, the Lagrangian speckle model estimator (LSME) [24,25,26] was used to compute strain distributions (or elastograms) within the region of interest (ROI). The sections below give an overview of the animal models, the experimental set-up, and the mathematical model that supports the LSME. Subsequently, results are presented and discussed, with remarks on our final conclusions.

2. MATERIALS

This investigation is conformed with Canadian CCAC ("Canadian Council of Animal Care") guidelines as well as the Guide *for the Care and Use of Laboratory Animals* published by the US National Institutes of Health (NIH Publication No 85-23, revised 1996), and all procedures were approved by the institutional Animal Care Committee of the Centre Hospitalier de l'Université de Montréal (CHUM).

2.1. MicroNIVE animal models

In order to investigate the feasibility of MicroNIVE, time-sequences of ultrasound RF data were acquired on ten 15-week old male rats: 5 normotensive Brown Norway (BN) rats and 5 spontaneously hypertensive rats (SHR), respectively. During ultrasound data acquisition, they were anesthetized by inhalation of 2.5 % isofluorane. The body temperature of each animal was monitored with a rectal probe (Thermalert TH-5, Physitemp Instruments, Clifton, NJ, USA) and maintained at 37 ± 1°C by using a heating surface. The systolic blood pressures were measured with a tail-cuff monitoring system (Kent Scientific, model XBP-1000, Torrington, CT, USA). It was measured locally in the tail and consequently it underestimated the systemic pressure. The hairs over the neck were shaved and further removed with a depilatory cream (Nair, Church and Dwight Co., USA). Sequences of RF data were acquired over longitudinal sections of the common carotid artery.

2.2. MicroNIKE animal model

A fresh 1.36 g-weight kidney was harvested from a 94-weeks old male RI rat, just following sacrifice by CO_2 gas inhalation. As illustrated in Fig. 1, for the purpose of acquiring RF data, the kidney was immersed in a gelatin-agar mixture while step-wisely compressed by the ultrasound probe. The probe of the ultrasound scanner was fixed to an extendable arm. The height of the arm was controlled by rotating a screw, which allowed a precise displacement of 1mm by revolution. Five images, corresponding to five steps of compression, were acquired. One step of compression was equivalent to an axial (vertical) displacement of the probe of 0.5 mm.

2.3. Experimental set-up

High-frequency imaging system and acquisition protocol

To allow computing elastograms of the carotid wall and of the excised kidney, a high-resolution ultrasound biomicroscope with access to the RF data (Vevo 660, Visualsonics, Toronto, Canada) was required. The Vevo 660 (Fig. 1c) is equipped with an encapsulated oscillating element transducer. A 40 MHz central frequency probe (f-number = 2, diameter = 3 mm, focal length = 6 mm and bandwidth at –6 dB = 110 %) was used for the carotid artery scanning, whereas a 20 MHz central frequency probe (f-number = 2, diameter = 3 mm, focal length = 15 mm and bandwidth at –6 dB = 110 %) was used for the kidney. The frame rate was 30 images/s in both cases. The RF signals were digitized with an acquisition board (Gagescope, model 8500 CS, Montreal, QC, Canada) installed in a personal computer. The sampling frequency was 500 MHz in an 8-bit format.

Data pre- and post-processing

The data pre-processing is described in details elsewhere [25]. The elastograms were computed by considering all pairs of consecutive RF images that were digitized, typically 8 RF images per data set. Each elastogram was post-processed using a 1×1 pixel kernel Gaussian-filter to smooth the visual appearance of all images. Regarding the carotid artery elastograms, manual segmentation was performed to display only the strain patterns within the vessel wall.

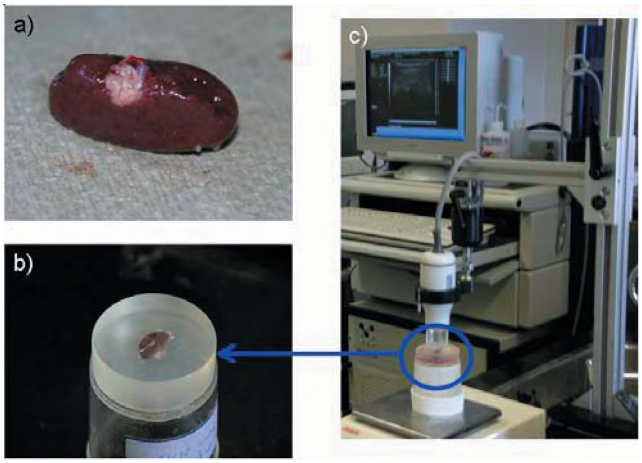

Fig. 1. a) Picture of the RI rat's fresh excised kidney. b) The kidney was immersed in a gelatin-agar mixture. c) Complete picture of the experimental set-up, including the Visualsonics Vevo 660.

3. METHODS

3.1. The Lagrangian speckle model estimator (LSME)

The Lagrangian speckle model estimator (LSME) is a 2D model-based estimator that allows computing the complete 2D-deformation matrix [19], given as:

$$\Delta = \begin{bmatrix} \frac{\partial U_x}{\partial x} & \frac{\partial U_x}{\partial y} \\ \frac{\partial U_r}{\partial x} & \frac{\partial U_r}{\partial y} \end{bmatrix}. \qquad (1)$$

In this equation, U_y and U_x are the axial and lateral displacement fields, respectively. The four components of Δ, in this specific Cartesian coordinates formulation, are Δ_{yy}, Δ_{yx},

Δ_{xx}, and Δ_{xy}, being the axial strain and shear, and the lateral strain and shear, respectively. The map of the distribution of each component of Δ (Δ_{ij}) provides a specific elastogram. It is also worth mentioning that Δ relates the strain tensor ε through the following equation:

$$\varepsilon_{ij}(t) = \frac{1}{2}\left[\Delta_{ij}(t) + \Delta_{ji}(t)\right]. \quad (2)$$

On the other hand, due to the limited lateral resolution of the current ultrasound scanners, axial motion parameters are more accurate. For the purpose of these studies, only the axial strain component ε_{yy} (= Δ_{yy}) was then used to image tissue mechanical properties.

3.2. Implementation of the LSME

To provide distribution of local strains within the region of interest (ROI), the LSME requires subdividing the RF data into several partitions (also known as measurement-windows), for which motion can be assumed as affine [26]. The parameter ε_{yy} was assessed for each partition using the optical flow-based implementation of the LSME [25]. The map of the distribution of ε_{yy} inside each ROI is defined as the elastogram. Each measurement-window was set at 108 µm axially by 312 µm laterally (80 samples × 20 RF lines) with 90 % axial and lateral overlaps. Regarding carotid arteries, comparisons between the BN and SHR were proceeded according to the maximum strain calculated from elastograms computed during the diastolic phase of the cardiac cycle (CC).

4. RESULTS

4.1. BN and SHR carotid artery data

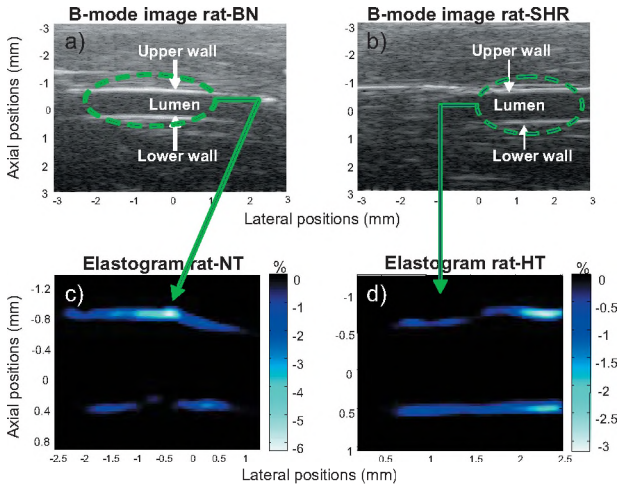

Fig. 2. a) and b) display B-mode images of BN and SHR's carotid arteries, respectively. c) and d) are elastograms computed from BN and SHR's carotid RF data, respectively.

The colorbar (in percent) gives the strain and indicates that the SHR's carotid artery is stiffer than that of BN's.

Elastograms were computed for each pair of successive RF images acquired from the SHR's and from the BN's common carotid arteries, typically over one CC. In most cases, it was difficult to have complete longitudinal sections of the artery, consequently only portions of the carotids are displayed on the B-mode images and on the elastograms. Figs 2a and 2b show two B-mode images obtained for one BN and one SHR, respectively. In both cases, the internal diameter of the carotid was around 1 mm, whereas the wall thicknesses were close to 200 µm. Figs 2c and 2d show two elastograms, computed for the BN and the SHR, respectively. The colorbar gives the strain in percent. The negative strain (ε_{yy}) values are indicative of vessel wall dilation (diastolic phase), i.e. lumen area reduction. It is shown that the BN's carotid deforms more than that of the SHR even though the systolic blood pressure (SBP) were higher. In other words, SHRs' arterial walls were, on average, stiffer than that of BN rats.

	SBP (mmHg)	HR (BPM)	S (%)
BN	80 ± 2	316 ± 19	6.76 ± 1.48
SHR	161 ± 12	354 ± 31	4.46 ± 1.79
Values of *p*	< 0.001	= 0.052	= 0.059

TABLE 1. Comparisons between SHR and BN. The SBP, HR and strains (S = ε_{yy}) were measured at 15-weeks old. S dictates that the SHR's carotid artery was 1.5 times stiffer than BN's one (p = 0.059), whereas the systolic blood pressure (SBP) of the SHR was twice higher than that of the BN (p < 0.001).

Table 1 summarizes the comparison between BN (n = 5) and SHR (n = 5) at 15-weeks old (the statistics were obtained with unpaired t-tests). Although the SBP of the SHR was twice that of the BN (p < 0.001), the strain (S) of the SHR's carotid artery was, on average, close to 50% less than BN's one (p = 0.059), which is indicative of stiffer arteries. The HR of the SHR was, on average, 12% higher than that of BN (p = 0.052).

4.2. RI's kidney data

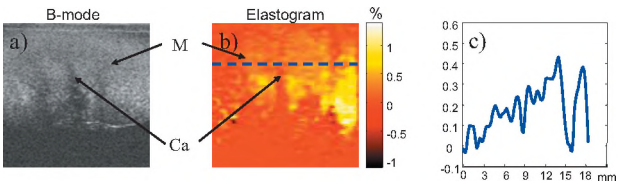

Fig. 3. a) B-mode image of a longitudinal section of the RI's kidney. b) Elastogram of the kidney clearly exhibiting the medulla (denoted M) with specific mechanical properties compared to calyces (denoted Ca). c) Strain plot traced from the elastogram (dotted blue line). The colorbar gives the strain in percent.

Fig. 3a displays a B-mode image acquired from a longitudinal section of the RI's kidney, whereas Fig. 3b shows an elastogram. The kidney medulla is clearly identified with

distinct mechanical properties. Fig. 3c reports a plot of strain values from the elastogram that shows 0.1 % to 0.4 % strain in the medulla. The ascending slope profile of the strain plot is explained in the discussion section.

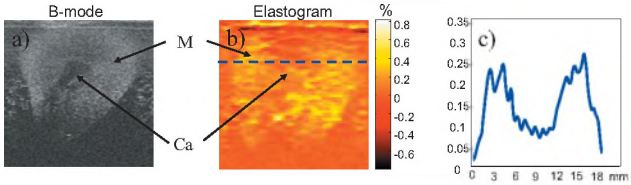

Fig. 4. a) B-mode image of a transverse section of the RI's kidney. b) Elastogram of the kidney clearly exhibiting the presence of the medulla (denoted M) surrounding the calyces (denoted Ca). c) Strain plot traced from the elastogram (dotted blue line). The colorbar gives the strain in percent.

Fig. 4a displays a B-mode image acquired from a transverse section of the RI's kidney, whereas Fig. 4b shows an elastogram. The presence of the medulla surrounding the calyces is clearly observed. Fig. 4c plots strain values from the elastogram. In this case, the medulla is clearly identified with around 0.25 % strain compared to calyces with a lower strain of 0.1%.

5. DISCUSSION

5.1. About the strain estimation

This paper has reported feasibility studies of MicroNIVE and MicroNIKE that propose to phenotype rat models of hypertension using the carotid artery and the kidney mechanical properties, respectively. The proposed ultrasound elastography techniques take advantage of high-resolution radio-frequency (RF) data.

5.2. About MicroNIVE data

An important result of this study was the quantitative observation that normotensive BN's carotid artery at 15-weeks old was, on average, softer than SHR's at the same age (p = 0.059). Interestingly, similar results were observed for the common carotid artery by Lichtenstein *et al.* [27] who compared, under static transmural pressures, SHR with normotensive Wistar-Kioto (WKY) rats. On the other hand, strain (ε_{yy}) is a relative measure that primarily depends on the pressure gradient ($\Delta P \equiv$ systolic pressure - diastolic pressure, in this case) and on the tissue stiffness. To provide an absolute and more robust characterization parameter of the vessel wall, ε_{yy} can be normalized with ΔP to estimate the elastic modulus. In the case where the pressure monitoring system would not allow appropriately measuring ΔP, another option could be to normalize the strain with respect to the heart rate and the imaging system frame rate, since they both may have influence on the elastographic measurement process. These options will both be of interest in further investigations.

Unfortunately, the relatively low frame rate of the RF data acquisition system (Vevo 660) constituted a drawback of the current study. Indeed, the higher the frame rate, the more correlated are the RF images within a sequence, improving the strain estimation. Additionally, the higher the frame rate, the shorter is the time elapsed between successive RF images within the time-sequence data set, and thus the lower will be the strain estimates. This also explains high strain values (up to 6.76%) computed for the carotid arteries with MicroNIVE in this study. It is important to note that the new Vevo 770 ultrasound system, commercialized by Visualsonics, now provides up to 120 images/s (full field of view) to 240 images/s (zoomed view).

5.3. About MicroNIKE data

In vitro preliminary data on a fresh excised kidney clearly allowed identifying the medulla with specific quantitative mechanical properties. An ascending slope profile was observed in Fig. 3c for the longitudinal elastogram. This artifact results from the application of a non uniform external stress to compress the kidney. On the other hand, the transversal elastogram allowed artifact-free images and the identification of the medulla with around 0.25 % strain. Whereas we are aware that the application of external compression could be tedious in vivo, namely due to the presence of fatty tissue located between the skin and the kidney, these results give confidence in the potential of MicroNIKE to phenotype rat models of hypertension using kidney's mechanical properties. Furthermore, in future experiments, it would be of interest to monitor the external applied stress to enable elastic modulus assessments that are known to be more appropriate than strains to characterize biological soft tissues.

6. CONCLUSION

This paper has addressed the feasibility of using the vessel wall (MicroNIVE) and the kidney (MicroNIKE) mechanical properties as potential phenotypes of hypertension in rat models. In the case of MicroNIVE, *in vivo* data were reported on SHR and BN rats showing SHRs' carotid arteries stiffer than that of BN at 15-weeks old. Regarding MicroNIKE, *ex vivo* data on an RI's excised kidney clearly demonstrated the potential of the method to identify and characterize different structures within this organ. In summary, combining novel *in vivo* imaging technologies with state of the art transgenic rodent models may represent unprecedented tools for gene identification in hypertension, which is part of our future investigations. The availability of MicroNIVE and MicroNIKE could lead to significant new discoveries in the fields of the pathophysiology and pharmacogenetics of hypertension.

7. ACKNOWLEDGEMENTS

This work was jointly supported by grants from the Réseau de

Recherche en Transgénèse du Québec, the Canadian Foundation for Innovation, the CardioGEN consortium of the Canadian Institutes of Health Research, and the Natural Sciences and Engineering Research Council of Canada (#312136-06). Dr Cloutier is recipient of the National Scientist award of the Fonds de la Recherche en Santé du Québec (FRSQ, 2004-2009). The salary of Dr Maurice is partially supported by a research scholarship award from FRSQ.

REFERENCES

[1] Joffres MR, Hamet P, Maclean DR, L'Italien GJ, Fodor G. Distribution of blood pressure and hypertension in Canada and the United States. *Am J Hypertension.* 2001;14:1099-1105.

[2] Ezzati M, Lopez AD, Rodgers A, Vander HS, Murray CJ. Selected major risk factors and global and regional burden of disease. *Lancet.* 2002;360(9343):1347-1360.

[3] Dutil J, Eliopoulos V, Tremblay J, Hamet P, Charron S, and Deng AY. Multiple quantitative trait loci for blood pressure interacting epistatically and additively on Dahl rat chromosome 2. *Hypertension.* 2005;45:557-564.

[4] Mulvany MJ. Modeling the vasculature: A judicious approach? Hypertension. 2005;46(4):652-653.

[5] Intengan HD, Schiffrin EL. Mechanical properties of mesenteric resistance arteries from Dahl salt-sensitive rats: Role of endothelin-1. *Journal of Hypertension.* 1998;16:1907-1912.

[6] LLoyd-Jones DM, Bloch KD. The vascular biology of nitric oxide and its role in atherogenesis. Ann Rev Med. 1996;47:365-375.

[7] Marin, R., Gorostidi, M., Fernandez-Vega, F., and Alvarez-Navascues, R., "Systemic and glomerular hypertension and progression of chronic renal disease: the dilemma of nephrosclerosis," Kidney Int.Suppl, no. 99, pp. S52-S56, Dec.2005.

[8] Zhao J, Day J, Yuan ZF, and Gregersen H. Regional artery stress-strain distributions referenced to the zero-stress state in the rat. *Am J Physiol Heart Circ Physiol.* 2002;282:H622-H629.

[9] Pravenec M and Kren V. Genetic analysis of complex cardiovascular traits in the spontaneously hypertensive rat. *Exp Physiol.* 2005;90(3):273-276.

[10] Dumas P, Sun Y, Corbeil G, Tremblay S, Pausova Z, Kren V, Krenova D, Pravenec M, Hamet P, and Tremblay J. Mapping of quantitative trait loci (QTL) of differential stress gene expression in rat recombinant inbred strains. *J Hypertension.* 2000;18(5):545-551.

[11] Hubner N, Wallace CA, Zimdahl H, Petretto E, Schulz H, Maciver F, Mueller M, Hummel O, Monti J, Zidek V, Musilova A, Kren V, Causton H, Game L, Born G, Schmidt S, Muller A, Cook SA, Kurtz TW, Whittaker J, Pravenec M, and Aitman TJ. Integrated transcriptional profiling and linkage analysis for identification of genes underlying disease. *Nat Genet.* 2005;37(3):243-253.

[12] Safar M. Arteries in Clinical Hypertension. *Lippincott – Raven Publishers.* 1996.

[13] Ophir J, Céspedes E I, Ponnekanti H, Yazdi Y, and Li X. Elastography: A quantitative method for imaging the elasticity in biological tissues. *Ultrasonic Imaging.* 1991;13(2):111-134.

[14] Garra BS, Céspedes EI, Ophir J, Spratt SR, Zuurbier RA, Magnant CM, and Pennanen MF. Elastography of breast lesions: Initial clinical results. *Radiology.* 1997;202(1):79-86.

[15] Lorenz A, Sommerfeld HJ, Garcia-Schurmann MG, Philippou S, Senge T, and Ermert H. A new system for the acquisition of ultrasonic multi-compression strain images of human prostate in vivo. *IEEE-Ultrasonics Ferroelectrics Frequency Control.* 1999;46(5):1147-1154.

[16] Pesavento A, Lorenz A, Siebers S, and Ermert H. New real-time strain imaging concepts using diagnostic ultrasound. *Phys Med Biol.* 2000;45:1423-1435.

[17] de Korte CL, Pasterkamp G, Van der Steen AFW, Woutman HA, and Bom N. Characterization of plaque components with intravascular ultrasound elastography in human femoral and coronary arteries in vitro. *Circulation.* 2000;102(6):617-623.

[18] de Korte CL, Van der Steen AFW, Céspedes EI, Pasterkamp G, Carlier SG, Mastik F, Schoneveld AH, Serruys PW, and Bom N. Characterization of plaque components and vulnerability with intravascular ultrasound elastography. *Physics in Medicine & Biology.* 2000;45(6):1465-1475.

[19] Maurice RL, Ohayon J, Finet G and Cloutier G. Adapting the Lagrangian Speckle Model Estimator for Endovascular Elastography: Theory and Validation with Simulated Radio-Frequency data. *JASA.* 2004;116(2): 1276-1286.

[20] Maurice RL, Brusseau É, Finet G, Cloutier G. On the potential of the Lagrangian speckle model estimator to characterize atherosclerotic plaques in endovascular elastography: In vitro experiments using an excised human carotid artery. *Ultrasound Med & Biology.* 2005;31:85-91.

[21] Maurice RL, Fromageau J, Brusseau É, Finet G and Cloutier G. On the Potential of the Lagrangian Speckle Model Estimator for Endovascular Elastography : In vivo Human Coronary Study. *Ultrasound in Medicine & Biology.* 2007 (in press).

[22] Bang J, Dahl T, Bruinsma A, Kaspersen JH, Hernes TAN, and Myhre HO. A new method for analysis of motion of carotid plaques from RF ultrasound images. *Ultrasound in Med & Biol.* 2003;29(7):967-976.

[23] Mai JJ, Insana M. Strain imaging of internal deformation. *Ultrasound in Med & Biol.* 2002;28(11/12):1475-1484.

[24] Maurice RL, Ohayon J, Frétigny Y, Bertrand M, Soulez G, and Cloutier G. Non-invasive vascular elastography: Theoretical framework. *IEEE Trans on Med Imaging.* 2004;23(2):164-180.

[25] Maurice RL, Daronat M, Ohayon J, Stoyanova É, Foster SF, and Cloutier G. Non-invasive high-frequency vascular ultrasound elastography. Physics in Medicine & Biology. 2005;50:1611-1628.

[26] Maurice RL and Bertrand M. Lagrangian speckle model and tissue-motion estimation – Theory. IEEE Trans on Med Imaging. 1999;18(7):593-603.

[27] Lichtenstein O, Safar ME, Mathieu E, Poitevin P, and Levy BL. Static and dynamic mechanical properties of the carotid artery from normotensive and hypertensive rats. *Hypertension.* 1998;32:346-350.

Lumbar Mechanics From Ultrasound Imaging

Geoffrey Desmoulin and Theodore Milner
School of Kinesiology, Simon Fraser University, 8888University Drive, Burnaby, B.C. Canada V5A 1S6
E-mail: geoffd@wayne.edu

ABSTRACT

The feasibility of estimating lumbar mechanics in-vivo was evaluated using ultrasound imaging. Images were obtained while subjects were seated, with the pelvis fixed, and pulled on an anchored cable by isometrically contracting trunk muscles at different force levels. Linear regression analysis was used to identify ultrasound measurements which were correlated with trunk force. Results suggest that ultrasound is more suitable for estimating lumbar mechanics during lateral flexion than extension of the trunk. A linear trend was found between changes in thickness of some muscles and trunk force, which could provide an alternative to invasive intramuscular electrodes for measuring the activity of non-superficial muscles. A significant limitation, however, is that the magnitude of the changes were frequently very close to the ultrasound resolution.

SOMMAIRE

La possibilité d'estimer la mécanique lombaire in-vivo a été évaluée par imagerie ultrasonique. Les images ont été obtenues, alors que le patient était assis, le bassin fixé, et étiré au moyen d'un câble, contractant isométriquement les muscles du tronc à différents niveaux de force. Une régression linéaire a été utilisée pour identifier les mesures d'ultrasons corrélées avec la force du tronc. Les résultats suggèrent que les ultrasons sont mieux adaptés à l'estimation de la mécanique lombaire durant une flexion latérale que pendant une extension du tronc. Une relation linéaire a été trouvée entre les changements d'épaisseur de certains muscles et la force du tronc, ce qui pourrait fournir une alternative aux électrodes intramusculaires invasives utilisées pour mesurer l'activité des muscles non-superficiels. Cependant, l'amplitude des changements, fréquemment très proche de la résolution ultrasonique, représente une limitation significative.

1. INTRODUCTION

Images of muscle can be obtained using B-mode or real-time ultrasound scanning techniques. Normal muscle parenchyma appears as a homogeneous echogenic matrix separated internally by hyperechogenic fascial planes (Fischer et al. 1988; Cady et al. 1983). Muscle fibers themselves generate few echoes because of their highly regular internal structure (Heckmatt and Dubowitz 1988; Ferrel et al. 1989; Walker et al. 1990) which does not reflect sound well. Furthermore, muscle fibers conduct sound anisotropically. Typically, it has been difficult to obtain images of muscles that lie over one another. As technology has evolved, this has become less of a problem but still remains a challenge in deeper structures, such as the psoas or paraspinal complexes (Walker et al. 2004).

Because most architectural parameters change with muscle contraction, ultrasonography may be used as a non-invasive method to detect or measure activity of specific muscles during isometric contractions. Ultrasound has been routinely used to estimate the cross-sectional area of muscles for clinical purposes such as the identification of dystrophic muscle (Heckmatt et al. 1988), the wasting of lumbar muscle in patients with low back pain (Hide et al. 1994) and the function of respiratory muscles during dynamic pulmonary changes (McKenzie et al. 1994), but only recently has it been applied to investigating muscle mechanics.

The first published study using ultrasound to quantify muscle mechanical parameters was conducted by Rutherford and Jones (1992) and examined changes in the angle of pennation of the vastus lateralis and vastus intermedius muscles with extension of the knee during isometric contraction. Herbert and Gandevia (1995) conducted a similar study of the brachialis muscles in which they also investigated changes in pennation angle with elbow torque. Pennation angle has also been measured in isometrically contracting triceps surae (Kawakami et al. 1998) and tibialis anterior (Maganaris and Baltzopoulos 1999) muscles. Changes in fascicle length of the gastrocnemius (Narici et al. 1996; Maganaris et al. 1998) and soleus (Maganaris et al. 1998) have also been measured during isometric contraction. Ultrasound has also been used for in vivo measurements of changes in tendon length to estimate tendon stress and strain (Maganaris and Paul. 1999; Muraoka et al. 2002), as well as to estimate muscle moment arms (Maganaris 2000; Ito et al. 2000). While ultrasound imaging of the lower limb for in vivo characterization of muscle and tendon mechanics is becoming common-place, few ultrasound imaging studies have examined the paraspinal muscles in relation to lumbar mechanics.

The objective of this project was to test whether changes in the shape of lumbar muscles that can be measured from ultrasound images are correlated with changes in trunk force. Our hypothesis was that the pennation angle and thickness of contracting muscles would increase with trunk force.

2 METHODS

Ten subjects, 6 female and 4 male, participated in this study. These subjects were all in good physical condition between the ages of 18 and 45 and had no history of disabling lower back pain in the past two years. Ethics approval was obtained from both the University of British Columbia and Simon Fraser University's Research Ethics Review Committees.

2.1 Apparatus

The subject sat in an apparatus consisting of an octagonal frame constructed from sections of 2 inch aluminum tubing. The pelvis was restrained by hip pads so that trunk movement would only involve bending of the spine. The subject wore a chest harness to which a cable was attached. During the experiment, the subject pulled isometrically on the cable, which was anchored to the frame (Fig. 1), while observing the output of a force transducer, in series with the cable, on a computer screen. The force was displayed as a bar whose length varied in proportion to the force. The subject was instructed to match the length of a target bar displayed beside the force.

2.2 Data Acquisition

Two-dimensional ultrasound images of the key lumbar muscles were recorded unilaterally (right side) using a GE Medical Systems Voluson 730 ultrasound machine equipped with a 4 – 8 MHz software adjustable transducer (RAB4-8P). All measurements from ultrasound images were made with software calipers by a professional sonographer. The calipers are a set of cross hairs that can be positioned anywhere on the image. The sonographer positioned the calipers but was not provided with information about the measured values to reduce observer bias. The force signal was sampled at 2000 Hz and stored for later analysis.

Figure 1. Apparatus used to fix the pelvis and allow isometric trunk contraction such as extension (shown) and lateral flexion.

2.3 Protocol

Ultrasound images were obtained for 4 different transducer positions while subjects performed either isometric extension or lateral flexion of the trunk. Four contraction levels were compared: 0%, 10%, 25% and 50% of the subject's maximum voluntary contraction (MVC). Each contraction was repeated 3 times.

The transducer was first positioned to obtain an image in the sagittal plane to the right of the midline, at the tips of the L1 and L2 transverse processes. Three caliper measurements were made from this image: erector spinae diameter at L1, erector spinae diameter at L2 and pennation angle of a longissimus fascicle (Fig. 2). The transducer was next positioned to obtain a transverse scan of the erector spinae muscles at the level of L2. Two caliper measurements were made from this image: diameter of the erector spinae at facet joint and diameter of the erector spinae at the tip of the transverse process. Subjects performed both trunk extension and lateral flexion for the first two transducer positions. The transducer was then moved laterally to obtain an image of the quadratus lumborum in the transverse plane at the L3 level (Fig. 3). This image included the lateral tip of the L3 transverse process. Three caliper measurements were made from this image: distance from the quadratus lumborum to the skin, anterior-posterior (A-P) diameter of the quadratus lumborum and

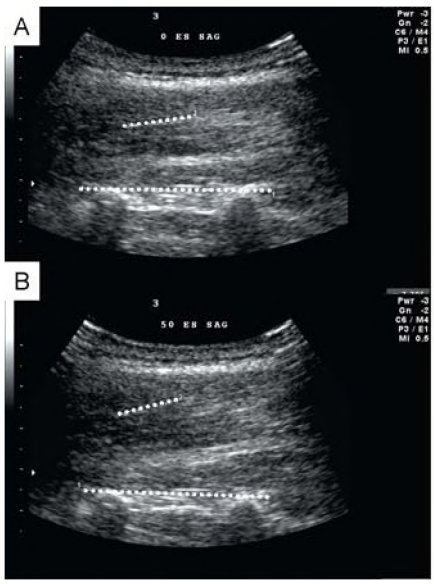

Figure 2 - B-mode ultrasound image of longissimus thoracis relaxed (A) and during exertion of 50% of maximal trunk extension force (B).

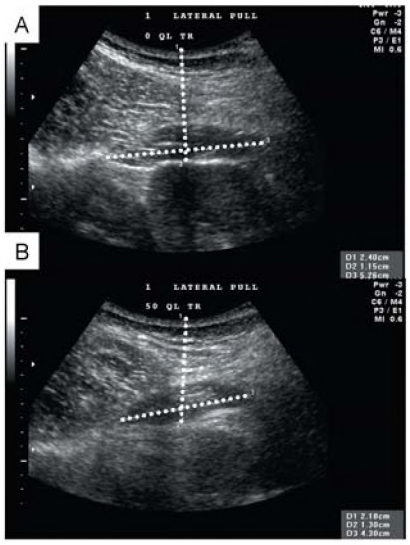

Figure 3 - B-mode ultrasound image of quadratus lumborum (right side) relaxed (A) and during exertion of 50% of maximal right lateral flexion force (B). Both images show the distance from the muscle to the skin (D1) A-P thickness (D2) and M-L thickness (D3).

medial-lateral (M-L) diameter of the quadratus lumborum. Finally, the transducer was placed at the iliac spine to obtain an image in the transverse plane, with the lower border of the transducer placed immediately superior to the iliac crest. This image included the three muscles of the abdominal group (external oblique, internal oblique and transversus abdominis). Measurements from this image were made in the M-L plane from a point located 2 cm to the right of the lateral tip of the transversus abdominis aponeurosis. The measurements included M-L diameter of the external oblique muscle, M-L diameter of the internal oblique muscle and M-L diameter of the transversus abdominis muscle. Subjects performed only lateral flexion for the last two transducer positions.

2.4 Statistical Analysis

Separate ultrasound images were obtained for each contraction (trial), providing 3 sets of measurements for each parameter. We used the coefficient of variation or CV (standard deviation/mean) of the repeated measurements of a given parameter as a measure of reliability. The CV is a useful statistic for comparing the degree of variation from one data series to another, even if the means are drastically different from each other. The ability of the ultrasound measurements to provide reliable information about a given anatomical feature was assessed from the mean coefficient of variation computed across all subjects. Linear regression was used to determine whether change in a particular parameter was correlated with trunk force. This was assessed from the R2 value. R2 is a measure of the ability of the chosen parameter to predict trunk force. R2 performs this by giving the ratio between the sum of squares (SS) of the regression line and the SS of the data points on a scale from 0 to 1. The closer R2 is to 1 the better the parameter is at predicting trunk force. The slope of the linear regression was also tested for statistical significance ($p<0.05$).

3 RESULTS

3.1 Ultrasound Images - Descriptive Statistics

The mean of the coefficients of variation for the three repeated measurements (trials) for the 10 subjects are listed in Tables 1 and 2. The least reliable parameters for lateral flexion were the longissimus thoracis pennation angle and the transversus abdominis diameter, with average coefficients of variation (CV) of approximately 0.14. The most reliable parameters were the longissimus thoracis at L1 diameter, longissimus thoracis at L2 diameter, erector spinae - lateral diameter and quadratus lumborum – distance from skin, all with an average CV of approximately 0.04. Similarly, for extension the longissimus thoracis pennation angle had the largest average CV (0.14), whereas the longissimus thoracis at L1 diameter, longissimus thoracis at L2 diameter and erector spinae - lateral diameter had the smallest average CV (0.04).

The mean coefficient of variation of the parameter values averaged across all force levels for the entire subject group were calculated. As with the repeated measurements, the longissimus thoracis pennation angle was the least reliable parameter for lateral flexion with an average CV of 0.34. However, the CV of most other parameters was also high, indicating that variability across subjects was greater than the variability of repeated measurements. The most reliable parameters across subjects were the erector spinae lateral and longissimus thoracis at L2 diameters with an average CV of 0.14. As in the case of the repeated measurements, the least reliable parameter for extension was the longissimus thoracis pennation angle with a CV of 0.27 whereas the longissimus thoracis at

Structure	Parameter	Coefficient of Variation
Longissimus thoracis	Pennation angle	0.14
Longissimus thoracis	Diameter at L1	0.04
Longissimus thoracis	Diameter at L2	0.04
Erector spinae	Diameter – Medial[1]	0.05
Erector spinae	Diameter – Lateral[2]	0.04
Quadratus lumborum	Distance from Skin[3]	0.08
Quadratus lumborum	Diameter – ML[4]	0.06
Quadratus lumborum	Diameter – AP[5]	0.06
External oblique	Diameter	0.08
Internal oblique	Diameter	0.08
Transversus abdominis	Diameter	0.14

Table 1 - Mean coefficients of variation for repeated measurements in lateral flexion (N=10)

Structure	Parameter	Coefficient of Variation
Longissimus thoracis	Pennation angle	0.14
Longissimus thoracis	Diameter at L1	0.04
Longissimus thoracis	Diameter at L2	0.04
Erector spinae	Diameter – Medial[1]	0.05
Erector spinae	Diameter – Lateral[2]	0.04

[1]Diameter measured at facet
[2]Diameter measured at tip of L2 transverse process
[3]Distance from skin to posterior plane of quadratus lumborum
[4]Diameter of quadratus lumborum in medial-lateral plane
[5]Diameter of quadratus lumborum in anterior-posterior plane

Table 2 - Mean coefficients of variation for repeated measurements in extension (N=10)

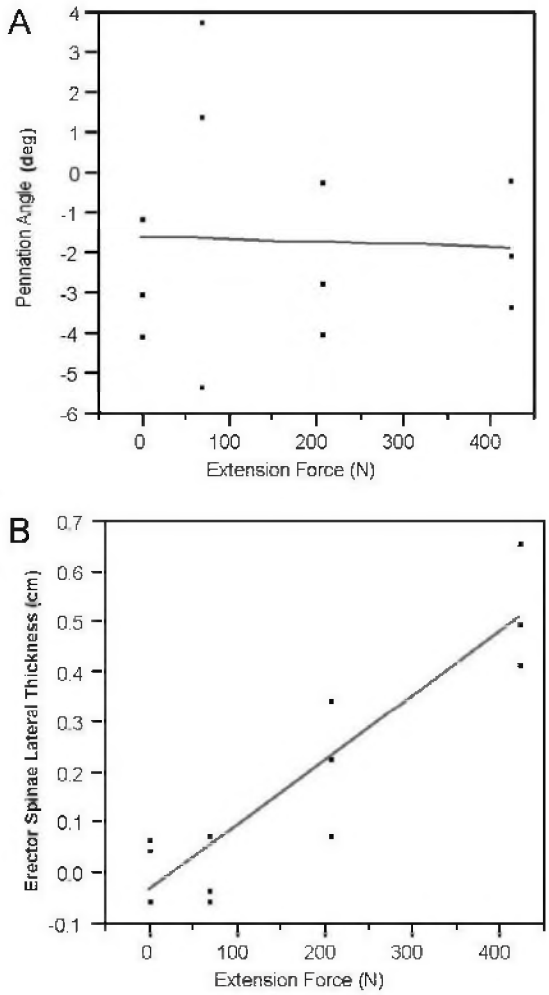

Figure 4 - Scatter plots of the ultrasound parameter with the lowest (A - longissimus thoracis – pennation angle) and the highest (B - erector spinae - lateral) correlation with trunk force in extension from one subject. (Normalized to 10% MVC).

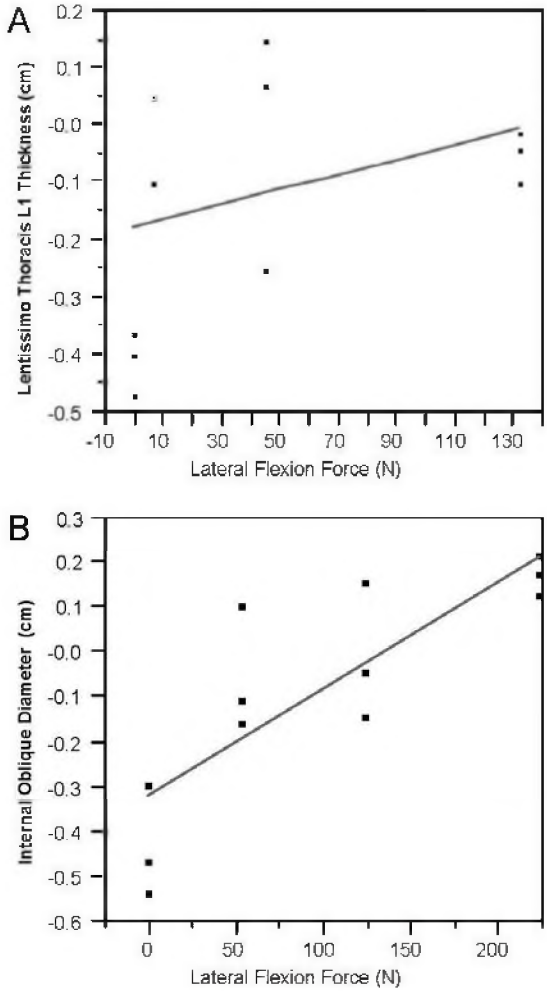

Figure 5 - Scatter plot of the ultrasound parameter with the lowest (A - longissimus thoracis – L1) and the highest (B - internal oblique diameter) correlation with trunk force in lateral flexion from one subject. (Normalized to 10% MVC).

L2 diameter again had the smallest CV (0.14).

3.2 Linear Regression Analysis

Linear regression analysis was conducted to determine the correlation between measured parameters and trunk force. To reduce the effect of anthropometric differences among subjects, the data for each subject were normalized by dividing parameter values by their average value at 10% MVC. Scatter plots for the parameters with the lowest and highest correlations are shown in Figs. 4 and 5 for lateral flexion and extension, respectively. Table 3 summarizes the results of linear regressions performed on the individual subject data. The heading "Significant" indicates the number of subjects for which the slope of the linear regression was significantly different from zero ($p<0.05$).

We found that the erector spinae lateral thickness was the best predictor of trunk extension force (average R2 = 0.60) and that the internal oblique diameter was the best predictor of lateral flexion force (average R2 = 0.68). Longissimus thoracis pennation angle was least correlated with trunk extension force (average R2 = 0.17) and longissimus thoracis thickness at L1 was least correlated with lateral flexion force (average R2 = 0.16).

Table 3 also indicates characteristic differences in the variability of different parameters. For example, in extension longissimus thoracis thickness at L2 and erector spinae medial have similar average R2, indicating that the spread of data points around the regression line is similar in both measurements. However, the average p-values are 0.14 (longissimus thoracis L2 thickness) and 0.037 (erector spinae medial thickness), indicating that the relationship between force and muscle thickness is much stronger for the medial measurement. Further, the standard deviation of the p-value for the longissimus thoracis thickness at L2 was relatively large (0.30), indicative of an unreliable measurement.

A second linear regression analysis was performed using the

Extension	LT-Pennation	LT - L1	LT - L2	ES-Medial	ES-Lateral	QL- Skin	QL-AP	QL-ML	EO	IO	TA
Significant[1]	2	6	8	7	8						
Intercept	-0.004	-0.040	-0.096	-0.083	-0.140						
Slope	0.012	0.0008	0.001	0.0009	0.002						
R^2	0.17	0.34	0.41	0.43	0.60						
P-value	0.35	0.25	0.14	0.037	0.013						
Lateral Flexion											
Significant[1]	3	1	2	2	5	4	4	4	7	10	6
Intercept	-0.026	-0.026	0.016	0.021	-0.065	-0.012	-0.032	-0.153	-0.081	-0.251	-0.044
Slope	0.017	0.0007	0.0009	0.0009	0.001	0.0006	0.00	0.002	0.001	0.003	0.0009
R^2	0.24	0.16	0.17	0.21	0.32	0.18	0.30	0.251	0.41	0.68	0.42
P-value	0.26	0.24	0.32	0.21	0.24	0.37	0.30	0.32	0.076	0.0030	0.13

Table 3 - Mean linear regression intercepts, slopes, R2 values and significance levels for individual subject data (N=10)

Extension	LT-Pennation	LT - L1	LT - L2	ES-Medial	ES-Lateral	QL- Skin	QL-AP	QL-ML	EO	IO	TA
Intercept	0.195	-0.059	-0.086	-0.071	-0.095						
Slope	0.003	0.0009	0.0009	0.0007	0.001						
R^2	0.047	0.45	0.41	0.56	0.48						
P-value	0.18	<0.0001	<0.0001	<0.0001	<0.0001						
Lateral Flexion											
Intercept	0.498	-0.031	0.022	0.016	-0.072	-0.043	-0.054	-0.189	-0.072	-0.187	-0.026
Slope	0.001	0.00006	0.0002	0.00008	0.001	0.0003	0.0008	0.0009	0.001	0.003	0.0008
R^2	0.001	0.001	0.017	0.0030	0.23	0.018	0.20	0.070	0.49	0.61	0.48
P-value	0.79	0.84	0.42	0.74	0.002	0.41	0.004	0.097	<0.0001	<0.0001	<0.0001

LT (longissimus thoracis), ES (erector spinae), QL (quadratus lumborum), EO (external oblique), IO (internal oblique), TA (transversus abdominis)
Parameters are defined in Table 1 (columns in Tables 3 and 4 correspond to rows in Table 1)
[1]Number of subjects for which the slope of the linear regression was significantly different from zero ($p<0.05$).

Table 4 - Linear regression intercepts, slopes, R2 values and significance levels for combined data from all subjects (N=10)

same data averaged over all subjects. As before, in order to reduce the effect of individual differences in resting anatomy the data for each subject were first normalized by the average value at 10% MVC. Figures 6 and 7 show scatter plots for the parameters which were best and least correlated with trunk force. We expected all of the muscle parameters being measured in the extension condition to be significantly correlated with trunk extension force since the measured parameters were selected to quantify changes in muscle geometry that occurred during contraction of the erector spinae muscles. Indeed, in contrast to the individual subject data, when averaged across subjects significant relations were found between all parameters and extension force ($p<0.0001$), with the exception of pennation angle (Table 4).

Since lateral flexion was not the primary function of most of the muscles that could be examined we did not expect many of the parameters to be significantly correlated with lateral flexion force. Nevertheless, the erector spinae lateral thickness ($p=0.002$), quadratus lumborum – anterior/posterior thickness ($p=0.004$), external oblique thickness ($p<0.0001$), internal oblique thickness ($p<0.0001$) and the transversus abdominis thickness ($p<0.0001$) were all significantly correlated with lateral flexion force, although the quadratus lumborum - medial/lateral diameter and quadratus lumborum – distance to skin and most of parameters measured from the erector spinae muscles were not significantly correlated with lateral flexion force.

4 DISCUSSION

In general, the relations between muscle thickness and trunk force were statistically significant. However, the correlation coefficients were generally low suggesting that changes in the shape of muscles at the lumbar level do not provide a good indication of the force being produced by the trunk muscles. Furthermore, pennation angle did not change significantly with trunk force. This is in marked contrast to studies measuring pennation angle in muscles surrounding the ankle and the elbow (Herbert and Gandevia 1995; Narici et al. 1996; Maganaris et al. 1998; Ito et al., 1998; Maganaris and Baltzopoulos 1999; Hodges et al. 2003). However, changes in pennation angle from rest to MVC can be very small, depending on the joint angle. In particular, Ito et al. (1998) and Maganaris and Baltzopoulos (1999) showed that changes in pennation angle of the tibialis anterior can be as small as 2 deg. Since the

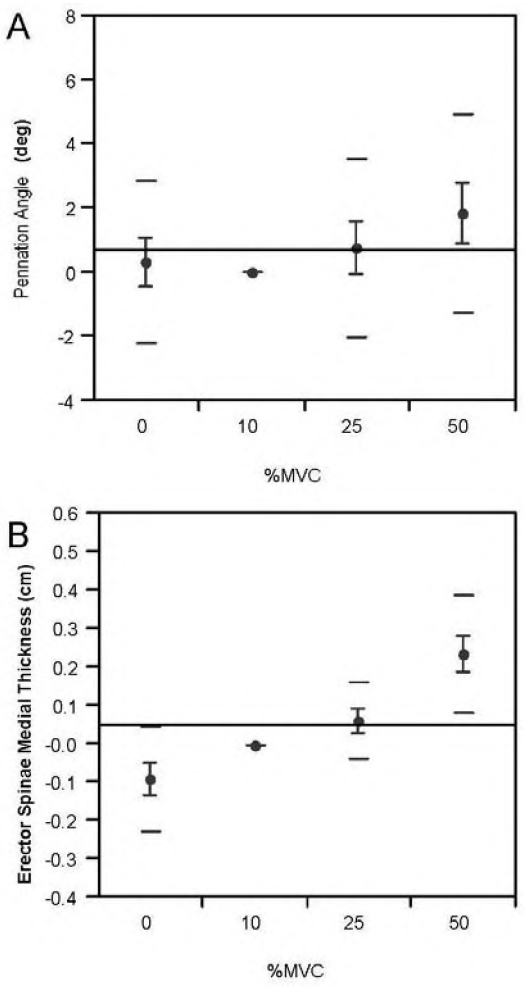

Figure 6 - Mean (dot), ±1 standard error (solid bar) and ±1 standard deviation (broken bar) for scatter plot of the ultrasound parameter with the lowest (A - longissimus thoracis – pennation angle) and highest (B - erector spinae – medial) correlation with trunk force in extension averaged over 10 subjects. (Normalized to 10% MVC).

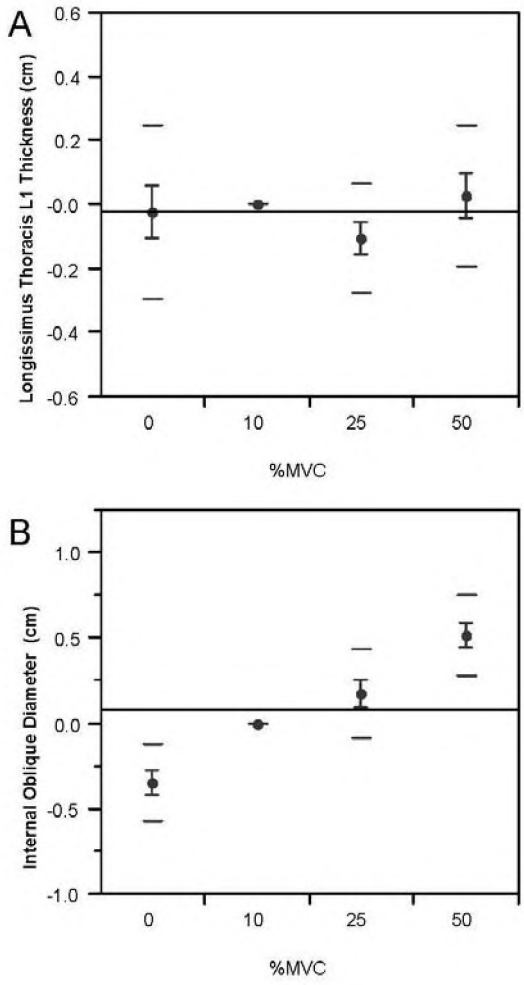

Figure 7 - Mean (dot), ±1 standard error (solid bar) and ±1 standard deviation (broken bar) for scatter plot of the ultrasound parameter with the lowest (A - longissimus thoracis – L1) and highest (B - internal oblique diameter) correlation with trunk force in lateral flexion averaged over 10 subjects. (Normalized to 10% MVC).

resting fascicle length of the longissimus thoracis (Delp et al. 2001) is about twice that of the tibialis anterior, even smaller changes in the pennation angle from rest to 50% MVC could be expected than for tibialis anterior. We observed that the orientation of the trunk changed slightly with increasing trunk force, particularly from rest. Therefore, changes in the muscle length due to changes in the angle or curvature of the spine may have obscured any systematic change in pennation angle with trunk force.

Further, the results of the descriptive statistics and the linear regression analysis showed that our CV values were larger and our R2 values for the linear regressions were lower than CV's and R2 values of similar studies of the lower limb (Rutherford et al. 1992; Narici et al. 1996; Fukunaga et al. 1997; Kawakami et al. 1998; Maganaris et al. 1998; Maganaris et al. 1999; Muramatsu et al. 2002). This indicates greater variance in our data, which was likely due to several factors. For example, compliance in the chest harness, the cable and the soft tissues of the torso allowed the trunk angle to change for different force levels. However, even if it had been possible to prevent the trunk angle from changing, the curvature of the spine might still have changed with increasing force. Changes to the geometry of the spine with trunk force could alter the muscle moment arms and, hence, change the relation between muscle force and trunk force.

Hodges et al. (2003) discuss other factors that can reduce the correlation between muscle shape changes and activation. In particular, muscle deformation varies due to variations in the pressure applied to the skin by the transducer, pressure applied by neighbouring active muscles and changes in internal pressure of the abdominal cavity. Although we attempted to minimize the effects of these sources of variability by having the sonographer try to apply a consistent amount of pressure to the transducer on all trials and by instructing the subjects not to breathe during the scan, we could not completely eliminate them.

The study of Hodges et al. (2003) is the only previously published study investigating contraction of trunk muscles with ultrasound images. Although they examined three of the same muscles as we did, namely the external oblique, internal oblique and transversus abdominis, they performed the scans from the anterior rather than the latero-posterior surface of the body, i.e., they obtained images of the muscles from the front rather than from the side of the body. Furthermore, they had the subjects perform isolated contractions of the abdominal wall, whereas our subjects performed isometric lateral flexion of the entire trunk. Hence, the task performed by their subjects was entirely different so the two experiments are not directly comparable. Hodges et al. (2003) reported that the thickness of the external oblique muscle was not strongly correlated with contraction level of the abdominal wall (R=0.23). In contrast, we found that the thickness of the external oblique was relatively highly correlated with trunk force (R=0.70 for mean subject data).

A recent study in which EMG of external oblique, internal oblique and extensor muscles of the trunk was recorded found that external oblique is maximally activated during lateral flexion and multifidus during extension (Ng et al. 2002). None of the other muscles were maximally activated in these force directions. This would correspond to the relatively strong correlation of external oblique thickness with trunk force during lateral flexion. We were unable to obtain clear images of multifidus due to its proximity to the vertebrae so we could not confirm a similar relation for extension. Thickness of the erector spinae muscles, including the longissimus thoracis muscle may have been affected by similar factors to those discussed for pennation angle. In addition, Watanabe et al. (2004) have shown that the thickness of erector spinae muscles increases with trunk extension angle. As well, it is more difficult to distinguish the boundaries of erector spinae muscles than the muscles of the abdominal wall which are more echogenic because of the surrounding aponeuroses. Thus, measurements tended to be less accurate for erector spinae muscles, introducing variability.

Analysis of the individual subject data showed that none of the three parameters for the quadratus lumborum were correlated with lateral flexion force, although averaged across all subjects the quadratus lumborum – anterior/posterior thickness was significantly correlated. The quadratus lumborum originates from the iliolumbar ligament, the transverse processes of the lumbar vertebrae and the twelfth rib and inserts on the posterior portion of the iliac crest. These lines of action would act to extend and laterally flex the torso as in our protocol. However, our measurements do not indicate this as they did not correlate strongly with either trunk extension or lateral flexion force. Andersson et al. (1996) showed that the quadratus lumborum is active for both dynamic trunk extension and lateral flexion activities, although these results cannot be strictly compared to the results of our study as our protocol involved isometric versions of these actions. McGill et al. (1996) showed that for lifting tasks the quadratus lumborum was activated to 74% of its MVC, on average. The same study also showed that for isometric side support postures where the body is held horizontally, almost parallel to the ground as the subjects supported themselves on one elbow and both feet, the quadratus lumborum was on average activated to 54% of its MVC. However, both studies did comment that even though the quadratus lumborum was generally active during extension and lateral flexion its activity depended on the specificity of the tasks. Although there is some evidence for contraction of the quadratus lumborum during the period of isometric lateral flexion, the results are equivocal. One explanation may lie in the ultrasound measurement itself. Figure 3 clearly shows that the lateral border of the muscle is not as echogenic as the rest of the cross section of the muscle. This is a function of the angle of incidence of the ultrasound beam. When the transducer angle is altered the image of the lateral border improves. However, the medial border no longer reflects with intensity strong enough to be seen. Hence, it was not possible to obtain an ideal image of quadratus lumborum for measuring shape changes.

Our calibration tests with the RAB4-8P ultrasound probe indicate that the resolution for measurements in the axial and lateral planes are about 1 mm and 2 mm, respectively. Therefore, in order to make reliable caliper measurements, changes in features being analyzed should be at least 1 mm for axial (along the direction of beam penetration) measurements and at least 2 mm for lateral measurements (along the direction of the beam scan). The mean changes from 0% to 50% MVC for axial measurements during lateral flexion were greater than 1 mm only for ES-Lateral, EO, IO and TA. As might be expected, the parameters with the largest changes from 0% to 50% MVC produced the highest correlations with trunk force. The single parameter that was measured in the plane of the beam scan was QL-ML, which had a mean change of 2 mm and was also significantly related to trunk force. In the case of trunk extension, the average change in all of the parameters measured in the axial plane was at least 1 mm and as such, they were all highly related to trunk force. Mean changes in pennation angle for both extension and lateral flexion were 1.6 and 0.9 deg, respectively. It is difficult to determine whether or not this is large enough to detect changes. However, it should be noted that the measurements (Fig. 2) were made in the plane of the beam scan where the resolution is worst, which likely contributed to our inability to detect systematic changes with trunk force.

In conclusion, ultrasound measurements were better correlated with parameters of lumbar mechanics during isometric lateral flexion than extension of the trunk. There was a statistically significant linear trend between change in muscle thickness and trunk force, although the correlation coefficients were generally low. This may have been partly due to the fact that changes in many parameters were below or near the limits of the resolution of measurements from ultrasound images. Although further research is required, findings indicate that muscle thickness measured by ultrasound may be used as a substitute for electromyography in estimating

the activity of some muscles during isometric contraction. This would allow the invasive procedures required for intramuscular recording of deep muscles of the lower back to be avoided.

REFERENCES

Andersson EA, Oddsson LE, Grundstrom H, Nilsson J, Thorstensson A. (1996) EMG activities of the quadratus lumborum and erector spinae muscles during flexion-relaxation and other motor tasks. Clinical Biomechanics, 11(7), 392-400.

Cady EB, Gardner JE, Edwards RHT. (1983) Ultrasonic tissue characterisation of skeletal muscle. Eur J Clin Sci, 13, 469-473.

Delp SL, Survanaravanan S, Murray WM, Uhlir J, Triolo RJ. (2001) Architecture of the rectus abdominis, quadratus lumborum, and erector spinae. J Biomech, 34:371-375.

Ferrell WG, Crowe N, Walker FO, Donofrio PD, Williams D. (1989) Force/diameter relationships in human muscle: an EMG and sonographic study. Muscle Nerve, 12, 759.

Fischer AQ, Carpenter DW, Hartlage PL, Carroll JE, Stephens S. (1988) Muscle imaging in neuromuscular disease using computerized real-time sonography. Muscle Nerve, 11, 270-275.

Fukunaga T, Ichinose Y, Ito M, Kawakami Y, and Fukashiro S. (1997). Determination of fascicle length and pennation in a contracting human muscle in vivo. J Appl Physiol, 82, 354-8.

Heckmatt JZ, Dubowitz V. (1988) Realtime ultrasound imaging of muscles. Muscle Nerve, 11, 56-65.

Heckmatt JZ, Pier N, Dubowitz V. (1988) Real-time ultrasound imaging of muscles. Muscle Nerve, 11, 56-65.

Herbert RD. Gandevia SC. (1995) Changes in pennation with joint angle and muscle torque: in-vivo measurements in human brachialis muscle. J Physiol, 484:523-532.

Hide JA, Stokes MJ, Saide M, Jull GA, Cooper DH. (1994). Evidence of lumbar multifidus muscle wasting ipsilateral to symptoms in patients with acute/subacute low back pain. Spine, 19(2), 165-72.

Hodges PW, Pengel LHM, Herbert RD, Gandevia SC. (2003) Measurement of muscle contraction with ultrasound imaging. Muscle Nerve, 27, 682-692.

Ito M, Akima H, Fukunaga T. (2000) In vivo moment arm determination using B-mode ultrasonography. J Biomech 33(2), 215-218.

Ito M, Kawakami Y, Ichinose Y, Fukashiro S, Fukunaga T (1998) Nonisometric behaviour of fascicles during isometric contractions of a human muscle. J Appl Physiol, 85:1230-1235.

Kawakami Y, Ichinose Y, Fukunaga T. (1998). Architectural and functional features of human triceps surae muscles during contraction. J Appl Physiol, 85(2), 398-404.

Maganaris CN. (2000) In vivo measurement-based estimations of the moment arm in the human tibialis anterior muscle-tendon unit. J Biomech 33(3), 375-379.

Maganaris CN and Baltzopoulos V. (1999). Predictability of in vivo changes in pennation angle of human tibialis anterior muscle from rest to maximum isometric dorsiflexion. Eur J Appl Physiol, 79, 294-7.

Maganaris CN, Baltzopoulos V, Sargeant AJ. (1998) In vivo measurements of the triceps surae complex architecture in man: implications for muscle function. J Physiol, 512(2), 603-614.

Maganaris CN and Paul JP. (1999) In vivo human tendon mechanical properties. J Physiol 521, 307-313.

McGill S, Jucker D, Kropf P. (1996) Quantitative intramuscular myoelectric activity of quadratus lumborum during a wide variety of tasks. Clinical Biomechanics, 11(3), 170-172.

McKenzie DK, Gandevia SC, Gorman RB, Southon FC. (1994) Dynamic changes in the zone of apposition and diaphragm length during maximal respiratory efforts. Thorax, 49(7), 634-8.

Muramatsu T, Muraoka T, Kawakami Y, and Fukunaga T. (2002). Intramuscular variability of the architechture in human medial gastrocnemius muscle in vivo and its functional implications. Adv Exerc Sports Physiol, 8, 17-21.

Muraoka T, Muramatsu T, Takeshita D, Kawakami Y, Fukunaga T. (2002). Length change of human gastrocnemius aponeurosis and tendon during passive joint motion. Cells Tissues Organs 171, 260-268.

Narici MV, Binzoni T, Hiltbrand E, Fasel J, Terrier F, Cerretelli P. (1996). In vivo human gastrocnemius architecture with changing joint angle at rest and during graded isometric contraction. J Physiol, 496, 287-97.

Ng JK, Kippers V, Parnianpour M, Richardson CA. (2002) EMG activity normalization for trunk muscles in subjects with and without back pain. Med Sci Sports Exerc, 34:1082-1086.

Rutherford OM, Jones DA. (1992) Measurement of fibre pennation using ultrasound in the human quadriceps in vivo. Eur J Appl Physiol occup Physiol, 65(5), 433-7.

Walker FO, Cartwright MS, Ethan RW, James C. (2004). Ultrasound of nerve and muscle. Clinical Neurophysiology, 115, 495-507.

Walker FO, Harpold JG, Donofrio PD, Ferrell WG. (1990) Sonographic imaging of muscle contraction and fasciculations: a comparison with electromyography. Muscle Nerve 13, 33-9.

Watanabe K, Miyamoto K, Masuda T, Shimizu K. (2004) Use of ultrasonography to evaluate thickness of the erector spinae muscle in maximum flexion and extension of the lumbar spine. Spine, 29:1472-1477.

Applications Of Therapeutic Ultrasound In Dentistry And In The Craniofacial Area: Present And Future

Tarek El-Bialy
University of Alberta, Faculty of Medicine and Dentistry, Orthodontic Graduate Program and Department of Biomedical Engineering, Edmonton, AB, T6G 2N8, telbialy@ualberta.ca

ABSTRACT

The aim of this article is to outline the applications of therapeutic ultrasound on tooth and bone formation in the craniofacial area. The scientific background and clinical applications will be highlighted. Many problems in dentistry and in the craniofacial area exist without a definitive treatment. This review will point out the current state of the art and potential uses of therapeutic ultrasound to solve most of these problems.

SOMMAIRE

Le but de cet article est de décrire les applications des ultrasons thérapeutiques sur la formation des dents et des os dans la région craniofaciale. Les fondations scientifiques et les applications cliniques seront accentués. Plusieurs problèmes dentaires et craniofaciales existent sans traitements définis. Cet article de revue fera le point des connaissances les plus récentes et des des applications potentielles des ultrasons thérapeutiques pour résoudre la plupart de ces problèmes.

1. INTRODUCTION

Ultrasound, a form of mechanical energy that is transmitted through biological tissues as an acoustic pressure wave at frequencies above the limit of human hearing, is used widely in medicine as a operative (That is used to crush renal and liver stones and usually of frequency range between 2 - 8 K Hz), therapeutic (that is used in physiotherapy and usually of frequency range between 20 K Hz 3M Hz and either in the continuous or pulsed modes), and diagnostic tool (usually of a frequency range between 1.6-12 M Hz).1-3 Both therapeutic US, and some operative US, use intensities as high as one to three W/cm2 and can cause considerable heating in living tissues. To take full advantage of this energy absorption, physical therapists often use such levels of US acutely to decrease joint stiffness, reduce pain and muscle spasms, and improve muscle mobility.4 The exact mechanisms by which ultrasound produces these effects are not fully understood. However, there is ample evidence in the literature that therapeutic ultrasound can produce stimulatory effects at the gene, cellular and tissue levels. The purpose of this review article is to present the effect of therapeutic ultrasound on cellular and subcellular levels and its potential use in other medical therapeutic applications.

2. TISSUE REPAIR AND STIMULATORY EFFECTS OF ULTRASOUND

Mechanical energy in the form of ultrasound or other types of mechanical loading is now accepted to have a stimulatory effect on bone and other tissues. Historically, Wolff demonstrated a relationship between the architecture of cancellous bone and the forces acting upon the skeleton.5 A recent report supports Wolff's conclusion that the form and architecture of bone adapt to the mechanical environment by remodeling to accommodate the magnitude and direction of the applied stress.6 Because ultrasound is a type of pressure wave, it was hypothesized that ultrasound can enhance healing of bone fractures, and it was proven to do so in 1952 in rabbits. 7 These findings were followed by the first clinical use of ultrasound to stimulate fracture-healing in 1953, when it was demonstrated that the ultrasound treatment was safe and produced an increase in periosteal callus (bone fracture healing tissue). 8 The use of therapeutic ultrasound to facilitate bone fracture healing re-emerged in the seventies and became more popular in the late 1990s with the FDA approval for clinical use of long bone fracture healing.9,10 Distraction osteogenesis, also known as Ilizarove technique or bone lengthening was first reported by Codvilla in 1905.11 This technique was popularized in Russia during World War II.12 This technique was introduced into the craniofacial region13 to lengthen short bones, such as the upper and lower jaws, and also to correct facial asymmetry in cases of congenital syndromes, Hemifacial microsomia, and craniosynostosis.14,15 One of the problems encountered in craniofacial or long bone distraction osteogenesis, especially with external appliances was the risk for potential trauma and patient incapacitation.16,17 Another problem when intraoral tooth-borne distraction devices were used was that the final result of bone lengthening was modified by the masticatory muscle forces. This led to bending of the newly formed bony callus.18 Moreover, with regular distraction osteogenesis technique, it is mandatory for the patient to have the distraction device for an extended period of time, usually 6-8 months, to ensure complete bone formation and maturation at the distraction site. In most scenarios, the patient can be incapacitated from

work and other life activities. Based on that, several researchers studied different methodologies to enhance bone healing during distraction osteogenesis. These techniques included the use of insulin-like growth factor, electrical stimulation and therapeutic ultrasound. 19-22

Therapeutic ultrasound produced growth modification of the endplate in the tibia of growing rats. 23 It has also been reported to produce growth modification of the mandibular condyle and stimulate mandibular growth in growing rabbits and monkeys.24,25 These results led to trying to use therapeutic ultrasound to stimulate mandibular growth in underdeveloped mandibles of patients with hemifacial microsomia. These therapeutic ultrasound results, however, were complemented by the use of lower jaw stretching appliances, known as functional appliances.26 These results however are limited to growing animals and or human patients. The long-term stability of these results as well as the potential stimulation in adults is a real scientific challenge. A historical discovery was reported in 2002, when the lower incisor of adult rabbits were sectioned during the course of mandibular osteotomy intended for osteodistraction. 27 That was the first time in history that new dental tissue (osteodentine and cementum) was formed in a few days using ultrasound. This discovery brought with it a questionable application to human teeth, since it is known that the teeth of rodents, including rabbits, are continually erupting throughout their life. This led us to move to an exploratory human trial. In orthodontics, many patients seeking treatment for crowded teeth usually require removal of their first or second premolars to provide the required spaces. These potentially extracted teeth are often candidates for human experimental studies, since the patients are going to lose them anyway. For this preliminary study, twelve orthodontic patients requiring removal of their first premolars were chosen and consented to participate in this study. Premolars on both sides in each patient were moved orthodontically to induce resorption of their roots. For each patient, one premolar was treated with ultrasound for twenty minutes per day for four weeks and the premolar on the other side was used as a self control. After four weeks, all premolars were extracted and examined with either a scanning electron microscope or histologically. Both examinations revealed that the ultrasound treated premolars showed healing of the root resorption with newly formed cementum and dentine, while the nontreated premolars showed increased areas of root resorption. 28 This is the first time in history that human teeth roots showed new dental tissue formation in the roots in four weeks, especially treating external tooth root resorption. The potential application of this treatment method is that other forms of tooth root resorption, like those after trauma or after root canal treatment, or root fracture may be treated with this type of ultrasound. However, more research is needed to test this methodology in such cases.

Another stimulatory effect of therapeutic ultrasound is on the healing of artificially cut, repaired and immobilized tendo-calcaneus in rabbits. It was found that ultrasound induced a significant increase in the tensile strength, tensile stress and energy absorption capacity of the tendons when applied for 5 minutes every day for 9 days. These findings suggested that sonication at similarly low intensities may enhance the healing process of surgically repaired human tendo-calcaneus.29 Also, ultrasound was found to promote the healing of medial collateral ligaments in rats when treated for 5-10 days.30

3. MECHANISM BY WHICH THERAPEUTIC ULTRASOUND ENHANCES TISSUE FORMATION

Long before its use in clinical situations, therapeutic ultrasound was tested on cellular levels and in animal experiments. In addition, the clinically achieved results of using ultrasound have been studied in-vitro and provided many explanations for those results. It was found that low intensity (0.75 MHz) ultrasound is effective in liberating preformed fibroblast growth factors from a macrophage-like cell line, possibly by producing permeability changes, whereas higher intensity (3.0 MHz) ultrasound appeared to stimulate the cell's ability to synthesize and secrete fibroblast mitogenic factors.31 Also, it has been recently reported that ultrasound stimulates type I and III collagen expression of tendon cells as well as upregulates the transforming growth factor beta in-vitro.32,33 It has also been shown that therapeutic ultrasound stimulates the expression of the proliferating cell nuclear antigen in cultured tendon cells as evaluated by immunocytochemistry and by reverse transcription-polymerase chain reaction. A dose-dependent increase in the cellularity of tendons was reported as ten minutes of treatment achieved maximum cellularity compared to 5 minutes of treatment time. 34 These facts provide an explanation of the clinical effect of therapeutic ultrasound in stimulating tissue repair.

Moreover, therapeutic ultrasound was reported to stimulate the proliferation of the cartilage cells without influencing cell differentiation. 35 Also, therapeutic ultrasound was reported to stimulate aggrecan mRNA expression and proteoglycan synthesis by chondrocytes.36 This may explain a means by which ultrasound enhances endochondral ossification (bone growth within the cartilage that is known to be the type of bone growth involved in bone fracture healing and long bone growth), increases the mechanical strength of fractures, and facilitates fracture repair.

Moreover, ultrasound can also affect vascular tone directly, and hence enhance tissue perfusion as well as increase vasodilation. It was reported that the application of 40 kHz ultrasound at intensities from 0.25 to 0.75 W/cm2 progressively improved perfusion over 60 minutes and reversed acidosis, but these effects were both completely blocked by pre-treatment with the nitric oxide synthase inhibitor. Histological examination showed greater capillary circumference in ultrasound exposed muscle compared to unexposed tissue with no other histological changes. 37 Moreover, it has been reported that therapeutic ultrasound stimulates matrix production by cementoblasts in vitro.38 This result supports previous research which reported that ultrasound stimulates teeth erup-

tion and formation, and repairs tooth root resorption after orthodontic treatment.27,28

4. SAFETY OF DAILY USE OF THERAPEUTIC ULTRASOUND FOR EXTENDED PERIODS OF TIME.

With the recent and more advanced applications of therapeutic ultrasound, there is an increasing concern about the safety of repeatedly using it for extended periods of time in humans for as long as months or years on a daily basis. In addition to reports that ultrasound is being used to diagnose early stages of cancer,39 it has been reported that when human patients used low-intensity pulsed ultrasound (LIPUS) to enhance bone fracture healing for 114 + 10 days, there were no reported complications related to its use.9 It has been reported that the current safety limit for diagnostic ultrasound is 0.72 W/cm2,40 which is almost three times that of the LIPUS power that has been approved by FDA and Health Canada (0.30 W/cm2). It is generally accepted that there is no real evidence of adverse human health effects of diagnostic ultrasound and its use is not contraindicated for medical purposes at the recommended levels.41 Moreover, ultrasound with an intensity of 7 W/cm2 with a frequency of 340 kHz for 30 minutes is being used for thrombolysis of cerebral infarction using continuous ultrasound insonation with no harmful effect on the brain.42 Previously, when LIPUS was used to repair orthodontically-induced tooth root resorption, an acoustic absorber was used to prevent any unwanted potential exposure of the neighboring tissues to unwanted LIPUS.28 In reviewing the available literature, no major concerns with repeated use of therapeutic ultrasound for extended periods of time were found. However, more in-vitro studies may be conducted to test if there is a potential for cellular damage due to ultrasound application for extended periods of time.

5. FUTURE DIRECTIONS

Future studies might be aimed at testing the effect of therapeutic ultrasound on tissue engineering of teeth, bone, and other body tissues/organs. The promises on gene as well as cellular stimulation by ultrasound can open a new era of investigations and applications for different clinical problems that have never been tested before. Moreover, its use to stimulate nerve and muscle function and growth is still a new area to be explored.

ACKNOWLEDGEMENT

The author would like to acknowledge Ms. Joanne Lafrance, at the graduate orthodontic program for her efforts in proofing and preparing the manuscript.

REFERENCES

1. Maylia E, Nokes LD. The use of ultrasonics in orthopaedics—a review. Technol Health Care 1999;7:1–28.
2. Ziskin MC. Applications of ultrasound in medicine—comparison with other modalities. In: Rapacholi MH, Grandolfo M, Rindi A, eds. Ultrasound: Medical Applications, Biological Effects, and Hazard Potential. New York, NY: Plenum Press; 1987:49–59.
3. Harris GR. Progress in medical ultrasound exposimetry. IEEE Trans Ultrason Ferroelectr Freq Control 2005 May;52:717-36.
4. Dyson M. Therapeutic applications of ultrasound. In: Nyborg WL, Ziskin MC, eds. Biological Effects of Ultrasound. New York, NY: Churchill Livingstone; 1985:121–33.
5. Wolff J. [The law of bone remodeling]. Berlin: Hirshwald; 1892. p 17-35. German
6. Huiskes R, Ruimerman R, van Lenthe GH, Janssen JD. Effects of mechanical forces on maintenance and adaptation of form in trabecular bone. Nature 2000;405: 704-6.
7. Corradi C, Cozzolino A. The action of ultrasound on the evolution of an experimental fracture in rabbits. Minerva Ortop 1952:55: 44-5, Italian (Quoted from [Rubin C, Bolander M, Ryaby JP, Hadjiargyrou M. The use of low-intensity ultrasound to accelerate the healing of fractures. J Bone Joint Surg Am 2001;83-A:259-70.]).
8. Corradi C, Cozzolino A. Ultrasound and bone callus formation during function. Arch Ortop 1953;66:77-98, Italian. (Quoted from [Rubin C, Bolander M, Ryaby JP, Hadjiargyrou M. The use of low-intensity ultrasound to accelerate the healing of fractures. J Bone Joint Surg Am. 2001;83-A:259-70.]).
9. Heckman JD, Ryaby JP, McCabe J, Frey JJ, Kilcoyne RF. Acceleration of tibial fracture-healing by non-invasive, low-intensity pulsed ultrasound. J Bone Joint Surg Am 1994;76: 26-34.
10. Kristiansen TK, Ryaby JP, McCabe J, Frey JJ, Roe LR. Accelerated healing of distal radial fractures with the use of specific, low-intensity ultrasound. A multicenter, prospective, randomized, double-blind, placebo-controlled study. J Bone Joint Surg Am 1997;79: 961-73.
11. Codivilla, A. On the means of lengthening, in the lower limbs, the muscles and tissues which are shortened through deformity. Am J Orthop Surg 1905;2: 353-69.
12. Ilizarov, GA. The tension-stress effect on the genesis and growth of tissues: part I The influence of stability of fixation & soft tissue preservation. Clin Orthop Relat Res 1989;238:241-81.
13. Snyder CC, Levine GA, Swanson HM, Browne EZ Jr. Mandibular lengthening by gradual distraction: Preliminary report. Plast Reconstr Surg 1973;51:506-8.
14. Scolozzi P, Herzog G, Jaques B. Simultaneous maxillo-mandibular distraction osteogenesis in hemifacial mi-

crosomia: a new technique using two distractors. Plast Reconstr Surg. 2006;117:1530-41; discussion 1542.

15. Meling TR, Hans-Erik H, Per S, Due-Tonnessen BJ. Le Fort III distraction osteogenesis in syndromal craniosynostosis. J Craniofac Surg. 2006;17:28-39.
16. Oh CW, Sharma R, Song HR, Koo KH, Kyung HS, Park BC. Complications of distraction osteogenesis in short fourth metatarsals. J Pediatr Orthop 2003;23:484-87.
17. van der Meulen J, Wolvius E, van der Wal K, Prahl B, Vaandrager M. Prevention of halo pin complications in post-cranioplasty patients. J Craniomaxillofac Surg 2005; 33:145-49.
18. Dessner S, Razdolsky Y, El-Bialy T, Evans CA. Mandibular lengthening using preprogrammed intraoral tooth-borne distraction devices. J Oral Maxillofac Surg 1999;57:1318-22.
19. Stewart KJ, Weyand B, van't Hof RJ, White SA, Lvoff GO, Maffulli N, Poole MD. A quantitative analysis of the effect of insulin-like growth factor-1 infusion during mandibular distraction osteogenesis in rabbits. Br J Plast Surg 1999;52:343-50.
20. Hagiwara T, Bell WH. Effect of electrical stimulation on mandibular distraction osteogenesis. J Craniomaxillofac Surg 2000;28:12-19.
21. El-Bialy TH, Royston TJ, Magin RL, Evans CA, Zaki Ael-M, Frizzell LA. The effect of pulsed ultrasound on mandibular distraction. Ann Biomed Eng 2002;30:1251-61.
22. Chan CW, Qin L, Lee KM, Zhang M, Cheng JC, Leung KS. Low intensity pulsed ultrasound accelerated bone remodeling during consolidation stage of distraction osteogenesis. J Orthop Res 2006;24:263-70.
23. Abramovich, A. Effect of ultrasound on the tibia of the young rat. J Dent Res 1970;49:1182.
24. El-Bialy T, El-Shamy I, Graber TM. Growth modification of the rabbit mandible using therapeutic ultrasound: is it possible to enhance functional appliance results? Angle Orthod 2003;73:631-39.
25. El-Bialy TH, Hassan A, Albaghdadi T, Fouad HA, Maimani AR. Growth modification of the mandible using ultrasound in monkeys: a preliminary report. Am J Orthod Dentofacial Orthop 2006;130:435.e7-435.e14.
26. El-Bialy T, Alyamani A, Albaghdadi T, Hassan A, Major PW. Treatment of hemifacial microsomia without surgery: an evidence-based approach. Proceeding of the 6th International Congress, 6, World Federation of Orthodontists, 8 Sep 2005.
27. El-Bialy TH, el-Moneim Zaki A, Evans CA. Effect of ultrasound on rabbit mandibular incisor formation and eruption after mandibular osteodistraction. Am J Orthod Dentofacial Orthop 2003;124:427-34.
28. El-Bialy T, El-Shamy I, Graber TM. Repair of orthodontically induced root resorption by ultrasound in humans. Am J Orthod Dentofacial Orthop 2004;126:186-93.
29. Enwemeka CS, Rodriguez O, Mendosa S. The biomechanical effects of low-intensity ultrasound on healing tendons. Ultrasound Med Biol 1990;16:801-7.
30. Leung MC, Ng GY, Yip KK. Therapeutic ultrasound enhances medial collateral ligament repair in rats. Ultrasound Med Biol. 2006;32:449-52.
31. Young SR, Dyson M.: The effect of therapeutic ultrasound on angiogenesis. Ultrasound Med Biol 1990;16:261-69.
32. Ebisawa K, Hata K, Okada K, Kimata K, Ueda M, Torii S, Watanabe H. Ultrasound enhances transforming growth factor beta-mediated chondrocyte differentiation of human mesenchymal stem cells. Tissue Eng 2004;10:921-29.
33. Tsai WC, Pang JH, Hsu CC, Chu NK, Lin MS, Hu CF. Ultrasound stimulation of types I and III collagen expression of tendon cell and upregulation of transforming growth factor beta. J Orthop Res 2006;24:1310-16.
34. Tsai WC, Hsu CC, Tang FT, Chou SW, Chen YJ, Pang JH. Ultrasound stimulation of tendon cell proliferation and upregulation of proliferating cell nuclear antigen. J Orthop Res. 2005;23:970-76.
35. Wiltink A, Nijweide PJ, Oosterbaan WA, Hekkenberg RT, Helders PJ. Effect of therapeutic ultrasound on endochondral ossification. Ultrasound Med Biol 1995;21: 121-27.
36. Yang KH, Parvizi J, Wang SJ, Lewallen DG, Kinnick RR, Greenleaf JF, Bolander ME. Exposure to low-intensity ultrasound increases aggrecan gene expression in a rat femur fracture model. J Orthop Res 1996;14:802-9.
37. Suchkova VN, Baggs RB, Sahni SK, Francis CW. Ultrasound improves tissue perfusion in ischemic tissue through a nitric oxide dependent mechanism. Thromb Haemost 2002;88:865-70.
38. Dalla-Bona DA, Tanaka E, Oka H, Yamano E, Kawai N, Miyauchi M, Takata T, Tanne K. Effects of ultrasound on cementoblast metabolism in vitro. Ultrasound Med Biol 2006;32:943-48.
39. Loch T. [Innovative approaches in prostate cancer ultrasound]. Urologe A 2006;45:692-701.German.
40. Vanbavel E. Effects of shear stress on endothelial cells: Possible relevance for ultrasound applications. Prog Biophys Mol Biol 2006 Aug 4; [Epub ahead of print].
41. Barnett SB. Live scanning at ultrasound scientific conferences and the need for prudent policy. Ultrasound Med Biol 2003; 29:1071-76.
42. Fatar M, Stroick M, Griebe M, Alonso A, Hennerici MG, Daffertshofer M. Brain temperature during 340-kHz pulsed ultrasound insonation: a safety study for sonothrombolysis. Stroke 2006;37:1883-87.

Better testing... better products.

The Blachford Acoustics Laboratory

Bringing you superior acoustical products from the most advanced testing facilities available.

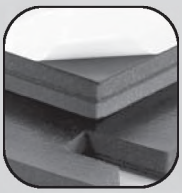

Our newest resource offers an unprecedented means of better understanding acoustical make-up and the impact of noise sources. The result? Better differentiation and value-added products for our customers.

Blachford Acoustics Laboratory features

- Hemi-anechoic room and dynamometer for testing heavy trucks and large vehicles or machines.
- Reverberation room for the testing of acoustical materials and components in one place.
- Jury room for sound quality development.

Blachford acoustical products

- Design and production of simple and complex laminates in various shapes, thicknesses and weights.
- Provide customers with everything from custom-engineered rolls and diecuts to molded and cast-in-place materials.

Blachford QS 9000 REGISTERED

www.blachford.com | Ontario 905.823.3200 | Illinois 630.231.8300

Diagnostic Ultrasound: Imaging and Blood Flow Measurements, By K. Kirk Shung CRC Press, 2005, List price: $109.95 USD (hardcover), 232 pp., ISBN: 0824740963

A pioneer in ultrasound research for over 30 years, Dr. K. Kirk Shung has recently authored a book on diagnostic ultrasound. His motivation was in part, as he states in his book, that "not a single book in ultrasound imaging on the market today contained sufficient technical material suitable for adaption as a textbook at the college or graduate school level, although many excellent books for clinician's technologists were in print". In that spirit, Dr. Shung wrote this book with the senior undergraduate or junior graduate student that requires an introductory course on ultrasound in mind. It should be noted that other books have also been recently published with this intended audience (e.g. Diagnostic Ultrasound Imaging: Inside Out, by Thomas Szabo, Elsevier Academic Press, 2004).

The book was based on notes for a graduate course on ultrasound imaging that the author has been teaching for the last 15 years at the Department of Bioengineering at Pennsylvania State University and the University of Southern California. In general, it does not delve into great detail in any of the topics presented, but tries to strike a balance between illustrating the necessary physics and engineering concepts to understand the formation of images and the estimation of flow using ultrasound.

After a very brief introduction to ultrasound in Chapter 1, Chapter 2 covers the fundamentals of ultrasound propagation. The stress strain relationships are covered and this material builds up to the acoustic wave equation, with brief coverage of topics such as intensity, impedance and radiation force. The author delves into more detail on the topics of attenuation, absorption and scattering. It is nice to see included a brief treatment of the non-linearity parameter. The Chapter ends with a description of the Doppler effect. Given the breadth of material covered, the Chapter is rather succinct and spartan, but adequate as introductory text. It could have been better referenced so that the reader seeking detail behind some of the material presented could consult these references.

Chapters 3 and 4 deal with ultrasound transducers/arrays and gray scale ultrasonic imaging in general. As transducer technology is one of the areas of specialization of the author, this is a well covered topic in the book, with judicious use of schematics and figures and coverage of topics such as transducer models, matching (mechanical and electrical), beam profiles and array theory and design. It is also well referenced. After the chapter on transducer technology, Chapter 4 introduces the components and processing of common ultrasonic imaging systems. The different imaging modes are introduced and several block diagrams of imaging systems are presented. The resolution of imaging systems is discussed, and issues such as beam forming, image quality (speckle, point spread function, spatial and contrast resolution) as well as other types of imaging (coded excitation, compound, synthetic aperture) are introduced. Again, due to the short description of several of the topics, a more comprehensive bibliography would have been beneficial.

Chapters 5 and 6 deal with the measurement of flow with ultrasound. The author discusses in Chapter 5 continuous wave and pulsed wave Doppler systems and has a fine description of the basis of such measurements, with a good level of analysis included. Chapter 5 ends with a description of the potential problems in Doppler measurement. Chapter 6 introduces flow and displacement imaging, first through the description of color Doppler flow systems and then elasticity imaging. This Chapter ends with a section on B-Flow imaging (which uses coded excitation techniques mentioned prior to equalize blood and tissue signals).

Dr. Shung presents contrast media and harmonic imaging in Chapter 7. Again, a nice balance is reached between depth and breath, as there is sufficient detail and discussion on bubble scattering and dynamics (including discussions of bubble encapsulation, bubble distribution and non-linear interactions of bubbles with ultrasound). Solutions to the appropriate equations are presented, even though a greater emphasis could have been placed to applications in this new and exciting field. The Chapter closes with a description of harmonic imaging.

In Chapters 8 and 9 intracavity and high frequency ultrasound, as well as multidimensional imaging are presented. Here the topics are glossed over, with greater emphasis on the technology and applications rather than the salient differences when imaging using these frequencies. Two dimensional arrays are discussed in Chapter 9, in which cMUT technology is also presented. The Chapter closes with a description of three dimensional imaging.

Very brief descriptions of bioeffects are presented in Chapter 10. Again, the basics are discussed, and some important tables and figures from the AIUM (American Institute of Ultrasound in Medicine) and AIUM/NEMA recommendations are used. The final Chapter focuses on methods that are used for measuring the speed of sound, attenuation absorption and scattering. As indicated by the author in the preface, this last chapter is optional in a semester course, but a useful addition for students and investigators planning to perform such ultrasonic experiments.

Overall, this is a well organized and illustrated book that fills a gap in the ultrasonic literature. It has enough material to be used in a one semester course on ultrasound imaging, however almost certainly other texts need to be consulted if any of the topics presented are to be studied in depth. I have found myself consulting the book on occasion in the preparation of lectures, and using it as a reference sporadically.

Dr. Michael Kolios
Department of Physics, Ryerson University, Toronto

Diagnostic Ultrasound Imaging: Inside Out
By Thomas L. Szabo
Elsevier Academic Press, 2004
List price: $94.95 USD (hardcover)
576 pp., ISBN: 0126801452

As a graduate student in medical physics I often encounter textbooks on a given imaging modality providing a comprehensive look at the essential physics with outdated examples, or excellent reviews of current applications with little to offer on the basic theory behind the modality. It was rather refreshing to come across this text by Thomas L. Szabo which covers the essential introductory physics and signal processing concepts of ultrasound as well as a breadth of advanced topics, including findings from the latest ultrasound research, all in a neat 540-page package.

Dr. Szabo is a Research Professor in the departments of Biomedical Engineering and Aerospace & Mechanical Engineering at Boston University. He is a fellow of the Acoustical Society of America and spent nearly 20 years in ultrasound research and development at Hewlett Packard (later Agilent).

This book has 15 chapters: 1) Introduction; 2) Overview; 3) Acoustic Wave Propagation; 4) Attenuation; 5) Transducers; 6) Beamforming; 7) Array Beamforming; 8) Wave Scattering and Imaging; 9) Scattering from Tissue and Tissue Characterization; 10) Imaging Systems and Applications; 11) Doppler Modes; 12) Nonlinear Acoustics and Imaging; 13) Ultrasonic Exposimetry and Acoustic Measurements; 14) Ultrasound Contrast Agents and 15) Ultrasound-induced Bioeffects.

Chapter 1 gives a historical overview of ultrasound, from the beginnings of sonar to current technologies and provides the reader with a comparison between existing imaging modalities. For those with little background in signal processing, chapter 2 introduces the Fourier Transform and signal processing concepts in the time and frequency domains using a building block approach that is carried through to the rest of the book. Additional information on Fourier Transforms and their applications are included as an appendix. Chapters 3 through 8, as well as chapter 10 comprise, what I consider, the "core" of the book, covering the essential physics, signal processing and application of ultrasound. The remainder of the book covers a variety of advanced topics. These range from imaging techniques such as Doppler ultrasound and color flow imaging, harmonic imaging and microbubble contrast agents to the use of ultrasound for tissue and transducer characterization and, finally, a chapter on the bioeffects of ultrasound as they relate to safety and to therapeutic applications.

Though the basic theoretical building blocks are covered, making this book accessible to the complete beginner reader in ultrasound, a background in mathematics and physics, specifically an understanding of calculus, complex numbers and some knowledge of electric circuits, is essential to fully benefit from this text. Graduate students in medical physics and biomedical engineering will find this book most useful as it provides a very comprehensive overview of ultrasound imaging physics with the option to progress to more advanced topics. Nevertheless, this book will also serve as a great reference for researchers, engineers and physicists well versed in ultrasound as its coverage of advanced topics is not trivial and includes the work of hundreds of contributors to the field.

Golnaz Farhat
Department of Medical Biophysics
University of Toronto, Toronto

The First European Forum on Effective Solutions for Managing Occupational Noise Risks

Lille (France) July 3-5 2007

This Forum will not be an academic conference but an event where all parties concerned can meet and exchange their experience and achievements regarding noise management and control at the workplace. Occupational safety and health specialists, factory doctors and inspectors, employers associations, trade union representatives, noise consulting companies, individuals and researchers having brought innovative solutions, manufacturers of low noise machines, providers of sound proofing equipment, industrial architects, professional buyers...all those who actively deal with noise management at work are welcome to bring a contribution or participate.

To get detailed information, or submit an abstract, please visit the conference website at http://www.noiseatwork.eu

The Forum is organized by INCE/Europe, CIDB and Association AINF, in collaboration with OSHA/EU, BAuA, CIOP, FIOH, HSE, INRS, IRSST, SUVA, CETIM... under the patronage of the European Acoustics Association (EAA), the French Society of Acoustics (SFA) and the French Ministries in charge of Labour, Health and Ecology.

NEWS / INFORMATIONS

CONFERENCES

If you have any news to share with us, send them by mail or fax to the News Editor (see address on the inside cover), or via electronic mail to stevenb@aciacoustical.com

2007

01-03 June. 2nd International Symposium on Advanced Technology of Vibration and Sound (VS Tech 2007). Lanzhou, China. Web: www.jsme.or.jp/dmc/meeting/vstech2007.pdf

03-07 June. 11th International Conference on Hand-Arm Vibration. Bologna, Italy. Web: www.associazioneitalianadiacustica.it/HAV2007/index.htm

04-06 June. Japan-China Joint Conference on Acoustics 2007. Sendai, Japan. Web: www.asj.gr.jp/eng/index.html

04-08 June: 153rd Meeting of the Acoustical Society of America. Salt Lake City, Utah, USA. Web: www.asa.aip.org

18-21 June. Oceans07 Conference. Aberdeen, Scotland. Web: www.oceans07ieeeaberdeen.org

25-29 June. 2nd International Conference on Underwater Acoustic Measurements: Technologies and Results. Heraklion, Crete, Greece. Web: www.uam2007.gr

02-06 July. 8th International Conference on Theoretical and Computational Acoustics. Heraklion, Crete, Greece. Web: www.iacm.forth.gr/~ictca07

03-07 July. 1st European Forum on Effective Solutions for Managing Occupational Noise Risks. Lille, France. Web: www.noiseatwork.eu

9-12 July: 14th International Congress on Sound and Vibration (ICSV14). Cairns, Australia. Email: n.kessissoglou@unsw.edu.au

26-29 August: Inter-noise 2007. Istanbul, Turkey. Web: www.internoise2007.org.tr

27-31 August: Interspeech 2007. E-mail: conf@isca-speech.org

2-7 September 19th International Congress on Acoustics (ICA2007), Madrid Spain. (SEA, Serrano 144, 28006 Madrid, Spain; Web:www.ica2007madrid.org

9-12 September: ICA2007 Satellite Symposium on Musical Acoustics (ISMA2007). Barcelona, Spain. Web: www.isma2007.org

9-12 September: ICA2007 Satellite Symposium on Room Acoustics (ISMA2007). Sevilla, Spain. Web: www,isra2007.org

17-19 September. 3rd International Symposium on Fan Noise. Lyon, France. Web: www.fannoise2007.org

19-21 September. Autumn Meeting of the Acoustical Society of Japan. Kofu, Japan. Web: www.asj.gr.jp/index-en.html

20-22 September: Wind Turbine Noise 2007, Lyon, France. Web: www.windturbinenoise2007.org

24-28 September. XIX Session of the Russian Acoustical Society. Nizhny Novgorod, Russia. Web: www.akin.ru

3-5 October. Pacific Rim Underwater Acoustics Conference, Vancouver, Canada. Web:

CONFÉRENCES

Si vous avez des nouvelles à nous communiquer, envoyez-les par courrier ou fax (coordonnées incluses à l'envers de la page couverture), ou par courriel à stevenb@aciacoustical.com

2007

01-03 juin. 2nd International Symposium on Advanced Technology of Vibration and Sound (VS Tech 2007). Lanzhou, China. Web: www.jsme.or.jp/dmc/meeting/vstech2007.pdf

03-07 juin. 11th International Conference on Hand-Arm Vibration. Bologna, Italy. Web: www.associazioneitalianadiacustica.it/HAV2007/index.htm

04-06 juin. Japan-China Joint Conference on Acoustics 2007. Sendai, Japan. Web: www.asj.gr.jp/eng/index.html

04-08 juin: 153rd Meeting de l'Acoustical Society d'America. Salt Lake City, Utah, USA. Web: www.asa.aip.org

18-21 juin. Oceans07 Conference. Aberdeen, Scotland. Web: www.oceans07ieeeaberdeen.org

25-29 juin. 2nd International Conference on Underwater Acoustic Measurements: Technologies and Results. Heraklion, Crete, Greece. Web: www.uam2007.gr

02-06 juillet. 8th International Conference on Theoretical and Computational Acoustics. Heraklion, Crete, Greece. Web: www.iacm.forth.gr/~ictca07

03-07 juillet. 1st European Forum on Effective Solutions for Managing Occupational Noise Risks. Lille, France. Web: www.noiseatwork.eu

9-12 juillet: 14th Congress Internationale sur Sound et Vibration (ICSV14). Cairns, Australia. Email: n.kessissoglou@unsw.edu.au

26-29 août: Inter-noise 2007. Istanbul, Turkey. Web: www.internoise2007.org.tr

27-31 août: Interspeech 2007. E-mail: conf@isca-speech.org

2-7 septembre 19e Congrès international sur l'acoustique (ICA2007), Madrid Spain. (SEA, Serrano 144, 28006 Madrid, Spain; Web: www.ica2007madrid.org

9-12 septembre: ICA2007 Satellite Symposium sur Musical Acoustics (ISMA2007). Barcelona, Spain. Web: www.isma2007.org

9-12 septembre: ICA2007 Satellite Symposium sur Room Acoustics (ISMA2007). Sevilla, Spain. Web: www,isra2007.org

17-19 septembre. 3rd International Symposium on Fan Noise. Lyon, France. Web: www.fannoise2007.org

19-21 septembre. Autumn Meeting of the Acoustical Society of Japan. Kofu, Japan. Web: www.asj.gr.jp/index-en.html

20-22 Septembre: Wind Turbine Noise 2007, Lyon, France. Web: www.windturbinenoise2007.org

24-28 septembre. XIX Session of the Russian Acoustical Society. Nizhny Novgorod, Russia. Web: www.akin.ru

3-5 Octobre. Pacific Rim Underwater Acoustics Conference, Vancouver, Canada. Web:

9-12 October. Canadian Acoustical Association Annual Conference. Montreal, Canada. Web: http://www.caa-aca.ca

22-24 October. Noise-Con 2007. Reno, Nevada, USA. Web: www.inceusa.org/nc07/index.asp

November 27 - December 02: 154th Meeting of the Acoustical Society of America. New Orleans, LA, USA. Web: www.asa.aip.org

2008

29 June - 04 July: Joint Meeting of European Acoustical Association, Acoustical Society of America, and Acoustical Society of France. Paris, France. Web: www.sfa.asso.fr/en/index.htm

7-10 July: 18th International Symposium on Nonlinear Acoustics (ISNA18). Stockholm, Sweden. E-mail: benflo@mech.kth.se

27-30 July. Noise-Con 2008. Dearborn, MI, USA.

28 July - 1 August: 9th International Congress on Noise as a Public Health Problem. Mashantucket, Pequot Tribal Nation, (CT, USA). Web: www.icben.org

22-26 September: Interspeech 2008 - 10th ICSLP, Brisbane, Austrailia. Web: wwwinterspeech2008.org

26-29 October: Internoise 2008, Shanghai, China. Web: www.internoise2008.org

01-05 November. IEEE International Ultrasonic Symposium. Beijing, China. Web: www.ieee-uffa.org/ulmain.asp?page=symposia

2009

23-26 August: Internoise 2009, Ottawa, Canada.

23-27 August: International Confress on Acoustics 2010. Sydney, Australia. Web: www.acoustics.asn.au

2010

23-27 August: International Confress on Acoustics 2010. Sydney, Australia. Web: www.acoustics.asn.au

9-12 Octobre. Canadian Acoustical Association Annual Conference. Montreal, Canada. Web: http://www.caa-aca.ca

22-24 octobre. Noise-Con 2007. Reno, Nevada, USA. Web: www.inceusa.org/nc07/index.asp

novembre 27 - decembre 02: 154th Meeting de l'Acoustical Society d'America. New Orleans, LA, USA. Web: www.asa.aip.org

2008

29 juin - 04 juillet: Joint Meeting d'European Acoustical Association, Acoustical Society d'America, et Acoustical Society du France. Paris, France. Web: www.sfa.asso.fr/en/index.htm

7-10 juillet: 18th International Symposium sur Nonlinear Acoustics (ISNA18). Stockholm, Sweden. E-mail: benflo@mech.kth.se

27-30 juin. Noise-Con 2008. Dearborn, MI, USA.

28 juillet - 1 août: 9th International Congress sur Noise as a Public Health Problem. Mashantucket, Pequot Tribal Nation, (CT, USA). Web: www.icben.org

22-26 septembre: Interspeech 2008 - 10th ICSLP, Brisbane, Austrailia. Web: wwwinterspeech2008.org

26-29 Octobre: Internoise 2008, Shanghai, China. Web: www.internoise2008.org

01-05 novembre. IEEE International Ultrasonic Symposium. Beijing, China. Web: www.ieee-uffa.org/ulmain.asp?page=symposia

2009

23-26 août: Internoise 2009, Ottawa, Canada.

23-27 août: International Confress sur Acoustics 2010. Sydney, Australia. Web: www.acoustics.asn.au

2010

23-27 août: International Confress sur Acoustics 2010. Sydney, Australia. Web: www.acoustics.asn.au

NEWS

We want to hear from you! If you have any news items related to the Canadian Acoustical Association, please send them. Job promotions, recognition of service, interesting projects, recent research, etc. are what make this section interesting.

EXCERPTS FROM "*WE HEAR THAT...*", IN *ECHOS*, ASA

James G Miller, Albert Gordon Hill Professor of Physics at Washington University (St. Louis), received the 2006 Achievement Award from the IEEE Ultrasonics, Ferroelectrics, and Frequency Control Society for his "outstanding contributions to ultrasonic tissue characterization and echocardiography." Jim is a Fellow of ASA, of IEEE, of the American Institute of Ultrasound, in Medicine and the American Institute of Medical and Biological Engineering. In 2004 he received the ASA Silver Medal in Biomedical Ultrasound/Bioresponse to Vibration. At Washington University he has also received the Faculty Teaching Award and the Emerson Teaching Award.

John J. Ohala, Professor Emeritus of Linguistics at the University of California, Berkeley, received the 2006 International Speech Communication Association (ISCA) Medal for Scientific Achievement. John is a Fellow of the ASA and served as president of the International Phonetic Association. His work was also recognized by an honorary degree from the University of Copenhagen.

Sean A. Genis, a physics major at the United States Naval Academy, has been named a Rhodes scholar. Genis is a student of Murray Korman, Chair of the ASA Technical Committee on Physical Acoustics.

H. Frederick Dylla has been selected as Executive Director of the American Institute of Physics (AIP). He will replace Marc Brodsky, who will retire March 31 after more than 13 years at AIP's helm. Dylla, who has been at the Thomas Jefferson National Laboratory at Newport News, Virginia since 1990, has a special interest in science education and helped to found the K-12 science education programs at Jefferson Lab.

Silver medalist **Bill Yost** tells an amusing incident about carrying his new medal through airport security on his way back from Honolulu. "It was in my carry on, and after several looks at my bag and after I told them that the medal was probably what they were seeing, they took the blue case with medal out of my bag and put it through the x-ray machine. Three of them huddled for a minute or so looking at the x-ray, and then they told me I could go. "You haven't opened the case; don't you want to see what is inside?' I said. In a very firm manner I was told that I could not open the blue box until I was well clear of the security area. Not sure what they had on their minds, but it was all I could do to suppress my laughter."

Low frequency sound can travel almost unimpeded from water into air according to a paper in the 20 October issue of *Physical Review Letters*. These theoretical results are in stark contrast to the conventional view that the underwater world is largely silent to observers above water and could have important implications for marine biology, climatology and geophysics. The simple ray theory of acoustics predicts that any sound produced underwater will be reflected at the surface rather than transmitted into the air. However, the simple ray theory breaks down when the wavelength of the sound is comparable to (or longer than) the depth of the source. Water-to-air transmission at low frequencies involves evanescent sound waves in addition to the more familiar plane waves. The intensity of evanescent waves decreases exponentially with distance from the source and for a shallow source at a depth of a fraction of a wavelength they are transmitted to the air.

"The troubled **song of the sand dunes**" is the title of an article in the November issue of *Physics World* that tells the story of strong disagreement between two French researchers over the mechanism responsible for the eerie song of "singing" sand dunes. In 2001 a group of researchers, including Stéphane Douady and graduate students Bruno Andreotti and Pascal Hersen were studying sand dunes in Morocco when they accidentally set off avalanches that were accompanied by loud booms. Douady came up with an explanation for the effect based on the "stick-slip" motion of sand grains moving down the slope as a single block. Andreotti thrashed out a more detailed explanation for how the motion of sand grains might produce sound. Douady reasoned that since sound is only produced when layers of sand above a certain thickness slide over one another, this means that the sound must arise from a resonance within the shear layer itself. Andreotti turned this logic around, arguing that the collisions between grains excite waves outside the shear layer on the dune surface that synchronize the collisions via a mechanism called wave-particle locking. Some three or four years after their first trip, it was time for the researchers to submit for publication the considerable amount of knowledge they had amassed about the song of the dunes. At first they agreed to write a paper with the names of all the investigators on it, but opinions diverged. In 2004 Andreotti published a paper in *Physical Review Letters*, and in 2006 Douady, et al. published a paper in the same journal. Meanwhile another group of investigators at Caltech have made extensive measurements on sand dunes and found that they have a layered structure that causes a dune to act as a waveguide. They point out that neither Douady's nor Andreotti's analayses explain why some dunes do not sing. "Sand-dune science may not dominate the research-funding agenda, but unraveling the mystery of the singing dunes offers a valuable insight into how science is done," comments the author of the article in *Physicsi World.*

---

877 816-5435
www.soundivide.com

Quiet Work Places, Tranquil Living Spaces

QUIETROCK SOUNDPROOFING DRYWALL

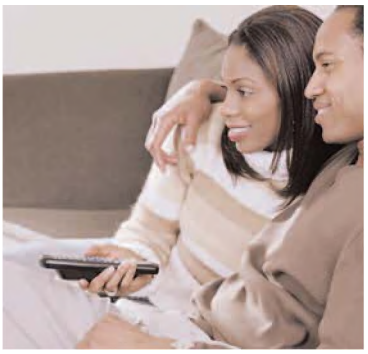

- cost-effectively achieves STC ratings of 51–80+ depending on assembly
- ready to use in standard 4' X 8' panels
- hangs like regular drywall–easy to install
- uses new visco-elastic technology to turn kinetic energy into intermolecular heat energy
- environmentally friendly
- fire rated
- THX certified

QUIETROCK PORTFOLIO

Product	QR-510 Basic	QR-525 Relief	QR-530 Serenity	QR-545 Solitude
	NEW PRODUCT			
Key Benefits	• Lowest cost; • Remodeling and upgrades	• Simple score, snap and hang	• Higher performance for retrofits	• Superb low frequency • THX-certified
STC	49-68	51-72	52-74	56-80
Thickness	1/2"	5/8"	5/8"	1-3/8"
Weight	2.2 lbs/sq ft	2.7 lbs/sq ft	2.8 lbs/sq ft	5.4 lbs/sq ft
Fire Rating	Not rated	1 hour	1 hour	

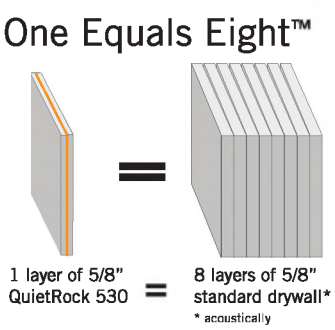

QUIETWOOD SOUNDPROOFING PLYWOOD

- multi-layer engineered panel made up of plywood, visco-elastic polymers and proprietary sound isolation layers
- ready to use in standard 4' x 8' panels
- quickly solves difficult STC and IIC noise problems between floors and rooms
- easy to install

QUIETWOOD PORTFOLIO

Product	Serenity QW-630	Serenity QW-631	Solitude QW-640
		NEW PRODUCT	
Key Benefits	• Thin, lightweight • Standard framing	• Structurally rated; • 1 hr fire; • for new construction	• Superb low frequency
STC	51-62	58*	54-68
Thickness	5/8"	1 1/8"	1-3/8"
Weight	2.3 lbs/sq ft	3.8 lbs/sq ft	4.4 lbs/sq ft

* In specified QuietHome assembly. Others may vary.

QUIETCOAT, QUIETGLUE, QUIETFOAM, QUIETPUTTY, QUIETSEAL, QUIETTILE

- next generation acoustical products designed for use with QuietRock and QuietWood

FOR MORE INFORMATION

To find out more about our innovative soundproofing products visit **www.soundivide.com** or contact us in Canada at **877 816-5435** For all US inquiries please call Quiet Solution at 800 797-8159

Canadian Acoustical Association

Minutes of the Board of Directors Meeting
12 May 2007
Toronto, Ontario

Present: Stan Dosso (chair), Dalila Giusti, David Quirt, Alberto Behar, Rich Peppin, Christian Giguère, Ramani Ramakrishnan, John Bradley, Tim Kelsall, Clair Wakefield

Regrets: Dave Stredulinsky, Nicole Collison, Anita Lewis, Vijay Parsa

The meeting was called to order at 10:05 a.m. The minutes of Board of Directors meeting on 10 October 2006 were approved as published in Canadian Acoustics (December 2006 issue). *(Moved R. Peppin, second R. Ramakrishnan, carried).*

President's Report

Stan Dosso reported that there have been no major problems in the affairs of the Association. He credits this to sustained efforts by Board members, who have kept all the major activities of the Association proceeding steadily. He suggested that the current priority is to update processes to support the Treasurer and Secretary, which may require some expense. Executive changes (Treasurer, Webmaster and President) are anticipated over the next 6 months. *(R. Peppin moved acceptance of report, second A. Behar, carried)*

Secretary's Report

David Quirt reported that memberships are steady; last year the total was 338 on 20 April, and this year's total on that date is the same.

Mailing list (20 April)	Canada	USA	Other	Change
Member	196	19	9	**+12**
Student	40	1	6	**-10**
Sustaining	36	3	1	–
Direct	2	2	–	**– 3**
Indirect	9	9	4	**+1**
		Total = 338		**(Steady)**

To ease membership renewal, the Secretary and Treasurer have continued the option of payments by VISA; about 41% used this method. A new credit card process is planned this year, as outlined in the Treasurer's report below, to reduce the frequent processing problems. To facilitate CAA communication via e-mail, and reduce errors in mailing *Canadian Acoustics*, systematic updating of membership address data including e-mail was continued in the renewal process; we have working e-mail addresses for over 2/3 of the members.

Secretarial operating costs for FY2006/07 to date were $692 (slightly lower than last year), mainly for mailing costs and postal box rentals.

Issues of Noise News International were mailed as they arrived, to 51 members who requested this option, but shipment from the publisher in the USA is consistently 6 months late, or worse.

With respect to CAA communications, David noted several items:

- Forms for annual filing with Corporations Canada have just been received.
- Invoice from I-INCE has been received and transferred to Treasurer for payment.
- A request for proposals to present an environmental noise course was received from the Municipal Law Enforcement Officers Association in January. CAA could not respond then, but several members expressed interest in pursuing development of such a course. This will be discussed further at the next meeting.
- A brief report on progress organizing InterNoise 2009 in Ottawa was received. This is now a firm commitment, with CAA as a co-sponsor. CAA is invited to nominate members for the Scientific Committee and Organizing Committee. Several members volunteered to participate; further suggestions should be

relayed to the Chair (Trevor Nightingale). It was decided to proceed with the usual CAA conference in October 2009, despite some expected overlap of papers with InterNoise.

- A request has been received from Tony Brammer for CAA to sponsor the 12th International Conference on Hand-Arm Vibration in 2011. The Board agreed to sponsor the conference, but made no commitment on financial involvement. However, the Board decided that for all conference sponsorship, any decision to provide funding must be based on a clear statement of benefit vs. risk for our Association.

As planned, David presented a preliminary set of options for new membership categories and fees, and this induced extended discussion. At this meeting, the Board endorsed specific changes for Emeritus Members, and a new category of "Retired Members". Proposals for other options such as Life Member and Fellow will be discussed in October. It was agreed that David should draft a set of proposals for the October meeting. These will be integrated with proposed fee changes, for presentation to the Annual General Meeting, following our tradition of approving all such changes at the AGM.

Implementation of supplementary charges for mailing institutional subscriptions, for 2008 renewals to USA ($8) and International ($15) was approved. *(Moved A. Behar, second T. Kelsall, carried)*.

Overall, David reported that the routine process of the Association is proceeding without major problems. *(S. Dosso moved acceptance of report, second C. Giguère, carried)*

Treasurer's Report

The Treasurer, Dalila Giusti, submitted a report and a preliminary financial statement, for the fiscal year to date. Most expenses were essentially as budgeted, and the conference in Halifax made a comfortable profit. It is a quite typical year in terms of cash flow, except that advertising revenue is delayed by a backlog in invoicing. The immediate problem is that interest on our capital fund has been very low and will not cover the anticipated $6250 for prizes in October 2007.

Investment strategy for the capital fund was discussed. Interest on GIC's and government bonds (our traditional form of investment) has risen noticeably. Two investment scenarios were submitted for consideration. It was agreed that approximately $220,000 should be invested using Scenario #1 (all GIC's); this will yield more than our annual prize total, with minimal risk. The Treasurer was requested to transfer $40,000 from operating to capital account and proceed with this adjustment of our investments. *(Moved R. Peppin, second R. Ramakrishnan, carried).*

Dalila noted her intent to propose a modest fee increase at the October meeting.

Handling payments by VISA causes operational problems for the treasurer and secretary, due to errors filling in the forms and changes in VISA accounts. Online payment via the website, using a service provider for secure transactions seems promising for both memberships and conference registration. However, the system has to provide suitable information for our records, and permit easy entry of credit card information submitted by mail. Stan will organize an ad hoc group (Dalila, Dave Q., Ramani, Dave S., Geoff, etc.) to investigate this quickly but thoroughly, and present a detailed proposal for e-mail approval by the Board as soon as feasible.

The Treasurer's report was accepted. *(Moved C. Wakefield, second A. Behar, carried.)*

Editor's Report

The Editor, Ramani Ramakrishnan, presented a brief report on issues related to content and publication process for *Canadian Acoustics*.

A special issue is planned in June 2007 featuring papers on medical ultrasound.

Ramani will be on sabbatical at Concordia next year, beginning in September. He anticipates that operation of the journal will proceed as usual, since most stages of publication are handled via email transfer of files. In that context, a template has been developed for authors wishing to submit papers via e-mail.

The major issue of discussion was a new initiative to move to online publication of the journal. One option would be to continue the pilot activity to convert old issues to pdf and develop our own system on the CAA website. However, Ramani is currently investigating another option that seems to offer better cost/benefit for CAA. A 4-year grant from CFI is financing a project to move small Canadian technical journals to online publication. The project includes conversion of old issues and mounting of old and new issues on a server operated by University of Toronto. The system includes password access capabilities, but older issues could be made freely accessible. Our publications would also be included in citation listings and readily accessible to search engines. Ramani will get further details, but was authorized to proceed at his discretion. *(Moved A. Behar, second C. Giguère, carried.)*

CAA Website

Stan Dosso led the discussion on the CAA website, on behalf of Dave Stredulinsky (who is ending his years as webmaster) and Geoff Morrison (who has offered to take over).

One immediate concern is improving the job posting pages using an online form for users to submit their data. The Board authorized spending up to $500 for this purpose. (Moved D. Giusti, second R. Ramakrishnan, carried.)

The option of online payment is under serious consideration for credit card payment of both memberships and conference registration. Dave has contributed strongly to researching our options. Now the Board wants to move ahead rapidly with implementing such a system, as discussed above in the Treasurer's Report.

CAA Conferences – Past, Present & Future

2006 (Halifax): The meeting at the Citadel Hotel in Halifax on 11-13 October 2006 was very successful. The final report has not been submitted, but Nicole Collison, the Chair, provided a preliminary report. Total attendance was 100, with a wide variety of papers, well-attended plenary sessions, 9 exhibits, and outstanding social events. Financially, net income was $4117. The Board expressed their satisfaction with a job well done by the Halifax team.

2007 (Montreal): The organizing team is proceeding with arrangements, led by Rama Bhat of Concordia University. Conference sessions will be in the Engineering and Visual Arts Building at Concordia. See *Canadian Acoustics* and the website for details.

Vancouver (2008): A team to organize the conference has been confirmed, with Murray Hodgson as Chair.

Awards

Christian Giguère presented a report. The submission deadline has just passed, and there appear to be valid applications for all awards. Rules for two specific prizes were considered:

- For student presentation awards at the conference, it was agreed that the judging process should be handled at discretion of the coordinator (currently A. Behar), with the guidance that having more papers per judge is desirable and using raw judging scores is acceptable. For student presentation awards, the Board authorized funds for up to four prizes of $500; four will be awarded if there is a tie for third place. *(Moved D. Quirt, second S. Dosso, carried.)*
- For the Canada-Wide Science Fair, the Board confirmed the previous e-mail ballot to award a prize in the junior category this year ($1000 cost), and supported including a brief paper in *Canadian Acoustics,* as in 2006. *(Moved D. Giusti, second A. Behar, carried.)*

A master list of award winners is nearly finished and will be added to the CAA website. The Board thanked Christian and his Coordinators.

Adjournment

Meeting adjourned at 2:10 p.m.
(Moved D. Quirt, second A. Behar, carried.)

Modular *Platform*

Type 2250's combination of software modules and innovative hardware makes the analyzer a dedicated solution for high-precision measurement tasks, in environmental, occupational and industrial noise application areas.

New software modules can easily be added, thus giving you the option of adding more functionality as your measurement requirements change. This way the platform ensures that your investment is securely protected now and in the future.

Currently available applications include:

- **Frequency Analysis Software** – for real-time analysis of 1/1- and 1/3-octave bands
- **Logging Software** – log broadband data and spectra at intervals from 1 s to 24 h
- **Enhanced Logging Software** – for continuous monitoring and logging of periodic reports
- **Sound Recording Option** – record measurements signals to identify and document sound sources

Type 2250 has been designed in co-operation with users to be easy, safe and clever.

For more information please contact your local sales representative or go to ***www.type2250.com***

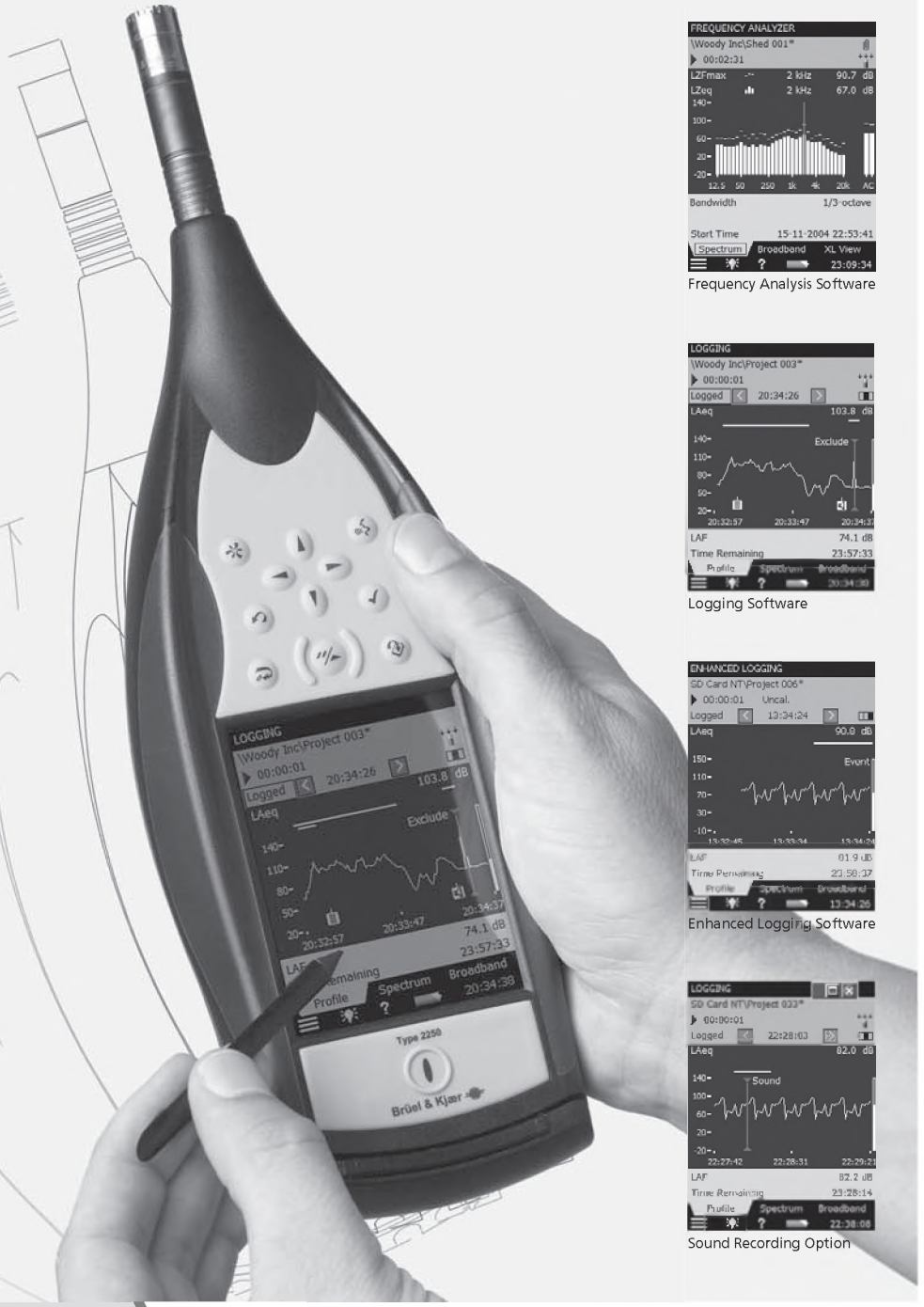

Frequency Analysis Software

Logging Software

Enhanced Logging Software

Sound Recording Option

HEADQUARTERS: DK-2850 Nærum · Denmark · Telephone: +4545800500
Fax: +4545801405 · www.bksv.com · info@bksv.com

USA: 2815 Colonnades Court · Norcross, GA 30071
Toll free (800) 332-2040 · www.BKhome.com · bkinfo@bksv.com

Hand-held Analyzer *Type 2250*

Brüel & Kjær

The Canadian Acoustical Association
L'Association Canadienne d'Acoustique

PRIZE ANNOUNCEMENT • ANNONCE DE PRIX

A number of prizes and subsidies are offered annually by The Canadian Acoustical Association. Applicants can obtain full eligibility conditions, deadlines, application forms, past recipients, and the names of the individual prize coordinators on the CAA Website (http://www.caa-aca.ca). • Plusieurs prix et subventions sont décernés à chaque année par l'Association Canadienne d'Acoustique. Les candidats peuvent se procurer de plus amples renseignements sur les conditions d'éligibilités, les échéances, les formulaires de demande, les récipiendaires des années passées ainsi que le nom des coordonnateurs des prix en consultant le site Internet de l'ACA (http://www.caa-aca.ca).

CAA conference Student Travel subsidies: visit **http://users.encs.concordia.ca/~caa-2007/**
Subventions pour frais de déplacement pour étudiants au congrès annuel de l'ACA : voir **http://users.encs.concordia.ca/~caa-2007/**

EDGAR AND MILLICENT SHAW POSTDOCTORAL PRIZE IN ACOUSTICS • PRIX POST-DOCTORAL EDGAR AND MILLICENT SHAW EN ACOUSTIQUE

$3,000 for full-time postdoctoral research training in an established setting other than the one in which the Ph.D. was earned. The research topic must be related to some area of acoustics, psychoacoustics, speech communication or noise. • $3,000 pour une formation recherche à temps complet au niveau postdoctoral dans un établissement reconnu autre que celui où le candidat a reçu son doctorat. Le thème de recherche doit être relié à un domaine de l'acoustique, de la psycho-acoustique, de la communication verbale ou du bruit.

ALEXANDER GRAHAM BELL GRADUATE STUDENT PRIZE IN SPEECH COMMUNICATION AND HEARING • PRIX ÉTUDIANT ALEXANDRE GRAHAM BELL EN COMMUNICATION VERBALE ET AUDITION

$800 for a graduate student enrolled at a Canadian institution and conducting research in the field of speech communication or hearing • $800 à un(e) étudiant(e) inscrit(e) au 2e ou 3e cycle universitaire dans une institution canadienne et menant un projet de recherche en communication verbale ou en audition.

FESSENDEN GRADUATE STUDENT PRIZE IN UNDERWATER ACOUSTICS • PRIX ÉTUDIANT FESSENDEN EN ACOUSTIQUE SOUS-MARINE

$500 for a graduate student enrolled at a Canadian institution and conducting research in underwater acoustics or in a branch of science closely connected to underwater acoustics. • $500 à un(e) étudiant(e) inscrit(e) au 2e ou 3e cycle universitaire dans une institution canadienne et menant un projet de recherche en acoustique sous-marine ou dans une discipline reliée à l'acoustique sous-marine.

ECKEL GRADUATE STUDENT PRIZE IN NOISE CONTROL • PRIX ÉTUDIANT ECKEL EN CONTRÔLE DU BRUIT

$500 for a graduate student enrolled at a Canadian institution and conducting research related to the advancement of the practice of noise control. • $500 à un(e) étudiant(e) inscrit(e) au 2e ou 3e cycle universitaire dans une institution canadienne et menant un projet de recherche relié à l'avancement des pratiques en contrôle du bruit.

RAYMOND HÉTU UNDERGRADUATE PRIZE IN ACOUSTICS • PRIX ÉTUDIANT RAYMOND HÉTU EN ACOUSTIQUE

One book in acoustics of a maximum value of $150 and a one-year subscription to *Canadian Acoustics* for an undergraduate student enrolled at a Canadian institution and having completed, during the year of application, a project in any field of acoustics or vibration. • Un livre sur l'acoustique d'un montant maximal de 150 $ et un abonnement d'un an à la revue *Acoustique Canadienne* à un(e) étudiant(e) inscrit(e) dans un programme au 1er cycle universitaire dans une institution canadienne et qui a réalisé, durant l'année de la demande, un projet dans le domaine de l'acoustique ou des vibrations.

CANADA-WIDE SCIENCE FAIR AWARD • PRIX EXPO-SCIENCES PANCANADIENNE

$400 and a one-year subscription to *Canadian Acoustics* for the best project related to acoustics at the Fair by a high-school student • $400 et un abonnement d'un an à la revue *Acoustique Canadienne* pour le meilleur projet relié à l'acoustique à l'Expo-sciences par un(e) étudiant(e) du secondaire.

DIRECTORS' AWARDS • PRIX DES DIRECTEURS

One $500 award for the best refereed research, review or tutorial paper published in *Canadian Acoustics* by a student member and one $500 award for the best paper by an individual member • $500 pour le meilleur article de recherche, de recensement des travaux ou d'exposé didactique arbitré publié dans l'*Acoustique Canadienne* par un membre étudiant et $500 pour le meilleur article par un membre individuel.

STUDENT PRESENTATION AWARDS • PRIX POUR COMMUNICATIONS ÉTUDIANTES

Three $500 awards for the best student oral presentations at the Annual Symposium of The Canadian Acoustical Association. • Trois prix de $500 pour les meilleures communications orales étudiant(e)s au Symposium Annuel de l'Association Canadienne d'Acoustique.

STUDENT TRAVEL SUBSIDIES • SUBVENTIONS POUR FRAIS DE DÉPLACEMENT POUR ÉTUDIANTS

Travel subsidies are available to assist student members who are presenting a paper during the Annual Symposium of The Canadian Acoustical Association if they live at least 150 km from the conference venue. • Des subventions pour frais de déplacement sont disponibles pour aider les membres étudiants à venir présenter leurs travaux lors du Symposium Annuel de l'Association Canadienne d'Acoustique, s'ils demeurent à au moins 150 km du lieu du congrès.

UNDERWATER ACOUSTICS AND SIGNAL PROCESSING STUDENT TRAVEL SUBSIDIES • SUBVENTIONS POUR FRAIS DE DÉPLACEMENT POUR ÉTUDIANTS EN ACOUSTIQUE SOUS-MARINE ET TRAITEMENT DU SIGNAL

One $500 or two $250 awards to assist students traveling to national or international conferences to give oral or poster presentations on underwater acoustics and/or signal processing. • Une bourse de $500 ou deux de $250 pour aider les étudiant(e)s à se rendre à un congrès national ou international pour y présenter une communication orale ou une affiche dans le domaine de l'acoustique sous-marine ou du traitement du signal.

SUPERIOR SOUND ISOLATION

Visit audioalloy.com to learn more

Green Glue Assembly

Low Frequency: Great
56 STC Rating
39 OITC

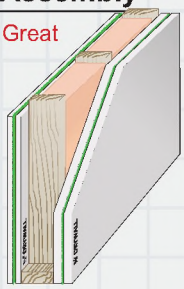

Soundboard

Low Frequency: Poor
46 STC Rating
32 OITC

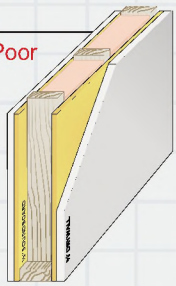

Conventional Drywall

Low Frequency: Poor
44 STC Rating
33 OITC

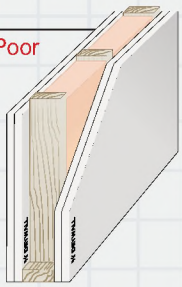

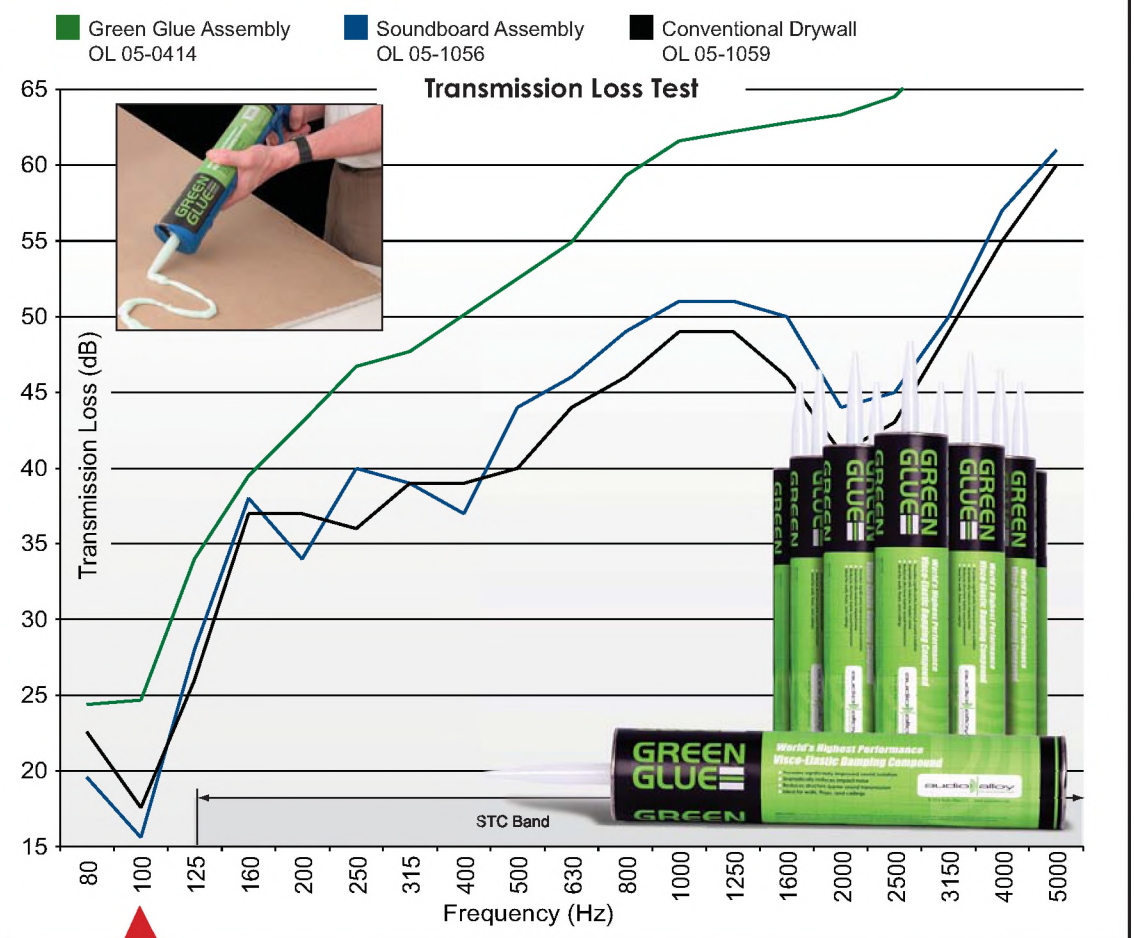

FOR SUPERIOR WALLS & FLOORS

GREEN GLUE

Third party
NVLAP
ACCREDITED LAB
results are available at
AudioAlloy.com

Large commercial job?
Green Glue is available in large 55 gallon drum and 5 gallon pails for commerical use.

Sound isolation problems are low frequency problems

Most sound isolation problems occur at frequencies below 125 Hz. Sources include subwoofers, auto and air traffic. Unfortunately the common STC system does not consider performance below 125 Hz. and that's where most of your problems are.

Questions & Sales: (989) 832-1602
www.audioalloy.com | info@audioalloy.com

- Superior Low Frequency Isolation
- Low Cost per square foot
- Easy Application
- Can be used over existing walls
- Dramatically reduces impact noise
- Reduces structure-borne sound transmission
- Ideal for walls, floor, and ceiling
- Third party NVLAP accredited lab results are available online.

audio alloy
the sound stops here

Canadian Acoustic Association Annual Conference

2007

CONCORDIA UNIVERSITY

Faculty of Engineering and Computer Science, Montreal, Canada
October 9-12, 2007

The Canadian Acoustical Association (CAA) Annual conference attracts researchers in various fields of Acoustical Sciences and Engineering, and Auditory Perception. The theme for the 2007 conference will be **AEROACOUSTICS,** befitting the reputation of Montreal as the "Aerospace Capital of the World". There will be three days of parallel sessions on diverse areas of acoustics, including some special sessions on emerging topics as well as an interesting array of exhibits showcasing acoustical applications and products.

Venue of the Conference

The conference will be held in the attractive new Engineering and Visual Arts Complex of the Concordia University in downtown Montreal. CAA conferences are always an opportunity to inform ourselves on the state of acoustical research, new developments, emerging topics. It is also an opportunity to meet our friends and to make new ones over a coffee during the conference, or over a drink after the sessions. The participants can enjoy Montreal filled with colors of Fall in the backdrop of comfortable October weather. In addition to the technical sessions, you are invited to attend the industrial exhibits of acoustic products, and a banquet.

Goals

- To provide a national and international forum for communicating most recent advances in the field of acoustics and auditory perception
- To provide an opportunity for information exchange among delegates from industry, research labs and academia.

Special Sessions

Several special sessions will be organized that will include invited and contributed papers in the areas of Aeroacoustics, Building Acoustics, Musical Acoustics, Audiology/Bioacoustics, Noise Control, Speech Communication, Instrumentation & Signal Processing in Acoustics, Acoustic Standards and Environmental Acoustics, Thermoacoustics, Electroacoustics, Photo Acoustics, Micro/Nano Acoustics. If you are interested in organizing a special session, please contact K. Siddiqui, the Technical Chair (technical-chair@caa-aca.ca).

Exhibits & Sponsors

During the conference there will be an interesting array of exhibits of acoustical products and services. The exhibit area will also be the central coffee break area. Please contact M. Packirisamy, the exhibit coordinator (exhibits@caa-aca.ca) for exhibitor information and sponsorship of various aspects of this conference.

Student Participation

Student members enrolled in Canadian universities may also enter into a competition for the best student presentation award. The student presenters may also get travel subsidy if they submit the request before 15th September 2007. This subsidy is subject to the availability of funds.

Important Dates

8 June 2007	- 250 word abstract
22 June 2007	- Notice of acceptance
16 July 2007	- 2 page paper
15 Sept. 2007	- Early registration Deadline
9 to 12 Oct. 2007	- Conference Dates

Organizing Committee

Conference Chair: R. Bhat conference@caa-aca.ca
Technical Programs Chair: K. Siddiqui technical-chair@caa-aca.ca
Exhibits Chair: M. Packirisamy exhibits@caa-aca.ca
Publications Chair: S. Narayanswamy conf-web@caa-aca.ca
Finance Chair: Z. Chen conf-treasurer@caa-aca.ca
Logistics Chair: W. Xie logistics-technical@caa-aca.ca

Conference URL: http://users.encs.concordia.ca/~caa-2007

Association Canadienne d'Acoustique
Congrès Annuel

2007

Université Concordia
Faculté de Génie et d'informatique
Montréal, Canada
du 9 au 12 Octobre 2007

L'Association Canadienne d'Acoustique (ACA) regroupe des chercheurs dans divers champs de génie et des sciences acoustiques, et les recherches sur la perception auditive. Le congrès annuel de l'association aura pour thème l'**AÉROACOUSTIQUE** en accord avec la réputation de Montréal comme "capitale mondiale de l'aérospatiale". La conférence de trois jours est organisée en session parallèles autour de divers domaines de l'acoustique et de la perception auditive, dont des séances spéciales et des expositions de produits acoustiques.

Lieu et hébergement
Le congrès se déroulera au centre-ville de Montréal, dans le très beau pavillon intégré Génie, informatique et arts visuels de l'Université Concordia. Les congrès de l'ACA fournissent toujours une occasion aux participants pour s'informer sur l'état courant des recherches en acoustique, nouveau développement et les sujets émergents. C'est aussi une excellente occasion de rencontrer nos amis et de faire de nouvelles connaissances durant les pauses café de la conférence. Les participants auront la chance d'apprécier la beauté de l'automne à Montréal en Octobre. En plus d'assister aux sessions techniques, les participants sont invités à des expositions par les industries sur leurs produits acoustiques et le banquet.

Objectifs
- Fournir un forum national et international pour partager les plus récentes avancées en matières de l'acoustique et de la perception auditive.
- Offrir une occasion pour l'échange d'information entre les représentants de l'industrie, des laboratoires de recherche et du milieu universitaire.

Séances spéciales
Un nombre de sessions spéciales seront organisées et présenteront des communications soumises et invitées sur le thèmes de l'Aéroacoustique, Acoustique des bâtiments, Acoustique musicale, Audiologie/Bioacoustique, Contrôle acoustique, Communication verbale, Instrumentation et traitement des signaux en acoustique, Normes acoustiques, Acoustique environnementale, Thermoacoustique, Électroacoustique, Photoacoustique, Micro/Nano acoustique. Pour en organiser une, veuillez contacter le président du comité technique à (technical-chair@caa-aca.ca).

Expositions est Commanditaires
Durant la conférence il y aura des espaces disponibles pour les présentations de services et produits acoustiques. Les espaces d'exposition seront également les espaces de pause. Prière de contacter M. Packirisamy, coordonnateur des expositions (exhibits@caa-aca.ca), pour tout renseignement sur les exposants et sur les possibilités de commanditer des activités du congrès.

Participation étudiants
Les étudiants inscrits à une université Canadienne sont éligibles pour le **Prix** de la meilleure communication étudiante. Les étudiants qui présenteront leur communications sont aussi admissibles à une subvention de déplacement, à condition de soumettre leur demande avant le 15 septembre 2007, sous réserve de la disponibilité des fonds.

Dates Importantes

8 Juin 2007	- Sommaire de 250 mots
22 Juin 2007	- Avis d'acceptation
16 Juillet 2007	- Communication de 2 pages
15 Septembre 2007	- Date limite pour le préinscription
9 au 12 Oct. 2007	- Congrès annuel

Comité organisateur
Président du congrès: R. Bhat conference@caa-aca.ca
Président Comité technique: K. Siddiqui technical-chair@caa-aca.ca
Coordonnateur des expositions: M. Packirisamy exhibits@caa-aca.ca
Chair des publications: S. Narayanswamy conf-web@caa-aca.ca
Trésorier: Z. Chen conf-treasurer@caa-aca.ca
Chair des logistiques: W. Xie logistics-technical@caa-aca.ca

Conférence URL: http://users.encs.concordia.ca/~caa-2007

INSTRUCTIONS TO AUTHORS FOR THE PREPARATION OF MANUSCRIPTS

Submissions: The original manuscript and two copies should be sent to the Editor-in-Chief.

General Presentation: Papers should be submitted in camera-ready format. Paper size 8.5" x 11". If you have access to a word processor, copy as closely as possible the format of the articles in Canadian Acoustics 18(4) 1990. All text in Times-Roman 10 pt font, with single (12 pt) spacing. Main body of text in two columns separated by 0.25". One line space between paragraphs.

Margins: Top - title page: 1.25"; other pages, 0.75"; bottom, 1" minimum; sides, 0.75".

Title: Bold, 14 pt with 14 pt spacing, upper case, centered.

Authors/addresses: Names and full mailing addresses, 10 pt with single (12 pt) spacing, upper and lower case, centered. Names in bold text.

Abstracts: English and French versions. Headings, 12 pt bold, upper case, centered. Indent text 0.5" on both sides.

Headings: Headings to be in 12 pt bold, Times-Roman font. Number at the left margin and indent text 0.5". Main headings, numbered as 1, 2, 3, ... to be in upper case. Sub-headings numbered as 1.1, 1.2, 1.3, ... in upper and lower case. Sub-sub-headings not numbered, in upper and lower case, underlined.

Equations: Minimize. Place in text if short. Numbered.

Figures/Tables: Keep small. Insert in text at top or bottom of page. Name as "Figure 1, 2, ..." Caption in 9 pt with single (12 pt) spacing. Leave 0.5" between text.

Line Widths: Line widths in techincal drawings, figures and tables should be a minimum of 0.5 pt.

Photographs: Submit original glossy, black and white photograph.

Scans: Should be between 225 dpi and 300 dpi. Scan: Line art as bitmap tiffs; Black and white as grayscale tiffs and colour as CMYK tiffs;

References: Cite in text and list at end in any consistent format, 9 pt with single (12 pt) spacing.

Page numbers: In light pencil at the bottom of each page.
Reprints: Can be ordered at time of acceptance of paper.

DIRECTIVES A L'INTENTION DES AUTEURS PREPARATION DES MANUSCRITS

Soumissions: Le manuscrit original ainsi que deux copies doivent être soumis au rédacteur-en-chef.

Présentation générale: Le manuscript doit comprendre le collage. Dimensions des pages, 8.5" x 11". Si vous avez accès à un système de traitement de texte, dans la mesure du possible, suivre le format des articles dans l'Acoustique Canadienne 18(4) 1990. Tout le texte doit être en caractères Times-Roman, 10 pt et à simple (12 pt) interligne. Le texte principal doit être en deux colonnes séparées d'un espace de 0.25". Les paragraphes sont séparés d'un espace d'une ligne.

Marges: Dans le haut - page titre, 1.25"; autres pages, 0.75"; dans le bas, 1" minimum; latérales, 0.75".

Titre du manuscrit: 14 pt à 14 pt interligne, lettres majuscules, caractères gras. Centré.

Auteurs/adresses: Noms et adresses postales. Lettres majuscules et minuscules, 10 pt à simple (12 pt) interligne. Centré. Les noms doivent être en caractères gras.

Sommaire: En versions anglaise et française. Titre en 12 pt, lettres majuscules, caractères gras, centré. Paragraphe 0.5" en alinéa de la marge, des 2 cotés.

Titres des sections: Tous en caractères gras, 12 pt, Times-Roman. Premiers titres: numéroter 1, 2, 3, ..., en lettres majuscules; sous-titres: numéroter 1.1, 1.2, 1.3, ..., en lettres majuscules et minuscules; sous-sous-titres: ne pas numéroter, en lettres majuscules et minuscules et soulignés.

Equations: Les minimiser. Les insérer dans le texte si elles sont courtes. Les numéroter.

Figures/Tableaux: De petites tailles. Les insérer dans le texte dans le haut ou dans le bas de la page. Les nommer "Figure 1, 2, 3,..." Légende en 9 pt à simple (12 pt) interligne. Laisser un espace de 0.5" entre le texte.

Largeur Des Traits: La largeur des traits sur les schémas technique doivent être au minimum de 0.5 pt pour permettre une bonne reproduction.

Photographies: Soumettre la photographie originale sur papier glacé, noir et blanc.

Figures Scanées: Doivent être au minimum de 225 dpi et au maximum de 300 dpi. Les schémas doivent être scannés en bitmaps tif format. Les photos noir et blanc doivent être scannées en échelle de gris tifs et toutes les phoots couleurs doivent être scannées en CMYK tifs.

Références: Les citer dans le texte et en faire la liste à la fin du document, en format uniforme, 9 pt à simple (12 pt) interligne.

Pagination: Au crayon pâle, au bas de chaque page.
Tirés-à-part: Ils peuvent être commandés au moment de l'acceptation du manuscrit.

The Canadian Acoustical Association
l'Association Canadienne d'Acoustique

Application for Membership

CAA membership is open to all individuals who have an interest in acoustics. Annual dues total $60.00 for individual members and $20.00 for Student members. This includes a subscription to ***Canadian Acoustics***, the Association's journal, which is published 4 times/year. New membership applications received before August 31 will be applied to the current year and include that year's back issues of ***Canadian Acoustics***, if available. New membership applications received after August 31 will be applied to the next year.

Subscriptions to *Canadian Acoustics* *or* Sustaining Subscriptions

Subscriptions to ***Canadian Acoustics*** are available to companies and institutions at the institutional subscription price of $60.00. Many companies and institutions prefer to be a Sustaining Subscriber, paying $300.00 per year, in order to assist CAA financially. A list of Sustaining Subscribers is published in each issue of ***Canadian Acoustics***. Subscriptions for the current calendar year are due by January 31. New subscriptions received before August 31 will be applied to the current year and include that year's back issues of ***Canadian Acoustics***, if available.

Please note that electronic forms can be downloaded from the CAA Website at **caa-aca.ca**

Address for subscription / membership correspondence:

Name / Organization _____

Address _____

City/Province _____ Postal Code _____ Country _____

Phone _____ Fax _____ E-mail _____

Address for mailing Canadian Acoustics, if different from above:

Name / Organization _____

Address _____

City/Province _____ Postal Code _____ Country _____

Areas of Interest: (Please mark 3 maximum)

1. Architectural Acoustics
2. Engineering Acoustics / Noise Control
3. Physical Acoustics / Ultrasound
4. Musical Acoustics / Electro-acoustics
5. Psychological / Physiological Acoustic
6. Shock and Vibration
7. Hearing Sciences
8. Speech Sciences
9. Underwater Acoustics
10. Signal Processing / Numerical Methods
11. Other

For student membership, please also provide:

_____ _____ _____ _____

(University) *(Faculty Member)* *(Signature of Faculty Member)* *(Date)*

I have enclosed the indicated payment for:

[ ] CAA Membership $ 60.00
[ ] CAA Student Membership $ 20.00
[ ] Institutional Subscription $ 60.00
[ ] Sustaining Subscriber $ 300.00
includes subscription (4 issues /year) to ***Canadian Acoustics.***

Payment by: [ ] Cheque
[ ] Money Order
[ ] VISA credit card *(Only VISA accepted)*

For payment by VISA credit card:

Card number _____

Name of cardholder _____

Expiry date _____

_____
(Signature) (Date)

Mail application and attached payment to:

D. Quirt, Secretary, Canadian Acoustical Association, PO Box 74068, Ottawa, Ontario, K1M 2H9, Canada

l'Association Canadienne d'Acoustique
The Canadian Acoustical Association

Formulaire d'adhésion

L'adhésion à l'ACA est ouverte à tous ceux qui s'intéressent à l'acoustique. La cotisation annuelle est de 60.00$ pour les membres individuels, et de 20.00$ pour les étudiants. Tous les membres reçoivent ***l'Acoustique Canadienne***, la revue de l'association. Les nouveaux abonnements reçus avant le 31 août s'appliquent à l'année courante et incluent les anciens numéros (non-épuisés) de ***l'Acoustique Canadienne*** de cette année. Les nouveaux abonnements reçus après le 31 août s'appliquent à l'année suivante.

Abonnement pour la revue *Acoustique Canadienne* et abonnement de soutien

Les abonnements pour la revue ***Acoustique Canadienne*** sont disponibles pour les compagnies et autres établissements au coût annuel de 60.00$. Des compagnies et établissements préfèrent souvent la cotisation de membre bienfaiteur, de 300.00$ par année, pour assister financièrement l'ACA. La liste des membres bienfaiteurs est publiée dans chaque issue de la revue ***Acoustique Canadienne***. Les nouveaux abonnements reçus avant le 31 août s'appliquent à l'année courante et incluent les anciens numéros (non-épuisés) de ***l'Acoustique Canadienne*** de cette année. Les nouveaux abonnements reçus après le 31 août s'appliquent à l'année suivante.

Pour obtenir des formulaires electroniques, visitez le site Web: **caa-aca.ca**

Pour correspondence administative et financière:

Nom / Organisation _____

Adresse _____

Ville/Province _____ Code postal _____Pays _____

Téléphone _____ Téléc. _____ Courriel _____

Adresse postale pour la revue Acoustique Canadienne

Nom / Organisation _____

Adresse _____

Ville/Province _____ Code postal _____Pays _____

Cocher vos champs d'intérêt: (maximum 3)

1. Acoustique architecturale
2. Génie acoustique / Contrôle du bruit
3. Acoustique physique / Ultrasons
4. Acoustique musicale / Electro-acoustique
5. Physio / Psycho-acoustique
6. Chocs et vibrations
7. Audition
8. Parole
9. Acoustique sous-marine
10. Traitement des signaux /Méthodes numériques
11. Autre

Prière de remplir pour les étudiants et étudiantes:

_____ _____ _____ _____

(Université) (Nom d'un membre du corps professoral) (Signature du membre du corps professoral) (Date)

Cocher la case appropriée:

[ ] Membre individuel $ 60.00
[ ] Membre étudiant(e) $ 20.00
[ ] Abonnement institutionnel $ 60.00
[ ] Abonnement de soutien $ 300.00
(comprend l'abonnement à ***L'acoustique Canadienne)***

Méthode de paiement:

[ ] Chèque au nom de l'Association Canadienne d'Acoustique
[ ] Mandat postal
[ ] VISA *(Seulement VISA)*

Pour carte VISA: Carte n° _____

Nom _____

Date d'expiration _____

_____

(Signature) (Date)

Prière d'attacher votre paiement au formulaire d'adhésion. Envoyer à :

Secrétaire exécutif, Association Canadienne d'Acoustique, Casier Postal 74068, Ottawa, K1M 2H9, Canada

The Canadian Acoustical Association
l'Association Canadienne d'Acoustique

SUSTAINING SUBSCRIBERS / ABONNES DE SOUTIEN

The Canadian Acoustical Association gratefully acknowledges the financial assistance of the Sustaining Subscribers listed below. Their annual donations (of $300.00 or more) enable the journal to be distributed to all at a reasonable cost.

L'Association Canadienne d'Acoustique tient à témoigner sa reconnaissance à l'égard de ses Abonnés de Soutien en publiant ci-dessous leur nom et leur adresse. En amortissant les coûts de publication et de distribution, les dons annuels (de $300.00 et plus) rendent le journal accessible à tous nos membres.

ACI Acoustical Consultants Inc.
Mr. Steven Bilawchuk - (780) 414-6373
stevenb@aciacoustical.com - Edmonton, AB

Acoustik GE Inc.
M. Gilles Elhadad - (514) 487 7159
acoustikge@videotron.ca - Cote St Luc, QC

Dalimar Instruments Inc.
Mr. Daniel Larose - (514) 424-0033
daniel@dalimar.ca - Vaudreuil-Dorion, QC

Eckel Industries of Canada Ltd.
Mr. Bruce Allan - (613) 543-2967
eckel@eckel.ca - Morrisburg, ON

Hatch Associates Ltd.
Mr. Tim Kelsall - (905) 403-3932
tkelsall@hatch.ca - Mississauga, ON

Integral DX Engineering Ltd.
Mr. Greg Clunis - (613) 761-1565
greg@integraldxengineering.ca - Ottawa, ON

Jade Acoustics Inc.
Ms. Dalila Giusti - (905) 660-2444
dalila@jadeacoustics.com - Concord, ON

MJM Conseillers en Acoustique Inc.
MJM Acoustical Consultants Inc.
M. Michel Morin- (514) 737-9811
mmorin@mjm.qc.ca - Montréal, QC

OZA Inspections Ltd.
Mr. David Williams - (800) 664-8263x25
oza@ozagroup.com - Grimsby, ON

Michel Picard
(514) 343-7617; FAX: (514) 343-2115
michel.picard@umontreal.ca - Brossard, QC

Royal Mat Inc
R. Ducharme, (418) 774-3694
R.Ducharme@Royalmat.com - Beauceville, QC

SNC/Lavalin Environment Inc.
M. Jean-Luc Allard - (514) 651-6710
jeanluc.allard@snclavalin.com - Longueuil, QC

Spaarg Engineering Ltd.
Dr. Robert Gaspar - (519) 972-0677,
gasparr@kelcom.igs.net - Windsor, ON

Tacet Engineering Ltd.
Dr. M.P. Sacks - (416) 782-0298
mal.sacks@tacet.ca - Toronto, ON

Wakefield Acoustics Ltd.
Mr. Clair Wakefield - (250) 370-9302
nonoise@shaw.ca - Victoria, BC

Wilrep Ltd.
Mr. Don Wilkinson - (905) 625-8944
info@wilrep.com - Mississauga, ON

ACO Pacific Inc.
Mr. Noland Lewis - (650) 595-8588
acopac@acopacific.com - Belmont, CA

Aercoustics Engineering Ltd
Mr. John O'Keefe - (416) 249-3361
aercoustics@aercoustics.com - Rexdale, ON

Dodge-Regupol
Mr. Paul Downey - (416) 440-1094
pcd@regupol.com - Toronto, ON

Enviro Noise Control Corp.
Alex V. Tardecilla - (403) 279-2764
alext@enctech.net - Calgary, AB

HGC Engineering Ltd.
Mr. Bill Gastmeier - (905) 826-4044
info@hgcengineering.com - Mississauga, ON

J.E. Coulter Associates Ltd.
Mr. John Coulter - (416) 502-8598
jcoulter@on.aibn.com - Toronto, ON

JASCO Research Ltd.
Mr. Scott Carr - (902) 405-3336
scott@jasco.com - Halifax, NS

Noble Environmental Power LLC
c/o Anna Giovinetto - (860) 581-5010
giovinettoa@noblepower.com - Essex, CT

Owens-Corning Canada Inc.
Mr. Salvatore Ciarlo - (800) 988-5269
salvatore.ciarlo@owenscorning.com - St.Leonard, QC

Pinchin Environmental Ltd.
(905) 363-0678; FAX: (905) 363-0681
nwilliams@pinchin.com - Mississauga, ON

Scantek Inc.
Mr. Richard J. Peppin - (410)-290-7726
peppinr@scantekinc.com, Columbia, MD

Soft dB Inc.
M. André L'Espérance - (418) 686-0993
contact@softdb.com - Sillery, QC

State of the Art Acoustik Inc.
Dr. C. Fortier - (613) 745-2003
sota@sota.ca - Ottawa, ON

Valcoustics Canada Ltd.
Dr. Al Lightstone - (905) 764-5223
solutions@valcoustics.com - Richmond Hill, ON

Water & Earth Science Associates (WESA)
Dejan Zivkovic, M.Sc. - (905) 639-5789 x151
dzivkovic@wesa.ca - Burlington

Acoustec Inc.
Dr. J.G. Migneron - (418) 834-1414
courrier@acoustec.qc.ca - St-Nicolas, QC

Bruel & Kjaer North America Inc.
Mr. Andrew Khoury - (514) 695-8225
andrew.khoury@bksv.com - Pointe-Claire, QC

Earth Tech Canada Inc.
Miroslav Ubovic - (905) 886-7022-x2215
noisevibration@earthtech.ca - Markham, ON

H.L. Blachford Ltd.
Mr. Dalton Prince - (905) 823-3200
amsales@blachford.ca - Mississauga, ON

Hydro-Quebec
M. Blaise Gosselin - (514) 840-3000x5134
gosselin.blaise@hydro.qc.ca - Montréal, QC

J.L.Richards & Assoc. Ltd.
Mr. Terry Vivyurka, P.Eng. - (613) 728-3571
mail@jlrichards.ca - Ottawa, ON

Mc SQUARED System Design Group
Mr. Wade McGregor - (604) 986-8181
info@mcsquared.com - North Vancouver, BC

Novel Dynamics Test Inc.
Mr. Andy Metelka - (519) 853-4495
metelka@aztec-net.com - Acton, ON

Peutz & Associés
M. Marc Asselineau +33 1 45230500
marc.asselineau@club-internet.fr
Paris, FRANCE

Pyrok Inc.
Mr. Howard Podolsky - (914) 777-7770
info@pyrokinc.com - Mamaroneck, NY

SILEX Innovations Inc.
Mr. Mehmood Ahmed - (905) 612-4000
mehmooda@silex.com - Mississauga, ON

SounDivide Inc.
C.W. Roy Bakker - (416) 208-3040
roy.bakker@SounDivide.com - Mississauga, ON

Swallow Acoustic Consultants Ltd.
Mr. John Swallow - (905) 271-7888
jswallow@jsal.ca - Mississauga, ON

Vibro-Acoustics
Mr. Tim Charlton - (800) 565-8401
tcharlton@vibro-acoustics.com - Scarborough, ON

West Caldwell Calibration Labs
Mr. Stanley Christopher - (905) 595-1107
info@wccl.com - Brampton, ON